

UNIVERSITÉ DU QUÉBEC  
INSTITUT NATIONAL DE LA RECHERCHE SCIENTIFIQUE  
Centre Énergie Matériaux et Télécommunications

# **SURFACE-CONFINED REACTIONS OF AROMATIC MOLECULES**

**Laurentiu Eugeniu DINCA**

Thèse présentée pour obtenir le grade de  
Philosophiae Doctor, Ph.D.  
Doctorat en Sciences de l'Énergie et des Matériaux

Membres Du Jury:

Directeur de recherche: Prof. Federico ROSEI, INRS-EMT, Université du Québec

Codirectrice: Prof. Dongling MA, INRS-EMT, Université du Québec

Examineur interne, et président: Prof. Royston PAYNTER,  
INRS-EMT, Université du Québec

Examineur externe: Prof. Antonella BADIA, Université de Montréal

Examineur externe: Prof. Louis CUCCIA, Université Concordia

UNIVERSITY OF QUÉBEC  
NATIONAL INSTITUTE FOR SCIENTIFIC RESEARCH  
Center for Energy, Materials and Telecommunications

# **SURFACE-CONFINED REACTIONS OF AROMATIC MOLECULES**

**Laurentiu Eugeniu DINCA**

A thesis submitted to the Department of Energy and Materials  
in conformity with the requirements for  
the degree of Doctor of Philosophy, Ph.D

Jury Members:

Director of research: Prof. Federico ROSEI, INRS-EMT, University of Québec

Co-director: Prof. Dongling MA, INRS-EMT, University of Québec

Internal examiner and president: Prof. Royston PAYNTER,  
INRS-EMT, University of Québec

External examiner: Prof. Antonella BADIA, University of Montreal

External examiner: Prof. Louis CUCCIA, Concordia University

# Abstract

The imaging and characterization of single-molecule reaction events is essential to both extending our basic understanding of chemistry and to applying these notions to face challenges at the frontiers of technology, *e.g.* in nanoelectronics. Driven by this demand, the aim of this work was to study the behavior of a few, closely related, aromatic molecules, giving special attention to their specific nanoscale transformations induced by surfaces on which they were resident. Even though conceptually unified, this work spanned several different projects that demanded different specific approaches.

Altogether, this work focuses on the catalytic processes occurring within the framework of surface confinement. The surface science approach to studying catalysis, and the subdivision of complex systems into basic, easy to model and study components, was first advocated by Ertl,<sup>1, 2</sup> Similar to his proposed method, in my studies we used atomically flat and clean single crystal surfaces under ultra-high vacuum (UHV) conditions as model catalysts. At this scale, scanning tunneling microscopy (STM) is a useful tool to reveal, indirectly, catalytic phenomena by imaging dissociative adsorption and the eventual recombination of molecules in various assemblies.

Herein, are reported well-directed studies of thiophene derivatives on Ni(111) (tetrabromo-tetrathieno-anthracene — TBTTA), and the synthesis of an important semiconducting organic molecule through a reaction of sulfur abstraction, observed with sub-molecular resolution. With no known literature analogue, this reaction allowed for the formation of new intramolecular C–C bonds, and cyclization to an unanticipated polycyclic five-ring linear product that was identified as pentacene. However, as STM yields limited structural information and chemical contrast, it was complemented with an additional analysis technique for the unambiguous identification of products, in our case time-of-flight secondary ion mass spectrometry (TOF-SIMS).

This reaction demonstrated the possibility to control the formation of polycyclic products following sulfur abstraction. As my studies demonstrate, planar polycyclic molecules are excellent candidates for discovering new reactions through STM, thus highlighting the ability of local probe techniques for revealing novel and unexpected chemical mechanisms.

In a similar way the presented work continued with systematic explorations of unbrominated derivatives of the above mentioned thieno-anthracene molecule, 2TTA and 3TTA, on the (111) facet of Cu, Pd and Ni. These sulfur-containing molecules were used as precursors to obtain a new polycyclic product or for building polymeric assemblies — by complete desulfurization; or metal-mediated structures — by dehydrogenation at specific positions, in the precursor.

My work also demonstrated that molecular architectures, comprising two-dimensional (2D) oligomers with electronic properties close to the polymer phase can be patterned with nanoscale precision on Cu(111), by using an STM tip.

Next, is reported the behavior of pentacene as an independent system or building block of a largely conjugated system – graphene. On Ni(111), the pentacene films were considered a new low temperature route to graphene synthesis from a large aromatic precursor.

The utility of STM for these types of experiments is clear. Despite a few limitations, there remains a wide variety of surface-confined reactions that STM would be well-suited to investigate; as this study demonstrates, reactions that take advantage of the stabilizing influence of the substrate, yielding products which remain surface-bonded, are excellent candidates for identification through STM.

Theoretical investigations of interfacial phenomena are incorporated throughout the thesis. By using density functional theory (DFT), single molecules are examined in the gas phase or on ideally flat and energetically homogeneous surfaces. Nowadays, in addition to experiment, computer simulations are treated as the necessary fundamental discipline of interface research, providing practical and indispensable insight into the physical phenomena at work, even before starting the experiment.

Keywords: STM, desulfurization, dehydrogenation, cyclization, organometallic, patterning, polymer, thiophene, pentacene, graphene.

# Acknowledgements

Little more than four years ago, I had the good fortune to be accepted at INRS in the Nano Femto Lab research group, which offered such a pleasant and friendly work environment, in large due to the students, postdocs and research associates.

I would like to thank first Prof. Federico Rosei for believing in my capabilities and providing the financial support that made possible the pursuance of the PhD program. In addition to Federico, I want to thank Prof. Dongling Ma, my co-director of research, for her very instructive group meetings.

Many thanks are addressed to Prof. Dmitrii Perepichka, from McGill University, for providing the customized molecules, for the genuine interest he showed in my work of “transforming the failure(s) in success”, and for his encouragements.

Additional financial support, provided by FRQNT, is gratefully acknowledged.

Administrative support, provided by Madam H el ene Sabourin, has always been appreciated.

I would like to thank my supervisor, Dr. Jennifer MacLeod for her patience and guidance she provided during the years spent on this thesis, and I am extremely grateful that I had the chance to work with her.

As part of this research group, my work would have not been possible without the constant support of other group members: Dr. Rico Gutzler (which introduced me into the principles of STM and DFT), Dr. Josh Lipton-Duffin (for ensuring a proper functionality of the scientific equipment and with whom I had invaluable scientific discussions), Dr. Luis Cardenas (for cooperation in some scientific experiments, and for his encouragements), and Dr. Szakacs Csaba (for discussions regarding the Siesta code).

Collaborating students and postdocs have been particularly kind and helpful: thanks to Chaoying Fu, Riccardo Gatti, Fabrizio De Marchi, Gianluca Galeotti and Dr. Stefano Desinan.

For their invaluable friendship and generosity, encouragement and moral support I would like to thank the Romanian colleagues: Dr. Anca Marian, Crina Popovici, Dr. Szakacs Csaba and his wife Alina, Dr. Liliana Braescu and Dr. Catalin Harnagea.

I would also like to thank the many other people, friends or collaborators, all of whom have played important, positive roles in my journey through INRS.

I thank my family for their moral support, especially to my daughter Anne-Marie for her understanding and tolerance.

Thanks, everyone!

## Table of Contents

Chapter 1 .....	1
Introduction .....	1
1.1. NFL group .....	1
1.2. Molecular assemblies .....	1
1.3. Thesis statement and structure .....	6
Chapter 2 .....	9
Interactions of organic molecules at surfaces.....	9
2.1. Surfaces .....	9
2.2. Wood's notation .....	11
2.3. Intermolecular and on-surface interactions .....	14
2.4. Conjugated structures and polymers .....	17
2.5. Reactions on surfaces (literature review) .....	20
Chapter 3 .....	65
Experimental Techniques .....	65
3.1. Scanning Tunneling Microscopy (STM).....	65
3.1.1. Basic concepts .....	66
3.1.2. The microscope .....	71
3.2. Time of flight secondary ion mass spectrometry (TOF-SIMS).....	73
3.3. Substrate and sample preparation.....	73
3.3.1. Nickel, copper and silver monocrystals .....	73
3.3.2. Organic molecules.....	75
3.4. Molecular structures .....	76
Chapter 4 .....	78
Transformation of Tetrathienoanthracene into Pentacene on Ni(111) .....	78
4.1. Results and Discussion.....	80
4.2. Conclusions .....	89
Chapter 5 .....	91
Tip-induced C–H activation and oligomerization of thienoanthracenes .....	91
5.1. Results and Discussion.....	92
5.2. Conclusions .....	101

5.3. Methods.....	101
Chapter 6.....	103
Surface-catalyzed reactions of tetrathienoanthracenes on transition metals .....	103
6.1. Results and Discussion.....	106
6.1.1. 2TTA.....	106
6.1.2. 3TTA.....	118
6.2. Conclusions.....	124
6.3. Methods.....	124
Chapter 7.....	126
Pentacene on Ni(111): room-temperature molecular packing and temperature-activated conversion to graphene.....	126
7.1. Results and Discussion.....	128
7.2. Conclusions.....	138
7.3. Methods.....	139
Chapter 8.....	141
Summary and Perspectives.....	141
Appendix A.....	143
List of acronyms and common symbols.....	143
Appendix B.....	144
Résumé.....	144
Chapitre 1.....	146
Introduction.....	146
Énoncé de la thèse et de la structure.....	151
Chapitre 4.....	153
Transformation sans précédent de Tetrathienoanthracene en pentacène sur Ni(111), la STM comme un instrument pour la découverte de nouvelles réactions.....	153
Chapitre 5.....	156
Impression moléculaire induite par la pointe avec une résolution nanométrique .....	156
Chapitre 6.....	159
Réactions de tetrathienoanthracenes catalysées sur des surfaces des métaux de transition, avec ouverture des anneaux thiophénique.....	159
Chapitre 7.....	163

Pentacène sur Ni(111): assemblage moléculaire à température ambiante et conversion en graphène activé par la température .....	163
Chapitre 8 .....	168
Résumé .....	168
Bibliography .....	170

# Chapter 1

## Introduction

### 1.1. NFL group

The Nanometer Femtosecond Laboratory (NFL) was established by Professor Federico Rosei in May 2002 at Centre Énergie, Matériaux et Télécommunications and Center for Self-Assembled Chemical Structures, Institut National de la Recherche Scientifique, in Varennes.

The target of the group is to design, fabricate, and characterize nanoscale materials with tailored structural and electronic characteristics. By understanding and exploiting the exceptional properties of these systems, the NFL also pursues diverse possible applications such as components for nanoelectronics, bio-applications, solar power harvesting or catalysts for green energy. Although my PhD project focused on the first category of studies, the various lab endowments allowed me to run side projects with implications in the latter, not described in this thesis.

The reader could find extended details about the group's history and achievements at: [nanofemtolab.qc.ca](http://nanofemtolab.qc.ca)

### 1.2. Molecular assemblies

The ability to direct the assembly of individual molecules at surfaces is one of the basic requirements for the bottom-up construction of novel molecular devices and electronics. Complete control of these processes must address not only placement and conformational arrangement,<sup>3</sup> but also fundamental issues of molecular composition and structure at the sub-molecular level.

One promising strategy to fulfill these requirements is to study and exploit specific reactions of molecules confined to reactive surfaces in an ultra-high vacuum environment,<sup>4</sup> by decomposing the system into its basic, simple model systems.<sup>5, 6</sup> On-surface chemistry has been described in both the academic and practical context for decades. However, one motivation for this new movement is the proven possibility for better control over the

synthesis and properties of these electronic (*e.g.* conjugated) materials, within one- or two-dimensional constraints.<sup>4, 7</sup> The odds of obtaining the expected characteristics of a 2D film depend on multiple factors.<sup>8-11</sup> The appropriate choice of the precursor, placed on the proper surface, and activated at the right temperature could deliver a satisfactory yield of conjugation length, and therefore good transport performance, with the functionality determined by the molecular interconnectivity and the spatial arrangement.<sup>12, 13</sup> Yet, at the beginning of this process, unless deliberately arranged/reacted on the surface (*e.g.* manipulation by scanning probe techniques),<sup>14</sup> the precursor molecules only associate spontaneously into weakly interacting and equilibrium-stable aggregates (self-assembly), joined by non-covalent bonds (reversible, and with low mechanical stability and weak electronic interaction).<sup>15</sup>

In fact, to achieve electronic interactions suitable for application in organoelectronics, the electronic coupling and robustness must be strengthened, while maintaining the structural order. Ordered organic networks, to satisfy these requirements, were indeed adequately obtained and identified by scanning tunnelling microscopy (STM), as based on metal-coordination,<sup>16-20</sup> or covalent and  $\pi$ -conjugated bonds.<sup>7, 19, 21, 22</sup> Strong bonding (*e.g.* covalent) is associated with a high defect density in the structure.

STM has been one of the various techniques sensitive enough not only to provide precious insight into these fundamental on-surface processes unfolding at the nanoscale, but also to manipulate organic material. Recent trends in complex 2D processes, extensively studied by STM, include:

(i) The use of multi-step reactions. At first, occurring at lower temperature one reaction stabilizes the precursor's shape on the surface (*e.g.* Ullmann coupling,<sup>23</sup> by dehalogenation or dehalogenation of only a particular type of halogen),<sup>24</sup> followed by a second reaction step, at higher temperature, to refine the shape or improve the chemical stability of the final product (dehydrogenation,<sup>25</sup> or dehalogenation of another type of halogen).<sup>24</sup> Although the Ullmann reaction (Figure 1.1(a)) uses halogen-terminated molecules in conjunction with metallic surfaces as a platform for the formation of 2D conjugated structures,<sup>23</sup> due to the ease (close to RT) of the rupture of C—X bonds (X = halogen),<sup>19, 24, 26-32</sup> on most of the studied metallic surfaces, it also yields reaction by-products which block the reactive sites on surface.

(ii) Dehydrogenation of designated bonds, taken as a single reaction, before an eventual C—C rebonding which stabilizes the newly formed system on the surface.<sup>22, 25, 33-35</sup>

Large systems of conjugated molecules have attracted much attention in recent years due to the favourable transport properties of their two dimensional films.<sup>4, 36-39</sup> However, slight changes in the morphology of the precursor can induce a considerable change not only in the electronic properties of the products,<sup>40</sup> but most of all, as will be shown in Chapter 6, even the odds of obtaining similar reaction products or structures.

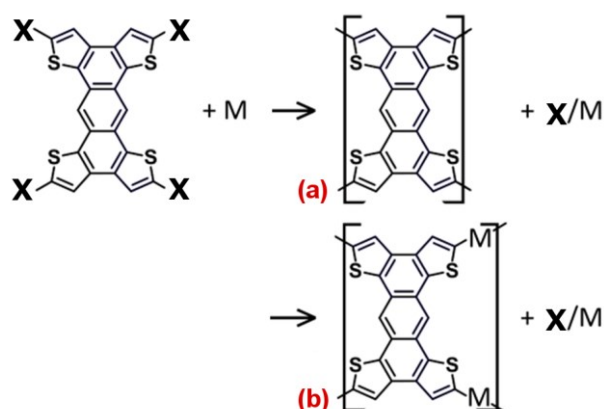


Figure 1.1. Schematic model for the polymerization, by Ullmann coupling, of halogen (X) terminated molecules is presented in the image (a). Depending on the nature of the metallic surface (M), the covalent-conjugated coupling could be preceded by an observable intermediate, coordinated by an adatom from the surface, as represented in the image (b). The cleaved halogens may remain co-adsorbed on the metallic surface.

The most fundamental example of 2D,  $\pi$ -conjugated system is graphene. Controlling the structure, composition and electronic properties of graphene, and extending its synthesis from scratch in two dimensions requires either precursors with a similar carbon density (which could be activated at a lower temperature), or techniques to transform the precursor to the basic carbon form (usually done at high temperature).

Of the various methods for the synthesis of graphene or graphene nanoribbons that involve epitaxial growth on metallic surfaces, chemical vapour deposition (CVD) is probably one of the most used,<sup>41, 42</sup> at high temperatures ranging from 300 to 1000 °C. Since the

majority of the organic precursors are hydrocarbon based,<sup>43-56 57-64</sup> and the strength of the C—H bond (438 kJ/mol, in H—CH<sub>3</sub>; 472 kJ/mol in H—C<sub>6</sub>H<sub>5</sub>)<sup>65</sup> is higher than C—C (377 kJ/mol in CH<sub>3</sub>—CH<sub>3</sub>),<sup>65</sup> the dehydrogenation reaction is highly unfavorable compared with the cracking of the hydrocarbon (but almost twice as favorable as breaking the C=C bond). To overcome this inconvenience, the above-mentioned Ullmann coupling, which is a coupling reaction between aryl halides, is used as an alternative to CVD,<sup>25, 66-69</sup> or coupled with (preceding) the on-surface thermally activated dehydrogenation.<sup>25, 70</sup> The strong C—H bond is a closed-shell  $\sigma$  orbital that can be broken by oxides (forming O—H bonds with strengths comparable to that of the C—H bond), or metal catalysts. A metal atom alone cannot abstract one hydrogen atom because the M—H bond is weaker than the C—H bond. On a metallic surface however, both C and H are coordinated with metal from the surface (a reaction seen as the insertion of a metal atom into the C—H bond, bridged), and the sum of the coordination energies exceeds the C—H bond strength, making the process thermodynamically possible.<sup>71</sup> The van der Waals interactions between the molecules and surface also increase the intramolecular strain, thereby weakening the C—H bonds.

Therefore, under adequate physical conditions,<sup>72</sup> or the presence of a suitable catalyst where the hydrogen is catalytically solvated,<sup>33, 73</sup> dehydrogenation can be carried out at a reasonable temperature and with minimal C—C bond rupture. This reaction path becomes more advantageous than thermal cyclo-dehydrogenation, where the stability and compatibility of the precursors with the reaction conditions is crucial;<sup>74</sup> or even than in solution where the formed graphene molecules/nanoribbons with poor solubility in conventional organic solvents tend to interact strongly by  $\pi$ - $\pi$  stacking.<sup>75</sup>

In general, the replacement of metallic surfaces as the support for graphene growth remains a big challenge.<sup>75</sup> However, among the metallic catalysts suited for the above reactions, besides Cu(111), Ni(111) has probably been one of the most extensively studied surfaces, due to the very close lattice matching with graphene,<sup>46, 76</sup> as well as the strong hybridization between the graphene  $\pi$ -states and the nickel  $d$ -states,<sup>77, 78</sup> which can lead to interesting electronic and magnetic effects.<sup>43, 79, 80</sup>

In contrast to graphenes prepared from top-down strategies (such as graphite exfoliation), the chemical approach, based on polycyclic aromatic molecules (bottom-up), offers a great opportunity to tailor the molecular size, shape, edge, and composition of

graphenes. A simple comparison between tetracene and triphenylene proves that these characteristics could dramatically change such properties as the ionization potential, HOMO-LUMO gap, thermal stability, etc., in isomeric polycyclic molecules or compounds.<sup>81, 82</sup> The synthesis of a large conjugated system, such as graphene, from small conjugated systems such as pentacene — a benchmark molecular semiconductor, is possible since the latter has an identical internal periodicity and density of carbon atoms. Considering these factors, pentacene activation to graphene has been reported on Cu(111) at ~800 °C.<sup>83</sup> Extensively studied in this thesis on Ni(111), the periodicity of the conjugated rings in pentacene matches that of nickel atoms on the (111) facet, along the  $\langle 1\bar{1}0 \rangle$  directions. By using dehydrogenation as a single step reaction, domains of graphene were obtained from pentacene at an activation temperature much lower than previously reported by other techniques.<sup>84</sup>

Electronically, the character of graphene is neither semiconductor (the bandgap vanishes at the Dirac points), nor purely metallic (the density of states of pristine graphene vanishes at the Dirac points).<sup>68, 85</sup> However, by doping, the Fermi energy is moved away from the Dirac point (with a finite density of states at the Fermi energy), and the graphene becomes metallic.<sup>85</sup> This enables the particular opportunity (at least theoretically), to tune the optoelectronic properties of graphene without changing the conjugated skeleton,<sup>22, 86, 87</sup> by incorporating heteroatoms in the precursor, such as sulphur in thieno-anthracenes (TTA, presented in this thesis). If the electron-rich nitrogen atom is periodically incorporated into polycyclic aromatic precursor molecules and therefore in the obtained graphene, such a heteroatom influences the electronic nature of the product without modifying the structure.<sup>86</sup> Furthermore, a proper combination of electron-donor and electron-acceptor atoms may result in a semi-conducting conjugated polymer with a tailored bandgap.<sup>88</sup> Depending on the design of the precursor, replacing carbon atoms at specific positions in the precursor (*e.g.* 1,3,5-tris(4-bromophenyl)-benzene (TBB)),<sup>30, 89</sup> by nitrogen, improves the core planarity and consequently the conjugation, by reducing the steric hindrance due to hydrogen atoms.

As discussed above, the STM technique has demonstrated its capacity for discovery, but what makes the STM so special, is the possibility to extend its usability beyond image acquisition and induce chemical reactions with nanoscale spatial resolution.<sup>90-96</sup> Its unique character, of generating high current density, cannot be obtained so locally with conventional electron sources. The application of a high current density on a small injection area (~100

A/cm<sup>2</sup>, at tunneling currents ~1 nA), reduces to a minimum the heating problem due to a rapid heat dissipation of the electrons (which otherwise could probably burn out the sample). This tunneling current can induce:

- (i) Electronic excitation (injection of electrons occurs *via* the LUMO,<sup>97</sup> and can involve a bonding configuration change),<sup>94,95</sup> or,
- (ii) Vibrational heating, which occurs through a multi-electron process and is generally initiated at relatively low bias voltages, on the order of hundreds of mV.<sup>98-100</sup>

So, after irradiation with electrons, the existence of an external charge briefly trapped in an unoccupied electronic state of the molecule can cause a geometrical rearrangement of molecular constituents by means of elongations/contractions and distortions of the molecular orbitals. Such kinetics could create vibrational modes, with lifetime dependent on the strength of molecule-surface coupling. A particular case, studied in the thesis, is the tip induced C–H bond activation, where in the manner described above the C–H bond is stretched on the surface in a coordinated position favorable for cleavage.

Recent examples of STM-induced phenomena include the tip-induced polymerization of 1,4-benzenediboronic acid,<sup>101</sup> light- and tip-induced polymerization of compounds with one 5-(10,12-tricosadiinyloxy) isophthalic acid or two 2,5-(10,12-heneicosadiinyloxy) terephthalic acid diacetylene functions,<sup>102</sup> engineering reactivity by inducing chemical reactions in the self-assembled chain of dimethyldisulfide,<sup>103</sup> electro-polymerization of poly(3-octylthiophene),<sup>104</sup> and the controlled polymerization of a substituted diacetylene such as 10,12-tricosadiynoic acid.<sup>105</sup> In these systems, similar to the approach in this thesis, by applying a voltage pulse, the STM tip is used to induce a reaction which then propagates into the adsorbed organic film without additional energy input until it is terminated by a defect,<sup>106</sup> or by the consumption of all available monomers.<sup>101</sup>

### 1.3. Thesis statement and structure

The work contained in this thesis is divided into three parts, which, although conceptually unified under the same surface science canopy, span different approaches presented in four original chapters.

Chapter 4, 5, and 6 deal with “single molecule events” of isomer molecules comprising thiophenic moieties fused to an anthracene core. Interesting properties are associated with both

the thiophenic moieties (planarity, conjugation, bandgap reduction) as well as the anthracene core (conjugation, high carrier mobility).

Chapter 7 deals with large assemblies of molecules. It is related to Chapter 4 and Chapter 6 by the type of the molecule, and to Chapter 5 by functionalization.

## **Chapter 1**

- Introduction of the NFL group, motivation and history of the most relevant processes involved in obtaining molecular assemblies, on surfaces and at the nanoscale. A list of the common acronyms and symbols is introduced in Appendix A.

## **Chapter 2**

- Provides the reader with general information about the terminology and processes, occurring at the nanoscale, on metallic surfaces and in UHV conditions. A long list of examples summarizing various reactions, precursors, and surfaces studied through the years and strongly related to this chapter, is also included.

## **Chapter 3**

- Dedicated to the most common experimental technique used to accomplish the work presented here, it shows the basic STM theory, as well as a description of the instrument itself. Some space is given to various procedures for cleaning the surfaces and to the sublimation of organic material.

## **Chapter 4**

- This is the first of four chapters in which the original results of my work are presented. It is devoted to the study and description of a new reaction mechanism (thiophene ring opening, desulfurization and new bond formation) which occurs on a reactive surface, respective to the transformation of thieno-anthracene precursors (TTAs) to a new product – pentacene, on Ni(111).

## **Chapter 5**

- Describes the process of patterning oligomers on surfaces, with nanoscale resolution: starting from a surface-confined gas of diffusing molecular monomers, the STM tip can be

used to dehydrogenate the precursor and ‘write’ spatially-defined 2D molecular aggregates on a copper surface.

### **Chapter 6**

- In a comparative STM study, unbrominated versions of TTA, whose structures were reported elsewhere,<sup>107</sup> were investigated on monocrystalline (111) surfaces of Ni, Pd, and Cu. For comparison, a polycrystalline nickel foil was also used. These studies complement previous observations (see Chapter 4),<sup>19, 20, 108</sup> and provide a clear distinction between the two observed nanoscale phenomena, desulfurization and dehydrogenation, which were the mechanisms of free bond creation.

### **Chapter 7**

- Describes the self-assembly of pentacene molecules on the Ni(111) surface and the processes which follow surface annealing. Above 220 °C, the pentacenes start to dehydrogenate and unite forming small domains of graphene.

### **Chapter 8**

- Draws general conclusions.

A French language resume of this thesis is attached in **Appendix B**.

# Chapter 2

## Interactions of organic molecules at surfaces

### 2.1. Surfaces

In the context of designing large-area organic films, in which the organic material shows long range ordered structures, the role of the substrate is critical as a support and/or catalytic medium, and can be chosen to enhance or suppress the molecule-molecule interaction.

Driven by the need to minimize the surface free energy, the surfaces can undergo two different types of rearrangements:

The first, known as reconstruction, involves mostly the outer or near surface layer, proceeding through large displacements of surface atoms (foreign, or the atoms of a host surface), that are then reordered into new domains, which often display a different periodicity or symmetry (*e.g.* sulfur and bromine/Ni(111)).

For the second process, relaxation, we may want to consider a crystal cut along a certain crystalline plane. Since the surface or near-surface atoms experience inter-atomic forces from only one direction (no forces from the open region, and without considering the in-plane forces), the surface layer changes its equilibrium position. It moves in a direction normal to the surface plane (experienced by most of the metals),<sup>109</sup> contracting towards the bulk, resulting in a smaller inter-layer spacing. Relaxation extends several layers deep into the solid without changing the periodicity or the symmetry of the surface (*e.g.* during the surface preparation of the supportive crystals, or preceded by a reconstruction — of Si(100) surface).<sup>110</sup> An interesting aspect of the relaxation is that the in plane component of the surface tension (defined as the surface “stress tensor” for the high-symmetry (111) and (100) surfaces and “surface free energy” for liquids),<sup>111</sup> does not decrease after relaxation since the positions of atoms in each layer don’t change. The outward relaxation increases the surface tension (observed in Al(100), Al(111), Pt(111), Cu(111) and Mg(0001),<sup>111</sup> due to the spill-out of electrons away from the surface resulting in an outward-pointing electrostatic force on the

positively-charged atoms of the first layer),<sup>112</sup> while the inward relaxation induces the decreasing of surface tension (since the outermost atoms prefer to reach a surrounding with a higher, bulk-like electron density).<sup>113</sup>

A direct relationship exists between the surface free energy, surface atom density, coordination number and surface stability. If we define the *fcc* system (face-centered cubic, the most used throughout the thesis) as the crystal system where the unit cell is in the shape of a cube and the constituent atoms are placed at the corners and in the center of the faces of this cube, and in the crystal (Bravais) lattice the Miller indices as the integer coordinates, *h*, *k* and *l*, these indices determine a family of lattice planes (*e.g.* (111), (100), (110), see Figure 2.1).

The reduced number of nearest neighbours on flat-surface geometries (with respect to the bulk), as well as the modification of interatomic distances (tensile strain) strongly affect the chemical properties of the surface.<sup>114</sup> In transition metals for example, this reduction is accompanied by change in overlapping of “*d*” states of neighbouring sites, leading therefore to changes in the “*d*” to “*sp*” hybridization.<sup>115</sup>

In this thesis, the studied molecules were adsorbed mostly on low index facets of *fcc* crystals. Terminology to define each of the adsorption sites is defined in Figure 2.1. On the (111) facet, extensively used throughout the thesis, four types of adsorption sites could be identified: top, bridge, and two hollow - *fcc* and *hcp* (hexagonal close-packed) respectively. Similar terminology (top, bridge and hollow) could be used for the (100) and (110) facets. For the (110) facet, due to the anisotropic character of the surface, two types of bridge adsorption sites are available: long and short.

The atomic coordination number for the bulk of the *fcc* structure is 12. To create dedicated surface planes, atoms have to be removed from above the plane, exposing atoms with a lower number of neighbors, thus lowering the coordination number. This has however important implications in the ability to catalyze specific reactions when it comes to the chemical reactivity of the created surface.<sup>116</sup>

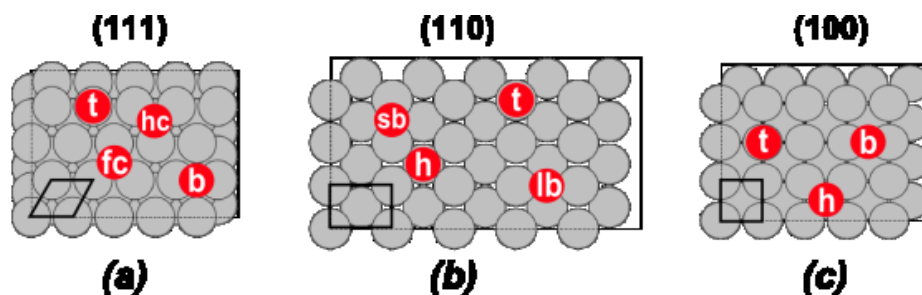


Figure 2.1. Adsorption sites on low-index facets of a *fcc* crystal. (a) (111) facet and corresponding top “t”, bridge “b”, hollow *fcc* “fc”, hollow *hcp* “hc” sites; (b) (110) facet with top “t”, hollow “h”, and as result of the anisotropic character of the surface the two bridge positions: short “sb”, and long “lb”, sites; (c) (100) facet with top “t”, bridge “b”, and hollow “h” sites. Each atomic structure was generated by using the AG editor (ASE-GUI package).<sup>117</sup>

## 2.2. Wood’s notation

In the experiments accomplished for this thesis, reaction byproducts including bromine, sulfur and copper atoms were observed to form particular surface reconstructions. There are two method of referring to a particular reconstruction, the matrix and the Wood’s notation.

The simplest of these, and therefore most commonly used, relates the position of the surface (adsorbed) atoms to the positions of underlying bulk atoms, and is called Wood’s notation.<sup>118, 119</sup> This describes the structure of an ordered phase in terms of the ratio between the lattice vectors of the newly formed lattice and substrate. In addition, the rotation angle between the vectors of the two superposed lattices may be indicated as well.

The first step for this representation is defining the substrate vectors. The substrate is described by a primitive unit cell, defined as the smallest unit which, by repetitive translations, could be used to construct the entire surface of the substrate.

Commonly, two vectors of arbitrary nomenclature,  $\vec{a}_1$  and  $\vec{a}_2$  are defined so that:

- $\vec{a}_1$  goes to  $\vec{a}_2$  in a counterclockwise direction (a right hand coordinate system);
- $\vec{a}_2 \geq \vec{a}_1$ ;
- when possible  $\vec{a}_1$  points down and  $\vec{a}_2$  points to the right;
- the angle between the vectors should be  $\geq 90^\circ$ .

Wood's terminology can only be used when the vectors describing the lattice formed by the reconstructed adsorbed species,  $\vec{b}_1$  and  $\vec{b}_2$ , are rotated through the same angle with respect to the surface vectors  $\vec{a}_1$  and  $\vec{a}_2$ .

For the general case, the Wood's notation is presented as it follows:

$$p \left( \frac{b_1}{a_1} \times \frac{b_2}{a_2} \right) R\theta - X, \quad 2.1$$

- where "p" denotes "primitive" and indicates that the unit cell is the simplest repetitive unit; similarly, the "c" terminology could be used instead of "p" and stands for centered surface lattice and is associated with an overlayer unit cell that contains an extra adsorbate atom located at its center (Figure 2.2(b));

- $\theta$  is the rotation angle between the superlattice and the substrate unit cell;
- X is the chemical symbol of the adsorbed species;

For the simplest case of orthogonal vectors (with  $\theta=0$ ) and the (100) facet, an example of Wood's representation could have the following forms (Figure 2.2(a)):

$$\text{fcc}(100)(2 \times 2)\text{-X or } p(2 \times 2)\text{-X}, \quad 2.2$$

with the ratio of the modules:

$$\left( \frac{b_1}{a_1} \times \frac{b_2}{a_2} \right) = (2 \times 2). \quad 2.3$$

For the (111) surface of a *fcc* metal, Wood's notation for a number of overlayers is displayed in Figure 2.3.

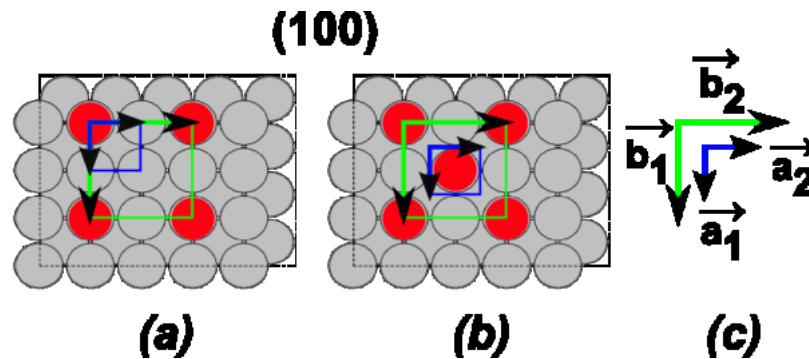


Figure 2.2. Two possible unit cells on the (100) facet of a face centered cubic crystal, constructed by the substrate's  $\vec{a}_1, \vec{a}_2$  (in blue) and adlayer's  $\vec{b}_1, \vec{b}_2$  vectors (in green) defining a primitive (a) and centered (b) adlayer unit cell containing an extra adsorbate at its center; the vector assignment is illustrated in (c).

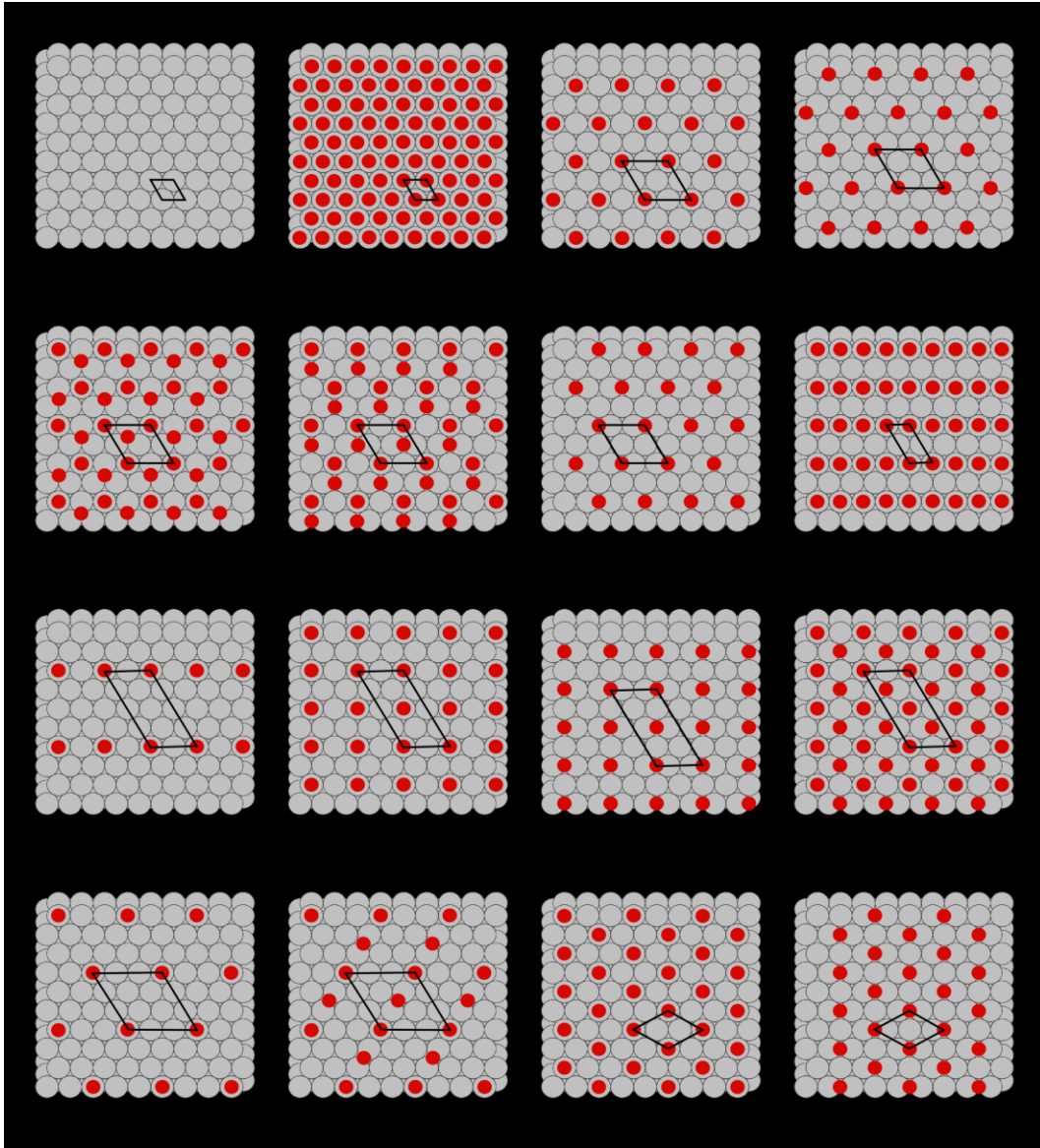


Figure 2.3. Wood's notation for a number of overlayers on the (111) facet of a *fcc* metal. (Figure adapted by author from Masel)<sup>120</sup>

The second representation method is the matrix notation which defines and relates individual ad-layer vectors to the both substrate surface vectors, by a linear combination. Similar arbitrary notation could be used, as for example  $\vec{b}_1$  and  $\vec{b}_2$ . A general representation is given by the following relations:

$$\vec{b}_1 = m_{11}\vec{a}_1 + m_{12}\vec{a}_2, \quad 2.4$$

$$\vec{b}_2 = m_{21}\vec{a}_1 + m_{22}\vec{a}_2, \quad 2.5$$

so that in a full matrix representation we can write the following:

$$\begin{pmatrix} \vec{b}_1 \\ \vec{b}_2 \end{pmatrix} = \begin{pmatrix} m_{11} & m_{12} \\ m_{21} & m_{22} \end{pmatrix} \begin{pmatrix} \vec{a}_1 \\ \vec{a}_2 \end{pmatrix}. \quad 2.6$$

For the particular case of the (100) surface shown in Figure 2.2(a), the matrix representation is:

$$\vec{b}_2 = 2\vec{a}_1 + 0\vec{a}_2, \quad 2.7$$

$$\vec{b}_1 = 0\vec{a}_1 + 2\vec{a}_2. \quad 2.8$$

This gives:

$$\begin{pmatrix} m_{11} & m_{12} \\ m_{21} & m_{22} \end{pmatrix} = \begin{pmatrix} 2 & 0 \\ 0 & 2 \end{pmatrix}. \quad 2.9$$

### 2.3. Intermolecular and on-surface interactions

Introduced by Whitesides,<sup>15</sup> the concept of “self-assembly” was defined as the spontaneous alignment of molecules into stable and well defined aggregates by non-covalent forces, as the system approaches equilibrium. Self-assembly can produce nearly defect-free structures over a range of microns.<sup>121</sup> Due to weak intermolecular forces, these structures are physically weak and unsuitable for transferring onto other surfaces; this type of robustness is found instead in covalently bonded structures.

Due to its attractive outcome of conjugation and conductivity, in our case between flat aromatic molecules, the covalence of the C–C bond is the most desirable intermolecular interaction. If the conditions for such an interaction are created (presence of free bonds to adjacent molecules and diffusivity), the strength (enthalpy) of the newly formed covalent bonds will be in the order of ~400 kJ/mol.<sup>65</sup>

If the molecules have no free bonds (not ionized), the intermolecular van der Waals forces interactions are weak (as taken individually), on the order of 4.2 kJ/mol (~RT) to 42 kJ/mole.

In a molecule with different species of atoms, electrons are also not equally shared; so that some atoms have the tendency to pull electrons away from other atoms, a characteristic called electronegativity, which could create charge dipoles. When two polar molecules approach each other in space (at a distance “*x*”), the dipole-dipole interaction occurs,

manifested through the attraction (falling off as  $\sim 1/x^3$ ) of regions of opposite charge within these molecules. By a similar mechanism, dipolar molecule(s) could interact with single atoms (as single charge) through a charge-dipole interaction, which induces a charge distribution in the surrounding molecule(s).

Another interesting bonding mechanism, electrostatically driven, is seen in halogen terminated molecules, where the peculiarity comes from the way an electronegative atom such as the halogen interacts attractively with an electronegative site of a molecule to which it is bonded. An explanation of this fact was first introduced by Brinck *et al.* in 1992, stating that some covalently bonded halogens have localized regions of positive electrostatic potential along the extension of their covalent bond, with negative potentials on their lateral sides (dipole-like),<sup>122</sup> which gives a certain directionality of halogen bonding. The origin of the positive potential was later explained by Clark *et al.*, as being due to the charge deficiency in the outer lobe of the *p*-type orbital involved in the covalent bond; this is the “ $\sigma$ -hole”,<sup>123</sup> a concept later extended to the groups IV,<sup>124</sup> V,<sup>125</sup> and VI.<sup>126</sup>

In this work, most of the molecules are hydrogen terminated. It is therefore important to describe a few types of hydrogen-based intermolecular interactions. In general, while bonded to another atom (for example O, N, S), by increasing the electronegativity of the bonding atom, the hydrogen atom tends to be stripped of its electron density, increasing thereby its partial positive charge, and the strength of the bond. This mechanism makes possible the participation of the hydrogen atom in a second bond (with another atom, and not a proton transfer reaction as in the acid-base reaction), similar to a Lewis base (as the fourth bond to N in NH<sub>3</sub>, or third to O in H<sub>2</sub>O). Although not covalent, those bonds can have strengths approaching that of covalent bonds at 84-170 kJ/mol in strong interactions. In weak interactions, the strength is 4-20 kJ/mol, on the order of the strength of dipole-dipole interactions.<sup>127</sup>

Contrary to the above, an interesting effect induced by the positive character of the hydrogen atom (but not characteristic of H only), called hindrance, promotes the repulsion of hydrogen terminated molecules. This process could be observed even at the intra-molecular level, where the repulsion of hydrogen atoms generates distortions or deviations from planarity.<sup>128</sup>

In terms of on-surface reactions which may exploit these effects, ensemble experiments involving organic materials on surfaces have existed for years. However, localizing the concept of surface-confined reactions, from large ensembles to a single molecule, can significantly focus the scope of fundamental chemistry towards identifying, with the aid of one- or two-dimensional spatial constraints, opportunities at the fundamental level for synthesizing new organic materials for nanotechnology.<sup>4, 7</sup>

The chemistry employed in surface reactions so far has largely been based on mimicking known reactions. Moreover, scanning probe microscopy offers the possibility both to image and to induce new chemical reactions with nanoscale spatial resolution.<sup>90-96</sup> Some of these chemical reactions are discussed in detail at the end of this chapter.

After sublimation of the adsorbate on a particular surface, the following process could be divided into four basic components: (i) adsorption of molecules on the surface, (ii) surface reaction, (iii) diffusion of the products from the catalytic center (byproducts, radicals), and eventually, depending on the precursor type (iv) intra- or inter-molecular bonding. Depending on the coverage, substrate, or temperature, the last step could be accompanied by the formation of a multilayer structure (stacked, *e.g.* multilayer graphene), or on the contrary, by the partial or total desorption of reactants or byproducts (atoms) from the surface.

On single crystal surfaces, commonly used as the physical support, compelled by symmetry, the process of transport of organic material is largely dictated by the temperature, surface topography and disposition of the adsorption sites.<sup>32, 129, 130</sup> Concerning the adsorption and the adsorption strength, two broadly similar situations could be encountered:

2.5.1. One in which the molecules occupy discrete positions and, although they may move from/to different positions, they are in an equilibrium state with the surface only when occupy adsorption sites – localized adsorption.

Here, two situations may occur:

- (a) At low coverage, the molecule may possess sufficient (thermal) energy (activation energy) to jump from the present to an adjacent site, over an energy barrier between the two sites.
- (b) Once the molecular coverage increases, the energetic molecule may very probably find the adjacent adsorption site already occupied; hence, it has then to

bounce back to the original position or become part of a liquid-like system (a property characteristic of ensembles of many molecules).<sup>131</sup>

From a dynamic point of view, in any of the above situations (a), a molecule may move on the surface but not leave the surface, whereas in (b) the subject molecule could leave a certain adsorption site towards another adsorption site of the same surface only through total desorption, as if leaving the surface into the gas-phase followed by re-adsorption.<sup>131</sup>

2.5.2. Another situation, seen as a particular case of (i) dependent on the temperature, and differing from (i) by the height of the hopping barrier (reduced here), occurs if the adsorbed molecule(s) are stable at any point on the surface, with almost the same potential energy – quasi-localized adsorption (rapid hopping from site to site); in this idealized case, once adsorbed the molecule will behave like a two-dimensional gas.<sup>131</sup>

The hopping rate, from one adsorption site to another, and the probability of successful hopping is characterized by an attempt frequency “ $\nu$ ”, and a thermodynamic factor (dependent on the temperature, and the diffusion potential energy barrier -  $E_{diff}$ ). The relationship for the jump or hopping rate is the following:

$$\Gamma = \nu e^{\frac{-E_{diff}}{k_B T}}, \quad 2.10$$

where  $T$  is the temperature, and  $k_B$  is the Boltzmann constant. This relation expresses how strongly the hopping rate varies with temperature. The manner in which diffusion takes place is dependent on the relationship between  $E_{diff}$  and  $k_B T$  in the thermodynamic factor.

In the particular case (ii) the thermodynamic factor approaches unity, as  $E_{diff} \ll k_B T$  and therefore  $E_{diff}$  ceases to be a meaningful barrier to diffusion.

Furthermore, before rebonding to other similar organic radicals, diffusion considerations must be also applied to the activated precursors.<sup>32</sup>

## 2.4. Conjugated structures and polymers

Despite the unutterable scientific satisfaction offered by uncovering the processes which govern at atomistic level, there is a clear and pragmatic drive to reveal the applicability of these processes to current technological challenges.

Organic materials with  $\pi$  electron delocalization along their polymer backbone, the conjugated polymers, could become an attractive new alternative to other materials like silicon

in nanoelectronics. The aromatics are preferred, since the planar closed loop of electrons gives great spatial stability to the  $\pi$  bonding. Since there are conjugated polymers which show a band-gap and therefore semiconducting properties,<sup>132</sup> in order to get efficient properties, the band gap has been one of the intrinsic attributes of these polymers targeted for control.<sup>133</sup> Therefore, besides applications in organic electronics, by matching the solar spectrum in the red and infra-red region, they are also well suited in photovoltaics.<sup>134</sup>

In the case of graphene, which has the best physical properties (such as strength, electrical and thermal conductivity); the zero band-gap in its free standing phase limits its usage to applications as a conductor. To extend its use, certain alterations to its conjugated structure are needed by introducing foreign atoms, functional groups, or defects, or by quantum confinement – making graphene into nanoribbons.<sup>135</sup>

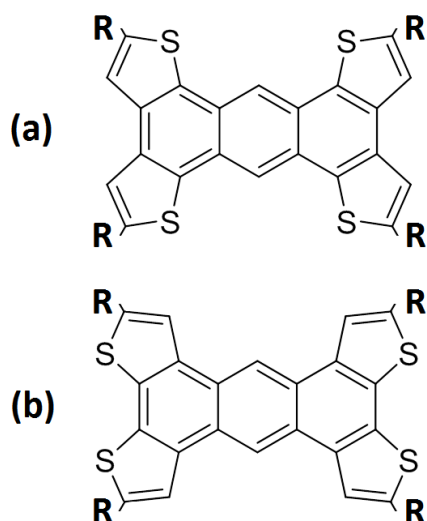
Generally, in the design and synthesis of conjugated polymers, there are two guiding principles: (i) the LUMO level is lowered by electron withdrawing moieties, as side groups or inherent constituents of a conjugated central chain; (ii) high HOMO levels are induced by the introduction of side or central electron donor groups.<sup>136</sup> Moreover, the extent of delocalization and alternation of single and double bonds sets the size of the energy band-gap, which determines the semiconducting character of the polymer.<sup>137</sup> A low lying LUMO level, below  $\sim 4$  eV with respect to the vacuum level, is associated with the n-type semiconductors. On the other hand, candidates for p-type semiconductors must exhibit a high lying HOMO level. In real applications, compromises should be made in setting the values of those levels due to an increase of the oxidative character by increasing the HOMO too high, while an excessively low position will make difficult the photogeneration of charge carriers in photovoltaics.<sup>136</sup>

One of the paths towards tailoring the band gap is the introduction of thiophene moieties into acene-type segments, both of which individually have good electron transport properties. Previous use of phenyl rings bridged to the same acene-type cores induced considerable deviation from planarity of the overall structure, due to the hydrogen hindrance.<sup>29</sup>

However, thiophene moieties fused to the core in the ortho- position as in the TTA or TBTTA molecules studied in this thesis (Scheme 2.1),<sup>107</sup> prevented the torsion favoring instead planarity, therefore improving the conjugation.<sup>40</sup> There is an important prerequisite when choosing these moieties. In this particular case, the general purpose was to induce slight electronic alterations, but their electronic affinities and the positions of the HOMO and LUMO

levels must remain similar to those of the core they are attaching to, or else, instead of allowing an adequate electronic coupling and efficient charge transport they serve as traps or barriers.<sup>138</sup>

An interesting fact about these anthra-thiophene molecules is that 1D polymers of the same unit give different values for the band-gap depending on the conformation in which they are covalently bonded.<sup>40</sup>



Scheme 2.1. Schematic representation of 2TTA (R = H) and TB2TTA (R = Br) in (a), and 3TTA (R = H) and TB3TTA (R = Br) in (b).

Another trick in tuning the band-gap is the way in which the thiophene ring fuses to the core. In this context, the 2TTA and 3TTA molecules were synthesized. Their different intramolecular morphologies at their thiophenic extremities confer different local transport characteristics, as in a 2D conjugated film, the charge streams by hopping from one block to another. The characteristic local morphology in the polymer, along this flow channel, will have an influence on the speed of the carriers, as some intra-molecular paths are much faster than others. Similarly, the molecular design or the way these molecular blocks connect could create preferential conduction channels in the 2D film; the charge could eventually not travel the full length of a molecule before changing its path, but hop instead to another neighboring molecular block.<sup>139</sup>

There are few decisive physical factors that could inhibit, or partially reduce to one dimensional, the charge transfer between the molecules in a 2D conjugated network. These factors are: direct ones – disorders or insulating defects, and some indirect – such as kinks and twists.<sup>139</sup> This was, as mentioned above, another reason for the introduction of planar functional units which reduces the intermolecular twisting and lowers the deviation from parallelism between adjacent  $\pi$ -orbitals involved in the conjugation.

However, obtaining these polymers/structures with the appealing electronic characteristics enumerated above is not always an easy task. Most of the time, by starting from self-assembled films, attempts to produce polymer films on the surfaces of transition metals that are rich in surface adatoms (such as Cu, Ag), have shown multimerization addressed towards coordination through a surface adatom. Early evidence of metal–ligand bonding (coordination) in molecular systems was found in UHV, for low-coverage benzoic acid adlayers on Cu(110), where two Cu adatoms bridge two opposite benzoate moieties.<sup>140</sup> A coordination complex like that is a compound formed typically between a molecule (electron donor), with a non-bonded pair of electrons, and another molecule or most commonly a metal atom which should be an electron acceptor, with low-energy unoccupied orbitals near the Fermi level.<sup>141</sup> It was however demonstrated that annealing these metal-organic structures on Ag(111) could generate covalent networks with a yield of roughly 50%.<sup>19</sup>

## 2.5. Reactions on surfaces (literature review)

*Diacetylene polymerization* has garnered considerable attention, due to the enhanced electronic properties of the polymer as compared to its precursors. Grim *et al.* reported the photo-polymerization of diacetylene moieties in an undecanol solution (Figure 2.4), self-assembled at the liquid-graphite interface and imaged with sub-molecular resolution by means of STM.<sup>181</sup> The as-deposited morphology of the surface consists of lamellae of molecules intersected by alternate lamellae of solvent (Figure 2.5). The polymerization reaction, which takes place at the liquid-graphite interface, was induced by irradiation with ultra violet (UV) light, and confirmed by the contraction of the intermolecular spacing between each second isophthalic acid (ISA) headgroup of the same lamella (Figure 2.6).

However, depending on the preparation method of the polymeric film, the molecules adopt different modes of mostly the close packing arrangement.

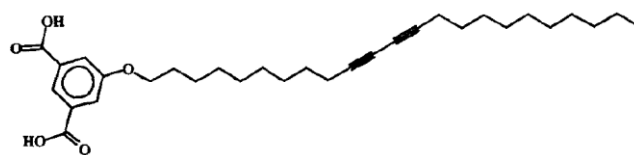


Figure 2.4. Diacetylene moiety, labeled as **1**.

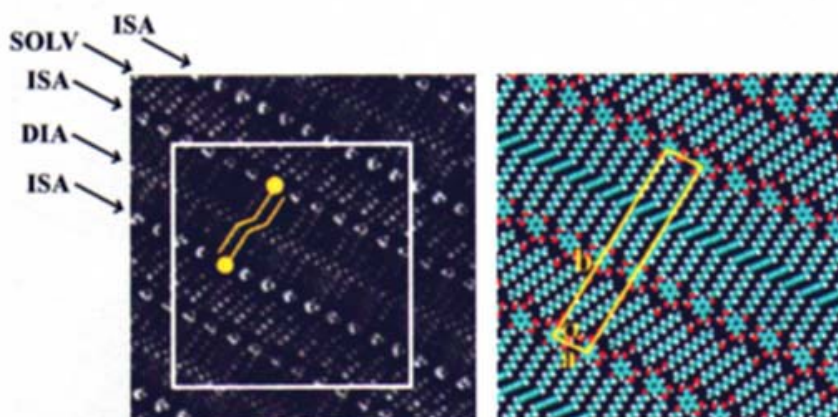


Figure 2.5. In the left image is presented a  $12.7 \times 12.7 \text{ nm}^2$  STM image of physisorbed molecules of compound **1** (ML) from solution of 1-undecanol, with monolayer coverage. The labeling corresponds to: ISA - the isophthalic acid headgroups, DIA - the diacetylene groups, and SOLV - solvent molecules. The modeling of the area indicated in the STM image, with superimposed unit cell, is represented in the right image. (Figure reproduced from Grim *et al.*, with permission of Wiley)<sup>181</sup>

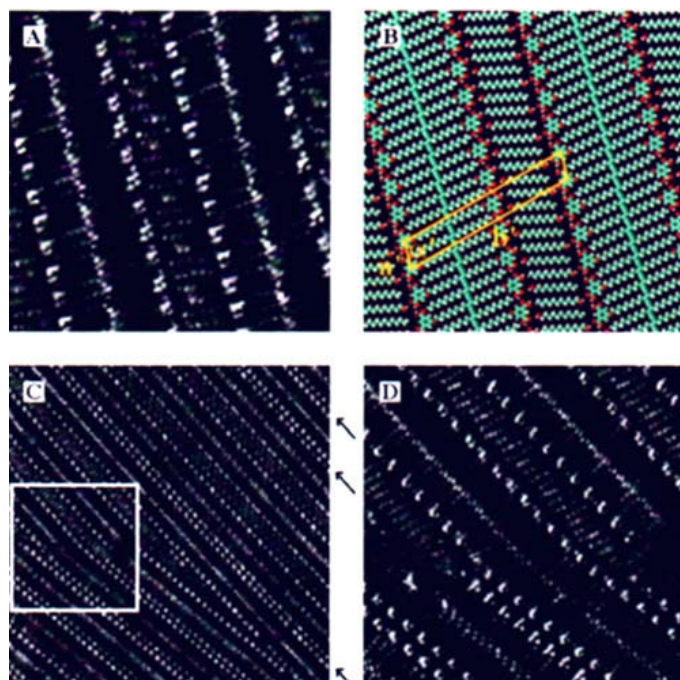


Figure 2.6. A).  $10.8 \times 10.8 \text{ nm}^2$  STM image of an irradiated monolayer. The schematic model of the imaged area in A, including the unit cell is presented in B). The  $38.5 \times 38.5 \text{ nm}^2$  STM image of a domain boundary separating a nonpolymerized (in the lower left) and a polymerized (rest of the image) region is presented in C). The arrows indicate the absence of solvent co-deposition inside the polymerized domain. A  $15.3 \times 15.3 \text{ nm}^2$  zoom of the indicated area in C is presented in D). (Figure reproduced from Grim *et al.*, with permission of Wiley)<sup>181</sup>

In the same category of reactions could be placed the light- and tip-induced polymerization of compounds with one 5-(10,12-tricosadiinyloxy) isophthalic acid (ISA-DIA) or two 2,5-(10,12-heneicosadiinyloxy) terephthalic acid (TTA-DIA) diacetylene functions investigated by Miura *et al.* at an air/solid interface.<sup>102</sup> Reaction models of self-assembly-to-polymers, for diacetylene as well as for these two molecules are presented in Figure 2.7.

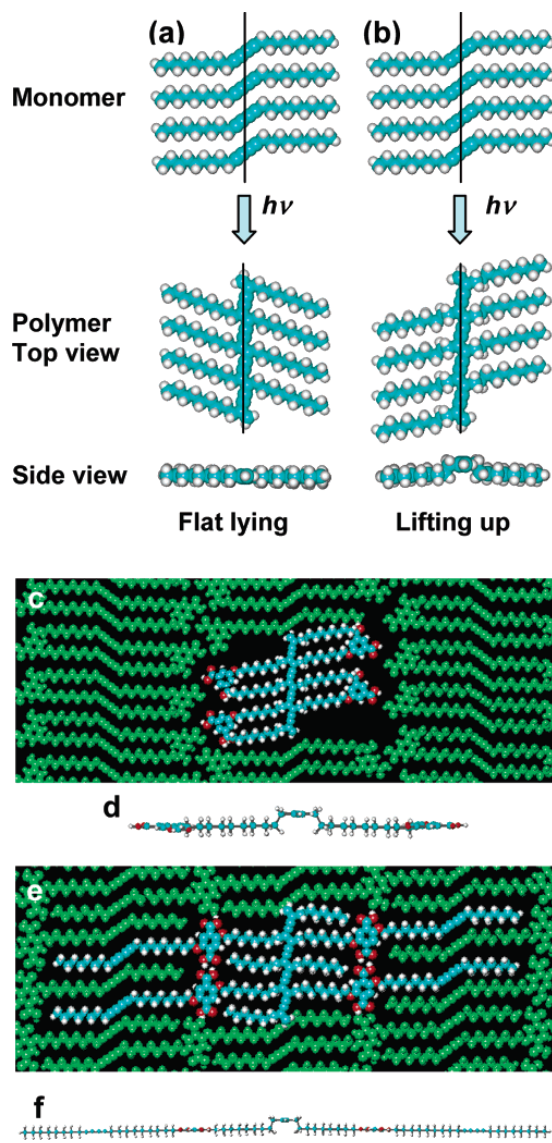


Figure 2.7. (a) Model of topochemical polymerization of diacetylene, (b) Lifted polymer backbone upon polymerization. (c) Model of polymerized ISA-DIA (blue) among non-polymerized ISA-DIA monomers (green). (d) Side view of polymerized ISA-DIA. (e) Molecular modeling of a mixture of polymerized TTA-DIA (blue) and TTA-DIA monomers (green). (f) Side view of polymerized TTA-DIA. (Figure reproduced from Miura *et al.*, with permission of American Chemical Society)<sup>102</sup>

A similar packing mode was obtained by Okawa and Aono in a four-step reaction on graphite starting from arrays of 10,12-pentacosadiynoic acid (Figure 2.8). From biradicals

obtained by optical ( $h\nu$ ) and vibrational excitation ( $kT$ ) they perfected the nanowire shape of the final products by means of addition and propagation reactions, initiated by the STM tip (Figure 2.9). A single step reaction was involved for 10,12-nonacosadiynoic acid. Both reactions propagate 1-dimensionally in both directions until a domain boundary or a structural defect is reached. For the system formed with 10,12-pentacosadiynoic acid the molecules are disposed in chains with each COOH termination placed in an opposite manner compared to those of its neighbor, with a water molecule linking each pair of opposing neighboring carboxylic groups. Furthermore, the conductivity of the obtained polydiacetylene backbone depends only on whether there is any charge transfer between the substrate and the polymer.

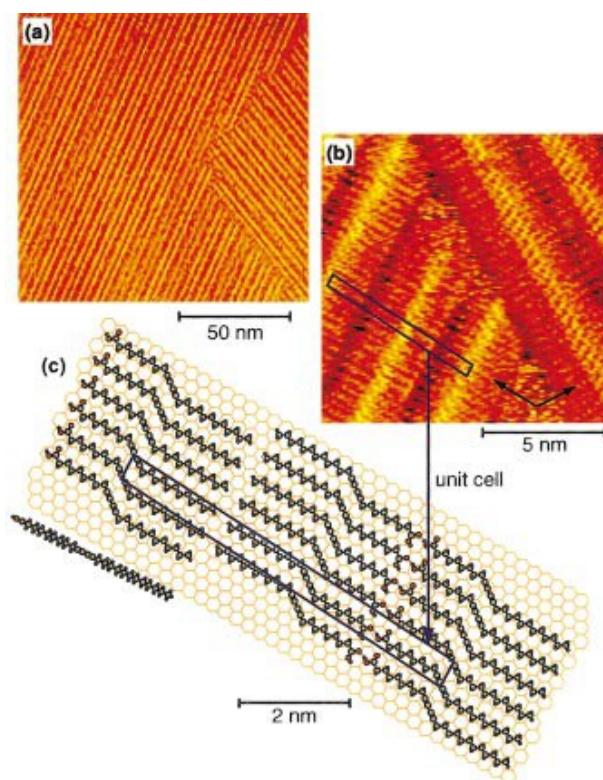


Figure 2.8. STM image of 10,12-pentacosadiynoic acid layer on graphite in (a) and (b). The main crystal axes of graphite ( $\langle 1 \frac{\bar{1}}{2} \frac{\bar{1}}{2} 0 \rangle$ ) are indicated by arrows. (c) Top and side views of an assembly model. (Figure reproduced from Okawa *et al.*, with permission of AIP Publishing LLC)

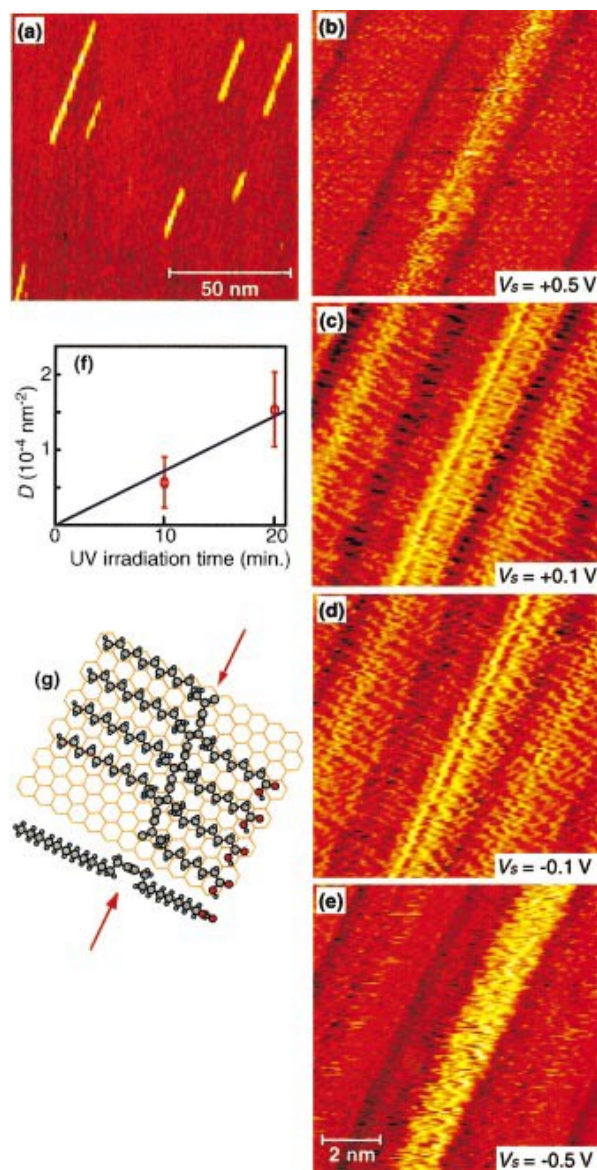


Figure 2.9. STM image obtained after ultraviolet irradiation (polymers) (a)–(e). The number density of photopolymerized polydiacetylenes versus the duration of irradiation is plotted in (f). (g) Proposed model for the polymer. (Figure reproduced from Okawa *et al.*, with permission of AIP Publishing LLC)<sup>106</sup>

Sullivan *et al.* performed controlled STM-tip-induced chain polymerization of substituted diacetylenes, such as 10,12-tricosadiynoic acid (TCDA) in octylbenzene, on HOPG surfaces.<sup>105</sup> As deposited, a self-organized monolayer was obtained at the liquid-solid interface (Figure 2.10), consisting of lamellae oriented almost perpendicularly to the fast scan

direction and interrupted at the edge of the surface domains, here termed “surface corals”. Due to the disrupted topo-chemistry, the confinement of the organic material was maintained inside the “coral” even after the application of a voltage pulse and polymerization *via* a reaction between close neighbors of TCDA.

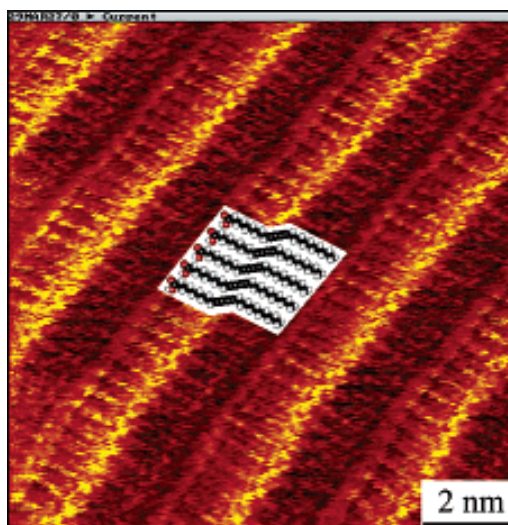


Figure 2.10.  $11 \times 11 \text{ nm}^2$  STM image of a self-ordered monolayer of TCDA/HOPG, in a solution with octylbenzene. (Figure reproduced from Sullivan *et al.*, with permission of the American Chemical Society)<sup>105</sup>

*Electrochemistry* is a conventional technique for synthesizing conjugated polymers on electrodes based on the application of a given number of positive pulses to an electrode submerged in an electrolyte.<sup>280</sup> Based on the step-by-step *electropolymerization* (*Electrochemical Epitaxial Polymerization*, ECEP) of 3-butoxy-4-methylthiophene (BuOMT) monomer electrolyte, soluble in dichloromethane (DCM), Sakaguchi *et al.* obtained conjugated polymer wires,  $\sim 75 \text{ nm}$  long (200 monomer repeat units) grown adsorbed on the iodine-covered Au(111) electrode (Figure 2.11).<sup>182</sup> The maximum conjugation length propagated along different substrate directions is limited by the competition between nonparallel neighboring long wires, which as a result promotes the propagation of shorter wires in the vacant spaces, and increases with the iodine concentration and with the number of applied pulses.

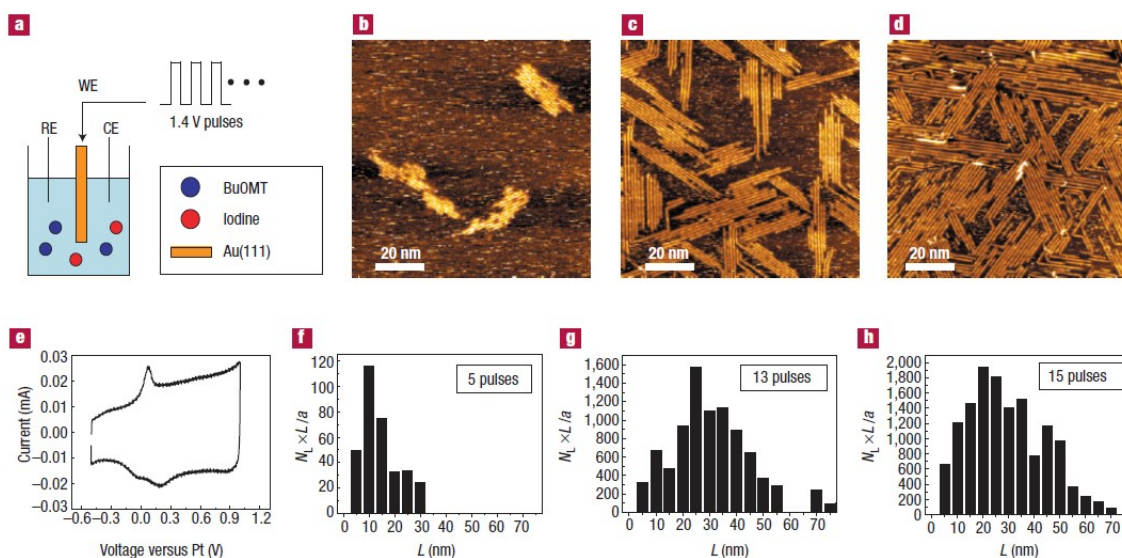


Figure 2.11. Electrochemical epitaxial polymerization of single-polythiophene wires. Experimental set-up in (a). STM images of the substrates obtained at different numbers of voltage pulses in (b)–(d). (e) Cyclic voltammogram of polythiophene wires, made by applying 30 pulses. (f)–(h) Histograms of wire-length distributions for substrates made by applying the respective number of pulses. (Figure reproduced from Sakaguchi *et al.*, with permission of Nature Publishing Group)<sup>182</sup>

Two distinctive features characterize these nanowires: (1) they are weakly bonded to the iodine-covered Au(111) substrate, which makes them able to jump onto adjacent polythiophene wires to form bilayer structures; (2) the blinking of single thiophene unit, which appears like a bright spot, within a single thiophenic wire (polymer) and not only within a self-assembled structure of molecules. The latest effect could have either topographic (change in the planarity) or electronic (due to the trapping sites of the oxidized state - ON/OFF polaron; or local iodine doping) origin.

Depending on the type of the monomer, various patterns of single thiophene wires could be obtained on the surface. Illustrated below is the case of the 3-octyloxy-4-methylthiophene (C8OMT) and 3-octyl-4-methylthiophene (C8MT) monomers which, by using the ECEP technique on the I-Au(111) electrode, produced weakly adsorbed hetero-wires of  $\sim 100$  nm and  $\sim 50$  nm in length, respectively (Figure 2.12).<sup>183</sup>

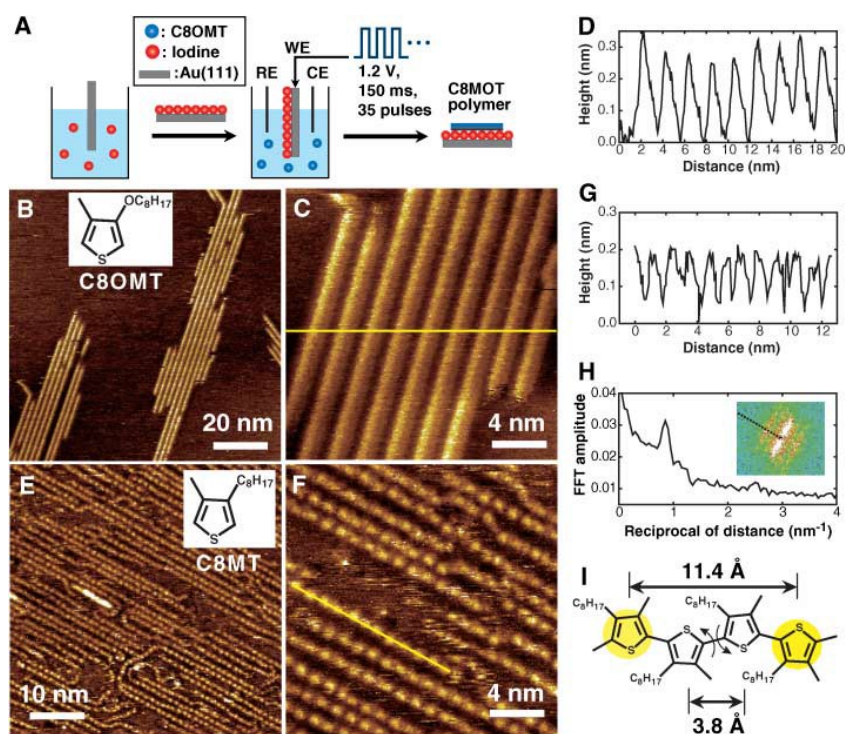


Figure 2.12. (A) Experimental set-up of ECEP to produce monopolymer wires. (B and C) STM images of C8OMT-polymer wires obtained after 35 pulses. (D) Cross section along the line shown in (C). (E and F) STM images of C8MT-polymer wires obtained after 150 pulses. (G) Cross section along the line shown in (F). (H) 2-dimensional FFT image of (F) (inset) and its cross section. (I) Proposed structure of C8MT polymer on the surface. (Figure reproduced from Sakaguchi *et al.*, with permission of The American Association for the Advancement of Science)<sup>183</sup>

The asymmetric reactivity of the monomer could induce a certain degree of torsion between the thiophene blocks in the chain and break the conjugation of  $\pi$  electrons. For this reason, the two structures appear different in the STM images; the C8OMT-polymer appears as continuously bright wires while C8MT appears as bright dots connected by dark nodes (bright dots - electronic orbitals on planar thiophene rings with high conjugation of  $\pi$  electrons; dark nodes – low conjugation in the distorted thiophene rings). However, this block-torsion seems to be dependent on the surface on which it is produced, as the periodic dot-like appearance was not observed on the I-free surface of Au(111).

The structures of these polymers were reproduced by using a different method, in which the C8MT-polymer was first created on the substrate and then the substrate was subsequently exposed to an electrolyte solution containing C8OMT, and both the C8MT polymer and C8OMT from solution were electropolymerized. Although in some regions the STM images show independently developed processes the second method creates hetero-junctions of interlinked polymers observed as a di-block and tri-block structure in which a C8MT-polymer wire is sandwiched between two C8OMT wires.

Electropolymerization, induced this time by an STM tip submerged in a solution of 3-octylthiophene molecules and electrolyte, was performed by Zhou *et al.*,<sup>104</sup> on an indium-tin-oxide (ITO)-coated glass substrate. Poly(3-octylthiophene) was then grown by applying a high anodic bias (5-6 V) on the substrate, with respect to the STM tip.

They found that 3-octylthiophene electro-polymerises *via* a 3-dimensional nucleation and growth mechanism giving rise to: firstly, a structure of nodes 3–10 nm diameter (at low tip pass number); and in addition, secondly, a helical structure 20–60 nm in length (above five tip passes, see Figure 2.13). Above 15 polymerization passes, the film morphology is dominated by the presence of granular and probably close packed structures.

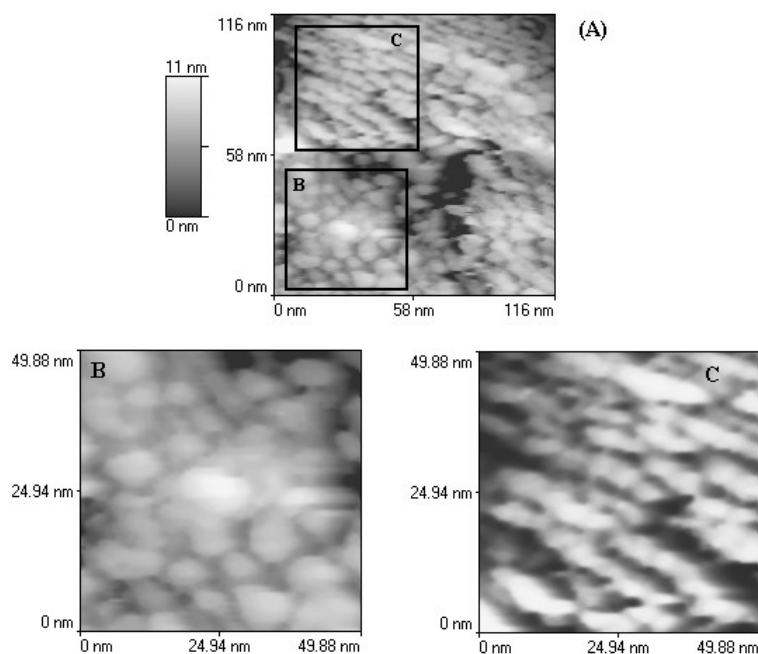


Figure 2.13. (a) STM image recorded at low bias voltage (200 mV), the content was obtained after five polymerization passes (5-6 V), evidencing three different structures: (1) helical, (2)

nodular, and (3) mixed. (b) Enlarged view of the nodular structures in (a). (c) Enlarged view of the helical structure in (a). (Figure reproduced from Zhou *et al.*, with permission of Springer)<sup>104</sup>

The electron induced reactions involving a STM tip and engineering the reactivity by promoting chemical reactions in a linear chain of assembled dimethyl-disulfide  $\text{CH}_3\text{SSCH}_3$  molecules on the (111) and (100) surfaces of gold at down to 5K, were probably the most detailed described by Maksymovych *et al.*<sup>103</sup>

The assembly redirects the energy flow and allows a facile propagation of the reaction, in steps, to up to 10 neighboring building blocks (on Au(100)) along the chain, reducing the activation energy.

In a simplistic way, the mechanism consists of: (i) hot electrons transported *via* a gold surface resonance; (ii) S-S bond scissions; (iii) recombination of  $\text{CH}_3\text{S}$ ; with eventual (iv) translation over the surface ( $\sim 2.5$  Å relative to the reactant molecules), and (v) realignment in a different way with respect to the surface directions producing the assembly of molecules of opposite conformation.

To inject the electrons into the system and obtain dissociated  $\text{CH}_3\text{S}$  fragments (as shown in Figure 2.14), a lower bias voltage was required (0.9-1.4 V),<sup>281</sup> than previously used by Zhou *et al.* ( $\sim 5$  V).<sup>104</sup> Of a considerable importance is the method of injecting the hot electrons. A substantially lower energy (0.7-1.0 eV) is required to obtain the same results as previously reported, but this time by injecting electrons from the tip positioned right above a molecular unit from the molecular chain.

Accompanying the dissociation of  $\text{CH}_3\text{SSCH}_3$  into  $\text{CH}_3\text{S}$ , the resulting fragments will gain considerable excess energy and push into neighboring molecular blocks. This will promote the S-S cleavage and the ejection of a new  $\text{CH}_3\text{S}$  fragment in the successive reaction step.

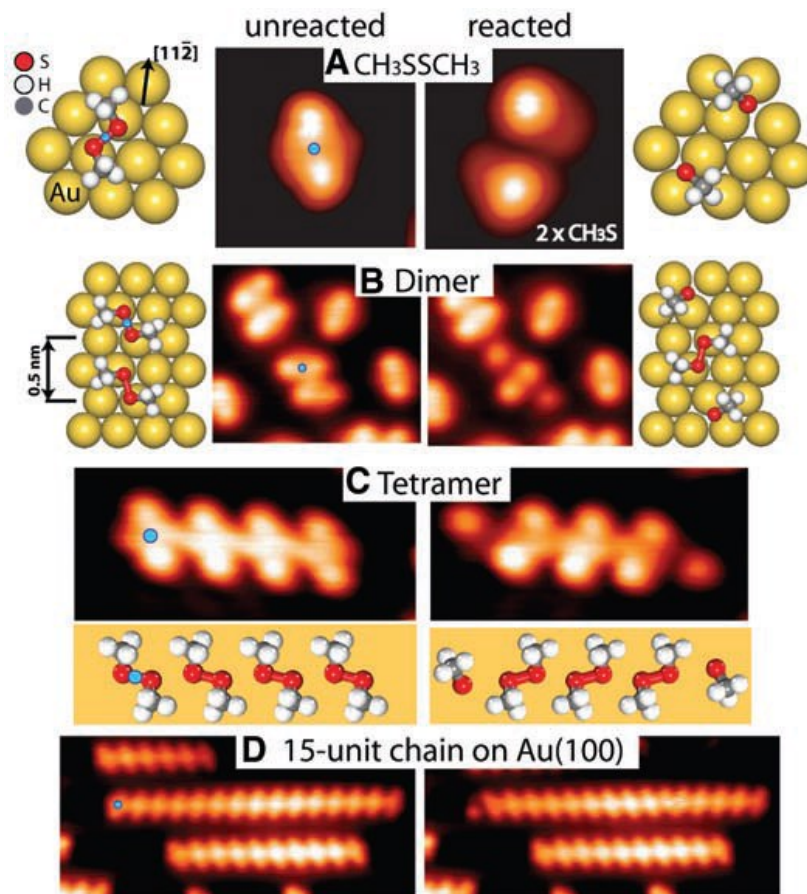


Figure 2.14. STM and schematic images presenting the evolution of single  $\text{CH}_3\text{SSCH}_3$  molecules on the Au(111) surface, before and after electron induced dissociation. (A) Dissociation of  $\text{CH}_3\text{SSCH}_3$  by a STM pulse.<sup>281</sup> (B and C) Recombination to  $\text{CH}_3\text{SSCH}_3$  and assembly on Au(111) induced by a voltage pulse. (D) Similar chain reaction on Au(100). (Figure reproduced from Maksymovych *et al.*, with permission of The American Association for the Advancement of Science)<sup>103</sup>

An interesting approach to polymerization is the formation of two component polymeric nanostructures by *polycondensation based on the Schiff base reaction* (Figure 2.15).

There is a liquid-solid approach, based on the thermodynamic control over equilibrium polymerization at the HOPG interface and in particular solution conditions (as the Schiff base bonding is generally regulated by concentration and pH), and a UHV approach on the Au(111) surface, both imaged with submolecular resolution.

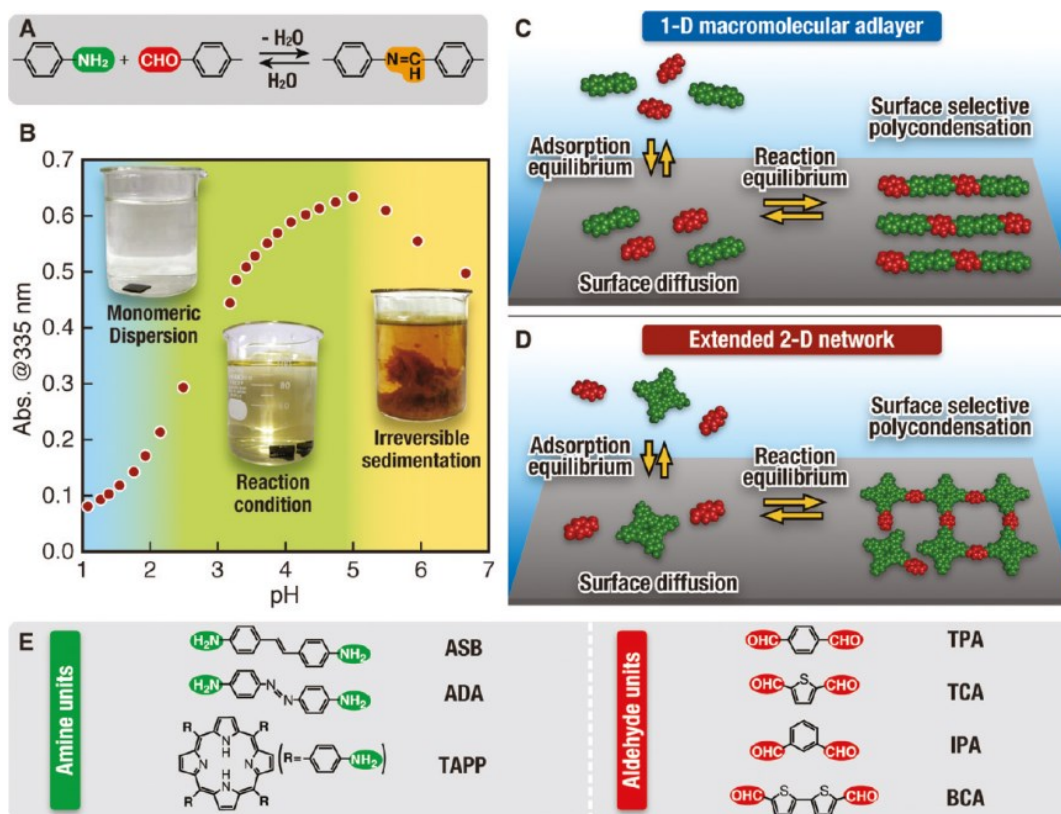


Figure 2.15. Reaction scheme of the Schiff base coupling reaction in (A); pH-dependence of the absorbance in (B), the reaction producing 1-D (C) and 2-D (D)  $\pi$ -conjugated nanoarchitectures; list of the molecular building blocks used with corresponding acronyms in (E). (Figure reproduced from Tanoue *et al.*, with permission of the American Chemical Society)<sup>186</sup>

In the first case, studied by Tanoue *et al.*,<sup>186</sup> any combination of molecules bearing two primary amino units, 4,40-diaminostilbene dihydrochloride (ASB) and 4,40-azodianiline (ADA), and two aldehyde units, terephthalaldehyde (TPA) and 2,5-thiophenedicarboxaldehyde (TCA), could create extended ordered domains of  $\pi$ -conjugated linear polymer arrays. When a meta-substituted building molecule, isophthalaldehyde (IPA) was used with ASB, a domain consisting of zigzag lines was observed.

5,10,15,20-tetrakis(4-aminophenyl) porphyrin (TAPP) provides however four possible linkages to other molecules. In combination with bifunctional connector molecules, 2D macromolecular meshes, composed of TAPP molecules interconnected by covalently bonded

linker molecules, were generated. Unconnected TAPP molecules also were observed as incorporated guests.

In UHV, Weigelt *et al.* obtained pores of 3-10 nm in size by condensation polymerization reactions, giving polymers connected by imine bonds, starting from tris(alkyl)aldehyde (trialdehyde) (Figure 2.16), and 1,6-diaminohexane (diamine).<sup>282</sup> However, upon co-deposition followed by annealing above 400 K, open filamentous structures are formed. The trialdehydes, with a characteristic Y shape with tert-butyl group protrusions are linked together and saturated by rod-like alkyl chains of the diamines.

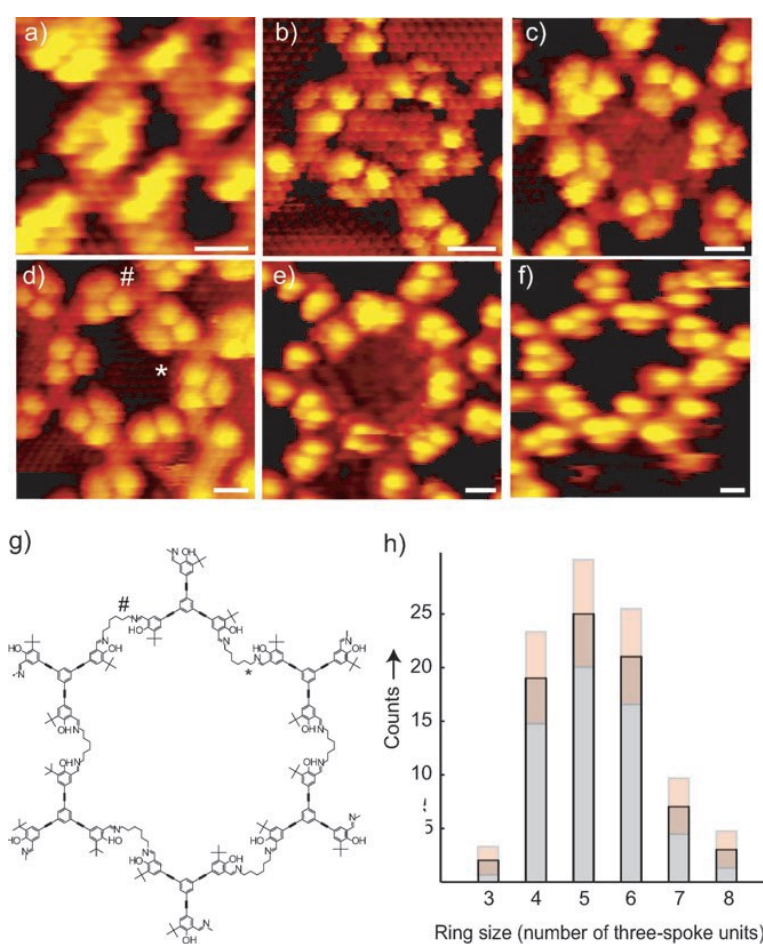


Figure 2.16. STM images of network pores formed by three to eight trialdehydes in (a)-(f) (scale bar: 1 nm). (g) Schematic representation of the six-membered pore from (d) with alkyl linkers placed at the inner (\*) and outer (#) pore wall. (h) Size distribution of the observed

pores (standard deviation is plotted in pink). (Figure reproduced from Weigelt *et al.*, with permission of John Wiley and Sons)<sup>282</sup>

To investigate if the order and connectivity in the polymer can be controlled, two different preparation procedures were applied. In the both, the trialdehyde was first dosed on the surface. The difference between the two methods was only in the moment of annealing at 400-500 K, before or after exposing to 1,6-diaminohexane. Due in principal to kinetic conditions during the reaction, the formation of smaller oligomers is favored by the first preparation method (ordered islands of trialdehydes are covered by multilayers of diamine, and all trialdehydes are saturated), whereas the second method induces formation of extended polymers (amines supplied at a high substrate temperature, free diffusion of melted trialdehydes; most likely to react).

A preference for rings with four to six interlinked trialdehydes was observed; the competition between the trialdehyde addition and intramolecular ring closure disfavors large pore sizes.

Probably the most effective reaction to obtain large and planar 2D networks of polymers, with yields of up to 100% is the *polycondensation of molecules functionalized with boronic acid*. However, the drawback of this approach consists in the instability of the formed bond in a hygroscopic environment.

The pioneering example of this surface covalent organic framework (SCOF) was emphasized by Zwaneveld *et al.* with the production of boronate-based nanoporous structures, covalently bonded on a clean Ag(111) substrate, by starting from two different precursors under UHV conditions.<sup>188</sup>

One reaction consisted in the molecular dehydration of 1,4-benzenediboronic acid (BDBA), with three boronic acid molecules reacting to form a six-membered B<sub>3</sub>O<sub>3</sub> (boroxine) ring with the elimination of water, and thermal stability up to 475 °C for a time, (Figure 2.17).

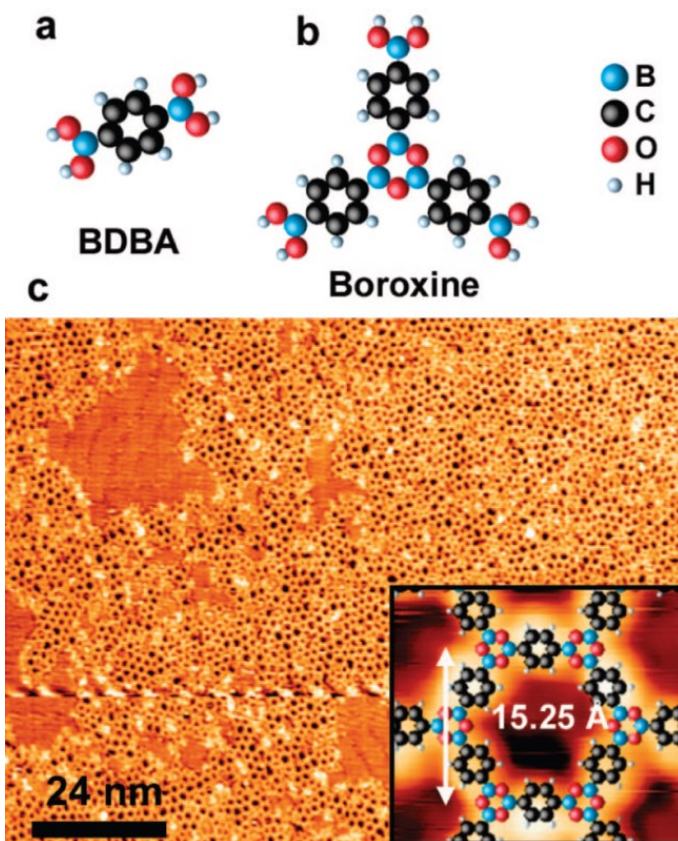


Figure 2.17. SCOF-1 type of products formed on Ag(111) from BDDBA precursor: (a) schematic representation of BDDBA structure; (b) schematic representation of the boroxine repeat unit; (c)  $120 \times 90 \text{ nm}^2$  STM image of a SCOF-1 film, close to a ML coverage. The inset shows the calculated chemical structure (DFT), superposed over an STM image. (Figure reproduced from Zwaneveld *et al.*, with permission from the American Chemical Society)<sup>188</sup>

To produce less defective networks, a second approach was proposed through the introduction of a second reaction. It proceeds with the condensation of BDDBA and 2,3,6,7,10,11-hexahydroxytriphenylene (HHTP), to form a dioxaborole heterocycle. To prevent the homopolymerization of BDDBA, one monolayer of HHTP was deposited first, followed by co-deposition of both the molecules (Figure 2.18).

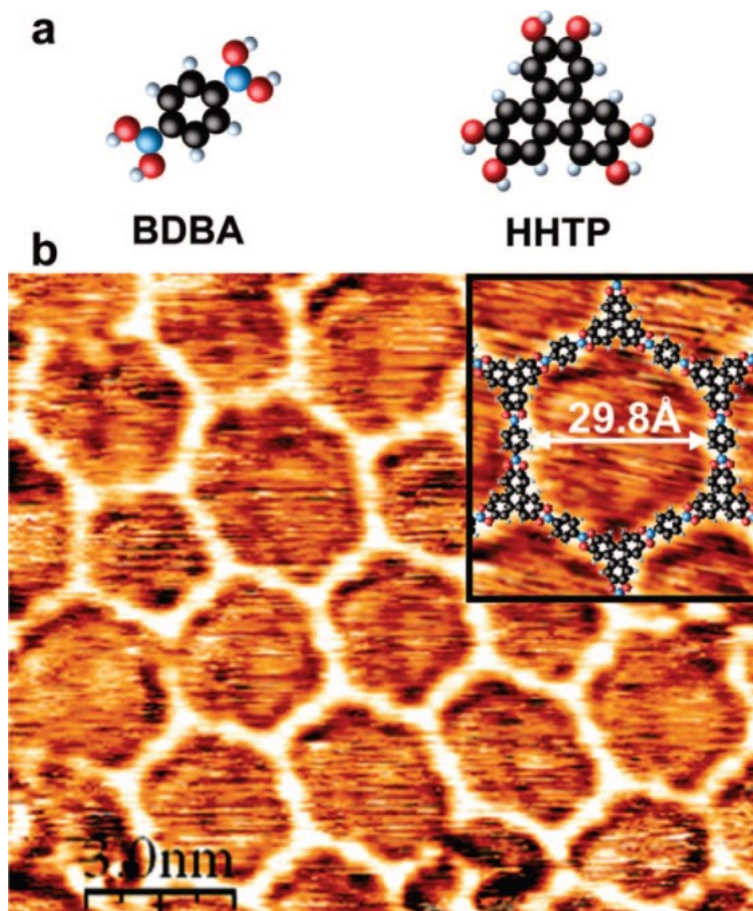


Figure 2.18. Schematic representation and STM images of SCOF-2 type formation from BDBA and HHTP molecules on Ag(111). (a) Schematic representation of the chemical structure of BDBA and HHTP; (b) STM image of SCOF-2. The inset shows the calculated chemical structure of the SCOF-2 network (DFT), superposed over an STM image. (Figure reproduced from Zwaneveld *et al.*, with permission from the American Chemical Society)<sup>188</sup>

A similar approach, by starting from BDBA was demonstrated by Dienstmaier *et al.* on a less reactive HOPG surface (Figure 2.19).<sup>244</sup> In a first synthetic route they pre-polymerized the BDBA at 250 °C into a nano-crystalline covalent organic frameworks (COFs) precursor, which was later drop-cast on the graphite surface. The domain size was increased by annealing. In a second route, the BDBA was deposited from solution directly onto graphite, thermally activating the condensation reaction.

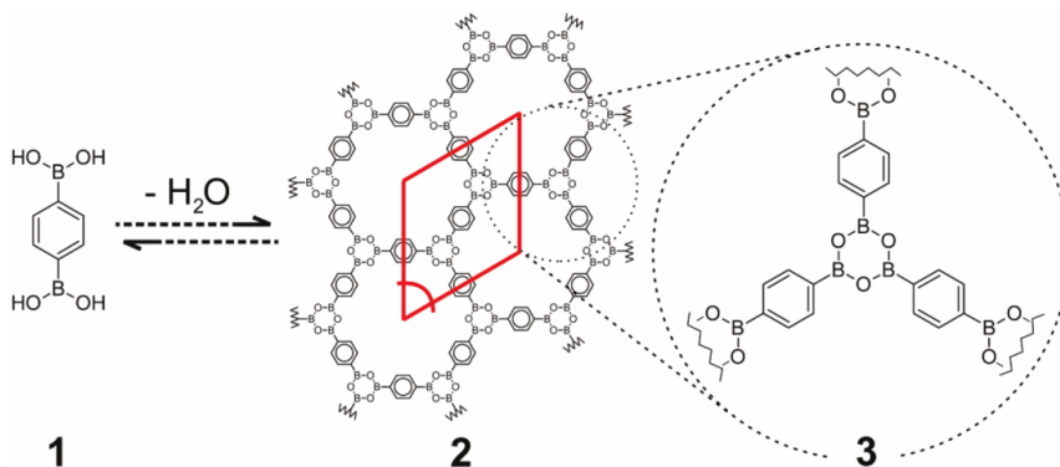


Figure 2.19. Schematic representation of the self-condensation reaction of BDBA from monomers (1) into single 2D COF-1 layer (2). During the condensation,  $\text{H}_2\text{O}$  is released. (3) A boroxine ring. (Scheme reproduced from Dienstmaier *et al.*, with permission from the American Chemical Society)<sup>244</sup>

A systematic study of 1,4-benzenediboronic acid (BDBA) molecular vapor deposited in ultra-high vacuum conditions on noble metal surfaces such as Ag(111), Ag(100), Au(111), and Cu(111) was performed by Ourdjini *et al.* (Figure 2.20),<sup>245</sup> with the intention of growing long range two-dimensional polymers.

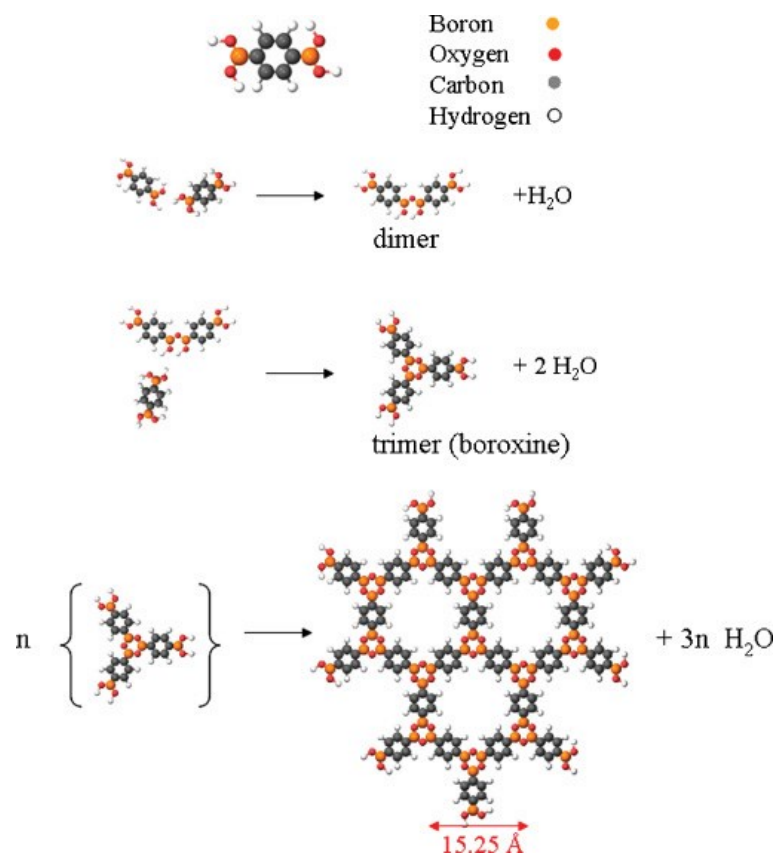


Figure 2.20. Schematic representation of a 2D polymer by dehydration of BDBA molecules. (Scheme reproduced from Ourdjini *et al.*, with permission of The American Physical Society)<sup>245</sup>

They concluded that, due to the correct trade-off between the adsorption strength and diffusivity conditions, Ag(111) and Ag(110) surfaces offer the best templates for polymer formation, with polymers extending from the steps to terraces, and thermal stability up to 450 °C. Hexagonal cells were predominant; however, various polygonal shapes, due to incompletely reacted BDBA molecules inside the molecular layer were still observed.

At the extremes were the Cu(111) and Au(111) surfaces. On Cu(111), the surface is too sticky at room temperature, and therefore the BDBA molecules diffuse too slowly. Once the first polymeric domains are formed, they are more difficult to reorganize and therefore this leaves more vacancies between the domains. On the other hand, on Au(111) (as well as Ag), at RT the diffusion is enough for an extended 2D hydrogen-bonded phase to form, preferably at steps, and extend over terraces (Figure 2.21). By annealing, due to a weak adsorption a large

part of this phase desorbs from the Au(111) surface, where the growth was only observed along the steps.

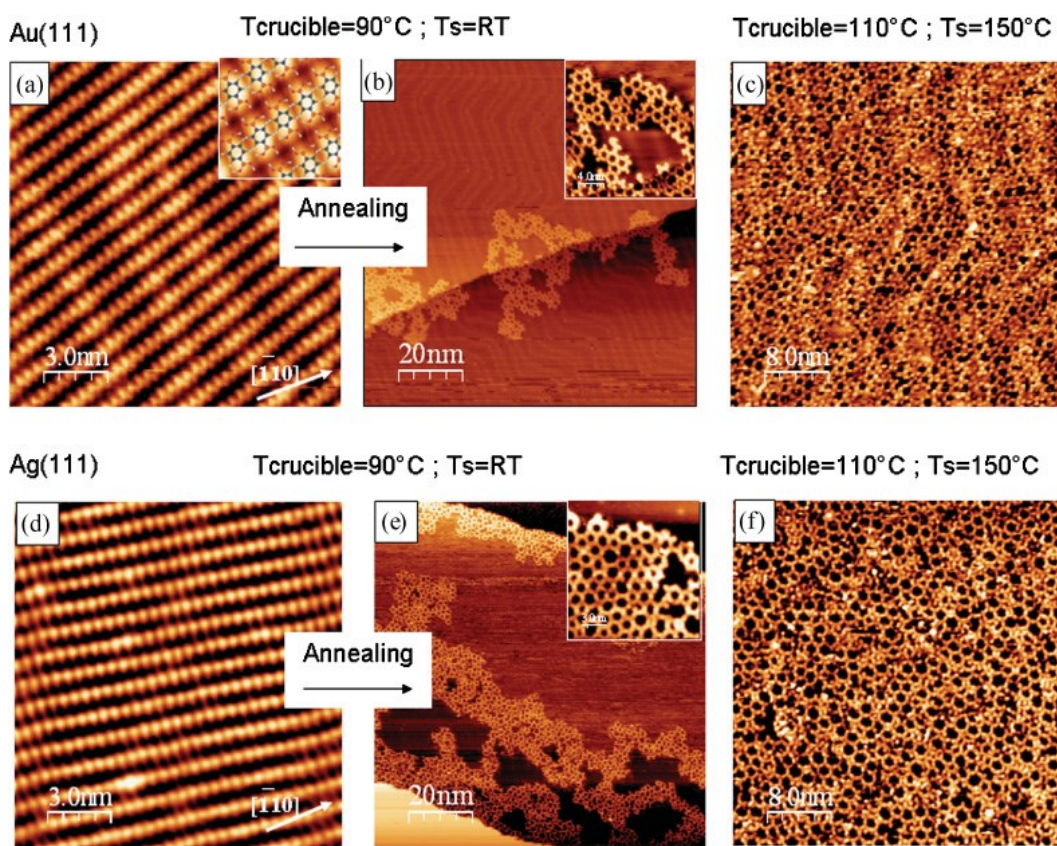


Figure 2.21. (a) STM images of H-bonded supramolecular phases formed from BDBA molecules deposited at low flux on Au(111) surface ( $T_c = 90^\circ\text{C}$  = crucible temperature,  $T_s = \text{RT}$  = surface temperature at the moment of deposition). (b) After annealing at  $350^\circ\text{C}$ ; (c) STM images after high flux deposition ( $T_c = 110^\circ\text{C}$ ,  $T_s = 150^\circ\text{C}$ ). (d) STM image showing a H-bonded supramolecular phase obtained from BDBA molecules deposited at low flux on Ag(111) ( $T_c = 90^\circ\text{C}$ ,  $T_s = \text{RT}$ ). (e) After annealing at  $350^\circ\text{C}$ . (f) High flux deposition on Ag(111) ( $T_c = 110^\circ\text{C}$ ,  $T_s = 150^\circ\text{C}$ ). (Figure reproduced from Ourdjini *et al.*, with permission of The American Physical Society)<sup>245</sup>

In these systems, by applying a voltage pulse, the STM tip could also be used to induce a reaction that then propagates without additional energy input until it is terminated by a

defect,<sup>106, 283</sup> or by consumption of all available monomers. Recent examples of STM-induced phenomena on Ag(100) surface in UHV conditions include the tip-induced polymerization of 1,4-benzenediboronic acid (BDBA), as reported by Clair *et al.* (model image in Figure 2.22).<sup>101</sup> In the same research group Ourdjini and Zwaneveld already demonstrated the thermally induced self-condensation (dehydration) of boronic acid on other surfaces.<sup>188, 245</sup>

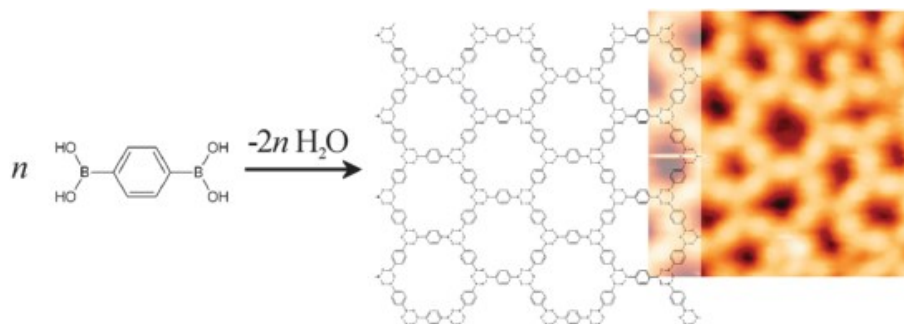


Figure 2.22. Reaction scheme of 1,4-benzenediboronic acid (BDBA) polymerization, and STM image of the real polymer network. (Figure and caption reproduced from Clair *et al.*, with permission of the Royal Society of Chemistry)<sup>101</sup>

The BDBA molecules assemble first in a supra-molecular phase of H-bonded domains which could eventually polymerize through different mechanisms. One of these polymerization mechanisms, although slower (tens of hours), is based on the intrinsic catalytic property of the surface alone, at room temperature. The steric effect between the molecules plays an important role in the reaction kinetics and subsequently in the quality and the range of polymerization, as molecules require a certain amount of free room to reconfigure from the H-bonded phase into the polymer geometry based on boroxine rings. The temporal evolution of this process is presented in Figure 2.23.

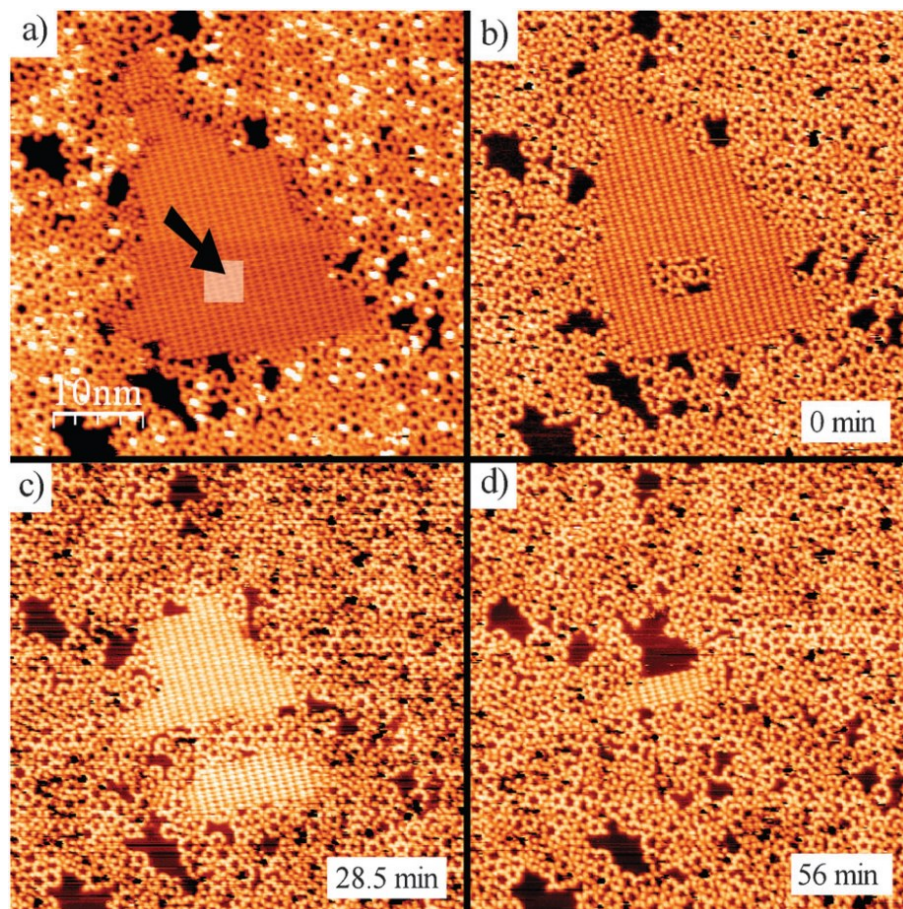


Figure 2.23. Tip-induced polymerization of BDBA (a)-(d), showing the reaction propagation until the total disappearance of the H-bonded phase. (Figure reproduced from Clair *et al.*, with permission of the Royal Society of Chemistry)<sup>101</sup>

The second mechanism found to contribute to polymerization is based on irradiation with electrons. Here, the reaction could be initiated by the STM tip (over nm-sized area) and enhanced over a long range, after few seconds, through bombardment with low-energy electrons (Figure 2.24).

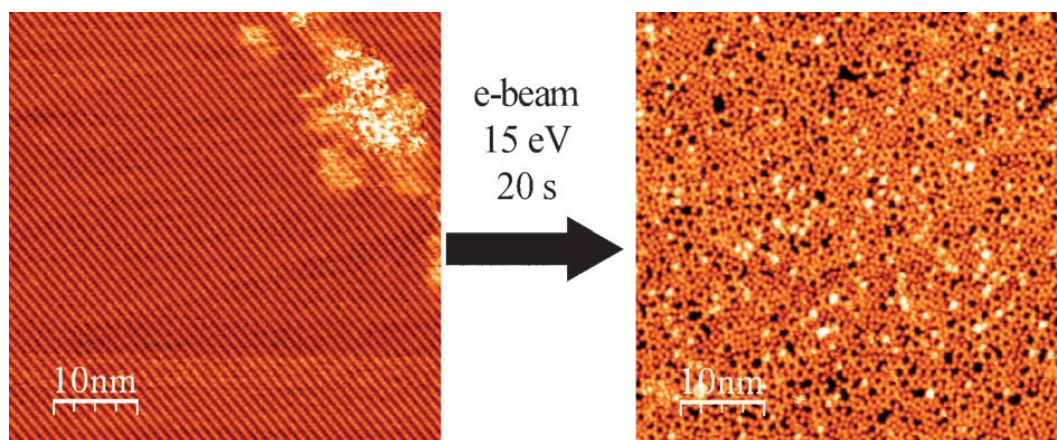


Figure 2.24. e-Beam induced polymerization of BDBA. (Figure reproduced from Clair *et al.*, with permission of the Royal Society of Chemistry)<sup>101</sup>

A different approach, using two different reactions in successive steps, was followed by Faury *et al.*,<sup>187</sup> by introducing a bi-functional precursor, p-bromo-benzene boronic acid (BBBA) which was vapor deposited in UHV on the Au(111) surface (Figure 2.25), which acts here as a catalyst.

At first, the boronic acid moieties react to form bromine-terminated trimers linked by covalent boroxine rings, which self-assemble in large domains by forming hydrogen bonds between halogen atoms and aromatic hydrogen. Afterwards, the bromine terminations are removed and Br— and C— radicals are first stabilized by coordination with the Au surface atoms,<sup>32</sup> and then transformed into C—C bonds between the trimers through a thermally activated Ullmann coupling reaction, at 250 °C. Although the boroxine yield was almost 100% the polymerization yielded only 88%; this sequential process produced honeycomb structures with a hexagonal pore size of about 23 Å and a high thermal stability up to 400 °C. However, due to the irreversible character of the covalent bonds, the prior formation of supramolecular phases in an improperly balanced, sterically hindered and surface confining environment induces kinetic limitations and so decreases of the overall reaction yield.<sup>101, 245</sup>

In a separate experiment, to increase the diffusion of the boroxine monomer before the Ullmann reaction, they deposited the BBBA on Au(111) substrate kept at 250 °C. By using different growth conditions, they almost doubled the surface area covered by polygons as

compared with the total polymer area. The efficiency of boroxine creation was maximal and the reaction yield for the Ullmann coupling increased to 94%.

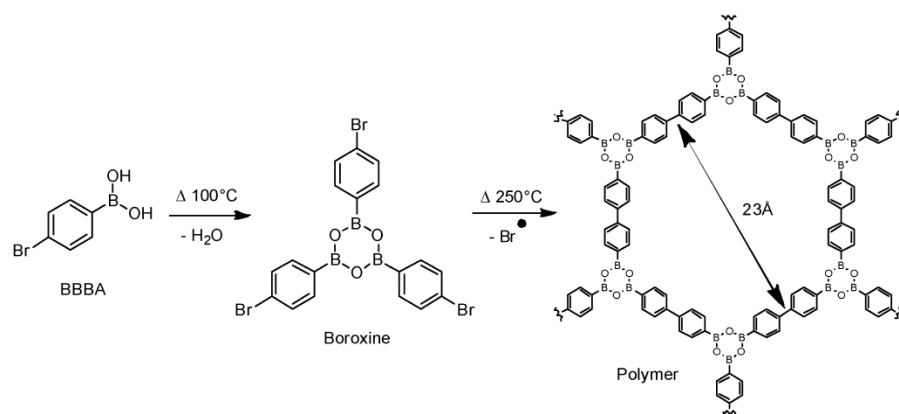


Figure 2.25. Reaction scheme of the sequential polymerization process of BBBA. (Scheme reproduced from Faury *et al.*, with permission of the American Chemical Society)<sup>187</sup>

The mechanism of new free bond formation has been explored by using the catalytic *desulfurization reaction of thiophene based organic precursors*, on the Ni(111) surface.

Dependent on the surface temperature (which should be relatively low, otherwise it could promote molecular cleavage), on the Ni(111) surface (which accepts  $\pi$  electrons from the molecule) and at low coverage thiophene adsorbs similar to benzene, bonded parallel to the surface as reported by Schoofs *et al.*<sup>242</sup> A parallel adsorption geometry was also reported on Cu(111).<sup>284</sup> With proper thermal treatment, thiophene decomposes on most of the transition metal surfaces. Detailed studies into this process on Ni(111), at low temperature, were performed by Huntley *et al.*<sup>192</sup> X-ray photoelectron spectroscopy (XPS) data show that S–C scission in the thiophenic ring occurs at a low temperature, about 90-100 K and completes at 150 K, with the carbon skeleton remaining intact. This contradicts the previous statements of Schoofs that thiophene could be present as a molecular species near room temperature.

In the work presented in the following chapters, the thiophene was included in a larger molecule with a large anthracene core. From the considerations of band-gap it introduces, in a perfect conjugated  $\text{sp}^2$  structures as graphene, it was important to consider studying its detailed behavior, and its usefulness to stay intact.

*Hydrodesulfurization of benzothiophene derivatives* has been used in the total synthesis of natural products although the reaction did not increase the molecular complexity of the product.<sup>195, 196</sup> However, experiments involving a pre-deuterized surface show, contrary to previous belief, that the ring hydrogenation does not precede the C–S bond scission. The first evidence of C–D bond formation occurs near 175 K, above the temperature at which the C–S bond scission is completed (150 K). Moreover, there is a consistent position dependent selectivity for the adsorbent cleavage between the 2,5-positions and the 3-position in the thiophene ring. The stronger cleavability in the 2,5-position suggests a stronger interaction between the surface and the molecule, close to the sulfur side, triggered probably by the initial thiophene-surface adsorption through the sulfur atom. At higher coverage, this may induce a tilt in the adsorption geometry, towards the sulfur position. Quantitatively, the reaction of 3-methylthiophene and 2,5-dimethylthiophene were examined by temperature programmed desorption (TPD) which shows that methyl groups in the 2- and 5-positions are cleaved first, and below 200 K.

There are few cases where a new type of reaction was suggested. One example is the unexpected *polymerization of tetra(mesityl)porphyrin into robust covalent porphyrin scaffolds via dehydrogenative C–C coupling*, proposed by Veld *et al.*,<sup>22</sup> on a Cu(110) surface in UHV conditions (see images with submolecular resolution in Figure 2.26), after annealing at 150–200 °C. Through a different reaction mechanism, covalently linked porphyrin arrays were reported by Grill *et al.*,<sup>185</sup> on Au(111) surface, starting from a bromine-terminated precursor tetra(4-bromophenyl)porphyrin (Br4TPP).

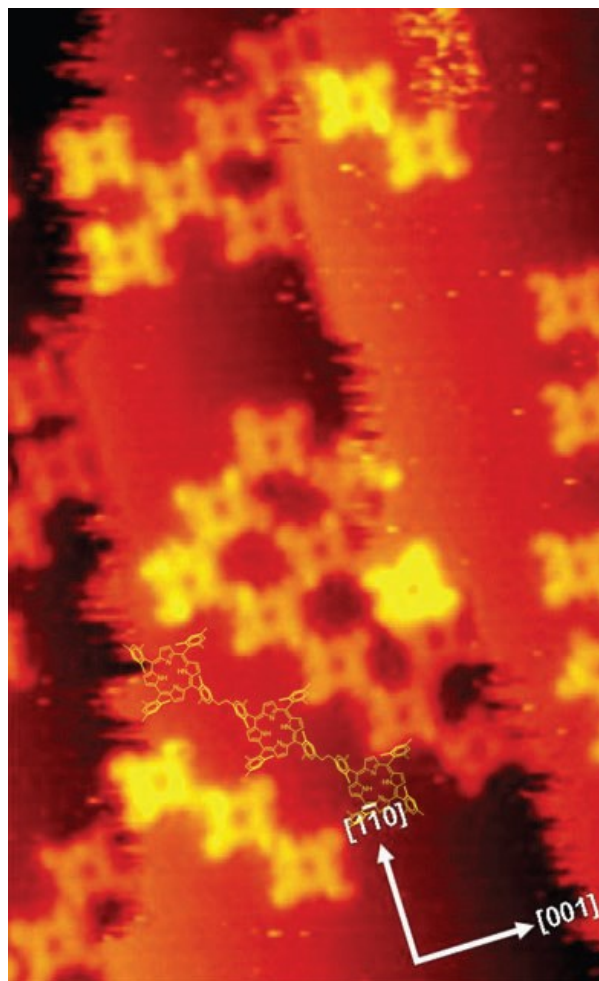


Figure 2.26.  $12.6 \times 20.6 \text{ nm}^2$  STM image of annealed tetra(mesityl)porphyrin on Cu(110). (Image reproduced from Veld *et al.*, with permission of the Royal Society of Chemistry)<sup>22</sup>

Another interesting reaction is the *addition polymerization of 1,3,8,10-tetraazaperopyrene (TAPP) via the tautomerization of N-heterocyclic end units to carbene intermediates* (Figure 2.27), where the formation of oligomers is an exothermic process.<sup>190</sup> On the Cu(111) surface a porous molecular network (as shown in Figure 2.28(a)), in which the molecules coordinate to Cu atoms through the lone pairs of their nitrogen atoms is formed below 150 °C (Figure 2.28(b)), either by deposition on the hot surface or by annealing the surface on which the TAPP was previously deposited at RT.

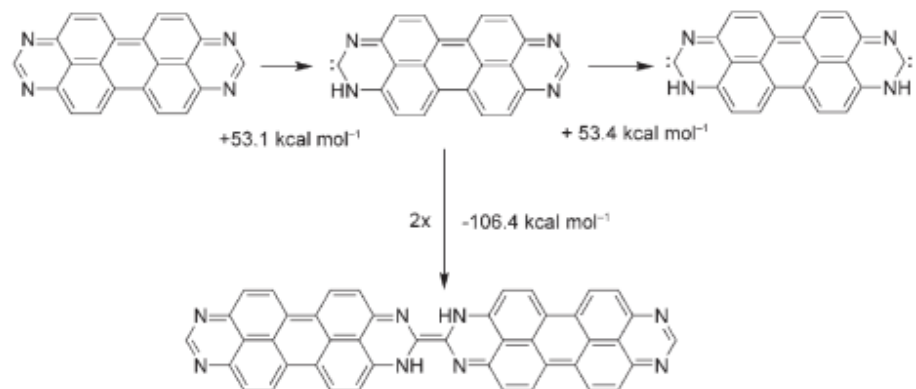


Figure 2.27. Single and double tautomerization of TAPP, with formation of a TAPP dimer. (Scheme reproduced from Matena *et al.*, with permission of John Wiley and Sons)<sup>190</sup>

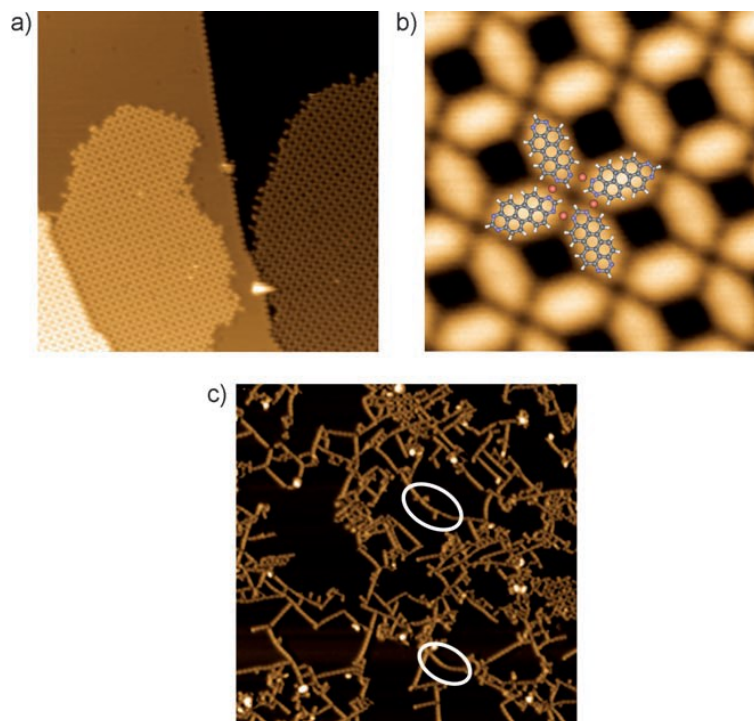


Figure 2.28. 70×70 nm<sup>2</sup> STM images of TAPP deposited (<ML) on Cu(111): (a) Showing TAPP assembly after annealing at 150 °C; (b) 5.3×5.3 nm<sup>2</sup> STM image of a surface coordinated network; (c) 80×80 nm<sup>2</sup> STM image of polymeric chains obtained after annealing at ~250 °C. (Figure reproduced from Matena *et al.*, with permission of John Wiley and Sons)<sup>190</sup>

The assembly is stable up to 190 °C. Above this temperature the long range ordering is lost, and oligo- and polymeric chains of various lengths and orientations, undetermined by the substrate symmetry, are formed at about 250 °C. This suggests a clear domination of the molecule-molecule interaction over the less influential molecule-substrate interaction.

A combination of covalent and metal-coordinated structures is formed by the side-to-side alignment of the dominant single-molecular chains, with Cu atoms placed between the nitrogen donor functions of the TAPP units, due to dehydrogenation of the NH group.

One of the most used reactions in the Nanofemtolab research group, as well as in the research community, is the *Ullmann reaction*, initially reported in 1901.<sup>23</sup> Due to the relentless search for new organo-materials with good electronic properties, promoted as long-range 2D networks, this reaction has been identified as a useful tool to generate active bonding sites and C–C couplings between aromatic nuclei (Figure 2.29).

Basically, two aryl halides react with finely divided copper at a high temperature, typically above 200 °C, to form a biaryl and a copper halide. On atomically flat surfaces however, the catalytic reaction is physically constrained.

It is generally assumed that the dehalogenated molecules form organometallic complexes with either metal adatoms (Figure 2.30),<sup>29, 31, 67, 246</sup> or directly with surface atoms (Figure 2.31).<sup>32, 66</sup> The exact nature of the metal-carbon coordination complex is still controversial and may depend on the choice of substrate, as shown by Wang *et al.*, using a combined STM/scanning tunneling spectroscopy (STS) study and DFT calculations.<sup>246</sup>

A schematic representation of Ullmann coupling reaction is presented and described in Figure 2.29.

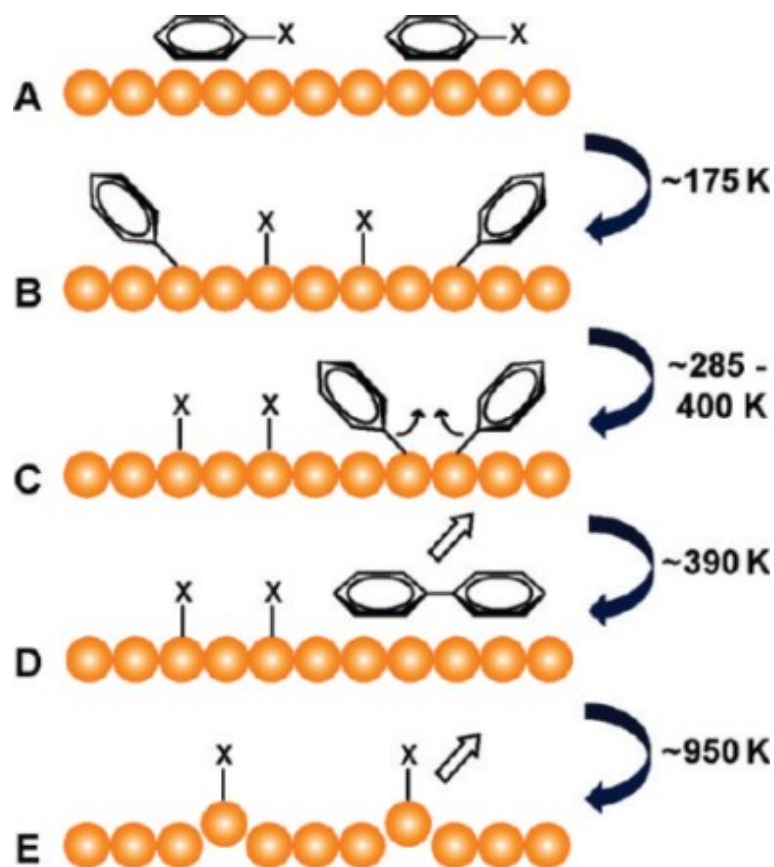


Figure 2.29. Schematic representation of an Ullmann coupling reaction on the Cu(111) surface. (A) Adsorption of aromatic halides. (B) Phenyl intermediates (still adsorbed on the surface) are formed *via* dissociative chemisorption at  $\sim 175$  K. (C) Coverage dependent recombination of phenyl radicals to biphenyl at  $\sim 285-400$  K. (D) Desorption of biphenyl at  $\sim 390$  K. (E) Desorption of X halogen or CuX species at annealing temperature  $\sim 950$  K. (Figure reproduced from Blake *et al.*, with permission of American Chemical Society)<sup>26</sup>

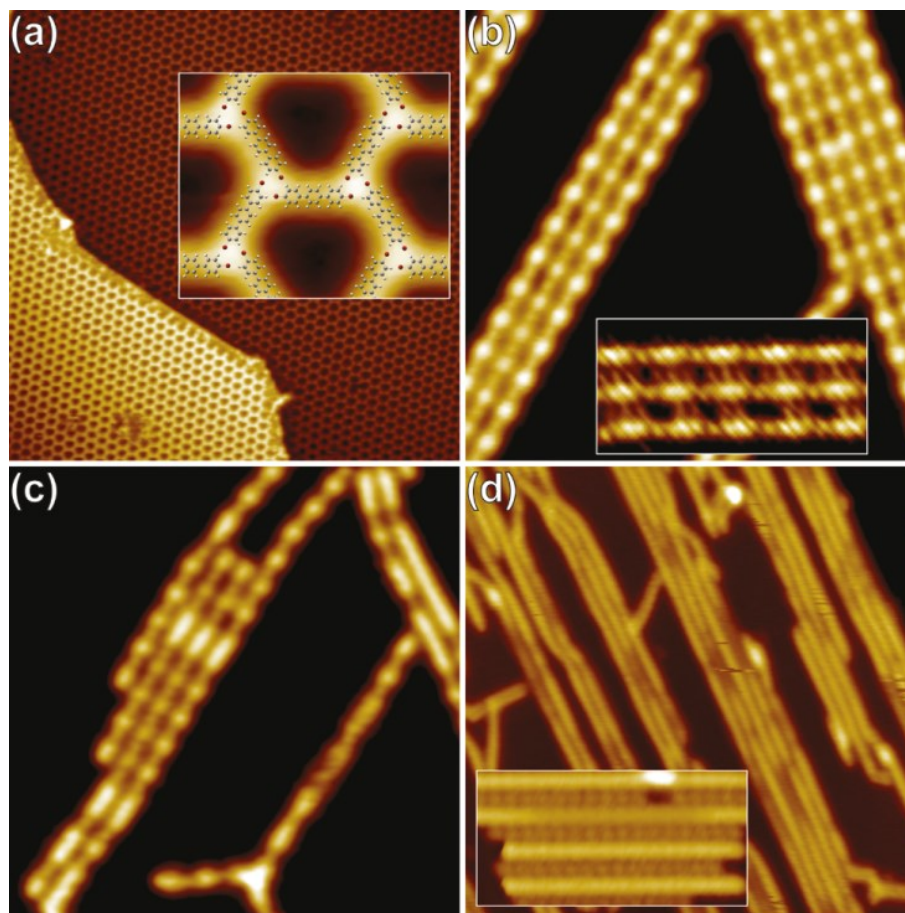


Figure 2.30. Surface-supported Ullmann coupling reaction from 4,4''-dibromo-*p*-terphenyl to poly(*para*-phenylene): (a)  $120 \times 120 \text{ nm}^2$  STM image of the as-prepared sample stabilized at 77 K ( $6 \times 5 \text{ nm}^2$  inset, Br in red). (b)  $20 \times 20 \text{ nm}^2$  STM image after annealing at 300 K ( $8 \times 4 \text{ nm}^2$ , inset); (c)  $20 \times 20 \text{ nm}^2$  STM image of the sample annealed at 393 K. (d)  $40 \times 40 \text{ nm}^2$  STM image after annealing at 473 K ( $8 \times 4 \text{ nm}^2$  inset) and formation of poly(*para*-phenylene) oligomers. (Figure reproduced from Wang *et al.*, with permission of the American Chemical Society)<sup>246</sup>

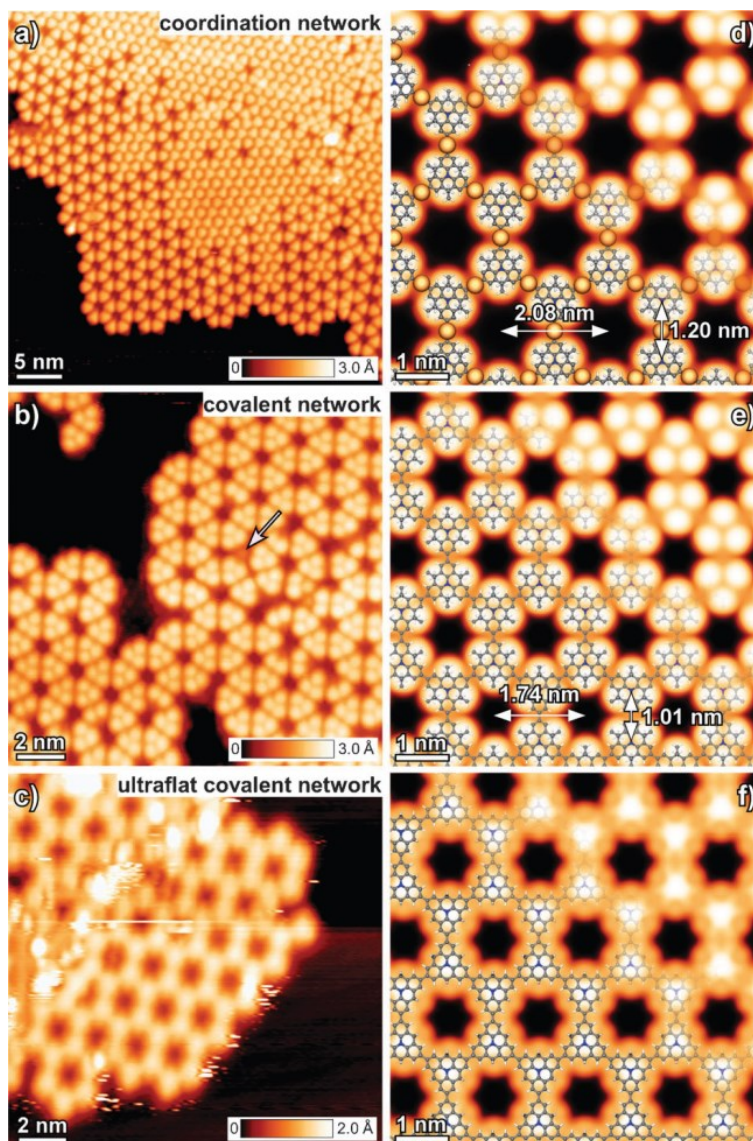


Figure 2.31. STM images of metal-coordinated DTPA and covalent conjugated polymers on Ag(111), in (a–c); the schematic models and calculated STM images are presented in (d–f). (a) STM image of coordination polymer formed at 200 °C with simulation shown in (d). The coordinating Ag atoms are shown in yellow. (b) STM image of the covalent conjugated polymer formed at 300 °C, with model and the simulated STM image in (e). (c) STM image of the ultra-flat, methyl-cleaved covalent network obtained by annealing to 400 °C, with the proposed model and calculated STM image in (f). In the model of the network, all the methyl groups were substituted by hydrogen. (Figure reproduced from Bieri *et al.*, with permission of the Royal Society of Chemistry)<sup>66</sup>

Initially using a copper catalyst, the reaction was later extended to other surfaces such as Ag, Ni, Pd, and Au. In the simplest situation of halogenated benzene, the temperature at which biphenyl is formed depends on the halogen atom, as well as on the nature of the substrate. At sub-monolayer coverage on the Cu(111) surface, iodobenzene ( $C_6H_5I$ ) dissociates at 175 K,<sup>27</sup> while in *p*- $FC_6H_4Br$  only the Br dissociates at 298 K.<sup>26</sup> Once the halogens are separated, more energy is however required to be supplied to the system ( $\sim 370$  K), so that the resulting phenyl intermediates could diffuse on the surface and couple to form biphenyls as demonstrated by Xi *et al.*<sup>27</sup>

One particular path of the Ullmann reaction is when the halogen-carbon scission, even at low temperature, is initiated by the STM tip. By applying a voltage pulse, starting from iodobenzene, Hla and coworkers were able to obtain phenyl intermediates at 20 K, manipulate them on the surface and bring them together to covalently couple by the application of a second pulse.<sup>91</sup>

Moreover, an incomplete Ullmann reaction is also possible. As shown for 1,4-dibromobenzene ( $C_6H_4Br_2$ ) on Cu(110) by Di Giovannantonio *et al* (Figure 2.32),<sup>285</sup> the halogens could be cleaved but the resulting unsaturated phenyls could diffuse and rebond forming biphenyls only when mediated by metal adatoms or halogen present on the surface.

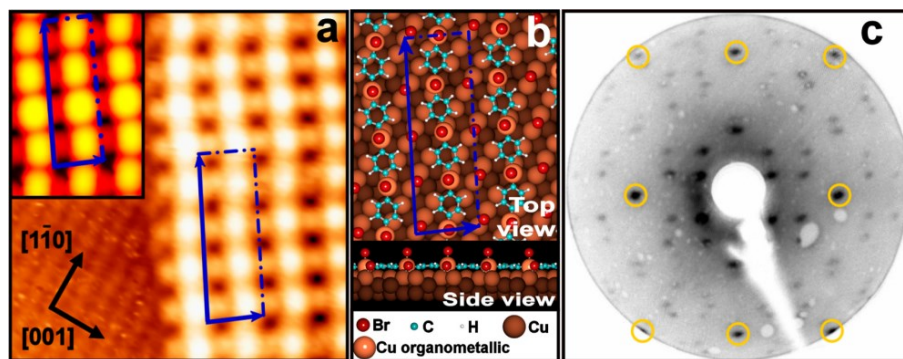


Figure 2.32. (a)  $5.5 \times 5.5$  nm<sup>2</sup> STM image of one dibromobenzene (dBB) domain on Cu(110) deposited at RT and sub-monolayer coverage. The inset shows a simulated  $2.1 \times 2.9$  nm<sup>2</sup> STM image for the RT geometry. (b) Top and side views of the optimized geometry (DFT) at RT. (c) Experimental LEED pattern of dBB on Cu(110) at RT and 1ML coverage; the  $1 \times 1$  spots

are indicated by circles. (Figure reproduced from Di Giovannantonio *et al.* with permission of the American Chemical Society)<sup>285</sup>

A different result was obtained by Lipton-Duffin *et al.* on the same surface by using a different halogen to functionalize the two positions in the phenyls. His results show a clear dependence of the polymerization geometry on the position of the halogen substituent on the molecule. Starting from 1,4-diiodobenzene (Figure 2.33) and 1,3-diiodobenzene (Figure 2.34) by annealing, he obtained different polymer wires, para-polyphenylene (PPP) and meta-polyphenylene (PMP) respectively, demonstrating the potential for synthesizing molecular architectures.<sup>31</sup>

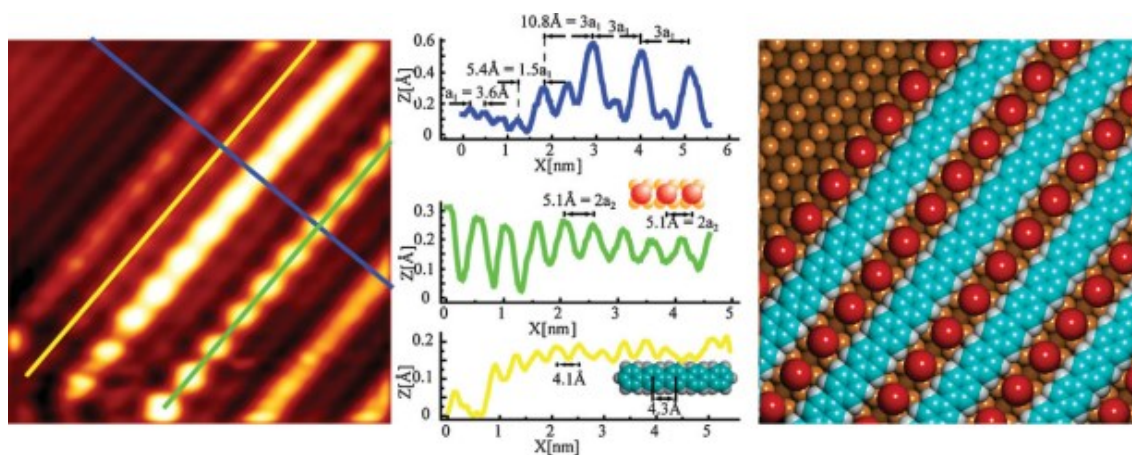


Figure 2.33.  $6.4 \times 6.4 \text{ nm}^2$  STM image of 1,4-diiodobenzene on Cu(110) after annealing at 500K (left) and its corresponding molecular model. (Figure reproduced from Lipton-Duffin *et al.*, with permission of John Wiley and Sons)<sup>31</sup>

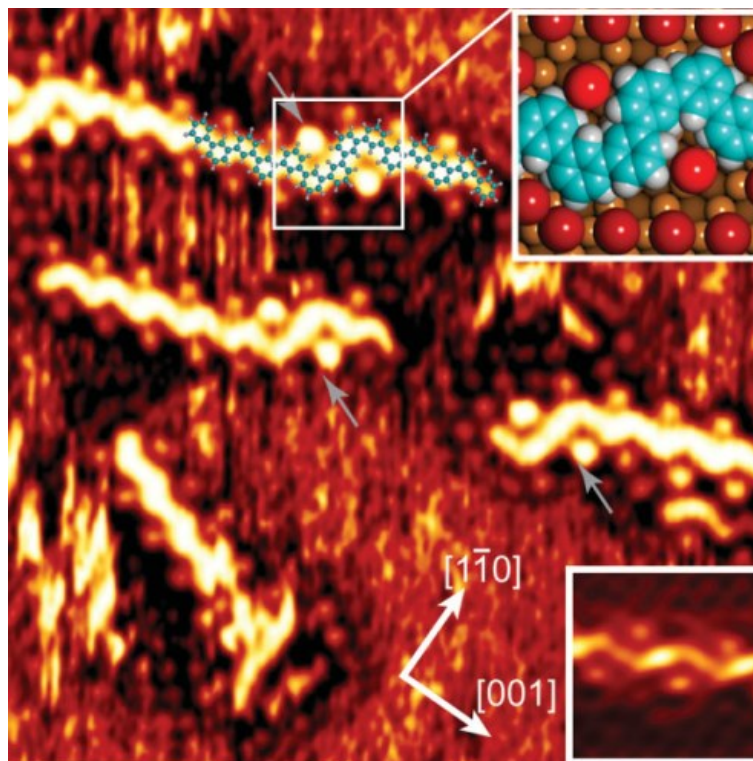


Figure 2.34.  $11.3 \times 11.3 \text{ nm}^2$  STM image of 0.2 L of 1,3-diiodobenzene on Cu(110), the substrate was held at 500 K. (Figure reproduced from Lipton-Duffin *et al.*, with permission of John Wiley and Sons)<sup>31</sup>

As discussed, transition metal surfaces act as catalysts, but due to the adatom gas present on the metal surface (on copper and silver in particular), intermediate organometallic products can be created.<sup>19, 285</sup> Annealing the surface can eventually lead, depending on the nature of the precursor/surface, to the breaking of the carbon-metal bonds and subsequent C–C coupling of molecules.<sup>24, 29, 31, 66, 67, 246, 286-290</sup> A few metal-intermediated structures were partially transformed into covalent polymers, in our group, as seen in the recently published work of Cardenas and Gutzler *et al.* who studied two brominated versions of thienoanthracene (TBTTA) on Ag(110) and Ag(111) surfaces.<sup>19, 20</sup> There, inside a metal-organic 2D network, covalent bonds were obtained by thermally expelling the silver atom intermediating two thieno-anthracene molecules.<sup>19</sup>

Polythiophenes are one of the cornerstone organic semiconductors,<sup>191</sup> and therefore a considerable effort has been expended toward the synthesis of conjugated polymers in the

surface-confined reaction of thiophene monomers,<sup>182, 183</sup> as in the recently reported surface-confined synthesis in UHV conditions of epitaxially ordered 1D poly(ethylenedioxy)thiophene (PEDOT) monolayers on Cu(110) surfaces (Figure 2.35).<sup>184</sup> However, in addition to conferring useful electronic properties, the presence of the thiophene groups introduces a literal weak link into the monomer.

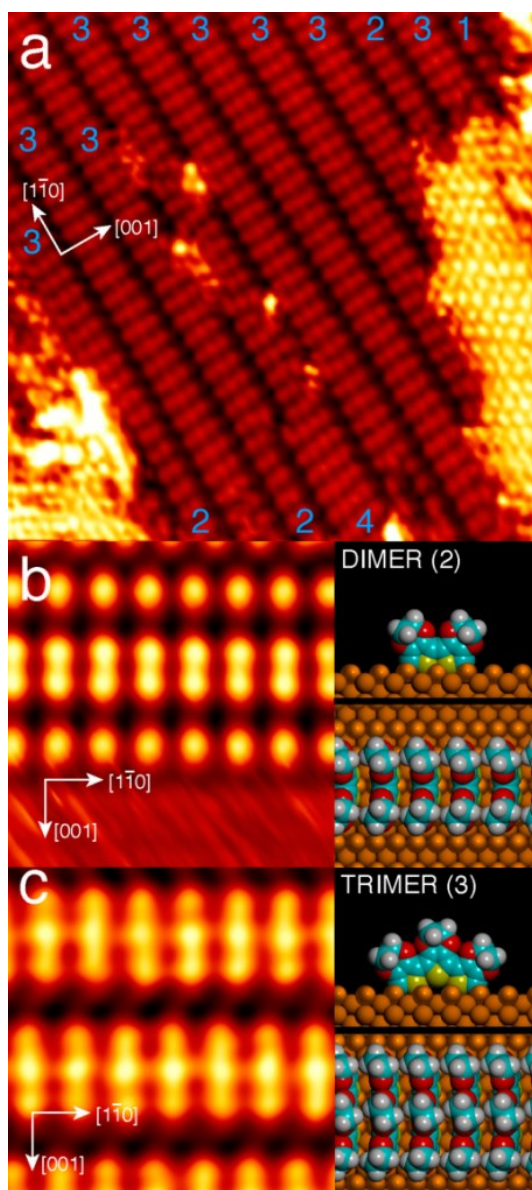


Figure 2.35. Well-organized oligomer overlayer formed from DIEDOT at higher dosage. (A)  $14.4 \times 14.4 \text{ nm}^2$  STM image revealing the fusing of the stack elements at high coverage, and monomer (1), dimer (2), trimer (3), and tetramer (4) stacks. STM data and characteristic

calculated structures by DFT are shown in (B) for dimer, and (C) for trimer stacks. (Figure reproduced from Lipton-Duffin *et al.*; with permission of Proceedings of the National Academy of Sciences)<sup>184</sup>

Since the Ullmann reaction requires relatively high temperatures, the thermal stability of the precursors becomes an important issue. It was found that C–C coupling cannot be selectively induced by thermal annealing.

The failure to obtain conjugated polymers, as attempted by Gutzler *et al.* on the Cu(111) and Cu(110) surface, is due to the thermal instability of thiophenic moieties on the copper surface at temperatures higher than 200 °C.<sup>20</sup> Unlike on Ag(111) and Ag(110) where annealing to 300 °C induced the formation of a mixture of disordered but planar organometallic and covalent networks, leaving the thiophene units intact, and where annealing at higher temperatures increased the amount of genuine polymers, on the Cu(111) surface however it produced only cleavage of the thiophenic rings. Similarly to Cu(111), only organometallic chains and surface-adsorbed Br atoms are observed on Cu(110).

Halogen functionalized porphyrin seems to be good candidate for on-surface assembly and the formation of 2D long-range covalently bonded networks, *via* the Ullmann reaction. In this regard, the most appealing results were recently reported by Krasnikov,<sup>286</sup> who obtained a long-range and flat well-ordered close packed molecular layer, by starting from (5,10,15,20-tetrakis(4-bromophenyl)porphyrinato)nickel(II) (NiTBrPP) molecules on the Au(111) surface (Figure 2.36). Annealing this assembly at 525 K led to the thermal dissociation of bromine, and covalent bonding of the remaining organic radicals to their phenyl substituents, giving covalent networks thermally stable below 800 K.

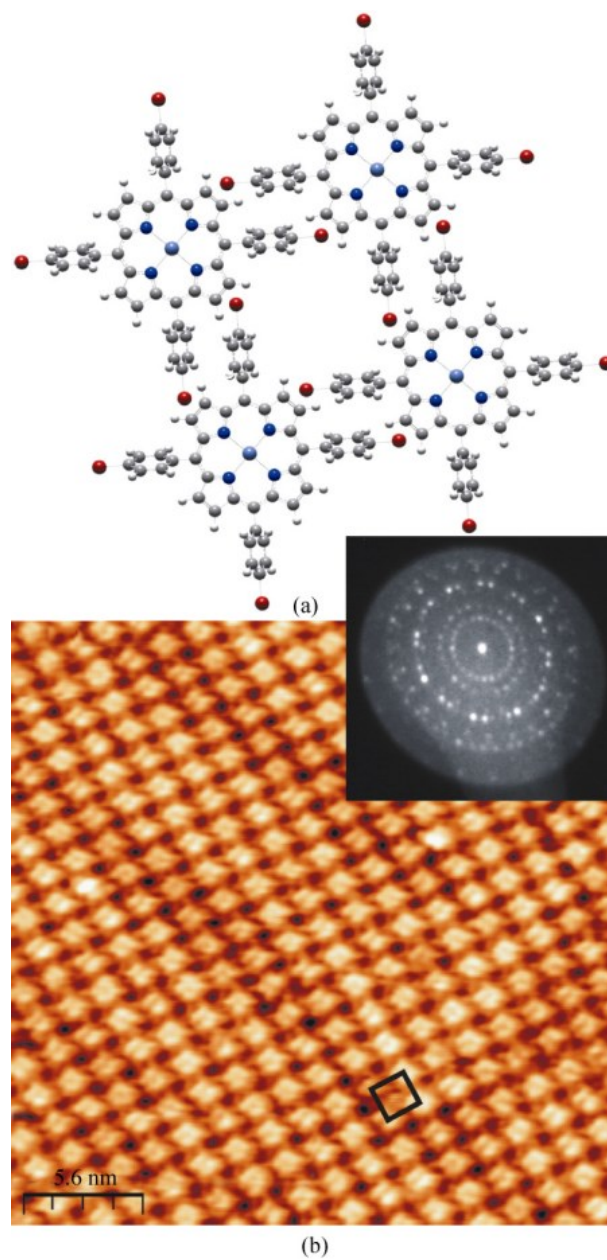


Figure 2.36. (a) Schematic representation of four self-assembled NiTBrPP molecules. (b)  $28 \times 28 \text{ nm}^2$  STM image of self-assembled NiTBrPP on Au(111). The inset shows a LEED pattern for NiTBrPP on Au(111) at 1 ML coverage. (Figure reproduced from Krasnikov *et al.*, with permission of Springer)<sup>286</sup>

With comparable results Grill *et al.* used the same halogen, bromine, as the labile substituent in tetra(4-bromophenyl)porphyrin ( $\text{Br}_x\text{TPP}$ ;  $\text{Br}_x = \text{Br}$ , *trans*- $\text{Br}_2$  or  $\text{Br}_4$ ).<sup>185</sup> To

stimulate or activate selective paths of the reaction they used two preparation methods, where the molecules were dehalogenated on the surface (i) or in the evaporator (ii). Figure 2.37 shows a schematic model for the reaction and representative STM images characteristic of the two preparation methods.

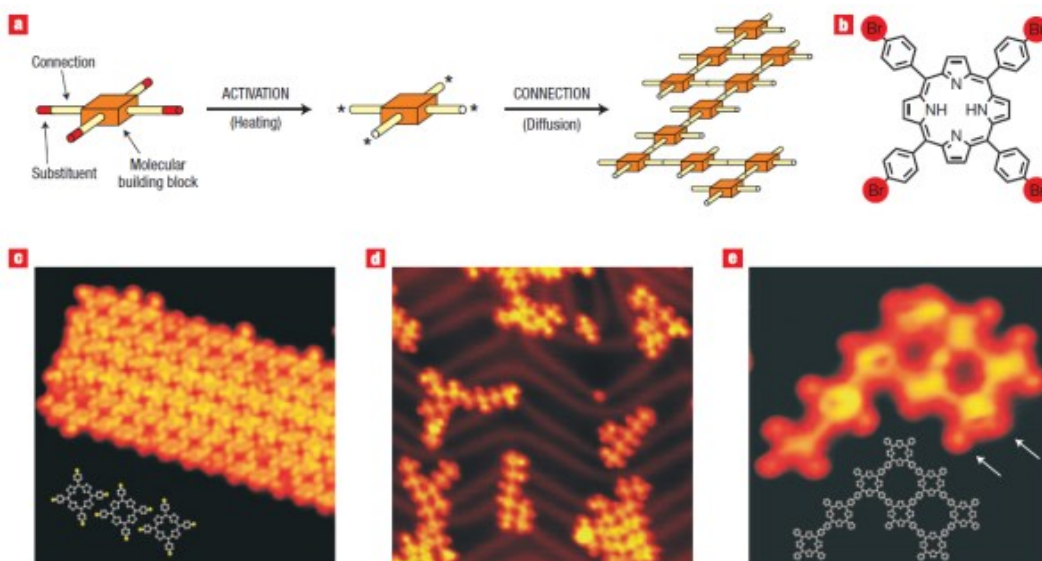


Figure 2.37. Covalently bonded networks of Br<sub>4</sub>TPP molecules. (a) Schematic representation of the formation of covalently bound networks. (b) Chemical structure of the Br<sub>4</sub>TPP molecule (the Br atoms are highlighted in red). (c) 20×20 nm<sup>2</sup> STM image of a molecular island on Au(111), sublimation at 550 K prior to activation. The corresponding chemical structures are presented in the inset. (d) 41×41 nm<sup>2</sup> STM image, after sublimation at 610 K evaporator temperature, when the molecular activation was induced to form networks by method (ii). (e) 8.5×8.5 nm<sup>2</sup> STM image of a network consisting of eight molecular building blocks. (Figure reproduced from Grill *et al.*, with permission of Nature Publishing Group)<sup>185</sup>

A more selective approach was pursued by Lafferentz *et al.* by involving two different halogens at substituting positions in the precursor.<sup>24</sup> They obtained 5,15-bis(4'-bromophenyl)-10,20-bis(4'-iodophenyl)porphyrin (trans-Br<sub>2</sub>I<sub>2</sub>TPP) molecules by endowing a central molecular building block, porphyrin, with two Br- or I-phenyl side groups, each in a linear *trans* configuration. This approach leads to a better control over the formation of heterogeneous architectures. A combination of these two halogen substituents enables

selective thermal dissociation of the two species (iodine, followed by bromine at a higher temperature). The molecule was studied on Au(111) (Figure 2.38), and Au(100) surfaces (Figure 2.39), alone or mixed with dibromoterfluorene (DBTF). Another advantage of this system is the ability to sequentially activate specific groups in individual molecules and create heterogeneous molecular assemblies (here, not shown, by addition of DBTF).

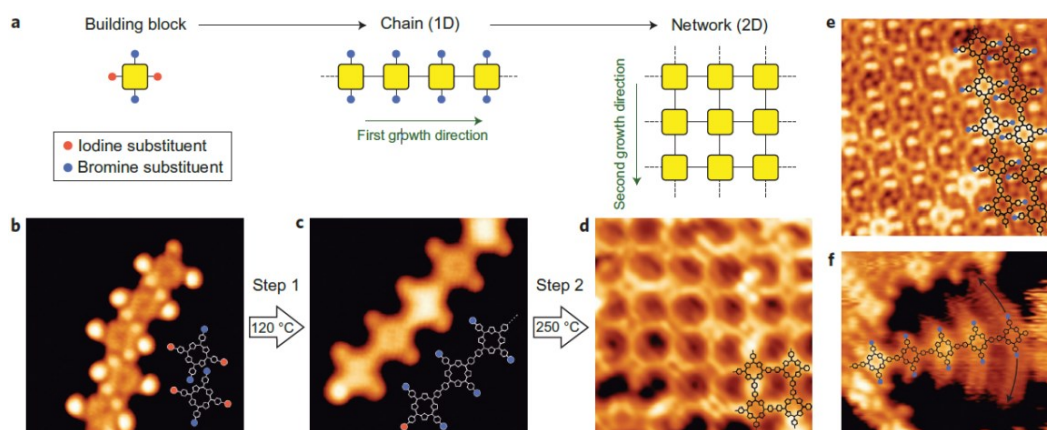


Figure 2.38. Hierarchical growth induced by sequential thermal activation. a) Activation mechanism. b)–d), STM images of  $8 \times 8 \text{ nm}^2$  in b), c); and  $10 \times 10 \text{ nm}^2$  in d) of trans-Br<sub>2</sub>I<sub>2</sub>TPP molecules on Au(111). The corresponding annealing temperatures were 80 K for b), 120 °C for the Step 1 of c), and 250 °C for the Step 2 in d) (imaging at 18 °C). e)  $10 \times 10 \text{ nm}^2$  STM image of a close-packed polymer island after the first heating step. f)  $12 \times 10 \text{ nm}^2$  STM image of a TPP chain. (Figure reproduced from Lafferentz *et al.*, with permission from Nature Publishing Group)<sup>24</sup>

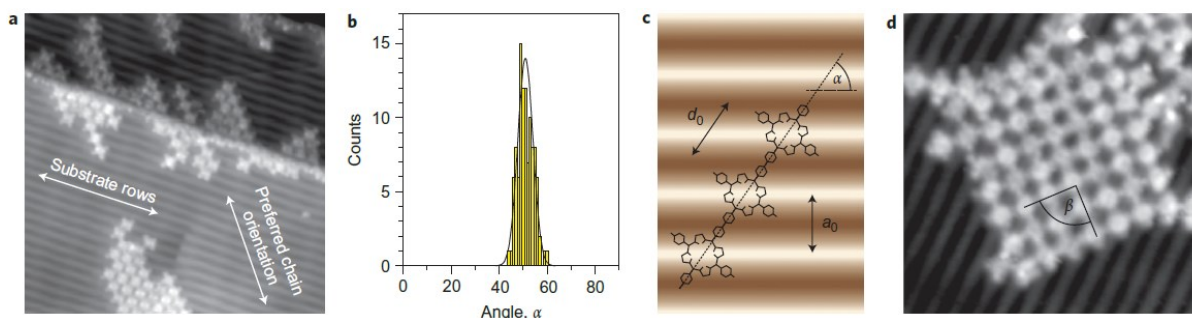


Figure 2.39. Substrate facilitated covalent linking. (a)  $42 \times 42 \text{ nm}^2$  STM image of the first growth step of trans-Br<sub>2</sub>TPP chains on Au(100). (b) Angular distribution for chains in (a). (c), Geometric scheme of the polymer adsorbed on the Au(100) surface. (d)  $20 \times 20 \text{ nm}^2$  STM image of a single molecular network after the second activation step. (Figure reproduced from Lafferentz *et al.*, with permission from Nature Publishing Group)<sup>24</sup>

The using of halogen-based aromatic molecules in correlation with metallic surfaces has continued for some time. There are situations when the desired reaction requires temperatures too high for the system to remain stable, mostly due to diffusion or even desorption of the precursors from the surface.

Due to these factors, there is an increased trend in the use of a *two-step reaction*: one at a lower temperature which stabilize the precursors on the surface, followed by a second which kicks in at a higher temperature and perfects the final product.

To achieve this, halogenated precursors are preferred, so that in the first reaction step the halogen substituents are removed, yielding molecular building blocks readily prepared for intermolecular bonding. The position of the halogens is carefully chosen so the first formed biradical species tailor and stabilize the shape of the macrostructure. Usually, the thermal energy supplied to the initial molecule, to induce dehalogenation is enough to produce the diffusion of the biradical species on the surface, furthering process of radical addition and polymer chain formation.

In the second reaction step, thermally activated at a higher temperature, an extended fully aromatic system is formed thanks to the surface assisted cyclodehydrogenation. The latter process, intra-molecular, was treated in detail by Treier *et al.*, and is described as an independent reaction in the next paragraph.<sup>33</sup>

To obtain chains of graphene nano-ribbons (GNRs), Cai *et al.* combined these two reactions in UHV conditions on Au(111) and Ag(111) surfaces.<sup>25</sup> In the first reaction, they used 10,109-dibromo-9,99-bianthryl monomers on the Au(111) surface “1” (Figure 2.40a). The first reaction, dehalogenation, was activated at 200 °C with the formation of C–C intermolecular bonds. The carbon-hydrogen sigma bonds (C–H), trapped inside the newly formed structures, will force the successive anthracenes to tilt in opposite directions around the sigma-bonds that connect them, to about 0.4 nm from planarity with respect to the metal

surface (Figure 2.40b). The fully aromatic system, with a reduced deviation from planarity to only 0.18 nm, was obtained by annealing at 400 °C (Figure 2.40c).

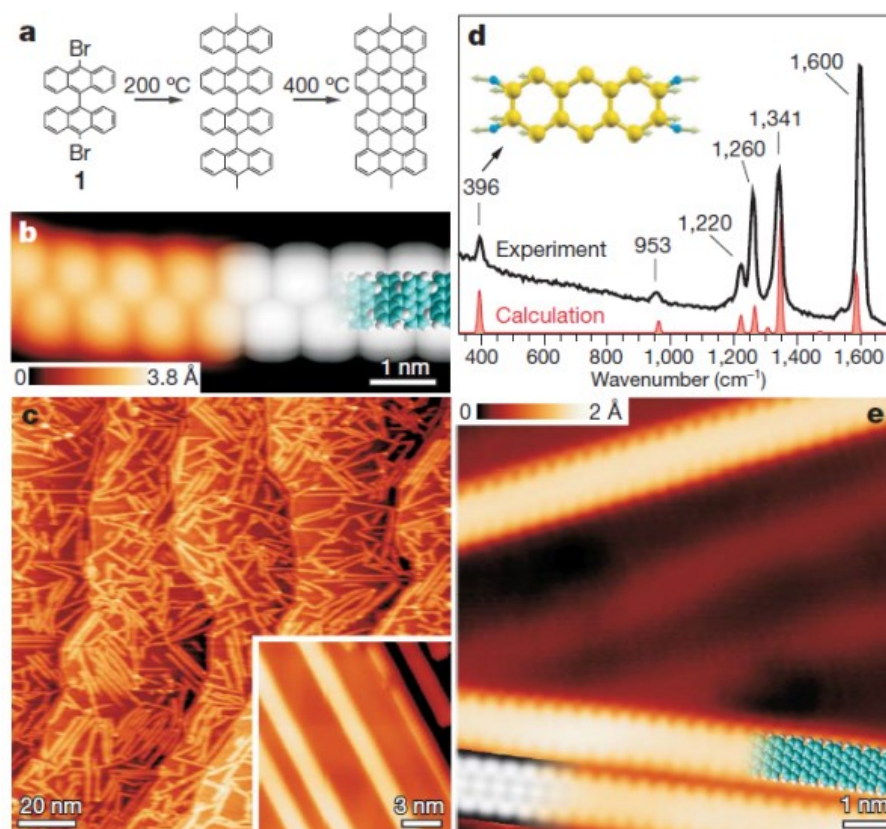


Figure 2.40. Graphene nano ribbons (GNRs) obtained from bianthryl monomers. (a) Reaction scheme from precursor 1. (b) STM image of the first polymerization step after annealing at 200 °C, showing a polyanthrylene chain (left, T=5 K). (c) STM image of the polymer after the second reaction step – cyclodehydrogenation, annealing at 400 °C (T=300 K). The inset shows an STM image taken at 35K. (d) Raman spectrum (N=7, excitation at 532 nm). (e) High-resolution STM image with overlaid molecular model (blue) of the ribbon (T=5K). (Figure reproduced from Cai *et al.*, with permission from Nature Publishing Group)<sup>25</sup>

Furthermore, chevron type GNRs were obtained from 6,11-dibromo-1,2,3,4-tetraphenyltriphenylene monomers “2” (Figure 2.41(a)). Here, this precursor was dehalogenated at 250 °C (Figure 2.41(b)) and the adjacent monomers are oriented in opposite directions in the chain. A slightly higher temperature, 440 °C, was also used to produce

intramolecular cyclo-dehydrogenation and complete the second reaction step, with a reduction in the deviation of planarity from 0.25 to only 0.18 nm, similar to the precursor “1” (Figure 2.41(c)).

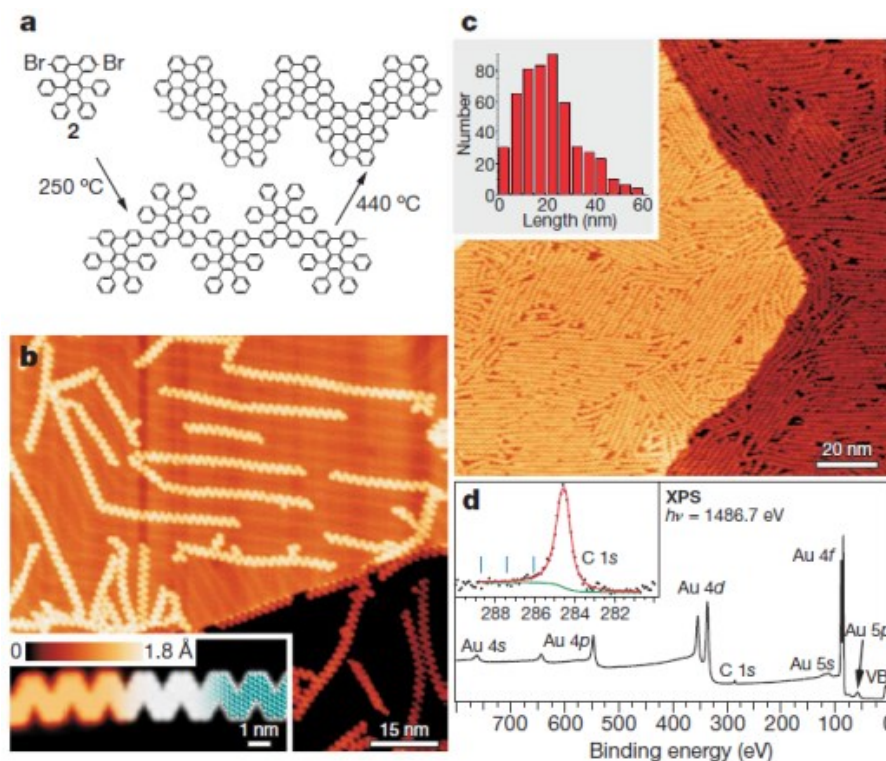


Figure 2.41. Chevron-type GNRs obtained from tetraphenyl-triphenylene monomers. (a) Reaction scheme from 6,11-dibromo-1,2,3,4-tetraphenyltriphenylene monomer **2** to chevron-type GNRs. (b) STM image of chevron-type GNRs on Au(111) ( $T=35$  K). The inset shows an STM image at  $T=77$  K and DFT-based simulation of the STM image (greyscale). (c) Chevron GNRs on Au(111), at ML coverage, with ribbon length distribution in the inset. (d) XPS survey spectrum of chevron-type GNRs at ML coverage. (Figure reproduced from Cai *et al.*, with permission from Nature Publishing Group)<sup>25</sup>

The range of possible usable surfaces was verified by studying the Ag(111) surface; it proves to be equally suitable for obtaining straight and chevron type GNRs (Figure 2.42(a)).

In a separate experiment they deposited the monomer “**2**” simultaneously, at 250 °C, with 1,3,5-tris(499-iodo-29-biphenyl)benzene “**3**” ( $C_3$  symmetry and no steric hindrance) and

annealed them at 440 °C; a preferred growth direction as well as an increase in the ribbon length along the herringbone reconstruction of the Au(111) substrate was observed (Figure 2.42(b)). However, by mixing two precursor monomers only homomolecular reactions seemed to be allowed while heteromolecular coupling was sterically hindered; showing a high degree of selectivity in the intermolecular coupling reactions.

Complementary with STM, XPS measurements show that the halogen by-products, resulting from the first reaction-step, desorb from the surface due to annealing, before completion of the second reaction step.

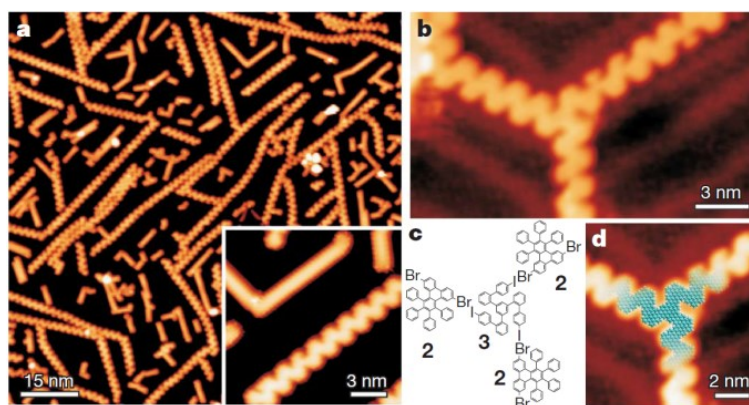


Figure 2.42. (a) STM image of coexisting straight N=7 and chevron-type GNRs on Ag(111) at T=5K. (b) STM image of a three-fold GNR junction obtained from 1,3,5-tris(499-iodo-29-biphenyl)benzene monomer on Au(111) (T=115 K). The monomers 2 and 3 were simultaneously sublimated at 250 °C, and annealed at 440 °C to induce cyclodehydrogenation. (c) Schematic model of the junction between 3 and 2. (d) Model of the junction overlaid on the STM image from (b). (Figure reproduced from Cai *et al.*, with permission from Nature Publishing Group)<sup>25</sup>

A particular situation comes into play when a single-step reaction, for instance dehydrogenation (as referred to in the previously discussed reaction mechanism – part of the second reaction step) is used as a head to tail reaction; graphically presented in Figure 2.43.<sup>33</sup>

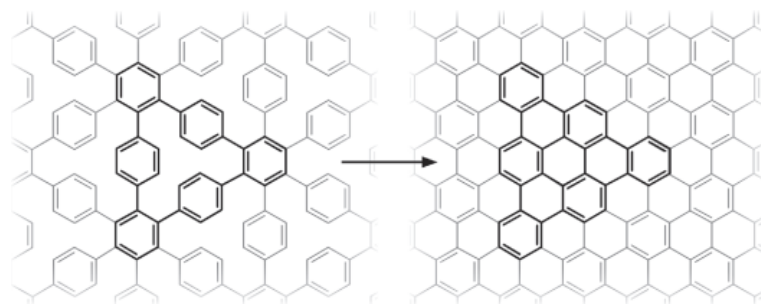


Figure 2.43. Cyclodehydrogenation (internal) of CHP to tribenzo[a,g,m]coronene (black lines) and corresponding dehydrogenation (external) of a polyphenylene to graphene (grey lines). (Scheme reproduced from Treier *et al.*, with permission of Nature Publishing Group)<sup>33</sup>

Treier *et al.* proposed an on-surface route to prepare graphene nano-flakes, starting from prototypical cyclic polyphenylene cyclohexa-o-p-o-p-o-p-phenylene (CHP) precursors on the Cu(111) surface (Figure 2.43), in UHV conditions. The phenomenon of intramolecular cyclodehydrogenation and aryl–aryl coupling reactions was studied by means of low temperature STM (Figure 2.44), and density functional theory.

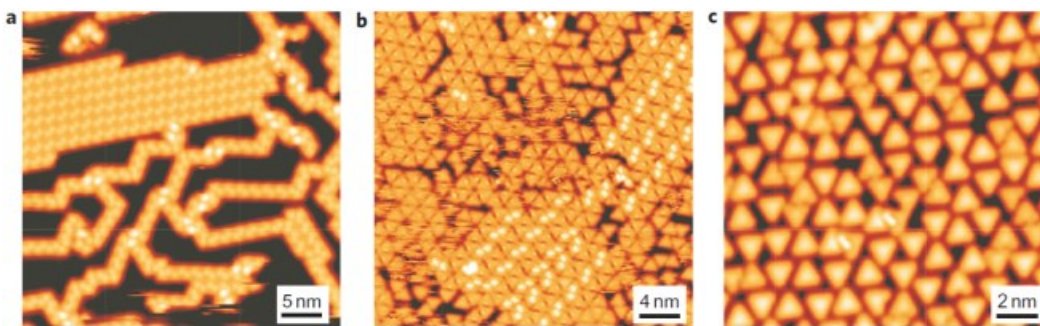


Figure 2.44. STM images of CHP cyclodehydrogenation on Cu(111). (a) As-deposited self-assembled structures (77 K). (b) Co-existing phase of CHP and final product after annealing at ~450 K (and imaged at 77 K). (c) The final phase of the final triangular planar poly-aromatic hydrocarbon, obtained after annealing at ~470 K (5 K). (Figure reproduced from Treier *et al.*, with permission of Nature Publishing Group)<sup>33</sup>

As deposited on Cu(111), CHP assembles into close packed and wire-like supramolecular structures (Figure 2.44(a)). Prolonged annealing at ~500 K fully transformed the non-planar CHP (due to the internal hindrance generated by the hydrogen atoms) into the fully planar tribenzocoronene (intermediate reaction steps presented in Figure 2.44(b),(c)).

Based on computational studies of the reaction barriers, the presence of the Cu(111) substrate and the subsequent van der Waals interactions play an active role in the reaction. The same DFT studies predict however that the Cu(111) substrate is not mandatory; the same reaction results could be obtained by using a non-catalytic surface at a slightly higher temperature.

A particular case of this reaction, used in the process of graphene formation from pentacene precursors on the Ni(111) surface is described in detail, as a contribution to this thesis, in the Chapter 7.

# Chapter 3

## Experimental Techniques

### 3.1. Scanning Tunneling Microscopy (STM)

The scanning tunneling microscopy (STM) principle dates back to the 1970's, to the work of Binnig and Rohrer and the investigation of nano-domains of thin oxide layers on metal surfaces. By scanning a surface simultaneously with local tunneling they were able to obtain topographic images of a surface, taking real space images of metal or semiconducting surfaces with atomic resolution.<sup>142, 143</sup> So, the STM instrument was born in 1981 at IBM Zurich (schematically represented in Figure 3.1 (a)), for which Binnig and Rohrer were awarded five years later the Nobel Prize in physics; with implications in many other surface probing techniques.

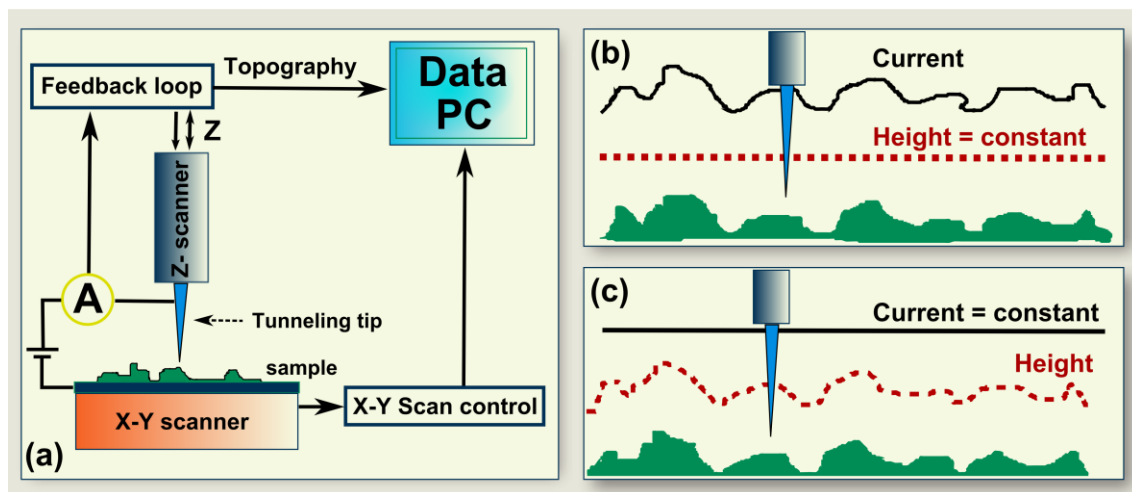


Figure 3.1. Principles and the schematic representation of STM are presented in (a), constant-height regime in (b), and constant-current in (c).

Scanning tunneling microscopes are most commonly used to collect images in one of the following two modes: (i) “current” or constant-height mode (Figure 3.1(b)), when the tip

sweeps above the surface in a horizontal plane, and generates images by displaying the current collected at each point; (ii) “topographic” or constant-current mode (Figure 3.1(c)), when the STM uses a feedback system to keep the tunneling current constant by adjusting the height of the scanner (via the applied  $z$  voltage) at each point. Images are generated by displaying the  $z$ -position of the scanner at each point.

### 3.1.1. Basic concepts

The basic concept of the STM, as an instrument, is simple. By placing a metallic tip very close (Angstroms) to a conductive surface, there is a probability that an electron will travel from the tip towards the surface or from the surface to the tip. This probability and the direction of these electrons could be biased by applying a small voltage ( $V_t \sim \text{mV}$ ) between the tip and surface, so that a non-contact electric current ( $I_t \sim \text{pA} - \text{nA}$ ) is generated. Imaging is done by rastering the tip over the surface and registering the current, which depends exponentially on the separation distance between the tip and the surface. This could be explained as based on the wave-like characteristics of the electron traveling across the separating distance ( $z$ ), and the associated tunneling process.

The wave function  $\psi_n$  of the electron  $n$ , traveling with energy  $E$  through an energy barrier of height  $U(z)$  is a solution of the Schrödinger equation (3.1) and has the expression (3.2).<sup>144</sup>

$$-\frac{\hbar^2}{2m} \frac{\partial^2 \psi_n(z)}{\partial z^2} + U(z) \psi_n(z) = E \psi_n(z), \quad 3.1$$

$$\psi_n(z) = \psi_n(0) e^{\pm ikz}, \quad 3.2$$

with:

$$\mathbf{k} = \frac{\sqrt{2m(E-U(z))}}{\hbar}, \quad 3.3$$

where  $\hbar$  is the reduced Planck's constant,  $z$  is the position, and  $m$  is the mass of the electron.

Inside the tunneling barrier however (between the tip and the surface),  $E < U(z)$  so the wave functions which satisfy this are decaying waves:

$$\psi_n(z) = \psi_n(0) e^{\pm kz}, \quad 3.4$$

Where:

$$\mathbf{k} = \frac{\sqrt{2m(U-E)}}{\hbar}, \quad 3.5$$

If an electron of energy  $E$  is incident upon an energy barrier of height  $U(z)$ , the probability for the electron to penetrate a certain barrier of width  $z$  is proportional to the magnitude of the wave function of the electron and has the expression (3.4):

$$P = |\psi_n(\mathbf{0})|^2 e^{-2kz}. \quad 3.6$$

For the tunneling to occur from the tip to the sample or vice versa, and therefore for a tunneling current to be registered, few requirements must be met. First, by applying a small bias voltage ( $U$ ), as the electrons run from the states ( $E_F - eU$ ) near the Fermi level of one material ( $E_F$ ), empty levels of the same energy as that of the traveling electrons must exist in the second material towards to which the electrons are traveling.

So, for a positive bias, with electrons traveling from the tip to the surface to image, the tunneling current has the following expression (3.7):

$$I = \sum_{E_F - eU}^{E_F} |\psi_n(\mathbf{0})|^2 e^{-2kz}. \quad 3.7$$

This relation gives the exponential character of the tunneling current in relation to the tunneling distance (tip-sample distance), which is reflected in current variations (contrast) induced by minor changes (corrugation or adsorbed atom) in the tip-surface distance.

Moreover, the intensity of the tunneling current is related to the local density of available states (LDOS) in the material (relation 3.8), to which the electrons are traveling, in the energetic interval ( $E_F - eU$ ). The measured current depends on both, topography ( $z$ -height) and the local density of states (LDOS). For the general case, the LDOS near an energy  $E$  in an interval energetic  $\varepsilon$ , at the position  $z$  (at the sample surface  $E=E_F$  and  $z=0$ ):

$$\rho_s(\mathbf{z}, E) = \frac{1}{\varepsilon} \sum_{E-\varepsilon}^E |\psi_n(\mathbf{z})|^2. \quad 3.8$$

STM images give what seems to be a topographic map of the surface, but assignment of different components of this image is not always an easy task. One of the reasons is due to the fact that what we image is the LDOS, in the  $E_F - eU$  tunneling interval, and in each point on that image. Moreover, the tip can undergo independent and uncontrollable structural geometrical or electronic changes during the process of scanning (the top-atom is lost and replaced with the same or different species in the same or different geometry, double tip, etc.), generating imaging artifacts.<sup>145</sup> The image should reflect intrinsic characteristics of the imaged surface, and, due to its size, also the characteristics of the imaging tip.

As seen in Chapter 5, the energetic electrons generated by a large bias voltage ( $> 3V$ ) between the tip and the surface is one of the factors that affect the chemistry of adsorbed species. It is important to consider that these physical alterations could be turned, by using the tip as an engineering tool, into useful mechanisms to tailor on the surface new chemical processes (Figure 3.2).<sup>91</sup> When a bias voltage is applied between the tip and the surface, the tip could be used as an electron gun. If the adsorbate is a molecule on the surface, these electrons are transferred to the molecule through resonant states; therefore, if this energy exceeds the intra-molecular dissociation energy then a bond could be broken.<sup>146</sup> Sophisticated manipulation of single atoms or organic structures on the surfaces is also possible (Figure 3.3).<sup>93, 147, 148</sup> The nature of the forces involved in three processes of lateral manipulations, “pulling”, “pushing”, and “sliding” was first analyzed by Bartels *et al.*<sup>149</sup>

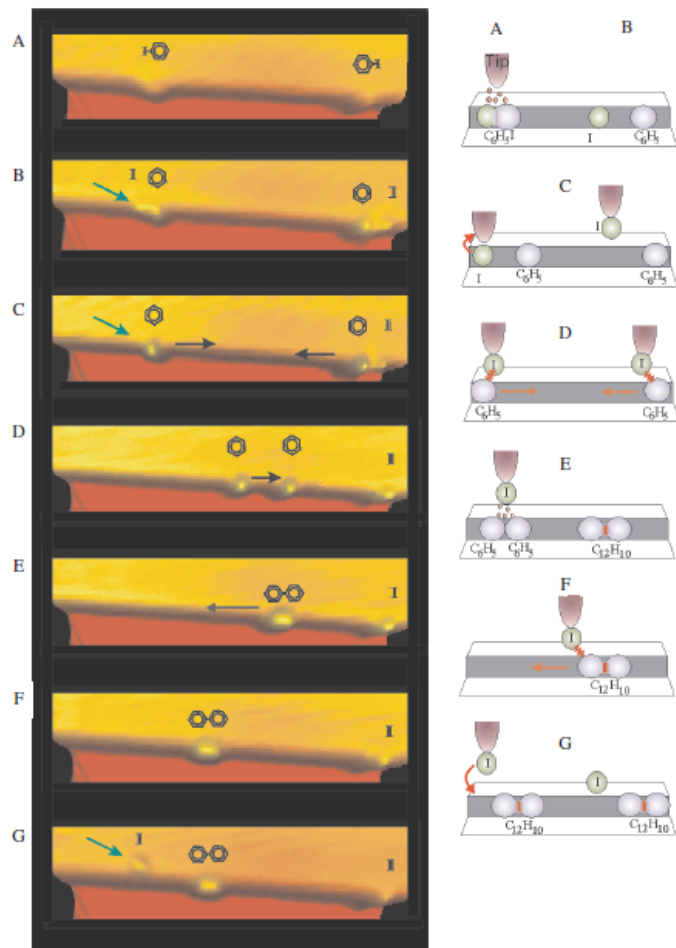


Figure 3.2. Single molecule Ullmann reaction: two iodobenzene molecules are adsorbed at a Cu(111) step (A). After dissociation with tunneling electrons, two phenyl radicals (larger bumps) and two iodine atoms are adsorbed at the Cu step-edge (B). After the iodine at the far left (indicated by a green arrow) has been transferred to the tip apex *via* vertical manipulation, the image contrast improves (C). The two phenyls are moved *via* lateral manipulation towards each other (D). When the two phenyls are in closest proximity, tunneling electrons having energies up to 500 meV are supplied to induce the biphenyl formation (E). Then, the newly synthesized biphenyl is pulled with the tip to the left side of the image proving successful chemical association (F). Finally, the iodine from the tip apex is transferred back to the substrate (G) (indicated by a green arrow). (Image and caption reproduced from Hla *et al.*, with permission of Elsevier)<sup>147</sup>

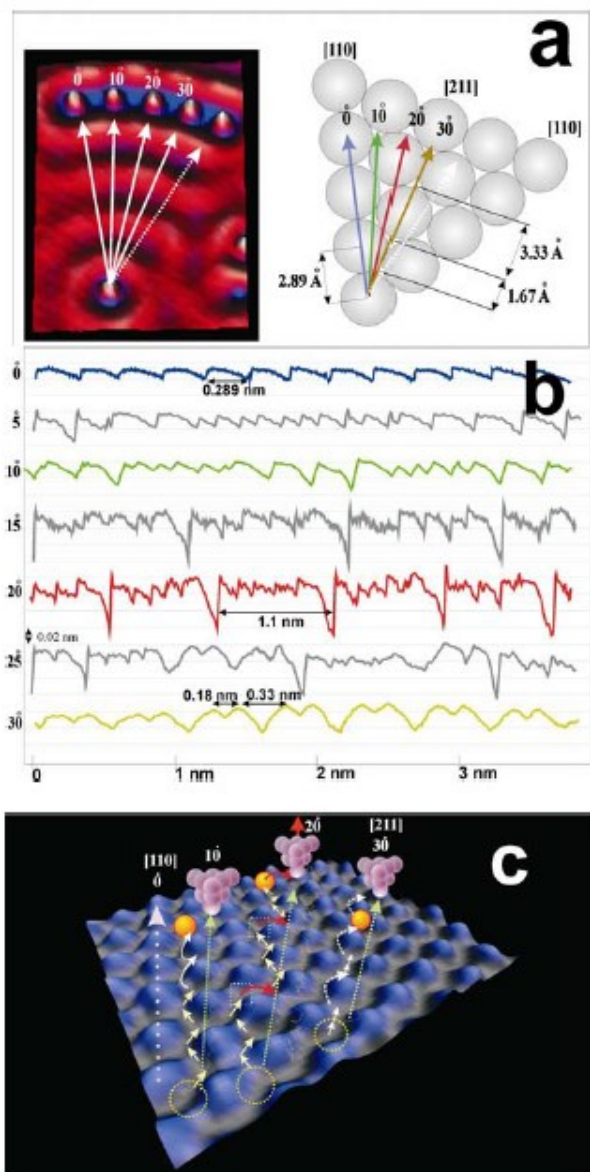


Figure 3.3. (a) An STM image and a model demonstrate the tip paths and Ag(111) surface geometry. (b) Atom manipulation signals along the tip-paths correspond to  $\theta = 0^\circ, 5^\circ, 10^\circ, 15^\circ, 20^\circ, 25^\circ,$  and  $30^\circ$ . (c) The atom movements are demonstrated over an atomically resolved 3-D STM image of Ag(111). At  $\theta = 5^\circ$  and  $10^\circ$ , the small steps in manipulation signals are due to fcc-hcp site hopping. At  $\theta = 15^\circ$  and  $20^\circ$ , the periodic downward slopes followed by a tip-height increase is due to the “rest” and “jump” action of the atom. At  $30^\circ$ , the atom slides over the first two near-by sites producing two consecutive bumps, and then it travels through a semi-circular path to reach the third site. At  $\theta = 25^\circ$ , the manipulation signal reveals both

structures of  $\theta = 20^\circ$  and  $30^\circ$ . (Images and caption reproduced from Hla *et al.*, with permission of AIP Publishing LLC)<sup>93</sup>

### 3.1.2. The microscope

The STM 150-Aarhus,<sup>150</sup> manufactured by SPECS GmbH and shown in Figure 3.4, is located in the STM-lab facility of NFL group, at INRS-EMT, in Varennes, Canada. The scanning system is fully automated and computer-controlled, and is capable of fast scanning acquiring images with a resolution of up to  $512 \times 512$  pixels, and with speed down to 3 ms/nm at a  $200 \times 200 \text{ nm}^2$  scan size.

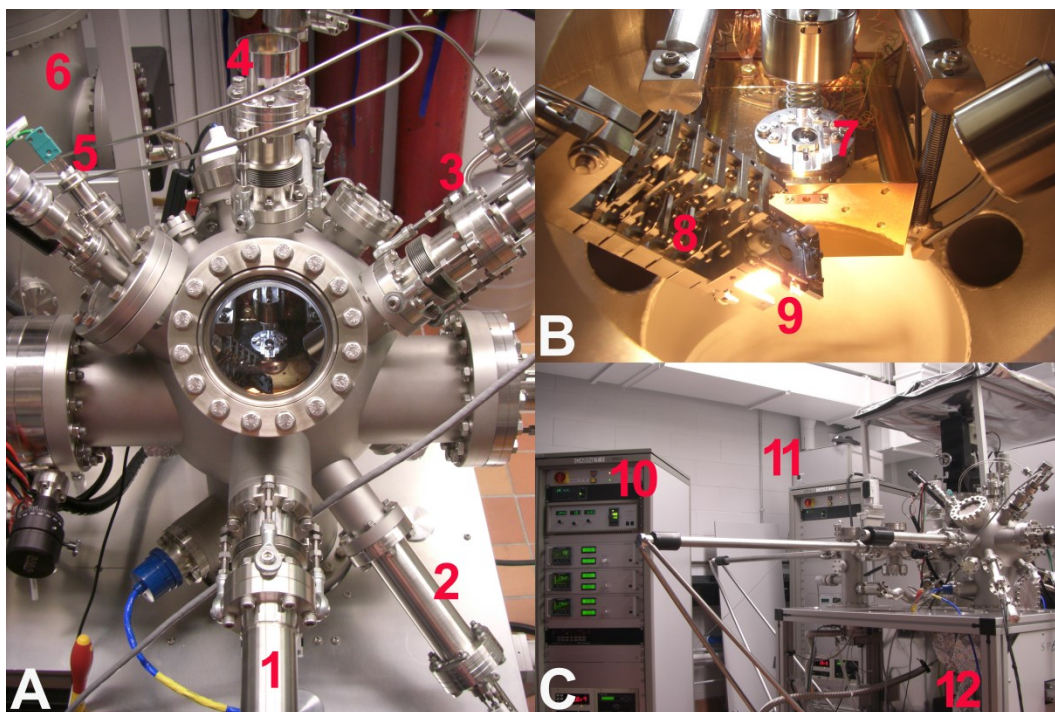


Figure 3.4. NFL's Aarhus-150 STM, system layout. An outside overview of the STM chamber is presented in (A), incorporating the sample-surface preparation systems in the fore plan, and the STM scanning unit in the background (B). Adjacent, are the short transfer arm (1), for sample transfer from the parking (8) to the imaging station on the STM stage (7). This arm was also used to position the substrate in front of the effusion cell (2), for the process of sublimating organic material. The main ion gun (3) was used for sputtering the sample, and the secondary (4) for sputtering the STM tip. (5) Thermocouple feed-through. The MBE

chamber (6), offers the possibility of complex preparation of the substrate. (7) STM stage. The parking stage (8), offers the possibility of storing five samples/substrates and one tip sputtering-plate, simultaneously, in the UHV environment. The sample heating system (9) was used for substrate preparation, and annealing procedures. The image (C) presents a general view of the full system: STM and MBE, with the heating and vacuum control electronics for MBE (10) and STM (11). A Varian *VacIon Plus 300* pump (12) was used separately or in tandem with a second ion pump, placed in the MBE chamber, in combination with the turbo-molecular (Pfeiffer) pump.

The samples were measured face down, accommodated in a molybdenum sample holder.

The scanning tip was made of electrochemically etched polycrystalline tungsten or cut Pt/Ir wire. The scanner set-up allows for *in-situ* tip cleaning by applying small voltage pulses to the tip. The tip could also be sputtered *in-situ* with argon ions, while still mounted on the scanning system. Bias voltages are reported with respect to the STM tip.

The scanner could handle temperature dependent studies on various kinds of substrates. The continuous cooling design improves the stability of the STM images, as long as increased drift is managed by compensation; addition of a heating system incorporated in the sample stage (by Zener diodes), and depending on the cooling reagent, could assure a constant sample temperature in the range of 73 – 433 K.

To achieve a good pressure in the STM chamber the whole system has to be baked. The residual gases in the chamber from 1 to 200 amu are identified with an Extorr XT300 series instrument. Unless specified in the corresponding chapters the majority of the STM images were obtained at room temperature using the commercial variable-temperature instrument described above.

To compensate for instrumental drift and creep the STM images were corrected to reflect lattice parameters of known structures wherever possible using WSxM software.<sup>151</sup> Flattening, smoothing and Fourier filtering were applied as needed to the images. The measured distances, in the images where it was not possible to conduct a thorough calibration based on the simultaneous imaging of the precursor/product and the lattice of the surface (but on successive images in the same session), were reported within the 0.05 nm uncertainty.

## 3.2. Time of flight secondary ion mass spectrometry (TOF-SIMS)

TOF-SIMS was carried out using an ION-TOF SIMS IV with a base pressure of  $10^{-10}$  mBar. The time-of-flight secondary ion mass spectrometry instrument uses a pulsed primary ion beam of bismuth to ionize and desorb various species of atoms or molecules from the investigated surface. The resulting secondary ions are analyzed in a mass spectrometer, by measuring their time-of-flight from the sample surface to the detector. In our experiments only the mass spectra were acquired to determine the elemental and molecular species on a surface, although imaging to visualize the distribution of individual species on the surface, or profile mapping by depth, were also available but not interesting for our case.

The incident  $\text{Bi}^+$  ions had an energy of 15 keV, and the beam sampled an area of approximately  $50 \times 50 \mu\text{m}^2$ . The probing was carried out at three different locations on each surface and the results were checked for consistency in all three locations.

## 3.3. Substrate and sample preparation

Particular methods, characteristic to each experiment may appear at the end of specific chapters.

### 3.3.1. Nickel, copper and silver monocrystals

The STM experiments were carried out in an ultrahigh vacuum (UHV) chamber, with a base pressure below  $10^{-10}$  mbar. Due to its high affinity for carbon, the Ni(111) substrate required a large number of cleaning cycles ( $>10$ ) by sputtering with 1 keV  $\text{Ar}^+$  for 15 minutes, followed by annealing at 850 °C for 20 minutes. Although reported to speed the cleaning procedure, oxygen gas was not used for the removal of surface bonded carbon species due to the complications with the remnant oxides, which require further hydrogen treatment.<sup>152</sup>

Exposure of nickel to different hydrocarbons can result in carbon containing phases on the treated surface. Below 400 °C, the dominant phase is carbidic carbon while heating above 400 °C leads to the formation of graphitic carbon, directly from hydrocarbons or by consuming the first phase.<sup>153</sup> Nickel carbide ( $\text{Ni}_2\text{C}$ ) was identified by its distinctive structure, previously extensively reported, as imaged by me on Ni(111) in Figure 3.5(a),<sup>53, 154</sup> or on Ni(110) in Figure 3.5(b).<sup>153</sup> On Ni(111) the carbide reconstruction has the  $\sqrt{39R}16.1^\circ \times$

$\sqrt{39}R16.1^\circ$  periodicity with respect to the Ni(111) lattice. The  $\bar{R}$  and  $R$  represent the rotation of the unit-cell vectors of the superstructure in the clock- and counter-clockwise directions, *i.e.* the unit cell is almost square with the two unit cell vectors enclosing an angle of  $92.2^\circ$  ( $60^\circ + 2 \times 16.1^\circ$ ).<sup>155</sup>

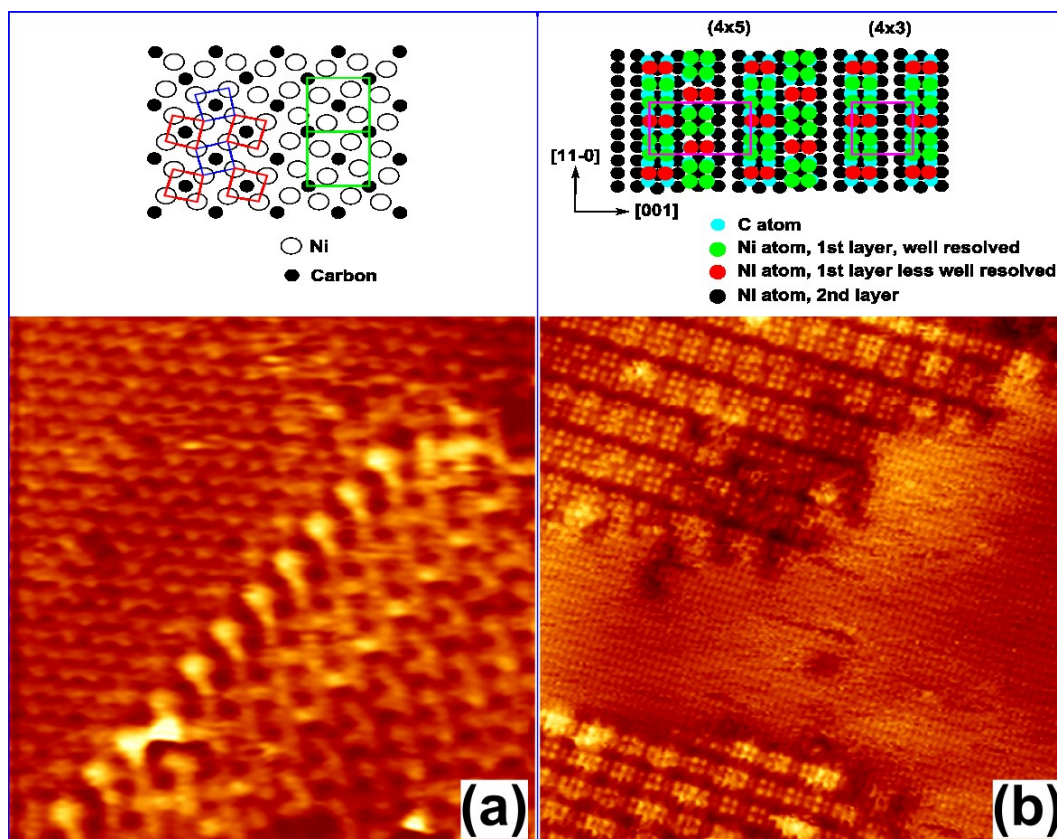


Figure 3.5. STM images of nickel carbide, on Ni(111) in (a) and Ni(110) in (b). Representative models characteristic of each structure are presented above the STM images. Image size and imaging parameters:  $5 \times 5 \text{ nm}^2$ , 0.83 nA, 2.14 mV in (a), and  $17 \times 17 \text{ nm}^2$ , -1.92 nA, -3.36 mV in (b). Models reproduced from Vang *et al.*,<sup>154</sup> and Klink *et al.*<sup>153</sup>

Similar studies were performed by Klink *et al.*,<sup>53</sup> with STM by exposing the Ni(111) surface to ethylene in UHV. They obtained real-space evidence which reveals that carbon in the carbidic phase transforms the Ni(111) surface into a so called “clock reconstruction” with an almost square  $\sim 5 \times 5 \text{ \AA}^2$  structure with a coincidence cell given by a  $\sqrt{39}\bar{R}16.1^\circ \times$

$\sqrt{39}R16.1^\circ$  surface mesh (from which it is seen that the topmost layer of the Ni(111) surface is reconstructed into an almost (100)-like quadratic structure but with the squares of Ni atoms rotated in a clockwise/anticlockwise fashion). The same group performed similar research by STM in UHV on the (110) surface of nickel and found that dissociation of ethylene resulted in the formation of two carbidic structures, (4×3) and (4×5),<sup>153</sup> similar to the ones presented in Figure 3.5(b), both of which are formed by a significant reconstruction of the surface involving a long-range mass transport of ~0.5 ML of Ni.

Similarly to nickel, the most commonly observed impurities on Cu(111) and Ag(111) monocrystals are carbon, oxygen and sulfur. To clean these surfaces, most investigators use successive cycles of sputtering with argon ions ( $\text{Ar}^+$ ) at an energy slightly below 1 keV, and annealing in UHV at temperatures in the range of 400–600 °C.<sup>152</sup> During bombardment, the temperature of the monocrystal was lowered to close to room temperature.

### 3.3.2. Organic molecules

In UHV, large molecules may crack during sublimation resulting in the adsorption of molecules and/or its fragments; therefore extra caution was used in the deposition procedures.

In all the experiments involving organic material, two Knudsen-type effusion cells have been used. One was manufactured by PLASMIONIQUE Inc., designed for the evaporation of organic materials in the temperature interval of 100-500 °C, without a dedicated cooling system. The second type, manufactured by CREATEC (Single Filament Effusion-Cell SFC-40-1 0-250-WK-SHM), could sublimate various materials, including high purity metals, from different kinds of crucibles with a temperature range between 100°C and 1400 °C. The heating system consists of a tantalum filament and PBN rings for electric isolation, equipped with an integrated water cooling system. A CREATEC DC unit was used for controlling the heating of both types of effusion cells. Prior to introducing any substances into the crucible, the crucible was degassed and cleaned in vacuum for a few hours, at temperature at least 100 °C above the temperature for sublimation of organic material.

In the deposition process, the effusion cell was fixed while the sample position was determined by the position of a transport manipulator. The molecules were sublimated onto the substrates held at room temperature or cooled down to -160 °C. The cooling procedure was executed discontinuously, and by running nitrogen gas through a large size screw that came

temporary into contact (during the cooling) with the housing of the piezoelectric scanner, which also acted as a heat sink. During the low temperature imaging, the piezoelectric core of the scanner was heated to and maintained at constant room temperature by a locally attached Zener diode.

TB2TTA,<sup>107</sup> TB3TTA<sup>156</sup> and 2TTA,<sup>107</sup> were synthesized as described elsewhere and were purified by vacuum sublimation ( $10^{-1}$  mbar; 300 °C). The TB2TTA and TB3TTA molecules were sublimated onto the substrates at ~210 °C, 2TTA and 3TTA at 180 °C. In separate experiments, pentacene (98% purity, provided by ACROS Organics) was sublimated at 190 °C.

### 3.4. Molecular structures

The modeling of molecular structures was based on the theoretical optimizations. The single-molecule structures were derived from density functional theory (DFT) methods, either in the gas phase, or by including a metallic surface slab.<sup>157</sup> Density functional theory (DFT) is presently probably the most used, and most promising quantum mechanical modeling approach in physics, chemistry and materials science, to investigate the electronic structure, principally the ground state, and geometry of molecular systems. With this theory, the properties of a many-electron system can be determined by using functionals, *i.e.* functions of another function, which in this case is the spatially dependent electron density.

More generally, the geometry optimization is used to find energy minima on the potential energy surface; these minimum energy structures represent the equilibrium structures. As a consequence of the spatial dependence of the electron density, during minimization the energy of the molecule is reduced by adjusting atomic coordinates.

More specifically, the geometry optimization starts with a beginning geometry (usually pre-optimized based on molecular mechanics methods). The density functional and the basis set are first declared, coupled eventually with a pseudo-potential. The program (*e.g.* Gaussian 09) will then compute the energy (and the gradient of the energy if the functional asks for it) at that point, and then the program decides if it has reached a stopping point (convergence - tolerance for energy typically  $10^{-7}$  Hartrees for DFT).<sup>158</sup>

There are three types of functional methods: local density approximation (LDA) which assumes an uniform density throughout the molecule (which is not always the case), gradient

corrected (GGA) which looks at the non-uniformity of the electron density,<sup>159</sup> and hybrid (*i.e.* B3LYP for reaction calculations,<sup>160, 161</sup> MPW1K for determination of kinetics problems).<sup>162</sup> Both gradient-corrected and hybrid methods provide high levels of accuracy in the determination of a geometry optimization. While the first two are pure DFT, the third incorporates features from *ab initio* methods (Hartree-Fock methods which, to describe any system, are using wavefunctions which are not physical observables) instead of electrons density. As compared to *ab initio* (scale factor  $N^4$ ), the DFT calculations are much faster due to a lower scale factor ( $N^3$ ,  $N$  = number of basis functions). Another advantage of DFT is that, unlike *ab initio* methods, it accounts for the electron correlation (defined as the difference between the Hartree-Fock energy and the exact solution of the Schrödinger equation), without an increase in computational time.

The basis sets are sets of functions, linear combinations of basic functions or atomic orbitals, centered on atoms, describing the valence electrons. Moreover, the so called *pseudo-potentials* or *effective core potentials* replace the remaining core electrons with an approximate potential (*i.e.* LANL2DZ,<sup>161</sup> accurate for transition metals). It includes all core states and the non-valence electrons, which, together with the nuclei, are considered rigid.

With a 6-31G(d) (accurately describing the organics) or better basis set, the B3LYP functional became almost a model chemistry analog for most systems, having the following mathematical (hybrid) form which includes complex mathematical functions (functionals) and various approximations such as: LDA, HF (~20%), Becke-1988 (B88), Lee-Yang-Parr 1988 (LYP88), and Vosko, Wilks, Nusair 1980 (VWN80).<sup>160, 163</sup>

In this thesis, the Gaussian 09 program was used at the B3LYP/6-31G(d) level (complemented with LANL2DZ, for metals),<sup>158</sup> to optimize the gas-phase structures. Avogadro, an open-source molecular builder and visualization tool, was used for producing basic molecular models.<sup>164</sup> For the drawing and basic modeling of the ball and stick images, the Discovery Studio product was used as well.<sup>165</sup>

Computational studies to determine the most probable molecular conformations on Cu(111) and Ag(111) surfaces were performed using first-principle DFT calculations, within the local density approximation (LDA).<sup>166</sup> The Perdew-Zunger (PZ) exchange-correlation energy functional was employed as implemented in the SIESTA software package.<sup>167-169</sup>

Le chapitre 4 a dû être retiré de la version électronique en raison de restrictions liées au droit d'auteur.

Unprecedented Transformation of Tetrathienoanthracene into Pentacene on Ni(111)  
Laurentiu E. Dinca, Chaoying Fu, Jennifer M. MacLeod, Josh Lipton-Duffin, Jaclyn L. Brusso, Csaba E. Szakacs, Dongling Ma, Dmitrii F. Perepichka, and Federico Rosei  
ACS Nano 2013 7 (2), 1652-1657

Vous pouvez le consulter à l'adresse suivante :

DOI : [10.1021/nn305572s](https://doi.org/10.1021/nn305572s)



# Chapter 5

## Tip-induced C–H activation and oligomerization of thienoanthracenes

The scientific material presented in this chapter was adapted from the following publication (with permission of The Royal Society of Chemistry):

Dinca, L. E.; MacLeod, J. M.; Lipton-Duffin, J.; Fu, C.; Ma, D.; Perepichka, D. F.; Rosei, F. Tip-Induced C–H Activation and Oligomerization of Thienoanthracenes. *Chem. Commun.* **2014**, *50*, 8791-8793.

The tip of a scanning tunneling microscope (STM) can be used to dehydrogenate freely-diffusing tetrathienoanthracene (TTA) molecules on Cu(111), trapping the molecules into metal-coordinated oligomeric structures. The process proceeds at bias voltages above ~3 V and produces organometallic structures identical to those resulting from the thermally-activated cross-coupling of a halogenated analogue. The process appears to be substrate dependent: no oligomerization was observed on Ag(111), or HOPG. This approach demonstrates the possibility of the controlled synthesis and nanoscale patterning of 2D oligomer structures on selected surfaces.

The demand for smaller electronic devices has fuelled the pursuit of methodologies for spatially controlled chemical reactions to fabricate electronic materials with nanoscale precision. Devices based on organic materials are an appealing alternative to traditional inorganic semiconductor devices, since they can be built from the bottom up using building blocks only a few atoms in width.<sup>7, 207</sup> Scanning probe microscopy offers the possibility to image,<sup>179</sup> manipulate,<sup>14</sup> and induce chemical reactions with nanoscale spatial resolution,<sup>90-92, 94-96</sup> making it a reliable instrument both for creating and characterizing molecular materials. Recent examples of STM-induced phenomena include localized atomic reactions on silicon,<sup>208, 209</sup> tip-induced polymerization of diboronic acids,<sup>101</sup> tip-induced polymerization of

diacetylenes,<sup>96, 102, 105</sup> and tip-induced S–S bond dissociation and recombination in dimethyldisulfides.<sup>103</sup> In these systems, the STM tip is typically used to induce a reaction that propagates without additional input until it is terminated by a defect,<sup>105, 106</sup> or until all available monomers are consumed.<sup>101</sup>

Herein is reported a new concept in STM-initiated reactions: starting from a surface-confined ensemble of diffusing molecular monomers, it is demonstrated that the STM tip can be used to activate surface-mediated dehydrogenation of molecular precursors, leading to the formation of oligomers on a copper surface. Cross-dehydrogenative C–C coupling is one of the fastest growing fields of synthetic organic chemistry,<sup>210</sup> and offers particularly interesting possibilities for on-surface reactions.<sup>22, 34</sup> Unlike previous tip-induced surface polymerization reactions,<sup>101, 102, 105, 106</sup> this reaction is initiated from surface-confined diffusing molecules, and is not self-perpetuating. The area patterned with molecules is defined by the scanned region, allowing for precise spatial control over the polymerized region.

## 5.1. Results and Discussion

The monomer used is trithieno[2',3':5,6:3',2':3,4:3',2': 7,8]anthra[1,2-b]thiophene (2TTA – schematically represented in the inset of Figure 5.1(a)).<sup>107</sup> Polythiophenes are widely used as organic semiconductors, due to their useful electro-optical properties.<sup>191, 211, 212</sup> The formation of disordered polymers through the surface-catalyzed polymerization of a brominated analogue of 2TTA (TB2TTA) was previously reported on Cu and Ag surfaces.<sup>19, 20</sup>

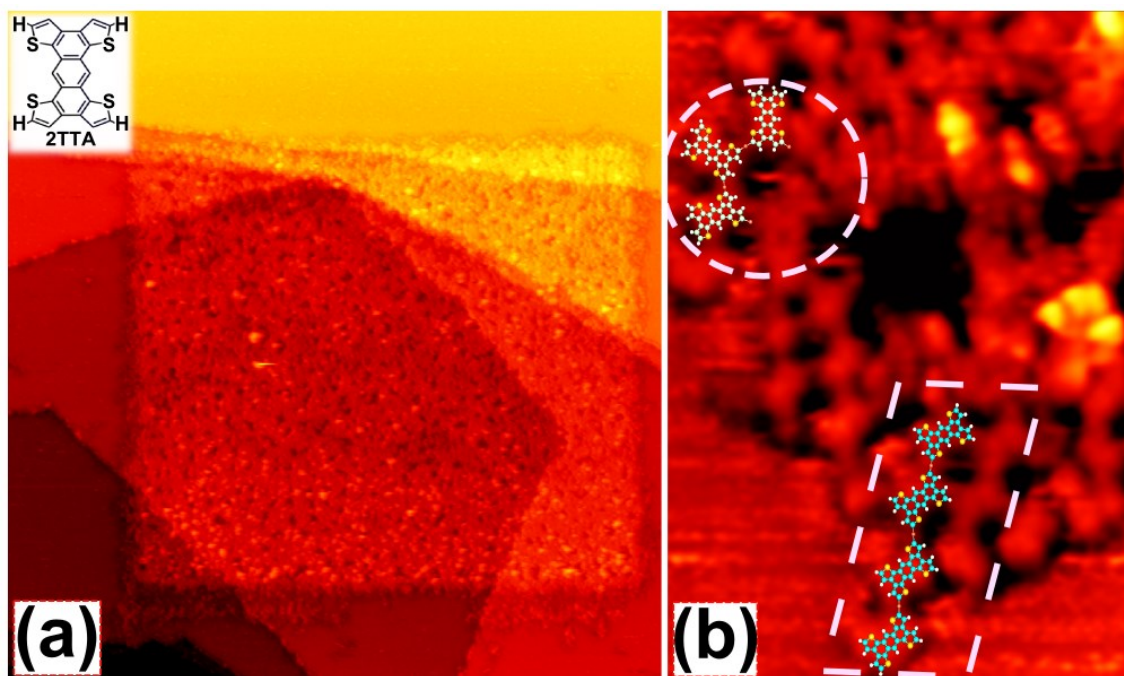


Figure 5.1. STM images of 2TTA on a Cu(111) surface. (a) A rectangular region ( $100 \times 90 \text{ nm}^2$ ) of patterned aggregates from 2TTA, at patterning bias  $U_{\text{bias,pattern}} \sim 5 \text{ V}$ . (b) The lower left corner of the patterned region from (a). Dashed regions highlight oblique (inside the rectangle; Figure 5.2(a)) and hexameric structures (inside the circle; structure “1” from Figure 5.2(c)). The inset in (a) shows the molecular structure of 2TTA. Scanning parameters:  $140 \times 140 \text{ nm}^2$ , tunneling current  $I_t = -0.41 \text{ nA}$ , bias voltage  $U_b = -831 \text{ mV}$  for (a); and  $8.5 \times 12 \text{ nm}^2$ ,  $I_t = 0.40 \text{ nA}$ ,  $U_b = 374 \text{ mV}$  for (b). By using a grid of  $100 \times 100 \text{ nm}^2$  with a lattice of  $10 \times 10 \text{ nm}^2$  inside the patterned region from image (a) (not shown), Estimative, (average over 10 points on each side of the patterned region, along the grid lines) the deviations between scanned and patterned distances:  $2.6 \pm 0.6 \text{ nm}$  at the right side,  $1.0 \pm 0.2 \text{ nm}$  at left,  $1.4 \pm 0.5 \text{ nm}$  at the top, and  $5.7 \pm 1.7$  at the bottom. (L.E. Dinca *et al.*, reproduced with permission of The Royal Society of Chemistry).<sup>213</sup>

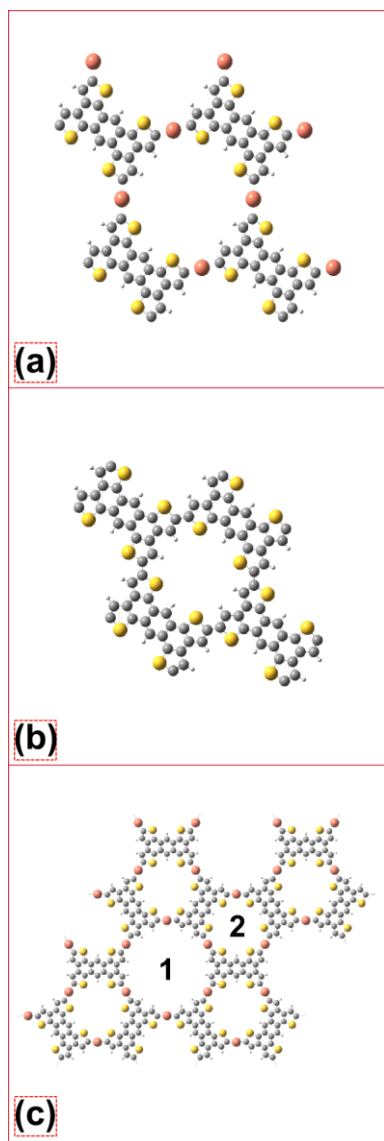


Figure 5.2. Schematic representation of 2-dimensional motifs of 2TTA: (a) Oblique organometallic. For the copper-coordinated network in this geometry the distance between the center of mass of any two neighboring molecules measures 1.45 nm (as reported by Gutzler *et al.*, from gas-phase DFT).<sup>20</sup> (b) For the oblique covalent structure, the same distance measures only 1.21 nm (gas-phase DFT).<sup>20</sup> (c) Kagome 2D-organometallic structure comprising conformations of six (cage 1) and three (cage 2) molecules. The structures were cut out of larger networks generated with periodic boundary conditions; the copper atoms are colored in red, sulfur - in yellow, and carbon - in grey color. (L.E. Dinca *et al.*, reproduced with permission of The Royal Society of Chemistry).<sup>213</sup>

After sublimation on Cu(111) it is not possible to image 2TTA at submonolayer coverage at room temperature due to its high mobility (see methods). Instead, STM images acquired at imaging biases below 1 V show an indistinct, flat surface overlaid with streaks along the fast-scan direction, as is typically observed in the presence of freely diffusing molecules.<sup>214</sup> However, after scanning the surface at a bias  $U_{\text{bias,pattern}} \sim 5$  V, subsequent imaging over a larger area reveals a patterned region (Figure 5.1(a); Figure 5.3). This region is “wear resistant” to scanning biases as low as 0.02 V and tunneling currents up to 4 nA. At its center, the patterned region comprises dense molecular aggregates, whereas distinct interconnected molecular geometries can be identified at the periphery (Figure 5.1(b), Figure 5.4).

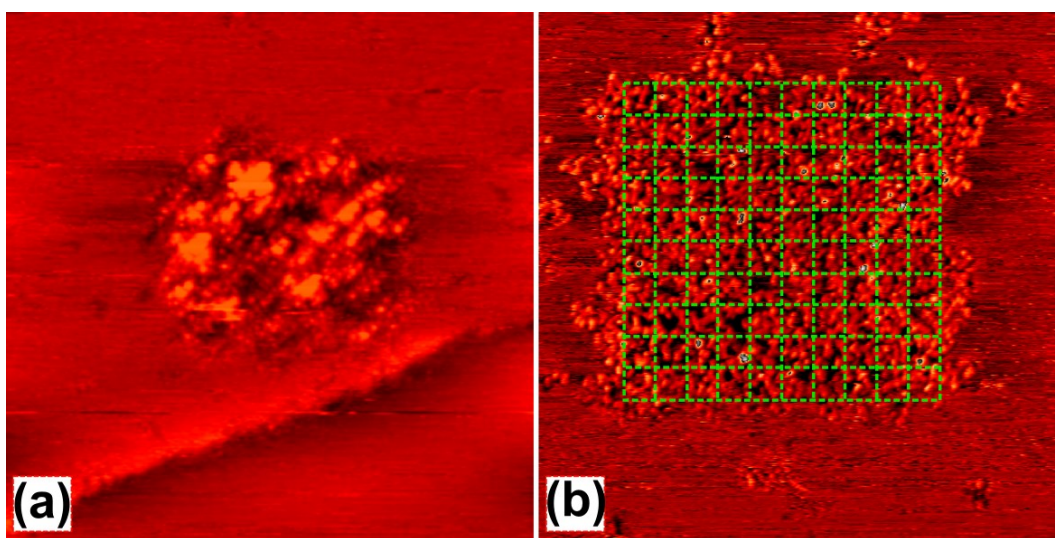


Figure 5.3. STM images of a square patterned from 2TTA on Cu(111) using  $U_{\text{bias,pattern}} \sim 5$  V. Image parameters:  $50 \times 50 \text{ nm}^2$  in (a) with a patterned region of  $20 \times 20 \text{ nm}^2$ ;  $50 \times 50 \text{ nm}^2$  in (b) with a patterned region of  $30 \times 30 \text{ nm}^2$ . Scanning parameters:  $I_t = 0.40 \text{ nA}$ ,  $U_b = 1903.69 \text{ mV}$  for (a) and  $I_t = -0.37 \text{ nA}$ ,  $U_b = -493.16 \text{ mV}$  for (b). A grid of  $30 \times 30 \text{ nm}^2$ , with the lattice of  $3 \times 3 \text{ nm}^2$ , was used in (b). Estimative, (average over 10 points on each side of the patterned region, along the grid lines) the deviations between scanned and patterned distances:  $2.2 \pm 0.8 \text{ nm}$  at the right side,  $2.5 \pm 0.7 \text{ nm}$  at left,  $0.7 \pm 0.4 \text{ nm}$  at the top, and  $1.2 \pm 0.5$  at the bottom. (L. E. Dinca *et al.*, reproduced with permission of The Royal Society of Chemistry).<sup>213</sup>

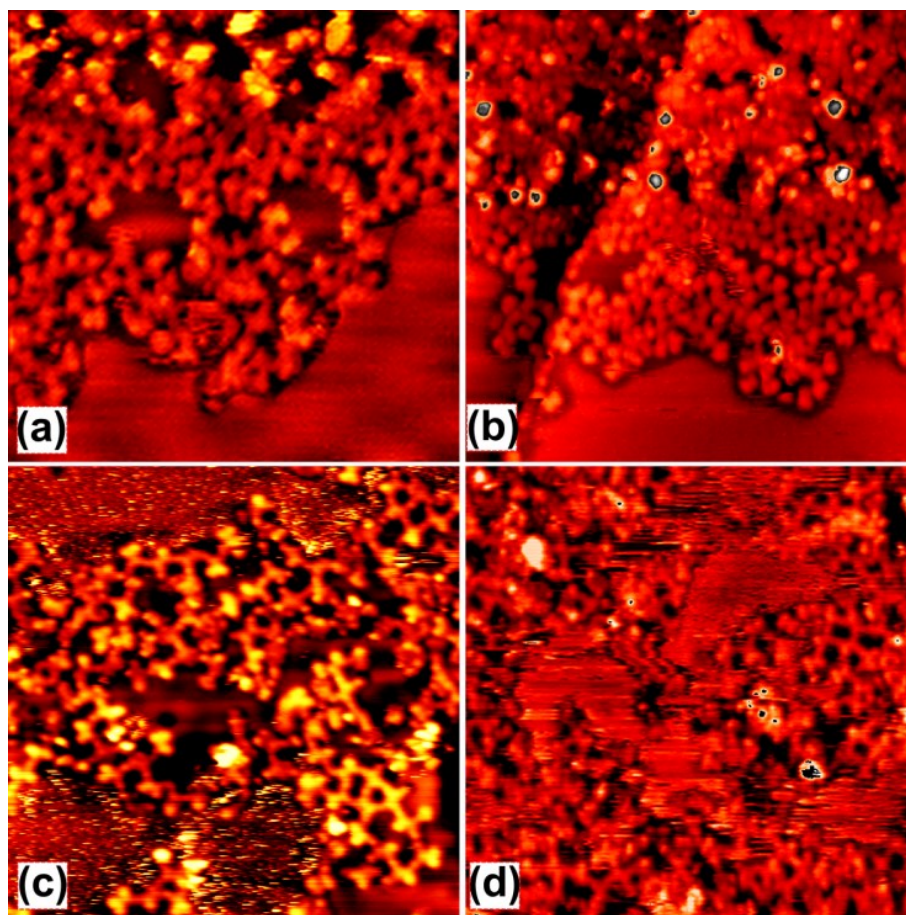


Figure 5.4. STM imaging of regions patterned from 2TTA on Cu(111) using  $U_{\text{bias,pattern}} = 5 \text{ V}$  for (a), (b) and (d), and  $\sim 3.5 \text{ V}$  for (c). Image sizes:  $20 \times 20 \text{ nm}^2$  in (a);  $30 \times 30 \text{ nm}^2$  in (b),  $15 \times 15 \text{ nm}^2$  in (c), and  $20 \times 20 \text{ nm}^2$  in (d). Scanning parameters: (a)  $I_t = -0.50 \text{ nA}$ ,  $U_b = -691.33 \text{ mV}$ ; (b)  $I_t = -0.42 \text{ nA}$ ,  $U_b = -691.22 \text{ mV}$ ; (c)  $I_t = 0.11 \text{ nA}$ ,  $U_b = 116.58 \text{ mV}$ ; (d)  $I_t = -0.34 \text{ nA}$ ,  $U_b = -670.47 \text{ mV}$ . (L. E. Dinca *et al.*, reproduced with permission of The Royal Society of Chemistry).<sup>213</sup>

It is possible to pattern regions with dimensions of the order of tens of nanometers,<sup>215, 216</sup> at  $U_{\text{bias,pattern}}$  as low as  $3 \text{ V}$  (Figure 5.5). The dimension of the patterned area corresponds approximately to the scan size, with the area of the patterned region slightly exceeding the scanned area (detailed measurements are presented in Figure 5.1 and Figure 5.3(b)). The slight spillover effect is spatially confined and is likely due to the finite radius of the tip. At lower

patterning voltages near 3 V, the molecular density within the patterned region is reduced. In particular, the dense molecular aggregates (center of Figure 5.1(a)) are largely absent, and lower-density well-defined oligomers dominate the patterned region (Figure 5.5).

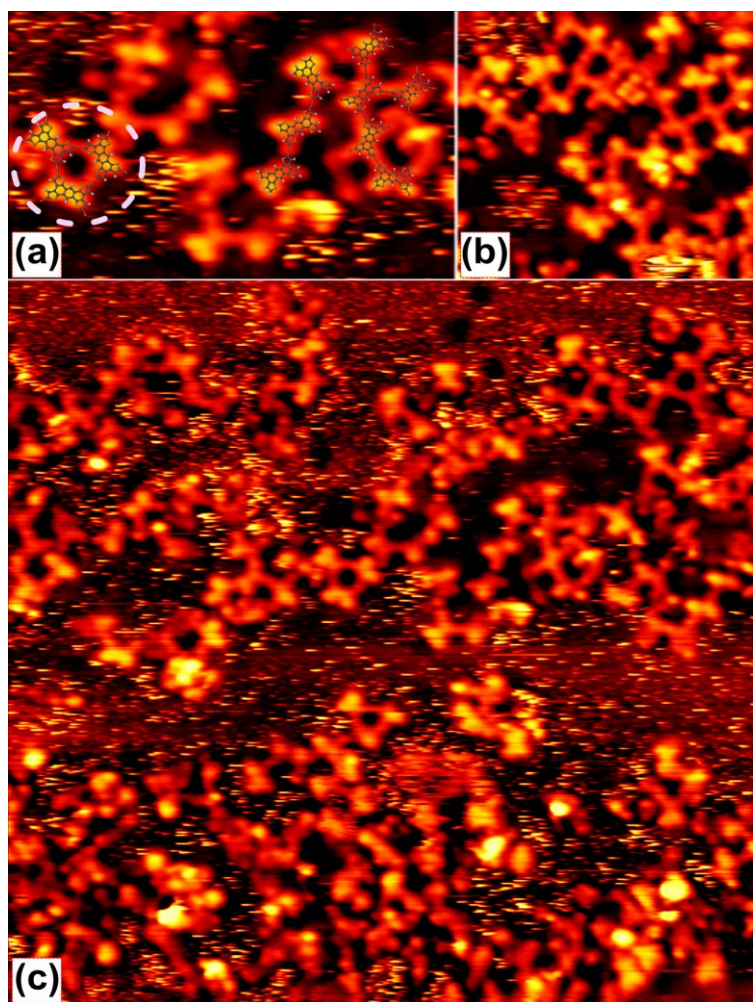


Figure 5.5. Oligomer motifs created by  $U_{\text{bias,pattern}} \sim 3.5$  V. Image sizes:  $5.3 \times 3.0$  nm<sup>2</sup> in (a),  $8.4 \times 7.3$  nm<sup>2</sup> in (b), and  $20 \times 20$  nm<sup>2</sup> in (c). Scanning parameters: (a-c)  $I_t = 0.12$  nA,  $U_b = 116.58$  mV. The molecular coverage on the surface in this particular set of images was estimated at  $\sim 1\%$  of a monolayer, based on molecular counting on a surface cooled to  $-160$  °C. The dashed circle highlights in (a) another type of organometallic oligomer – a trimer (structure “2”, as part of a Kagome lattice in Figure 5.2(c)). (L. E. Dinca *et al.*, reproduced with permission of The Royal Society of Chemistry).<sup>213</sup>

The structures observed in Figure 5.1(b) and Figure 5.5 are similar to the organometallic networks formed through the surface-catalyzed dehalogenation of TB2TTA on the (111) surfaces of Cu and Ag.<sup>19, 20</sup> In the present experiments, an average distance of  $1.43 \pm 0.06$  nm has been measured between the centers of mass of any two neighboring connected molecules in the oblique structure (Figure 5.2). Based on these bond-length measurements we also identified the products of the tip-induced process as organometallics.<sup>20</sup>

The geometry of the structures indicates that oligomerization occurs following dehydrogenation at the  $\alpha$ -carbons in the 2TTA thiophene rings, likely due to tunneling electron induced molecular activation. A similar STM tip-induced dehydrogenation of benzene has been demonstrated previously on Cu(110),<sup>95</sup> and Cu(001).<sup>94</sup> In both cases, the geometry of the benzene molecule switches from planar to upright adsorption with the activated bond(s) coordinated into the surface after dehydrogenation, and no cross-coupling was observed.<sup>217</sup> In the tip-induced dehydrogenation and oligomerization, two key factors could work together to favor intermolecular bonding over coordination of the activated bond into the Cu surface: (1) the TTA molecule is much larger and therefore more strongly adsorbed to the surface than benzene, and (2) at room temperature we can assume the presence of freely diffusing Cu adatoms on the surface,<sup>218, 219</sup> which would facilitate the coordination of activated bonds to Cu adatoms rather than substrate atoms. At room temperature the liberated hydrogen is not retained on Cu(111),<sup>220</sup> avoiding one of the challenges encountered in on-surface Ullmann coupling of halogenated monomers, where an accumulation of reaction byproducts occupies surface sites on the substrate.<sup>221</sup>

A limited number of tunneling electron related processes can induce bond-breaking. The possible mechanisms include vibrational heating and electronic excitation.<sup>99</sup> While vibrational heating occurs through a multi-electron process and is generally initiated at relatively low bias voltages (on the order of hundreds of mV),<sup>98, 99</sup> in the case of electronic excitation, the injection of electrons occurs *via* the lowest unoccupied molecular orbital (LUMO).<sup>95, 97</sup> We interpreted the dehydrogenation as being due to electronic excitation following electron injection into the LUMO of 2TTA (see Figure 5.6).

Whereas on HOPG no observable change was produced by the high-bias scanning (even after extensive scanning at 5-6 V), on Ag(111) the process produced pits in the surface and, depending on the molecular coverage, small domains of adsorbed molecules in the

regions around and between these pits (Figure 5.7). The mechanism for the immobilization of 2TTA/Ag(111) is not immediately apparent, but is qualitatively similar to the tip-induced chemisorption of copper phthalocyanine (CuPc) on Cu(111).<sup>222</sup> In the present case, the molecules seem to preferentially adsorb around pits etched in the substrate, suggesting that the undercoordinated atoms at the edges of these pits may help anchor the molecules.

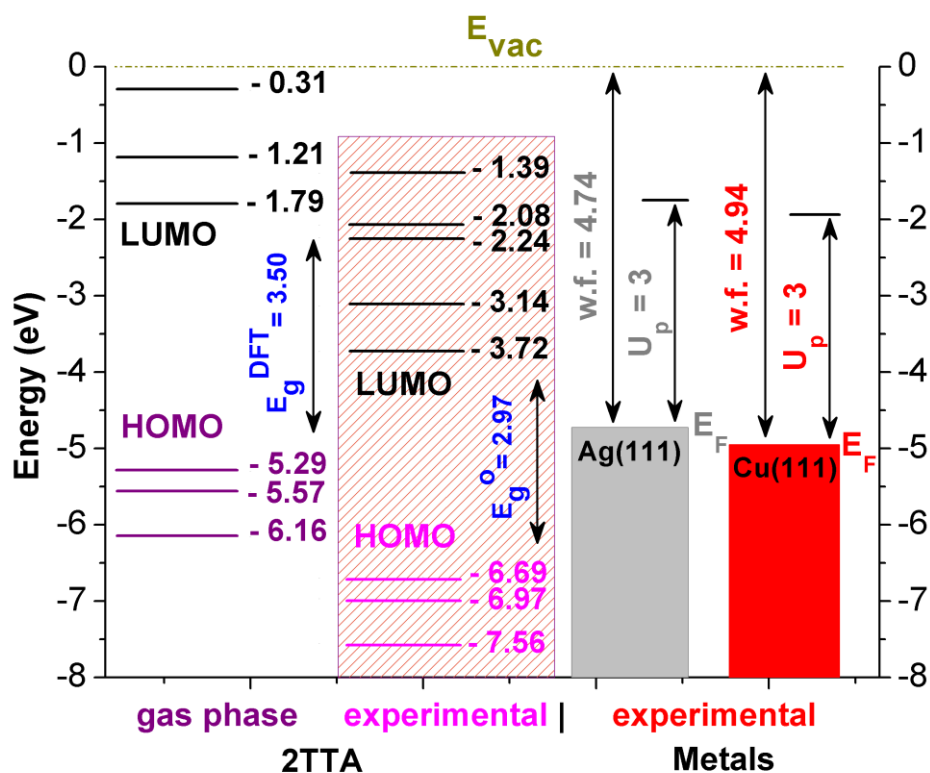


Figure 5.6. Schematic representation of energetics in the 2TTA, Cu(111) and Ag(111) systems. The eigenvalues of a single 2TTA molecule were obtained from the gas-phase DFT calculations of the molecular orbitals (at the B3LYP/6-31G(d,p) level). The work functions (w.f.) of Cu(111),<sup>223</sup> and Ag(111),<sup>224</sup> are published experimental values. The dashed rectangle contains the energy levels of 2TTA based on the reported experimental values of the HOMO (-6.69 eV) and the optical bandgap ( $E_g^o = 2.97$  eV);<sup>107</sup> the remaining energy levels are the DFT-derived values, and are referenced to the LUMO (unfilled states) and HOMO (filled states). In the diagram,  $E_{vac}$  = energy of the vacuum level,  $E_g^{DFT}$  = calculated value for the bandgap of 2TTA (3.5 eV),  $E_g^o$  = optical band-gap of 2TTA measured experimentally;  $E_F$  = energy of the Fermi level, HOMO – highest occupied molecular orbital, LUMO – lowest

unoccupied molecular orbital;  $U_p$  = bias voltage at which patterning occurs ( $\sim 3$  V). This diagram represents a first order approximation, where: (1) the molecules are physisorbed, and (2) the molecule-metal vacuum levels are aligned. The presence of the metallic surface will introduce perturbations to the positioning of these molecular energy levels obtained from gas-phase calculations; metallic surfaces are acknowledged as lowering, and broadening the molecular orbitals, by direct coupling of the surface electronic states with the molecular states.<sup>225, 226</sup> However, with these in mind, the diagram provides a visual representation of the possible molecular levels involved in the charge injection scheme at  $U_p = 3$  V bias ( $E_F + U_p \geq E_{LUMO}$ ), associated with molecular patterning on Cu(111). (L. E. Dinca *et al.*, reproduced with permission of The Royal Society of Chemistry).<sup>213</sup>

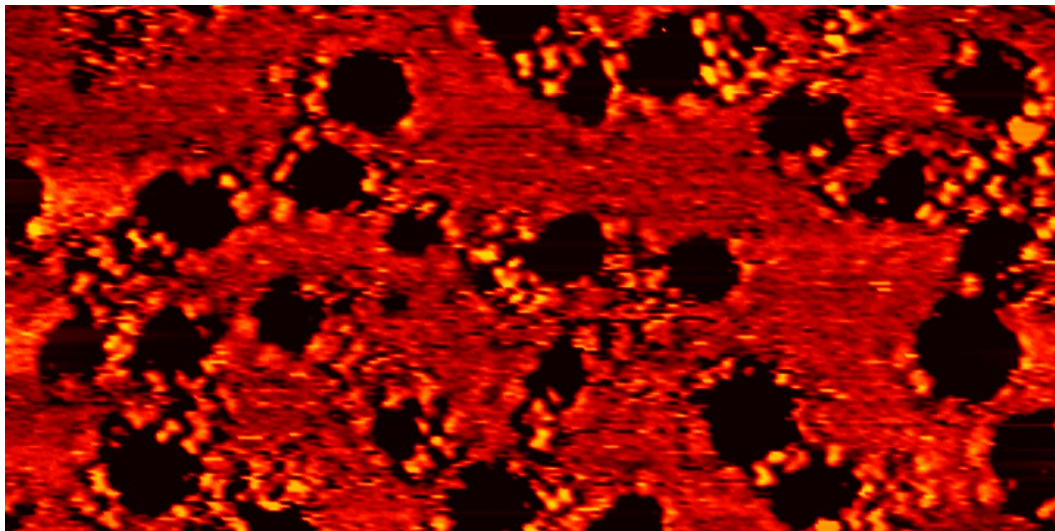


Figure 5.7.  $34 \times 17$  nm<sup>2</sup> STM image of a patterning attempt of 2TTA on Ag(111), showing aggregation of molecules around the pits formed on the surface ( $U_{\text{bias,ppattern}} \sim 5$  V). Scanning parameters:  $I_t = 0.55$  nA,  $U_b = 968.93$  mV. (L. E. Dinca *et al.*, reproduced with permission of The Royal Society of Chemistry).<sup>213</sup>

The negative results on Ag(111) could result from a lower reactivity of silver in the C–H insertion reaction. Furthermore, facile molecular diffusion on Ag(111) and HOPG could lead to decreased exposure to tunneling electrons.

Electronic excitation can also involve a bonding configuration change,<sup>94, 95</sup> as theoretically predicted for the dehydrogenation of small aromatics, where the hydrogen must be oriented into a preferred surface site.<sup>227</sup> The transition states associated with this process depend on the substrate adsorption,<sup>227</sup> since their positions could be shifted depending on the adsorption strength between molecule and surface. Moreover, the available adsorption sites (and energetics) change on different surfaces. Moreover, another influencing factor is through its particular distribution of the adsorption sites; since the C–H bond need to be stretched in a coordinated position favorable for cleavage. This is consistent with our finding that the reaction progresses on Cu(111) but not on Ag(111) or HOPG.

## 5.2. Conclusions

This work demonstrates that molecular patterns comprising 2D oligomers can be ‘drawn’ onto Cu(111) with nanoscale precision using an STM tip. The tip-induced reaction is manifested through the formation of oligomers and amorphous molecular aggregates in regions scanned at 3-5 V. Although similar oligomers were previously produced without spatial control using a brominated derivative of the 2TTA molecule on the Cu(111) surface *via* Ullmann dehalogenation, the present method not only allows for precise spatial control, but also avoids the creation of reaction byproducts that remain adsorbed on the surface.<sup>20</sup> Geometric considerations indicate that in this tip-induced process, the creation of free bonds is due to C-H bond activation. Experiments performed in an identical manner on HOPG or Ag(111) did not produce any oligomers, indicating that the surface plays an important role in the reaction.

## 5.3. Methods

The STM experiments were carried out in an ultra-high vacuum (UHV) chamber with a base pressure of  $10^{-10}$  mbar. The Cu(111) and Ag(111) substrates were cleaned by repeated cycles of sputtering with 1 keV Ar<sup>+</sup> for 10 minutes followed by annealing at 500 °C for 20 minutes. The HOPG substrate (Structure Probe Inc., grade SPI-2) was cleaved in air and subsequently transferred into the vacuum system. The resulting surfaces had large terraces with randomly distributed steps.

2TTA, the synthesis of which was described elsewhere,<sup>107</sup> was purified by vacuum sublimation ( $10^{-1}$  mbar; 300 °C). In our UHV experiments, the molecule was sublimated from a pyrolytic boron nitride (PBN) crucible in a Knudsen-type effusion cell at approximately 170 °C. For each surface, the same evaporation time (5 minutes) has been used. Presumably, due to the lower sticking coefficient there was a lower amount deposited on the Ag(111) and the HOPG than on the Cu(111).

Except for the estimation of surface coverage, when the surface was cooled at -160 °C, during the depositions (for the “patterning” experiments) the substrate was held at RT.

STM characterization was performed at room temperature using a commercial variable-temperature instrument (Aarhus 150, SPECS GmbH) equipped with cut Pt/Ir tips. Bias voltages are reported with respect to the STM tip.

Tunnelling current was maintained near 1 nA for all patterning experiments. Systematic tests of different tunnelling currents (0.2 - 1.5 nA) did not produce noticeably different results. Scan speeds during patterning were between 3 and 6 ms/nm. There were no noticeable differences in the results using scan speeds in this range.

Because of the lack of substrate resolution near the patterned regions (likely due to diffusing molecules), the images were calibrated based on atomic resolution images of the surface acquired during the same imaging session. This calibration allowed us to measure intermolecular distances with sufficient precision to differentiate between covalent and metal-coordinated molecules.

# Chapter 6

## Surface-catalyzed reactions of tetrathienoanthracenes on transition metals

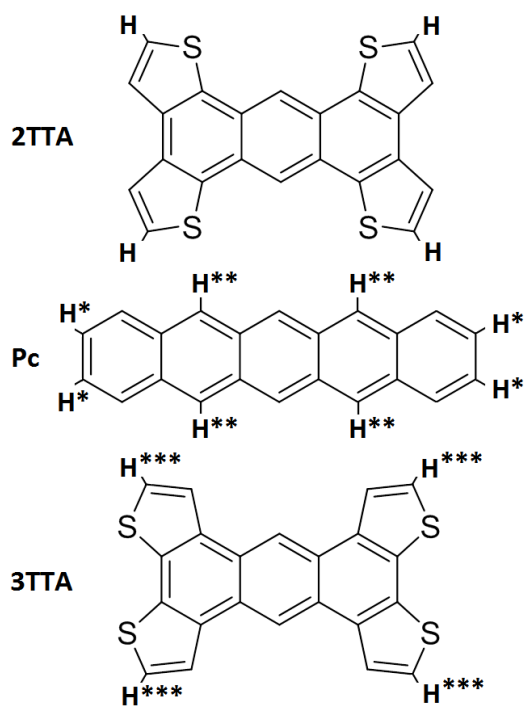
Oligothiophenes provide rich opportunities for surface confined chemistry reactions leading to two-dimensional molecular architectures. We performed systematic studies of tetrathienoanthracene (TTA) based molecules on different transition metal surfaces to reveal details of this type of on-surface chemistry. On the (111) surfaces of Ni, Pd and Cu, we observe sulfur abstraction from the monomer following thermal activation that varies with the metal surface. On Ni(111) and Pd(111) the internal design of the 2TTA isomer promotes intramolecular rebonding to produce pentacene, whereas geometrical constraints prevent the 3TTA isomer from intramolecular rebonding, promoting oligomerization. On Cu(111), desulfurization is preceded by dehydrogenation, which introduces metal-mediated intermolecular coupling in both 2TTA and 3TTA. This organometallic phase is stable up to 200 °C. On all surfaces, retained sulfur and dehydrogenated sites are important factors in defining the bonding geometries of the products.

A deeper understanding of surface-confined reactions in molecules with multiple reactive sites is a key step towards tailoring the synthesis of sophisticated molecular architectures in two dimensions.<sup>7, 9, 221, 228, 229</sup> Probing into the processes that occur at the sub molecular level (*e.g.* bond breaking and covalent coupling) which calls for thoughtful experimental approaches, has been tackled recently with success by the “surface science approach”, which involves approximating a complex physical system with an appropriate surface of a single crystal.<sup>4-6</sup> This approach can provide useful insights into the studied systems, although it cannot always be easily extrapolated to “real life” conditions (temperature, pressure, contamination).<sup>230-232</sup>

Among the chemical nanoscale building blocks that have received considerable attention, thiophene moieties have been incorporated into a range of interesting molecules and

structures with the ability to form networks and specific binding morphologies such as nanoribbons,<sup>40, 211</sup> and with electronic bandgaps that can be easily modified.<sup>19</sup> However, surface-confined reactions of thiophenes that require heating must be approached carefully, since the sulfur can be easily abstracted on reactive transition metal surfaces.<sup>192</sup> It is therefore important to establish a systematic understanding of how these systems behave when interacting with themselves or with different surfaces.

We recently reported a new reaction involving the catalytic abstraction of sulfur from thiophene moieties in trithieno[2',3':5,6:3',2':3,4:3',2':7,8]anthra[1,2-*b*]thiophene (2TTA) (Scheme 6.1), with subsequent (*intramolecular*) cyclization on Ni(111).<sup>108</sup>



Scheme 6.1. Schematic representations of 2TTA, pentacene (Pc) and 3TTA. Based on our observations, the most reactive positions were denoted as following: “H” —  $\alpha$ -hydrogen removed from 2TTA by electron-induced dehydrogenation;<sup>213</sup> “H\*” — hydrogen catalytically removed from the polycyclic backbone (pentacene radical); H\*\* — reactive sites obtained after total desulfurization of 2TTA; H\*\*\* —  $\alpha$ -hydrogen most likely to be removed from 3TTA through dehydrogenation.

By using the same molecule on Cu(111) we were able to initiate dehydrogenation, induced by a scanning tunneling microscope (STM) tip. The 2TTA molecules could be reductively dehydrogenated, while the ancene core remains intact.<sup>213</sup> Following dehydrogenation, the activated 2TTAs form into characteristic (*intermolecular*) organometallic assemblies mediated by Cu adatoms, and are therefore easily recognizable on the surface by STM imaging. A similar promotion of intermolecular reactions was observed following annealing of the structural isomer of TB2TTA, 2,5,9,12-tetrabromotrithieno-[2',3':3,4:2',3':7,8:3',2':5,6]anthra-[2,1-*b*]thiophene (TB3TTA) on Ni(111).<sup>108</sup> Hence, 2TTA and its isomer trithieno-[2',3':3,4:2',3':7,8:3',2':5,6]-anthra[2,1-*b*]thiophene (3TTA) (Scheme 6.1), may provide a useful model system for studying the effect of the substrate on molecular reactions.

The systematic study of the behavior of TTA isomers on different transition metal surfaces can provide insight into the mechanisms underlying the chemistry of these molecules, leading to an improved understanding of how to tailor molecule/substrate pairs to produce desired products.<sup>9, 233, 234</sup> More precisely, by investigating relationships between the structure of the molecule and the resulting products could lead to predictive control over these surface-confined reactions. Of particular interest is the ability to predict selectivity for intra- or intermolecular reactions and facilitate strategies to identify and design precursors capable of targeting specific reactions.

This chapter presents an investigation of the 2TTA and 3TTA molecules on transition metal surfaces, annealed to different temperatures, and studied by STM. The low-energy (111) surfaces were selected based on symmetry and structure considerations. Such surfaces present at least four types of possible adsorption sites but the atomic density of the surface creates little variation of the heat of adsorption between the sites (which on other surfaces could reportedly vary up to 30% from site to site).<sup>116</sup>

The types of the surfaces, Ni, Pd and Cu were chosen to represent a range of reactivity, and represent three of the metals most often used as catalysts in C—C coupling reactions in bulk. The catalytic activity of a certain type of metal is correlated to its *d*-shell occupancy or the *d*-band center of mass ( $\epsilon_d$ ) with regard to the position of the Fermi level ( $E_F$ ), with activity decreasing from up to down or from left to right in the periodic table.<sup>235</sup> Nickel has the closest  $\epsilon_d$  to its  $E_F$ , and is also the last of the *3d* group of transition metals. It is particularly interesting

since it is placed “fundamentally” in the periodic table with respect to the other two metals: Pd (*4d* series) and Cu (*3d 4s* series, with the *3d* filled and the *4s* having a low density of states at the Fermi level).<sup>116</sup> Thus, this array of substrates allowed us to explore the effect of substrate reactivity on the resulting products.

## 6.1. Results and Discussion

For 2TTA the reactions on all surfaces yield similar reaction products (Table 6.1). The difference, characteristic to each surface, is the thermal energy required by the system to activate the reaction. More differences arise in the 3TTA case. As opposed to 2TTA, where the desulfurization is followed by *intramolecular* C—C rebonding (cyclization), we must also take geometric factor into considerations, because the S abstraction leaves the 3TTA in a reactive state, enabling *intermolecular* connectivity.

T(°C)	Ni(111)	Ni(foil)	Pd(111)	Cu(111)
<b>RT</b>	½(TTA), Pc, ½ Pc	×	TTA	diffusing TTA
<b>100</b>	Pc	Pc	TTA	×
<b>150</b>	Pc, Pc dimer	×	Pc, Pc+(S/Pd)	TTA, TTA+Cu
<b>200</b>	Pc multimer	×	Pc, Pc+(S/Pd), Pc dimer	TTA+Cu, Pc, Pc+Cu
<b>250</b>	×	×	×	Pc, Pc multimer

Table 6.1. A summary of the reaction products of 2TTA on the (111) surface of Ni, Pd, and Cu, at different annealing temperatures. The phases marked with “×” were not investigated. The “½” stands for incomplete desulfurization (2TTA) or cyclization (pentacene).

Described below are the studies of the main reactions, complemented with interesting phenomena observed in the byproducts, showing how different surfaces assert themselves when the precursor is optimized for either intermolecular or intramolecular bonding.

### 6.1.1. 2TTA

#### 6.1.1.1. 2TTA to pentacene

After the sublimation of 2TTA on Pd(111) at RT, with subsequent annealing up to 100 °C for 15 minutes, STM imaging reveals molecular features whose shape is similar to that calculated for 2TTA in the gas phase. The four thiophene rings appear as characteristic

protrusions in the STM images (Figure 6.1(a)).<sup>236</sup> On Cu(111), the 2TTA is highly diffusive following RT deposition, and therefore only streaky and indistinct features could be imaged by STM.<sup>214</sup> Cooling the surface to -160 °C shows the 2TTA molecules with the same full appearance as those seen on the Pd surface, but assembled in a herringbone-like structure (Figure 6.1(b)).<sup>237</sup>

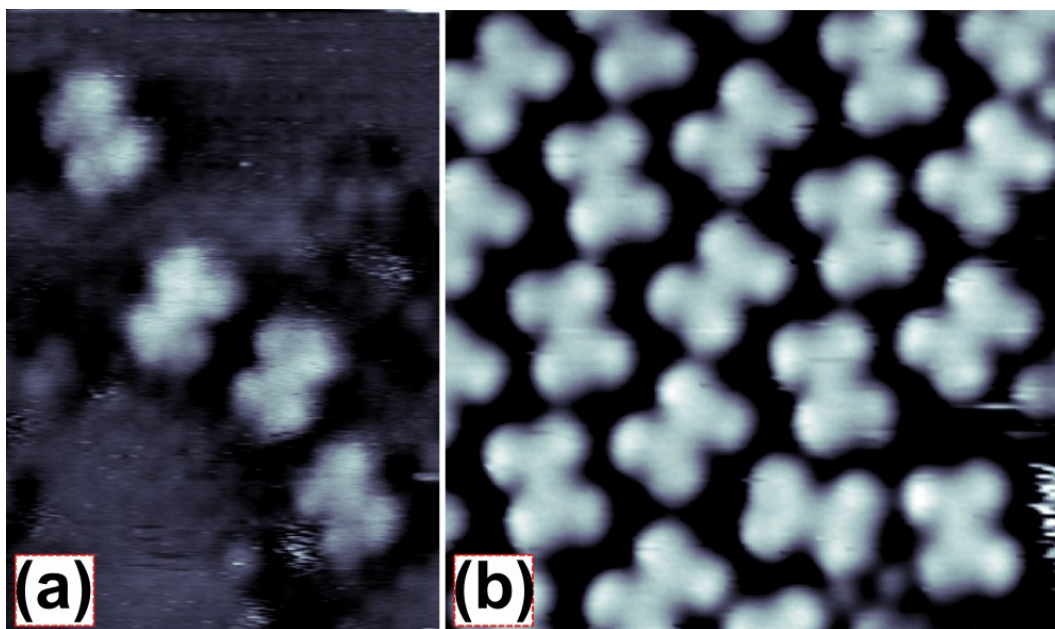


Figure 6.1. STM images showing 2TTA on Pd(111) in (a)  $4.5 \times 5.5 \text{ nm}^2$  at RT, and on Cu(111) in (b)  $5 \times 5 \text{ nm}^2$  by deposition at -160 °C, annealing at RT, and imaging at -160 °C. Scanning parameters:  $I_t = 0.47 \text{ nA}$ ,  $U_b = 524 \text{ mV}$  for (a); and  $I_t = -0.52 \text{ nA}$ ,  $U_b = -883 \text{ mV}$  for (b).

On the contrary, on Ni(111), RT was sufficient to transform the 2TTAs into a mixed organic phase comprising partially desulfurized 2TTAs and five-ring pentacene-like products (that will be henceforth referred to as pentacene, although this product is likely not saturated with hydrogens).<sup>108</sup> The four thiophene units of the 2TTA can undergo sulfur extraction followed by the reorientation of the remaining dangling bonds and their recombination to form new aromatic rings. On Ni(111) all reactions are driven to total cyclization by annealing to 100 °C for 15 minutes, when the mixed partially desulfurized 2TTA/pentacene phase is completely transformed into pentacene.

To verify whether an extended crystalline surface is required for the cyclization reaction to occur, the 2TTA was also sublimated onto a clean polycrystalline Ni foil. Following annealing at 50 °C, secondary ion mass spectrometry (TOF-SIMS) spectra contain a peak consistent with the mass of pentacene. The mass spectrum of the positive ions with masses up to 400 amu is shown in the Figure 6.2, where aside from the  $\text{Pb}^+$  and  $\text{Al}^+$  impurities emerging from the substrate, the peak corresponding to pentacene ( $\text{C}_{22}\text{H}_{14}^+$ ) is the dominant above 200 amu. Based on these results, the reaction appears to be robust and translatable to less well-defined surfaces, closer to “real” conditions.

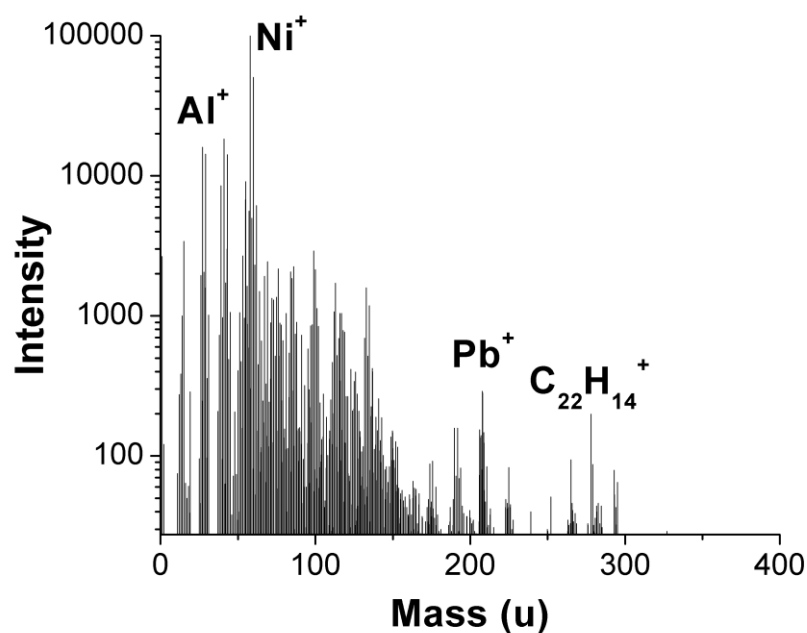


Figure 6.2. Positive ion TOF-SIMS spectrum of the 2TTA/Ni-foil sample. The peaks corresponding to nickel and pentacene ( $\text{C}_{22}\text{H}_{14}^+$ ) ions have been labeled, as well as the peaks of  $\text{Al}^+$  and  $\text{Pb}^+$  impurities.

To facilitate complete conversion to pentacene, which is achieved on Ni(111) at temperatures below 100 °C, both Pd(111) and Cu(111) require a higher temperature: up to 150 °C on Pd(111) (Figure 6.3) and 250 °C on Cu(111) for about 15 minutes. In the latter case, the reaction appears to start above 200 °C, as shown in Figure 6.4. Whereas on Ni and Pd the

transformation of 2TTA to pentacene is direct, on Cu(111) this final phase is preceded by an organometallic intermediate.

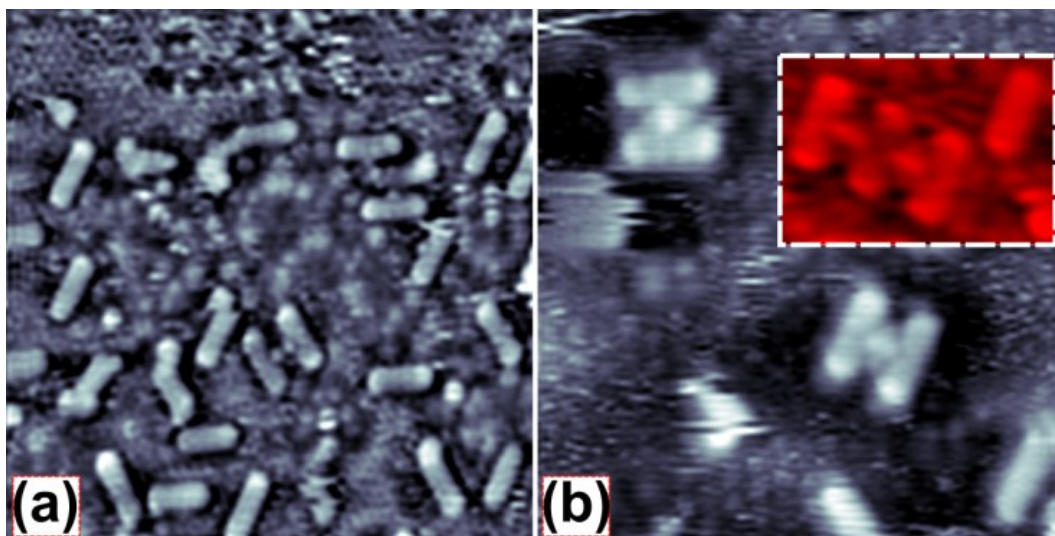


Figure 6.3. Room temperature STM images of 2TTA on Pd(111).  $10 \times 10 \text{ nm}^2$  in (a) (pentacene), and  $7 \times 7 \text{ nm}^2$  in (b) (pentacene and pentacene dimers) after annealing at  $150 \text{ }^\circ\text{C}$  for 15 minutes ( $3.5 \times 2.5 \text{ nm}^2$  for the inset image in (b) which shows one Pc and one Pc trimer). Scanning parameters:  $I_t = 0.49 \text{ nA}$ ,  $U_b = 19 \text{ mV}$  for (a);  $I_t = 0.48 \text{ nA}$ ,  $U_b = 362 \text{ mV}$  for (b) ( $I_t = -0.66 \text{ nA}$ ,  $U_b = -21 \text{ mV}$  for the inset in (b)).

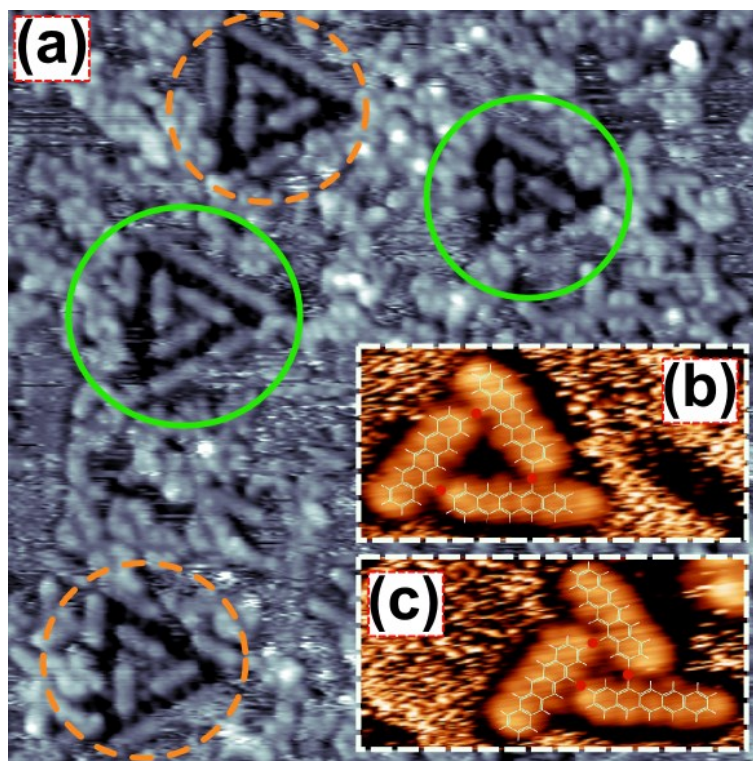


Figure 6.4. STM image of 2TTA on Cu(111), after annealing at 200 °C for 15 minutes.  $18 \times 18 \text{ nm}^2$  in (a), the green (solid) and orange (dashed) circles surround two chiral pentacene phases (2TTA coverage close to 1 ML). Framed by rectangles, the two  $3.9 \times 2.5 \text{ nm}^2$  STM images in (b) and (c) show at -160 °C common assemblies formed by three pentacene-like byproducts (starting coverage of 2TTA  $< 0.25 \text{ ML}$ ). Scanning parameters:  $I_t = 0.16 \text{ nA}$ ,  $U_b = 341 \text{ mV}$  for (a), and  $I_t = -0.89 \text{ nA}$ ,  $U_b = -968 \text{ mV}$  for (b),(c). Molecular models have been superposed over the molecular structures in the images (b) and (c).

#### 6.1.1.2. 2TTA to organometallics on Cu(111)

On Cu(111), after annealing at 150 °C for 15 minutes, former 2TTA molecules partially coalesce into interconnected structures (Figure 6.5, Figure 6.6). The absence of sulfur reconstruction from the Cu(111) surface, which depending on the coverage and temperature could form a number of characteristic patterns,<sup>238</sup> suggests that thiophene moieties in the 2TTA may not be yet broken (Figure 6.5). This implies only the activation of 2TTA at few of its positions, *e.g.* its  $\alpha$ -carbons denoted by “H” (see Scheme 6.1), followed by intermolecular coupling mediated by an atom (which appears as a protrusion in the STM contrast).

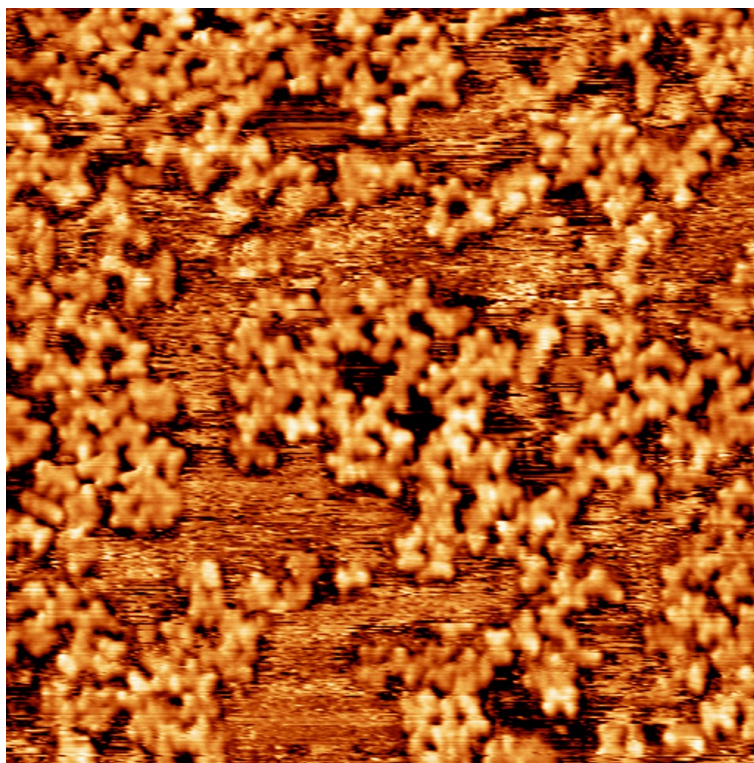


Figure 6.5. Room temperature  $20 \times 20 \text{ nm}^2$  STM images of 2TTA on Cu(111), after annealing at  $150 \text{ }^\circ\text{C}$ . Scanning parameters:  $I_t = 0.49 \text{ nA}$ ,  $U_b = 856 \text{ mV}$ .

In previous reports on Cu(111),<sup>20</sup> annealing the derivative of 2TTA (TB2TTA) at similar temperatures produced organometallic 2D films. Locally ordered structures, found within the film, included oblique (at RT) and kagome motifs (which appeared subsequent to annealing at  $200 \text{ }^\circ\text{C}$ ). The spacing between the centers of mass of any two adjacent connected 2TTA molecules (Figure 6.6), agree with those previously reported from DFT calculations for the organometallic phase formed by the TB2TTA molecule with copper ( $1.35 \text{ nm}$ , see schematic model in the inset of Figure 6.6).<sup>20</sup> Our STM images show bright spots coupling every two adjacent molecules, placed  $1.34 \pm 0.05 \text{ nm}$  apart, hence we interpret these structures as being metal (copper) coordinated. The calculated length of the covalently coupled structure,  $1.10 \text{ nm}$  (Table 6.2), is below the range indicated by our measurements.

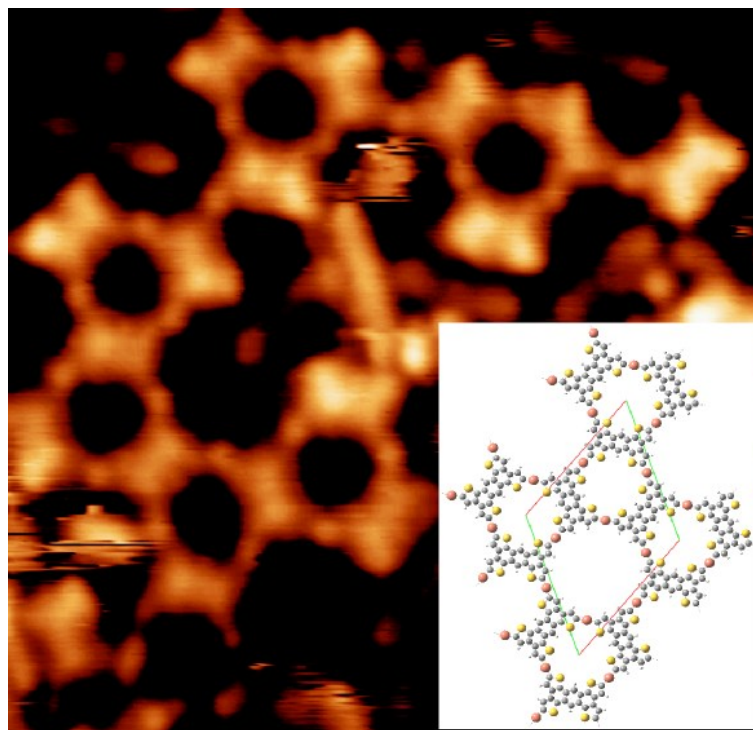


Figure 6.6.  $8 \times 8 \text{ nm}^2$  STM image of 2TTA on Cu(111), after annealing at  $150 \text{ }^\circ\text{C}$  (20 minutes) and imaging at  $-160 \text{ }^\circ\text{C}$ . Scanning parameters:  $I_t = 0.26 \text{ nA}$ ,  $U_b = 1238 \text{ mV}$ . The inset depicts the schematic model of 2TTA and Cu based organometallic structure — kagome lattice.

The reaction pathways for the conversion of isolated TB2TTA and 2TTA molecules to organometallic networks have similarities, but require different temperatures: TB2TTA debrominates at RT on Cu(111), whereas 2TTA requires additional thermal energy to undergo hydrogen cleavage at one of its most reactive “H” positions. In both cases, the influence of the substrate on the reaction is twofold: the Cu(111) acts not only as a catalyst, but due to the adatom gas present on the bulk metal surface,<sup>218, 219</sup> it also furnishes metal coordination centers for the formation of organometallic structures. X-ray photoemission analysis of the C 1s and S 2p core levels suggests that on Cu(111), the thiophene moieties of TB2TTA are completely ruptured between  $200 \text{ }^\circ\text{C}$  and  $300 \text{ }^\circ\text{C}$ , and the electropositive signature of the coordinated Cu atoms is still evident beyond this temperature. Thus, conversion of the organometallic phase to a covalent poly-(2TTA) phase, which requires the elimination of the coordinated Cu, appears impossible to keep the coordinated 2TTA ligands intact in this reductive elimination step. Conversely, on Ag(111) a metal-organic phase of the same

TB2TTA molecule was transformed into a covalently bonded polymer (50% yield) by annealing.<sup>19</sup> The very low activity of silver towards desulfurization left the TB2TTA block intact.

### 6.1.1.3. Secondary structures

Since the pentacene-like product is missing hydrogen atoms, its reactive sites can lead to the formation of other metal-coordinated phases on Cu and Pd, some of which are presented here to illustrate the versatility of these building blocks for creating nanostructures.

On Cu(111) the individual pentacene radicals adsorb both near the steps and on large terraces, where they arrange in triangular structures along the  $\langle 1\bar{1}0 \rangle$  directions. Two enantiomer structures of concentric triangles, built of what appears to be sulfur mediated right- and left-handed chiral superstructures of pentacene, can be identified after annealing above 200 °C for 15 minutes (Figure 6.4(a)).<sup>239</sup>

The partially dehydrogenated pentacene cores can form at least two additional types of three-molecule triangular assemblies on Cu(111) at low 2TTA coverage ( $<0.25$  ML) and temperature  $\sim 200$  °C (Figure 6.4(b),(c)). Comparing the STM images with DFT calculated molecular models suggests that these additional phases might be dehydrogenated metal-linked pentacene trimers (models in Figure 6.4(b),(c)). The distance between the central rings of any two bonded adjacent pentacene molecules in the STM images measures  $1.09 \pm 0.05$  nm, in agreement with the calculated value of 1.10 nm for the organometallic phase in (b), whereas the calculated spacing is 0.88 nm for covalent bonding. The similar structure in (c) measures  $1.20 \pm 0.05$  nm, in agreement with the calculated value of 1.21 nm for the organometallic phase, whereas the calculated spacing for the covalent phase is only 1.03 nm (Table 6.2).

Structure size (nm)\location	Figure 6.4-b	Figure 6.4-c	Figure 6.6	Figure 6.13
$d_{\text{covalent}}$	(0.88)	(1.03)	(1.11)	(1.16)
$d_{\text{organometallic}}$	<b>1.09</b> (1.10)	<b>1.20</b> (1.21)	<b>1.34</b> (1.35)	×
$d_{\text{sulfur-free}}$	-	-	-	<b>1.14</b> (1.14)

Table 6.2. Calculated (by DFT, shown between the brackets) and estimated (STM,  $\pm 0.05$  nm) values for the sizes of the most representative oligomer structures made by 2TTA or 3TTA.

A high resolution image of a pentacene-sulfur phase formed at 250 °C on Cu(111) is shown in Figure 6.7(a). The residual sulfur heteroatoms extracted from the 2TTA, apparently are mostly decorating the steps by forming triangular domains (Figure 6.7(b)).<sup>238, 240</sup> About 8 sulfur atoms, placed  $0.50 \pm 0.05$  nm apart on each side of the triangle are aligned along the  $\langle 1\bar{1}0 \rangle$  directions. This sulfur phase is identical, within the experimental error, to the  $(2 \times 2)$  reconstruction reported by Wahlström *et al.*<sup>240</sup>

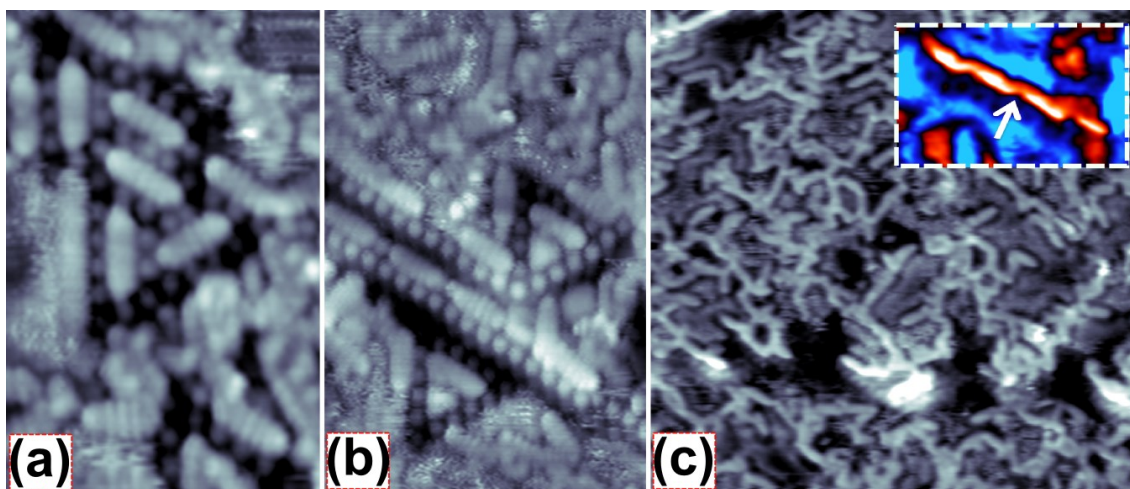


Figure 6.7. Room temperature STM images of 2TTA on Cu(111) after annealing for 20 min. at 250 °C in (a)  $5 \times 7$  nm<sup>2</sup>, and (b)  $7 \times 9$  nm<sup>2</sup>; and for 3 hours in (c)  $20 \times 20$  nm<sup>2</sup> (the  $5 \times 3$  nm<sup>2</sup> shows a linear structure with multiple kinks, one pointed out by the white arrow). Scanning parameters:  $I_t = -0.81$  nA,  $U_b = -202$  mV for (a);  $I_t = -0.76$  nA,  $U_b = -202$  mV for (b); and  $I_t = -1.5$  nA,  $U_b = -1683$  mV for (c) (inset:  $I_t = -1.05$  nA,  $U_b = -1358$  mV).

When the system is annealed for 3 hours at 250 °C, additional morphological changes take place and the discrete pentacene molecules are replaced by elongated, spaghetti-like structures (Figure 6.7(c)). Better evidence of this oligomerization process is highlighted at the steps, where the annealing process transforms the discrete linear assembly of pentacene (Figure 6.7(b), Figure 6.8) into chains of segments enclosing up to four kinks occurring with periodicity commensurate with the length of one pentacene molecule (inset of Figure 6.7(c), Figure 6.9). The hydrogen free positions “H\*” in pentacene facilitate intermolecular C–C

couplings, conferring a zigzag appearance to the linear structure. Similar kinking was observed above 200 °C in the reaction products of TB2TTA on Ni(111), where due to debromination the pentacene-like product had unsaturated “H\*” carbon positions (Scheme 6.1), producing zigzag-like 1D polymers.<sup>108</sup>

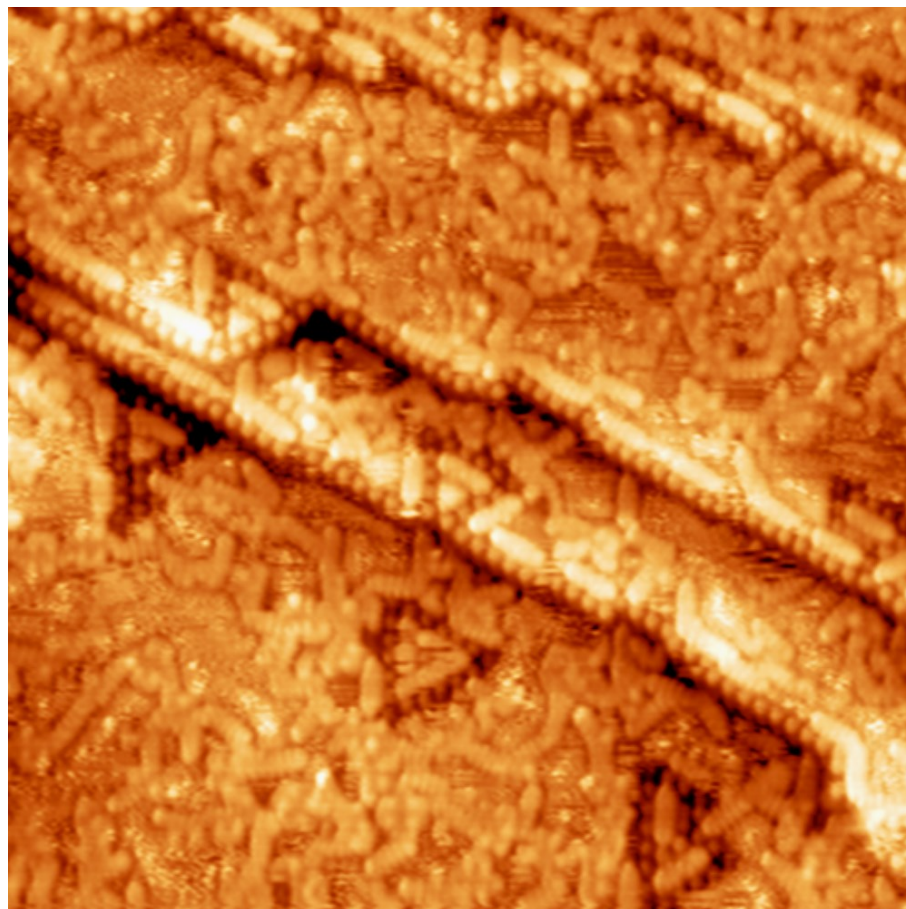


Figure 6.8.  $20 \times 20 \text{ nm}^2$ , STM images of 2TTA on Cu(111) after annealing for 20 minutes at 250 °C. Scanning parameters:  $I_t = -0.82 \text{ nA}$ ,  $U_b = -202 \text{ mV}$ .

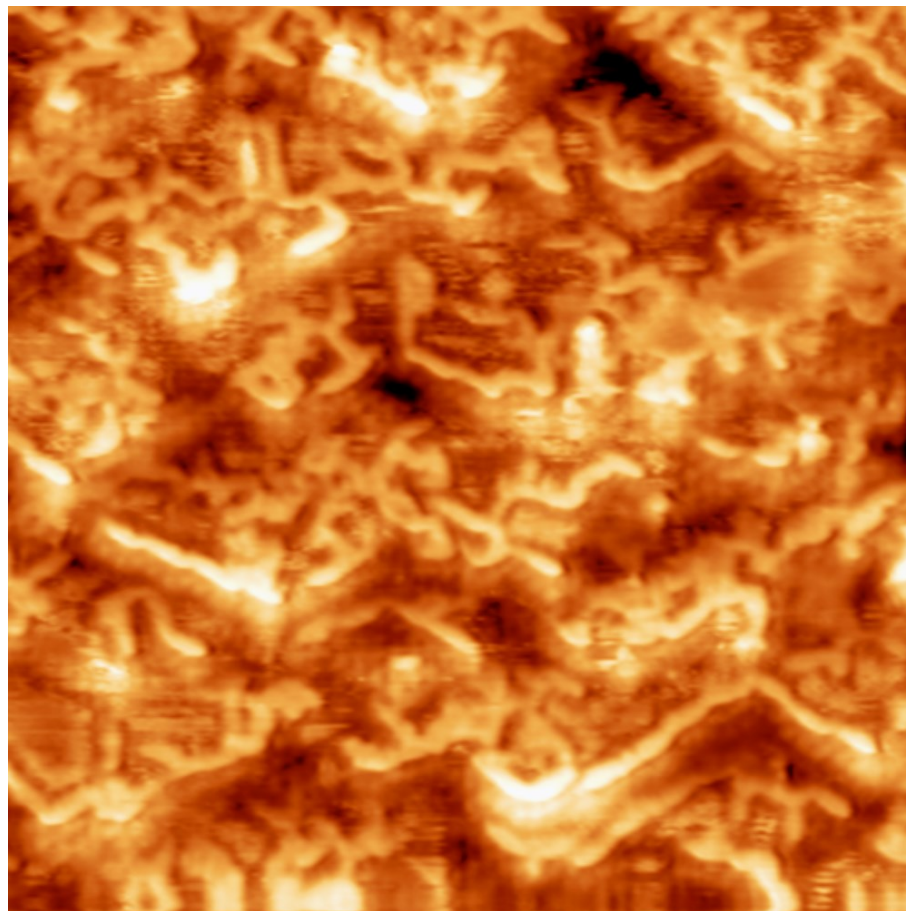


Figure 6.9.  $20 \times 20 \text{ nm}^2$ , STM images of 2TTA on Cu(111) after annealing for 3h at 250 °C. Scanning parameters:  $I_t = -1 \text{ nA}$ ,  $U_b = -1358 \text{ mV}$ .

On Pd(111), in addition to pentacene formation, H-shaped structures appear after annealing at 150 °C for 15 minutes (Figure 6.3(b)). They occur predominantly under conditions of low precursor coverage, and comprise up to three parallel pentacene molecules,  $0.97 \pm 0.05 \text{ nm}$  apart (see the inset in Figure 6.3(b)). High-resolution STM images show two discrete protrusions linking the molecules. The distance between the two protrusions oriented along the direction of pentacene molecules measures  $0.65 \pm 0.05 \text{ nm}$  (A-B, Figure 6.10(c)), while the distance between the transversals measures only  $0.18 \pm 0.05 \text{ nm}$  (B-C, Figure 6.10(c)). To explain this, we have to consider that on Ni(111), thiophene ring opening could not be decoupled from desulfurization at RT. On Pd(111) however, some molecules could conceivably undergo incomplete desulfurization (Figure 6.10(b)), positions of interest labeled

as “H\*\*” in Scheme 6.1, or totally desulfurize and bind to Pd surface adatoms, forming dimers or trimers (Figure 6.10(c)). The presence of sulfur or palladium,<sup>241</sup> in the region between pentacene products could modify the local density of states, brightening the appearance of the two hydrogen atoms in the middle of the dimeric structure (Figure 6.10(c),(d)). Gas-phase calculations of the structures mediated by S and Pd both give values for the distances A-B and C-D that are within our experimental uncertainty of  $\pm 0.05$  nm.

Sublimation of 3TTA onto Pd(111) (Figure 6.11(a),(b)), and Cu(111) (Figure 6.12(a)), and subsequent annealing up to 150 °C for 15 min. leaves the majority of the molecules intact.

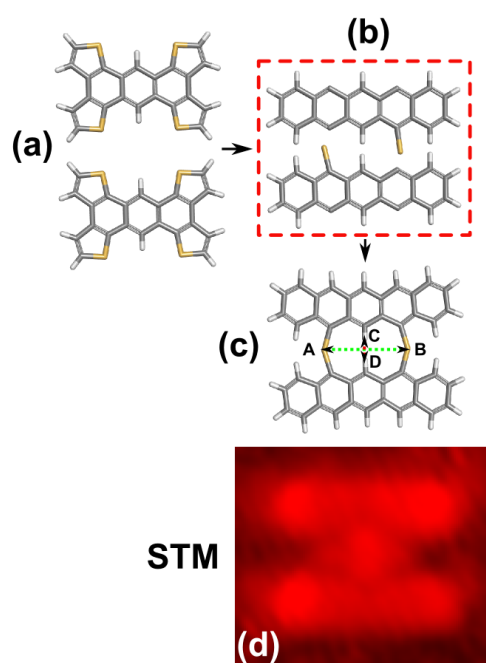


Figure 6.10. One of the two proposed mechanisms for the formation of the H-shaped structures observed in STM images of pentacene on Pd(111). The sulfur atoms shown in (b) are the result of thiophene ring opening without desulfurization. The gas phase structures in (a) were optimized using DFT at the B3LYP/6-31G(d) level. Furthermore, to better emphasize the mechanism, the structures in (b) and (c) were obtained by: (1) opening the thiophenic rings in (a), (2) partial desulfurization, (3) formation of the two pentacene cores, and (4) reuniting the two organic radicals into a new structure (in the DFT calculations the Pc cores were saturated with H atoms). The distances A-B and B-C, labeled in the image (c) correspond to distances of  $0.65 \pm 0.05$  nm (A-B) and  $0.18 \pm 0.05$  nm respectively (C-D) in the STM image

shown in (d). A structure similar to (c) could also be built on the Pd(111) surface with Pd adatoms instead of S. The distances A-B and C-D in the calculated structures in (c) measure 0.62 and 0.14 nm for S phase (B3LYP/6-31G(d)), and 0.67 and 0.15 nm for Pd (B3LYP/6-31G(d) + LANL2DZ).

### 6.1.2. 3TTA

Sublimation of 3TTA onto Pd(111) (Figure 6.11(a),(b)), and Cu(111) (Figure 6.12(a)), and subsequent annealing below 150 °C leaves the majority of the molecules intact.

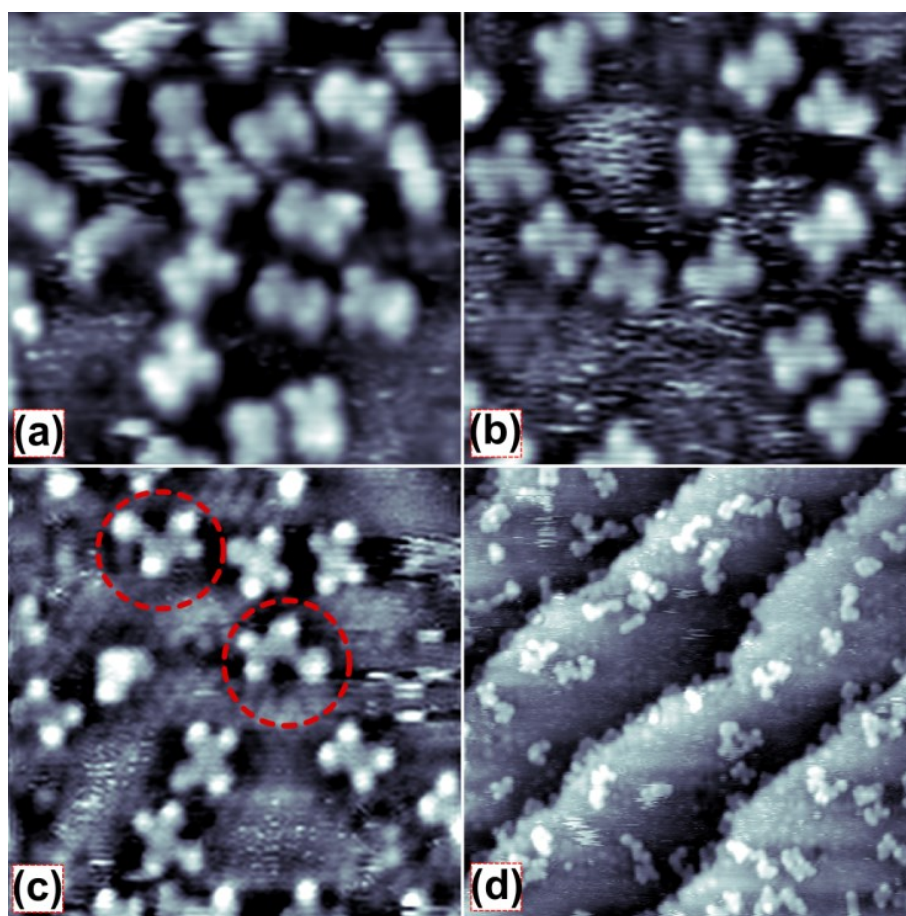


Figure 6.11. Room temperature STM images of 3TTA on Pd(111). (a)  $7 \times 7 \text{ nm}^2$ , as-deposited; (b)  $7 \times 7 \text{ nm}^2$  after annealing at 100 °C; (c)  $7 \times 7 \text{ nm}^2$ , annealed at 150 °C for 15 minutes; (d)  $20 \times 20 \text{ nm}^2$ , annealed at 200 °C for 15 minutes. Scanning parameters:  $I_t = 0.13 \text{ nA}$ ,  $U_b = 1030$

mV for (a);  $I_t = 0.38$  nA,  $U_b = 1250$  mV for (b);  $I_t = 0.69$  nA,  $U_b = 258$  mV for (c); and  $I_t = 0.64$  nA,  $U_b = 493$  mV for (d).

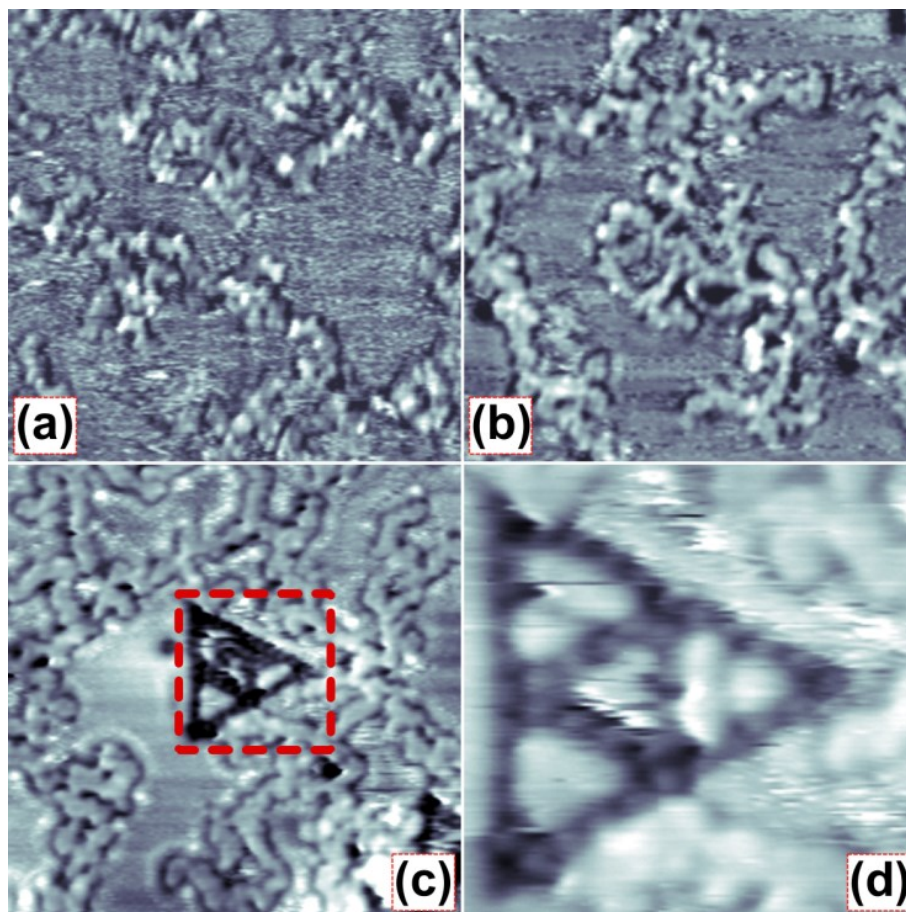


Figure 6.12. Room temperature STM images of 3TTA on Cu(111). Image size:  $15 \times 15$  nm<sup>2</sup> in (a-c) and a  $5 \times 5$  nm<sup>2</sup> magnified red-dashed selection from (c) is presented in (d). Scanning parameters:  $I_t = 1.39$  nA,  $U_b = 251$  mV, annealing at 150 °C for 15 minutes in (a);  $I_t = 0.59$  nA,  $U_b = 228$  mV, annealing at 200 °C for 15 minutes in (b);  $I_t = -0.15$  nA,  $U_b = -478$  mV, annealing at 250 °C for 15 minutes in (c); and  $I_t = -0.15$  nA,  $U_b = -478$  mV for (d).

Above 150 °C, some opening of the thiophene rings becomes evident. Due to geometric restrictions, the dangling bonds formed in 3TTA on each side of its anthracene core cannot rebond to one another at intramolecular level, but only with those from a different radical. Moreover, some molecules on Pd(111) have single thiophene units that appear

unfurled (Figure 6.11(c)). The incomplete desulfurization likely prevents polymerization, as suggested by the fact that dimers were the only oligomers observed following annealing at 200 °C (Figure 6.11(d)).

We were not able to gain a clear insight into the origin of the free bonds necessary for the oligomer formation at this stage, and annealing to 250 °C did not noticeably change the organic phase, although it did provide evidence of desulfurization through the formation of triangular domains associated with sulfur reconstruction.<sup>241</sup> The generation of dangling bonds extending from the anthracene core has already been observed for the brominated 3TTA (TB3TTA) on Ni(111),<sup>108</sup> where it was attributed to the cleavage and complete desulfurization of the thiophene moieties. The same annealing temperature on Cu(111) produces spaghetti-like structures without any long-range ordering (Figure 6.12(b),(c)).

Figure 6.13 shows representative STM images of as-deposited 3TTA on Ni(111), where aromatic radicals form chains of up to six diagonally interconnected blocks. Each block partially retains the gas-phase shape of the precursor.

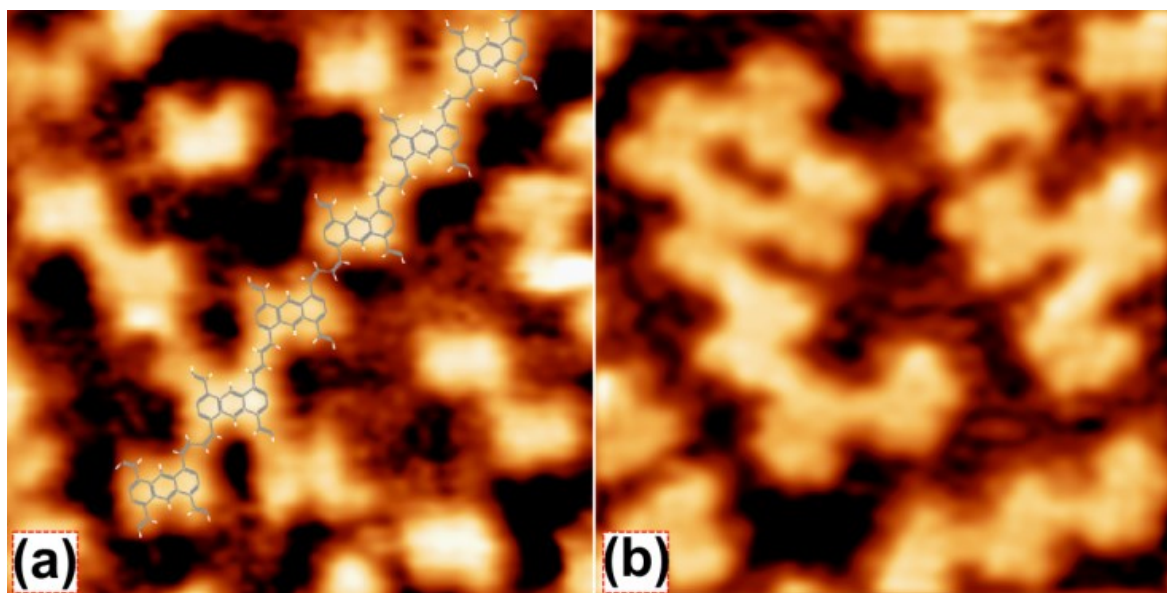


Figure 6.13.  $5 \times 5 \text{ nm}^2$  STM images (RT) of as-deposited 3TTA on Ni(111), in (a,b). Scanning parameters:  $I_t = 0.58 \text{ nA}$ ,  $U_b = 50 \text{ mV}$  for (a) and  $I_t = -1.63 \text{ nA}$ ,  $U_b = -103 \text{ mV}$  for (b).

The chemical nature of the oligomers, and thus the formation/reaction path, was investigated by estimating the distance between the centers of mass of consecutive building blocks in the network (Figure 6.13). The average value was found to be  $1.14 \pm 0.05$  nm, from images calibrated based on the known sulfur  $c(9 \times 5\sqrt{3})$ -rectangular reconstruction found in nearby domains.<sup>108</sup> Gas phase density functional theory (DFT) calculations were performed on 3TTA trimers, with either intact thiophene rings (Figure 6.14(a)), obtained through dehydrogenation at the “H\*\*\*” positions in 3TTA (see Scheme 6.1), or by total desulfurization (see Figure 6.14(b)). Both calculated polymeric structures have core spacing values within the uncertainty interval given by the experimental results: 1.16 nm for the thiophene based polymer (Figure 6.14(a)), and 1.14 nm for the sulfur-free polymer (Figure 6.14(b), Table 6.2). The presence of a large number of sulfur atoms on the surface implies desulfurization, which suggests that the oligomers respect the model shown in Figure 6.14(b).

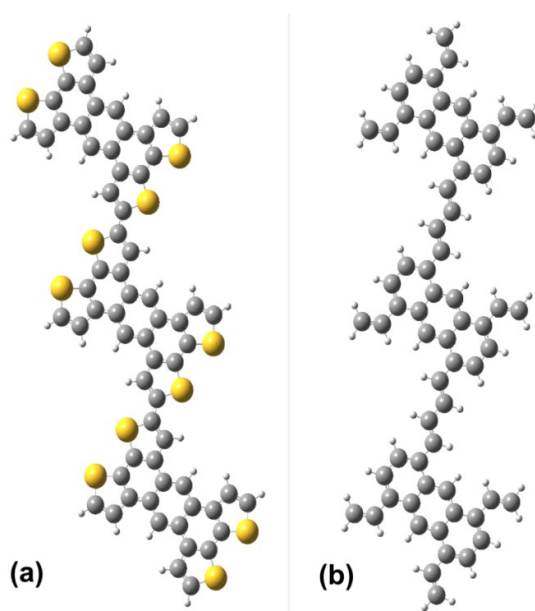


Figure 6.14. Proposed polymerization models of 3TTA molecule. *Via* dehydrogenation (on Cu(111)) in (a) or desulfurization in (b). The gas-phase structures were optimized using DFT at the B3LYP/6-31G(d) level, with the structure constrained to a flat geometry.

These long interconnections lead to the flexibility of the oligomeric structure, which can manifest in structural disorder. On Ni(111) however, the epitaxial molecule-substrate

match led to the formation of linear oligomers. The spatial extent of these covalent assemblies is dependent on the diffusion of the radicals on the surface, which may be hindered by retained sulfur (Figure 6.15). The inhibition effect becomes especially important at high precursor coverage since the quantity of byproduct is maximized as shown, on the nickel surface, in Figure 6.15. At low precursor coverage, on the same surface the sulfur atoms migrate to reconstruct in rectangular domains that are often found above step-edges (Figure 6.15). On surfaces where this occurs, polymeric assemblies are found to form on the terrace centers.

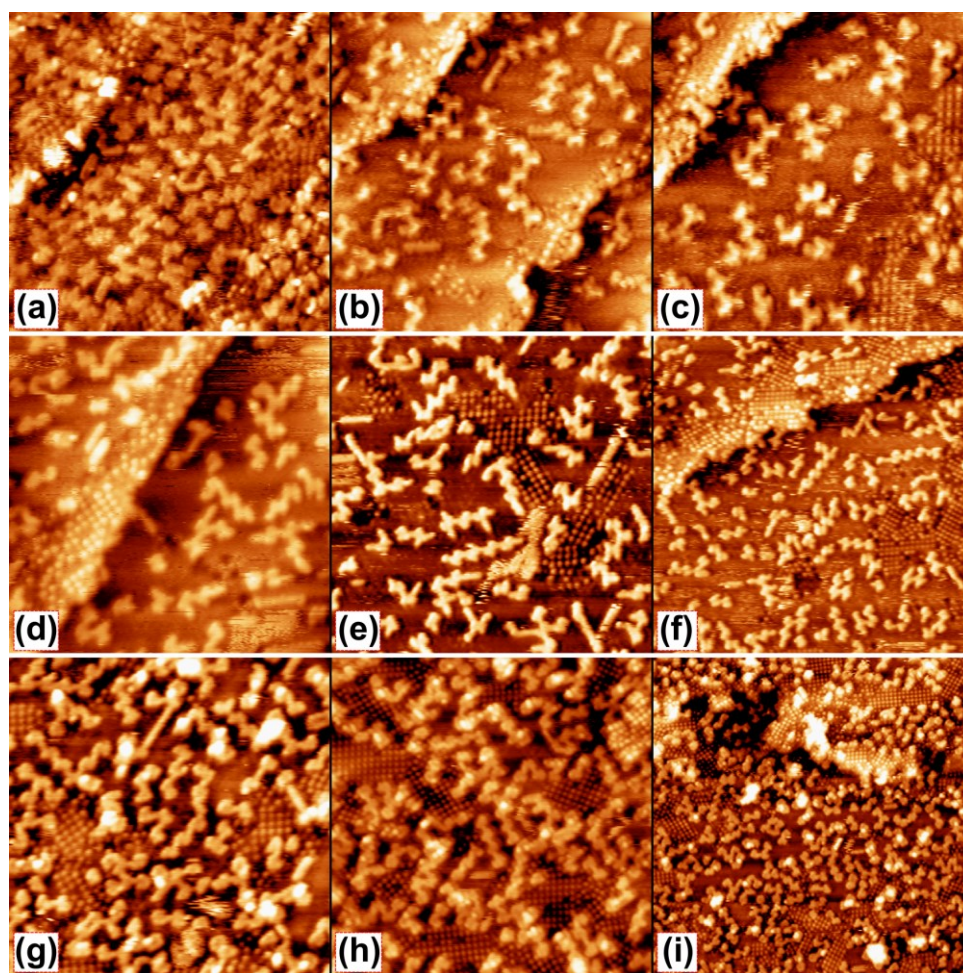


Figure 6.15. STM images of 3TTA on Ni(111) at various coverages and annealing temperatures. (a-c) As-deposited (RT), (d-f) after annealing at 100 °C, and (g-i) after annealing at 150 °C. Image and scanning parameters:  $15 \times 15 \text{ nm}^2$ ,  $I_t = -1.07 \text{ nA}$ ,  $U_b = -43.64 \text{ mV}$  for (a),  $15 \times 15 \text{ nm}^2$ ,  $I_t = -0.13 \text{ nA}$ ,  $U_b = -20.14 \text{ mV}$  for (b),  $14 \times 14 \text{ nm}^2$ ,  $I_t = -0.13 \text{ nA}$ ,  $U_b =$

-20.14 mV for (c),  $15 \times 15 \text{ nm}^2$ ,  $I_t = -0.95 \text{ nA}$ ,  $U_b = -32.95 \text{ mV}$  for (d),  $17 \times 17 \text{ nm}^2$ ,  $I_t = 0.93 \text{ nA}$ ,  $U_b = 4.88 \text{ mV}$  for (e),  $24.4 \times 24.4 \text{ nm}^2$ ,  $I_t = 0.22 \text{ nA}$ ,  $U_b = 4.88 \text{ mV}$  for (f),  $15 \times 15 \text{ nm}^2$ ,  $I_t = -0.44 \text{ nA}$ ,  $U_b = -184.63 \text{ mV}$  for (g),  $20 \times 20 \text{ nm}^2$ ,  $I_t = -0.19 \text{ nA}$ ,  $U_b = -55.85 \text{ mV}$  for (h), and  $30 \times 30 \text{ nm}^2$ ,  $I_t = -0.44 \text{ nA}$ ,  $U_b = -61.04 \text{ mV}$  for (i).

In the results discussed here, and previously reported,<sup>108</sup> thiophene desulfurization is a key step in sequential reactions that end with the formation of a partially saturated pentacene (using a 2TTA precursor) or a reactive radical that forms oligomeric structures (using a 3TTA precursor). The extent of desulfurization increases with the reactivity of the metallic surface, which is directly correlated with the position of its *d*-band center. A smaller energy difference between the *d*-band center and the Fermi level results in a strong adsorbate-surface bonding, so that from copper to palladium and nickel, the system requires less external energy. 2TTA ultimately yields similar products on each of the three different surfaces tested (Table 6.1).

As a substructure in the TTAs (2TTA and 3TTA), thiophene is adsorbed more parallel to the surface than the isolated thiophene, when its desulfurization occurs by electron transfer at its  $\alpha$ -carbon to one of the unoccupied *d* orbital of nickel.<sup>242</sup> The fact that oligomers were not observed below the cyclization temperature suggests that on Ni(111) and Pd(111) desulfurization occurs either prior, or simultaneous with dehydrogenation at the  $\alpha$ -carbon positions on the TTA. Cu(111) however, exhibits a markedly different behavior, with the dehydrogenated metal organic phase occurring at a temperature  $\sim 50 \text{ }^\circ\text{C}$  lower than that required for desulfurization.

The process of dehydrogenation could not be ruled out in 3TTA on any of the studied surfaces. The different molecular morphology of 3TTA as compared with 2TTA leads to a different multimerization geometry. Since both reactions occur at the same position on the molecule, it is not possible to clearly indicate the type of reaction through which the oligomerization of 3TTA/Ni(111) occurs, *i.e.* dehydrogenation or desulfurization, or whether desulfurization occurs prior to polymerization or after. Comparison of the experimental data with DFT calculations (Figure 6.14) also fails to distinguish between the two processes due to the structural similarity of the products.

Unlike other polymerization reactions where the byproducts are readily desorbed from the surface (*i.e.* water in some poly-condensation reactions,<sup>101, 188, 243-245</sup> halogens on

Au(111),<sup>24, 185, 187</sup> or hydrogen),<sup>22, 25, 33, 246</sup> the desulfurization of TTA “premonomer” leaves sulfur on the surface. Once adsorbed on the surface, the liberated sulfur can change the reaction barriers and block surface sites.<sup>32</sup> In contrast to sulfur, the hydrogen byproducts readily desorb at RT from Cu(111),<sup>220</sup> below the temperatures at which dehydrogenation occurs. The desorbed hydrogen leaves free active sites on the surface, providing a key advantage of dehydrogenation over desulfurization if the spatial extent of polymers is to be maximized.

## 6.2. Conclusions

Two on-surface reactions at the intra- and single-molecular level have been described on the (111) facets of Cu, Pd and Ni. The main reactions, complemented with interesting phenomena observed in the byproducts, demonstrate how different surfaces assert themselves when the precursor is optimized for either intermolecular or intramolecular bonding. These two reactions allow for the creation of free bonds at reasonably low annealing temperatures that retain the aromatic carbon rings in the precursor molecules. The rebonding that defines the products strongly depends on the position of the under-coordinated carbons, and therefore on the position of catalytically removed atoms (*i.e.* sulfur in the thiophene). In desulfurization, changing the position of the sulfur *via* isomerization allows for the promotion of either intramolecular bonding (2TTA) or intermolecular aggregation (3TTA). However, the molecular products come at the expense of the electronic modifications introduced by thiophene, which are lost with desulfurization, and leads to the surface adsorption of sulfur byproducts that passivate the active sites and obstruct the diffusion of organic products. Dehydrogenation has a certain practical advantage over desulfurization, since it leaves the molecular cores intact and yields byproducts that readily desorb from the surface. With the proper choice of the organic precursor, these reactions, *i.e.* thiophene ring opening and desulfurization, and dehydrogenation, can be used as pathways to design and synthesize complex macromolecular structures.

## 6.3. Methods

STM experiments were carried out in an ultrahigh vacuum (UHV) chamber with a base pressure of  $10^{-10}$  mbar. The Ni, either single crystal or foil (99% purity) and the Pd substrates

were cleaned by repeated cycles of sputtering with 1 keV Ar<sup>+</sup> for 10 minutes followed by annealing at 850 °C for 20 minutes. The Cu substrate was cleaned in similar conditions, except that the annealing was performed only at 500 °C.

The 2TTA and 3TTA molecules were synthesized as described elsewhere,<sup>107</sup> and purified by vacuum sublimation (10<sup>-1</sup> mbar, 300 °C). On the surfaces of interest, they were sublimated from a Knudsen-type effusion cell at a temperature of approximately 180 °C by using pyrolytic boron nitride (PBN) or Al<sub>2</sub>O<sub>3</sub> crucibles. During deposition, the substrates were held at room temperature (RT). After deposition and characterization of the molecular layer, the samples were annealed at specific temperatures for 15 minutes.

STM characterization was performed at RT using a commercial variable-temperature instrument (Aarhus 150, SPECS GmbH) equipped with cut Pt/Ir tips. Bias voltages are reported with respect to the STM tip.

Time-of-flight secondary ion mass spectrometry (TOF-SIMS) was carried out using an ION-TOF SIMS IV with a base pressure of 10<sup>-10</sup> mbar. A 15 keV Bi<sup>+</sup> beam was used to sample an area of approximately 50×50 μm<sup>2</sup>. Both, positive and negative SIMS, were performed at three different locations on the surface.

The optimized shapes of precursor molecular structures, result from the gas phase calculations using Gaussian 09 at the B3LYP level of theory by using 6-31G(d) basis set (for C, H, Br, S), complemented where needed with an effective core potential LANL2DZ (for Cu and Pd).<sup>158</sup> Avogadro,<sup>164</sup> and Discovery Studio Visualization,<sup>165</sup> open-source molecular builders and visualization tools, were used for producing basic molecular models.

# Chapter 7

## Pentacene on Ni(111): room-temperature molecular packing and temperature-activated conversion to graphene

Using scanning tunneling microscopy, the adsorption of pentacene on Ni(111) has been investigated at room temperature and the behavior of these monolayer films with annealing up to 700 °C. The conversion of pentacene into graphene begins from as low as 220 °C, with the coalescence of pentacene molecules into large planar aggregates. Then, by annealing at 350 °C for 20 minutes, these aggregates expand into irregular domains of graphene tens of nanometers in size. On surfaces where graphene and nickel carbide coexist, pentacene shows preferential adsorption on the nickel carbide phase.

Conversion of polycyclic aromatic molecules to graphene has recently gained attention,<sup>75, 83, 247, 248</sup> as it may provide an easy route to synthesizing one of the most remarkable systems of recent years.<sup>249</sup> The growth of graphene has been carried out using various organic precursors,<sup>75, 83, 250</sup> at temperatures ranging from 300 to 1000 °C. A recent report shows the feasibility of low temperature nickel-promoted synthesis of graphene multilayers on non-conductive surfaces, such as plastic or glass.<sup>251</sup> On Ni(111) (Table 7.1), the growth of graphene is of special interest due to the very close lattice match between the two materials, allowing the formation of a 1×1 overlayer structure,<sup>76</sup> and hybridization between the graphene  $\pi$ -states and the nickel  $d$ -band and shallow surface states.<sup>252</sup> These interaction channels induce the strong adsorption of graphene on Ni(111) as compared to other metallic surfaces:<sup>253</sup> the graphene-nickel substrate separation is up to 0.12 nm shorter than for bulk graphite (0.335 nm),<sup>254</sup> while on Cu(111) this reduction is only 0.05 nm.<sup>255</sup> This strong interaction modifies the electronic structure of the graphene overlayer on Ni(111), as compared to free standing

graphene, and leads to very interesting electronic (band-gap opening),<sup>253</sup> and magnetic effects.<sup>43</sup> Graphene overlayers can also provide new opportunities for the growth of self-assembled architectures by tailoring the surface reactivity of the supporting metallic surfaces,<sup>256</sup> motivating thereby the study of molecules at graphene interfaces.<sup>257, 258</sup>

Surface	Precursor	T [°C]	Quality-check/Ref.
Ni(111)	CO	> 300	ILS, ELS, <sup>44</sup>
	Ethylene (C <sub>2</sub> H <sub>4</sub> )	475	Auger, <sup>46</sup>
	Propylene(C <sub>3</sub> H <sub>6</sub> )	500	47-52
	Ethylene (C <sub>2</sub> H <sub>4</sub> )	400-500	STM, <sup>259</sup>
	Ethylene (C <sub>2</sub> H <sub>4</sub> )	425-525	STM, <sup>55</sup>
	Ethylene (C <sub>2</sub> H <sub>4</sub> )	~550	LEEM, <sup>260</sup>
	Toluene (C <sub>7</sub> H <sub>8</sub> )	400-650	STM, <sup>54, 55</sup>
	Ethylene (C <sub>2</sub> H <sub>4</sub> )	460-650	STM, Auger, <sup>62, 65</sup>
	Ethylene (C <sub>2</sub> H <sub>4</sub> )	675	STM, <sup>45</sup>
Ni(111)/W(110)	Propylene(C <sub>3</sub> H <sub>6</sub> )	400	ARPES, <sup>45</sup>
Ni(111)/MgO(111)	Propylene(C <sub>3</sub> H <sub>6</sub> )	600-680	STM, LEEM, <sup>261</sup>
Ni/SiO <sub>2</sub>	Graphite powder	25-260	Raman, <sup>251</sup>
Ni/plastic/glass	Graphite powder	< 160	Raman, <sup>251</sup>

Table 7.1. Graphene growth on Ni(111) as well as plastic/glass surfaces coated with a Ni film (the Ni films in Ref.<sup>251</sup> had a strong (111) texture; reported precursors and thermal conditions. Results from extended temperature, up to 1000 °C, are presented in the Table S1, ESI. (ILS – ionization loss spectroscopy, ELS – energy-loss spectroscopy, LEED – low-energy electron diffraction, STM – scanning tunnelling microscopy, LEEM – micro LEED, ARPES – angle-resolved photoemission spectroscopy.)

Pentacene (C<sub>22</sub>H<sub>14</sub>) is a polycyclic aromatic hydrocarbon containing 5 benzene rings. It has been widely studied in three-dimensional crystals,<sup>12</sup> and in 2D films on surfaces,<sup>237, 262</sup> because of its relatively high carrier mobility and consequently good performance as a semiconductor in organic electronic devices. In essence, pentacene can be considered as a structural element of graphene. Conversion of pentacene to graphene by covalent C–C coupling between pentacene molecules requires C–H bond breaking and subsequent rebonding of the undercoordinated carbon atoms.<sup>83</sup> Unlike coronene,<sup>263</sup> whose symmetry matches the final symmetry of graphene, pentacene has a lower symmetry. This symmetry reduction may make pentacene a good candidate for

growing novel graphene nanoarchitectures, such as *e.g.* ribbons,<sup>25</sup> under suitable synthetic conditions.

The adsorption of pentacene on Ni(111) has been studied by means of scanning tunneling microscopy (STM). The temperature-activated conversion of pentacene to graphene and the subsequent adsorption of pentacene on the newly formed graphene layer were explored.

## 7.1. Results and Discussion

Following RT deposition onto Ni(111), pentacene molecules pack into a “random tiling” phase, as shown in Figure 7.1. A similar structure for pentacene monolayers has been reported on Cu(111).<sup>237</sup> These investigations, reported in detail in Figure 7.2 revealed a slight preference for pentacene adsorbed in the vicinity of terrace edges to align with its long axis parallel to the steps. However, away from steps, this preferential adsorption was lost, and the molecules oriented randomly (Figure 7.2(e),(f)).

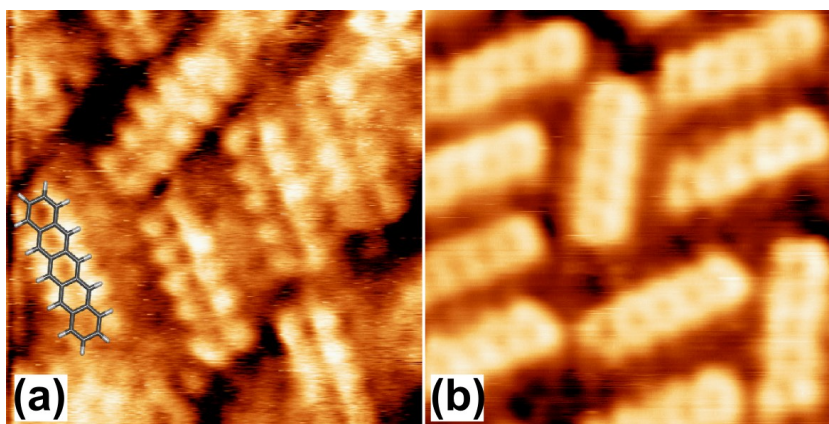


Figure 7.1.  $3 \times 3 \text{ nm}^2$  STM images of pentacene molecules adsorbed on a Ni(111) substrate at RT. (1.49 nA and 1.8 mV for (a); 0.53 nA and 31.1 mV for (b)).

Unlike the random tiling phase observed on Cu(111),<sup>237</sup> where the apparent lengths of pentacene molecules are not equivalent, due to oscillations between adsorption sites, in the Ni-supported phase all the pentacene molecules have equal apparent length indicating that the molecules are strongly adsorbed to the surface.

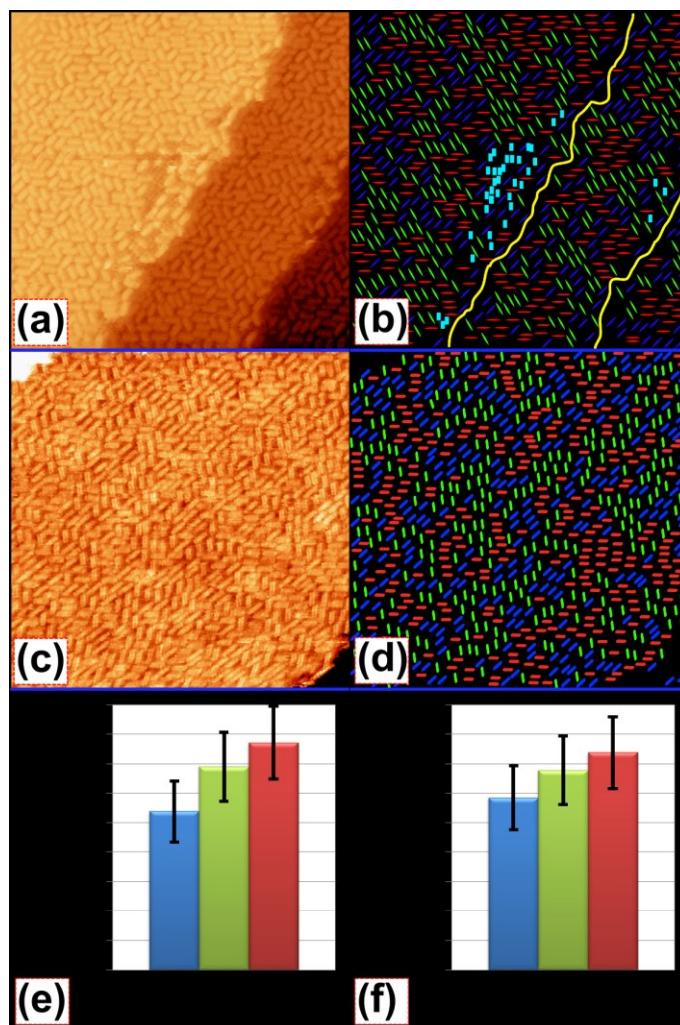


Figure 7.2. Quantitative analysis of pentacene orientation on Ni(111). STM image of pentacene as-deposited on Ni(111) surface centered on a step abundant region is presented in (a) and away from the stepped region in (c). Both images are  $30 \times 30 \text{ nm}^2$ . Scanning parameters: 1.36 nA, 1.8 mV for (a); 2.05 nA and 2.5 mV for (c). A statistical analysis of pentacene distribution in images (a) and (c) is presented in the color-coded images (b) and (d) respectively, with blue, green and red lines representing the pentacene molecules and, each color type corresponding to orientation along one of the  $\langle 1\bar{1}0 \rangle$  directions; long yellow lines depict the lines of the step edges, while in (b) the cyan scattered spots represent the nickel-carbide structures. The quantitative representation of the molecular abundance, related to the specific colors of (b) and (d) is plotted in (e) and (f) respectively. The numerical values in the error bars were calculated as the standard deviation assuming Poisson statistics.

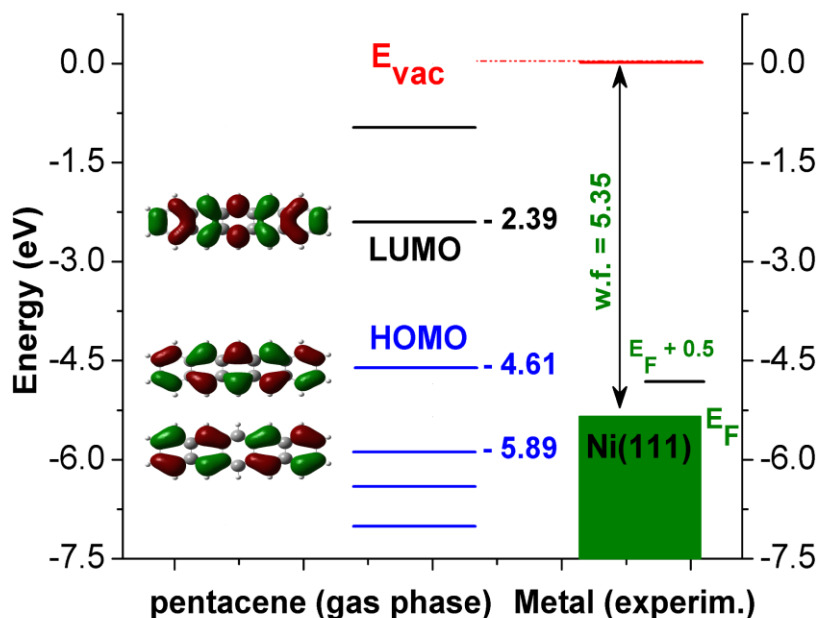


Figure 7.3. Basic energetics of pentacene and Ni(111), as separate systems. The calculated molecular orbitals of a single pentacene molecule (iso value = 0.02 electrons/Bohr<sup>3</sup>) are visually represented alongside the corresponding energies for the HOMO (Highest Occupied Molecular Orbital) and LUMO (Lowest Unoccupied Molecular Orbital). The calculations were performed using DFT at the B3LYP/6-31G(d) level. A representation of the nickel Fermi energy ( $E_F$ ) is schematized as well, using the literature reported value of 5.35 eV (experimental) for the work function (w.f.) of its (111) facet.<sup>264</sup> Since the Fermi level of Ni(111) is about 5.35 eV below the vacuum level and 0.74 V below the HOMO,<sup>264</sup> a first order approximation suggests that the HOMO is emptied upon adsorption on Ni(111). At either positive (+0.5 V) or negative (-0.5 V) bias voltages commonly used to image the pentacene on the Ni(111) surface, HOMO-1 is the most accessible molecular state. However, systematic sub-molecularly resolved STM images at biases close to the Fermi level of Ni(111) (Figure 7.1(a)) show a remarkable similarity with the calculated HOMO orbitals of pentacene, which should normally be revealed at a much higher bias voltage. This suggests that pentacene adsorbed on Ni(111) is chemisorbed, and that the presence of the metallic surface lowers and broadens the pentacene molecular orbitals,<sup>253</sup> by direct coupling of the surface electronic states with the molecular states.<sup>225, 226</sup> The Ni(111) surface possesses indeed three surface states. The

first two, close to the Fermi level, are at 20 and 250 meV. Originating in the  $d$  bands of the outermost Ni(111) atomic layer, a third surface state is placed 1.19 eV away of the  $E_F$ .<sup>252</sup>

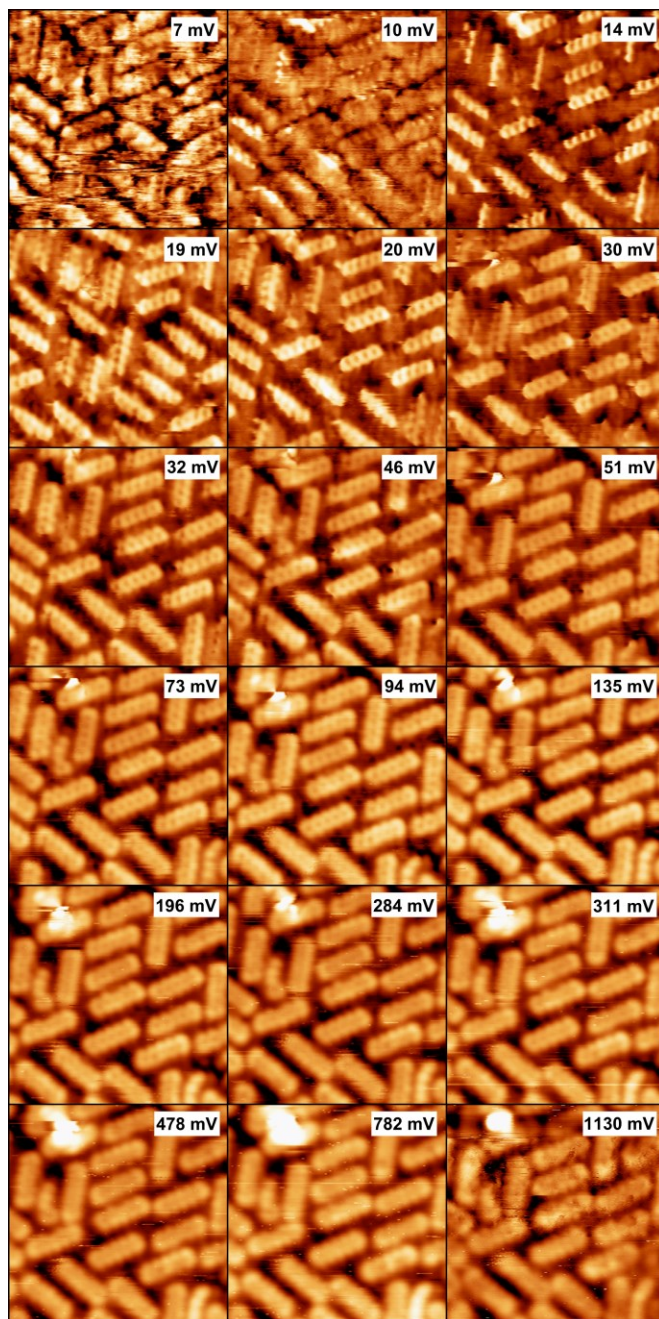


Figure 7.4. Bias-dependent STM images of pentacene on Ni(111). Image parameters:  $5 \times 5$  nm<sup>2</sup>, 0.94 nA and bias voltage as indicated on the upper-right corner of each STM image.

To assign a model to the random tiling phase, six possible adsorption geometries were investigated by using DFT. An isolated pentacene molecule finds its minimum energy in one of the “*hollow-fcc*” or “*bridge-top*” positions (the variation in binding energy is less than 0.06 eV), as shown in Figure 7.5(d) and (e) respectively.

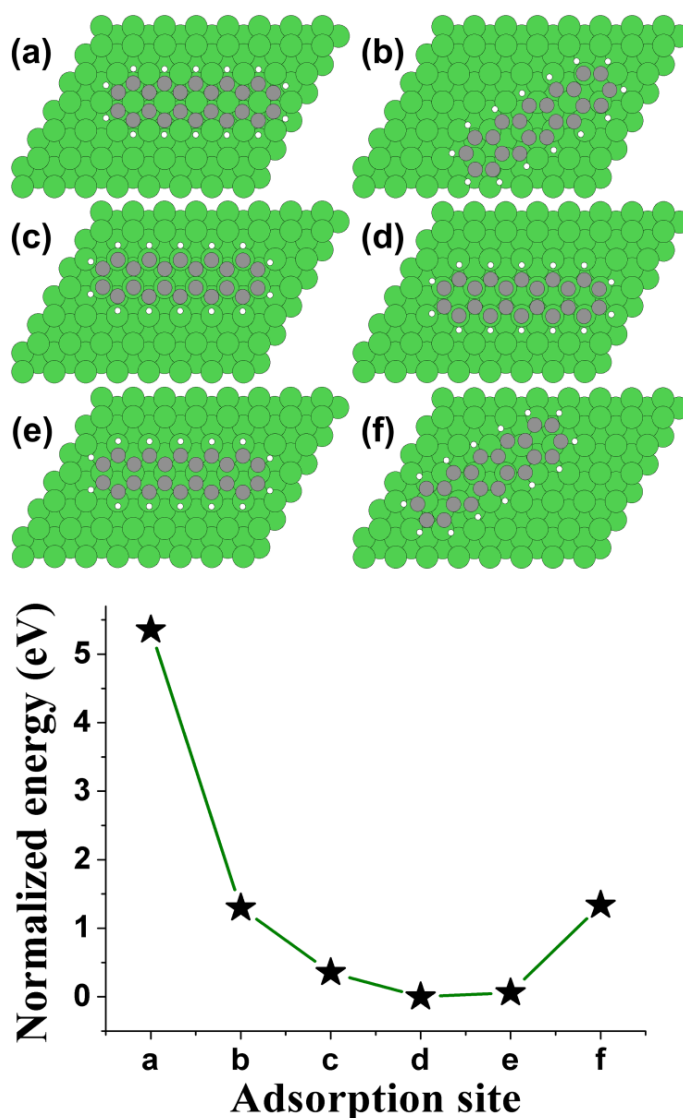


Figure 7.5. Site dependent pentacene adsorptions on the Ni(111) substrate. The calculated binding energies (LDA) are visually represented with respect to the energetically most stable conformation in (d), which is the most negative value of the energy. Adsorption sites are graphically defined and represented as: planar pentacene adsorption with the central carbon ring on top of a nickel atom and aligned parallel to one lattice direction is depicted in the (a) top-0°, with the phenyl rings centered on nickel atoms along the  $\langle 1\bar{1}0 \rangle$ ; (b) hollow-30°, where

the pentacene is oriented along  $[2\bar{1}1]$  with the central ring centered on a nickel fcc site; (c) hollow-hcp, the pentacene oriented along the  $\langle 1\bar{1}0 \rangle$  with all the rings centered on fcc nickel sites, one carbon is placed atop of a nickel atom and the next carbon above of a fcc site; (d) *hollow-fcc*, the pentacene oriented along the  $\langle 1\bar{1}0 \rangle$  with all the rings centered on hcp surface sites, one carbon atom atop of a nickel atom and the next carbon above of a hcp site; (e) *bridge-top* and (f) *bridge-30°*, similar to bridge-top but rotated to 30° along the  $[2\bar{1}1]$ . Angles are expressed in reference to the  $[1\bar{1}0]$  directions.

Annealing leads to the coalescence of the pentacene molecules, and converts the uniformly distributed monolayer of individual molecules into small domains of graphene. The process starts at 220 °C (Figure 7.6), and the domain size improves by annealing at 250 and 350 °C for 30 and 20 minutes respectively, as shown in Figure 7.7(a) and (c). High-resolution imaging of these domains reveals hexagonal features (Figure 7.7(b) and (d)), with a measured periodicity of  $0.24 \pm 0.05$  nm, consistent with both the in-plane lattice constant of graphite (0.246 nm) and the lattice constant for the (111) surface of nickel (0.249 nm).<sup>265</sup>

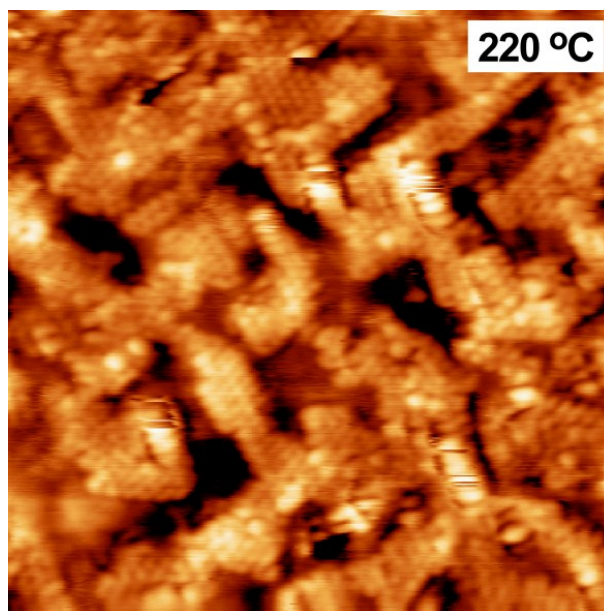


Figure 7.6. High resolution  $10 \times 10$  nm<sup>2</sup> STM image of graphitic domains on the Ni(111) substrate; prior to imaging the sample was annealed for 15 minutes at 220 °C. STM parameters: 1.47 nA, 10.68 mV.

The epitaxial growth of graphene on Ni(111) has been widely studied, and graphene was shown to grow in two distinct geometries:<sup>266</sup> the *top-fcc*, with one carbon atom adsorbed at the on-top position and the other on the *hollow-fcc* site, and *bridge-top* position, with two carbon atoms equivalently positioned and shifted off-centre above one Ni atom. The geometries for these phases are similar to the ones presented for single pentacene molecule adsorbed on the Ni(111) surface, in Figure 7.5(d) and (e), respectively.

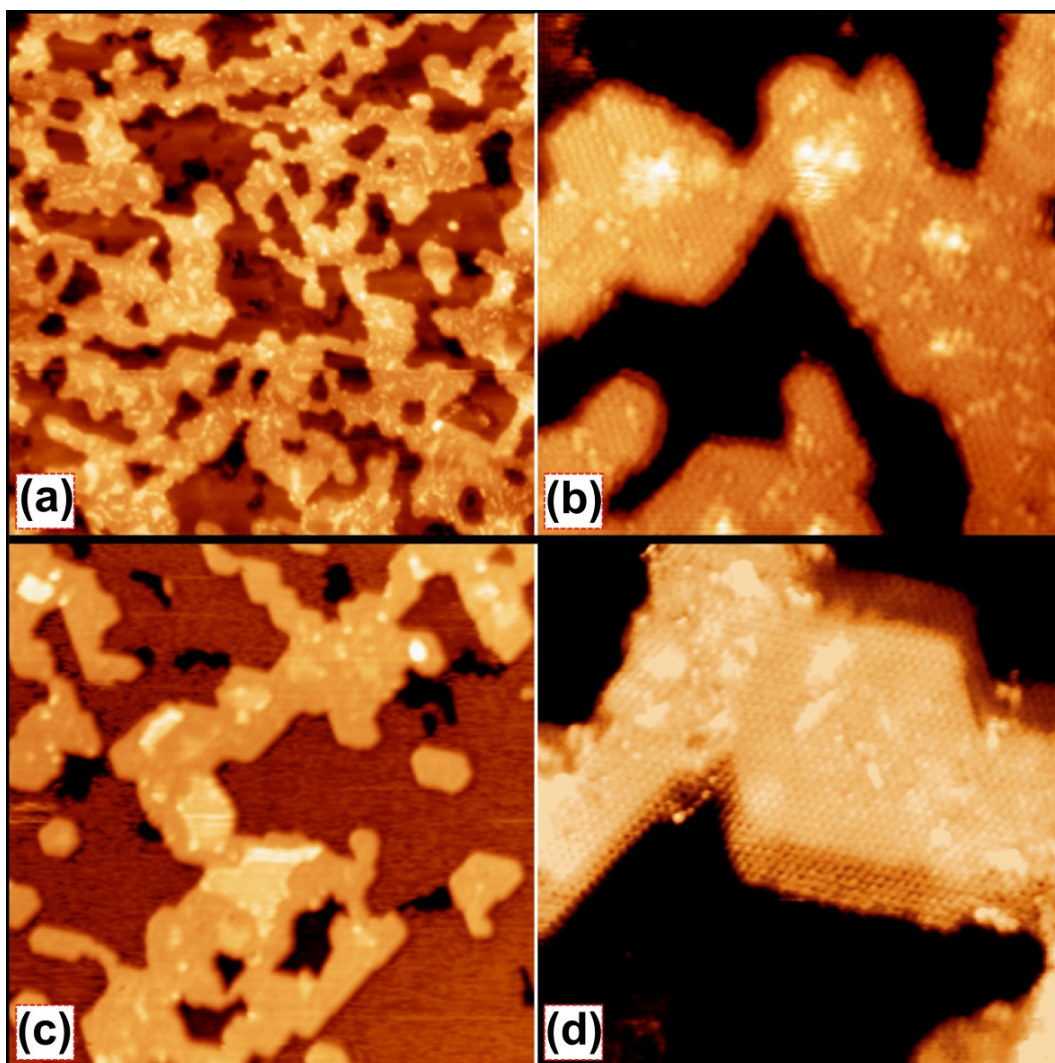


Figure 7.7. STM images of graphitic domains on Ni(111). Prior to imaging, the samples were annealed for 30 minutes at 250 °C in (a) and (b), and for 20 minutes at 350 °C in (c) and (d).

STM parameters:  $50 \times 50 \text{ nm}^2$ , 1.77 nA, 4.58 mV in (a);  $10 \times 10 \text{ nm}^2$ , -5.28 nA, -1.22 mV in (b);  $50 \times 50 \text{ nm}^2$ , 0.65 nA, 3.36 mV in (c);  $10 \times 10 \text{ nm}^2$ , -1.52 nA, -19.53 mV in (d).

The graphene formation has been attributed to dehydrogenation of the pentacene precursor,<sup>83</sup> and subsequent intermolecular rebonding with molecular diffusion occurring at one or more points in the process. In a number of recent reports, this strategy of C–H bond activation has been demonstrated to be effective for on-surface polymerization.<sup>25, 33-35, 267</sup> Partial dehydrogenation of pentacene leading to peripentacene and related C–C coupled products has also been suggested to occur during high-temperature vacuum sublimation in an inert gas flow (350 °C),<sup>84</sup> and likely attributable to catalytic impurities in the sample. In our case, using Ni(111) both as a catalyst and support, the activation temperature was reduced to roughly 220 °C.

The structural order of the graphene domains improves by increasing the annealing temperature, as shown in Figure 7.7. However, the graphene growth is patchy and incomplete, which can be attributed to compacting after hydrogen removal. The morphology depends on the annealing temperature as well as on the initial coverage of pentacene. At a similar activation temperatures, a pentacene coverage below 1 monolayer (<ML) produces graphene with a low defect density and large domains (up to  $650 \text{ nm}^2$ ), which could be due to the fact that all molecules experience catalytic interaction with the substrate. At >ML pentacene coverage, annealing temperatures near 600 °C produced large domains of high-quality graphene, whereas annealing below 400 °C produced domains with poor internal quality (Figure 7.8).

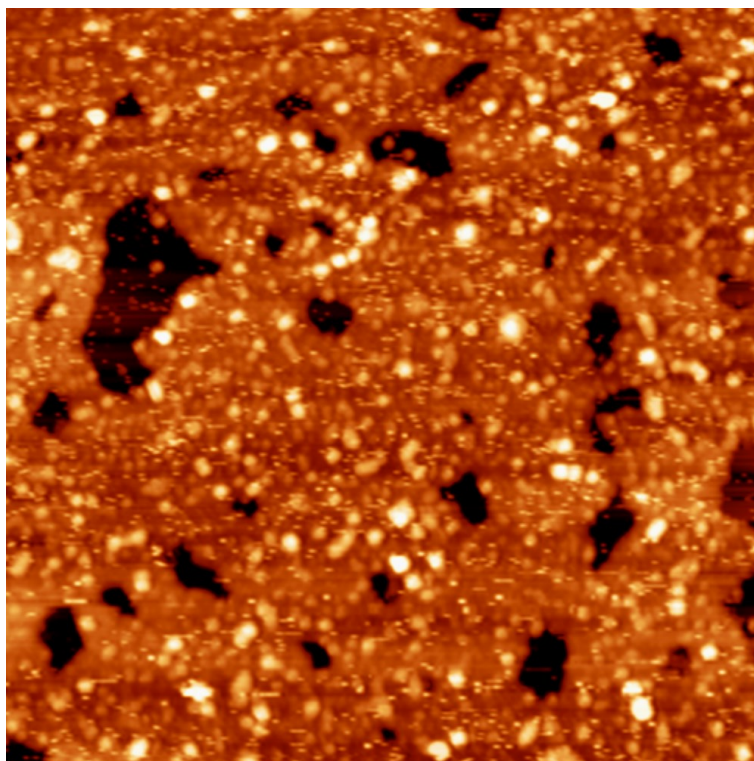


Figure 7.8.  $50 \times 50 \text{ nm}^2$  STM image of graphitic domains on Ni(111), starting from pentacene coverage  $> \text{ML}$ ; prior to imaging the sample was annealed for 15 minutes at  $250 \text{ }^\circ\text{C}$ . STM parameters:  $-0.93 \text{ nA}$ ,  $-6.71 \text{ mV}$ .

DFT calculations<sup>268, 269</sup> and various experimental reports suggest that the step edges are more reactive in dissociating small diatomic molecules such as CO, NO, O<sub>2</sub> and N<sub>2</sub>.<sup>269</sup> Experiments at room temperature involving ethylene on Ni(111) show a more pronounced reactivity towards the breaking of carbon-carbon bonds than carbon-hydrogen bonds at step edges,<sup>154</sup> suggesting that the flat (111) facets may therefore play an important role in dehydrogenation. As a consequence of carbon-carbon bond dissociation, carbidic domains localized at the step edges can form on the Ni(111) surface at temperatures as low as  $200 \text{ }^\circ\text{C}$ .<sup>53</sup> Monolayer graphene growth from large aromatic precursors should be thermodynamically favored with respect to the nickel carbide (Ni<sub>2</sub>C) surface phase on Ni(111), although the latter may be promoted at low carbon density.<sup>63</sup> In my experiments, nickel carbide, which was identified by its known

$\sqrt{39} \bar{R}16.1^\circ \times \sqrt{39} \bar{R}16.1^\circ$  reconstruction,<sup>44, 53</sup> formed at step edges on surfaces annealed to 700 °C for 20 minutes (Figure 7.9).

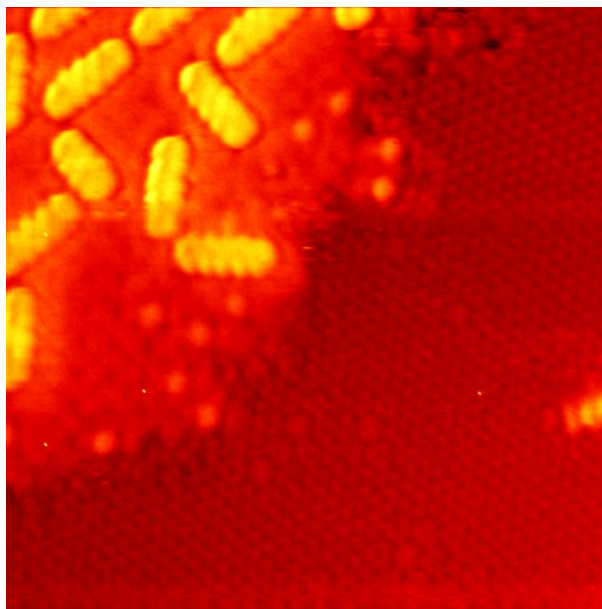


Figure 7.9.  $8 \times 8 \text{ nm}^2$  STM image of pentacene on a Ni(111) surface with coexisting domains of nickel carbide (left upper) and graphene (right lower). The pentacene preferentially adsorbs on the nickel carbide. Scanning parameters: and 0.97 nA, 3.36 mV.

In general, it is difficult to create mixed carbide and graphene domains above 600 °C due to the continuous consumption of the carbide structure by the advancing graphene front.<sup>270</sup> Their coexistence following higher annealing temperatures in the present experiments may be explained by the relatively short annealing times used.

By depositing pentacene onto graphene/Ni(111) surfaces on which  $\text{Ni}_2\text{C}$  coexists with graphene, held at room temperature, we were able to compare the relative adsorption properties of the two phases (Figure 7.9).<sup>55</sup> The single molecules adsorbed preferentially on the  $\text{Ni}_2\text{C}$ , implying their stronger interaction with the nickel carbide than with graphene, consistent with the low adsorption energies reported for graphene.<sup>154, 257</sup>

Raman spectroscopy is widely applicable in the characterization of the strain and defects present in graphene layers. However, for the particular case of monolayer

graphene on Ni(111), the Raman signal is suppressed due to the strong graphene-nickel interaction.<sup>253</sup> Hybridization of the nickel *d*-electrons with  $\pi$ -electrons of graphene induces a down shift in the  $\pi$  bands, opening a gap in the electronic structure of graphene and therefore annihilating the electron-phonon coupling essential for a detectable vibrational effect by Raman spectroscopy.<sup>271</sup> Accordingly, we did not observe any Raman response in my graphene/Ni(111).<sup>272, 273</sup>

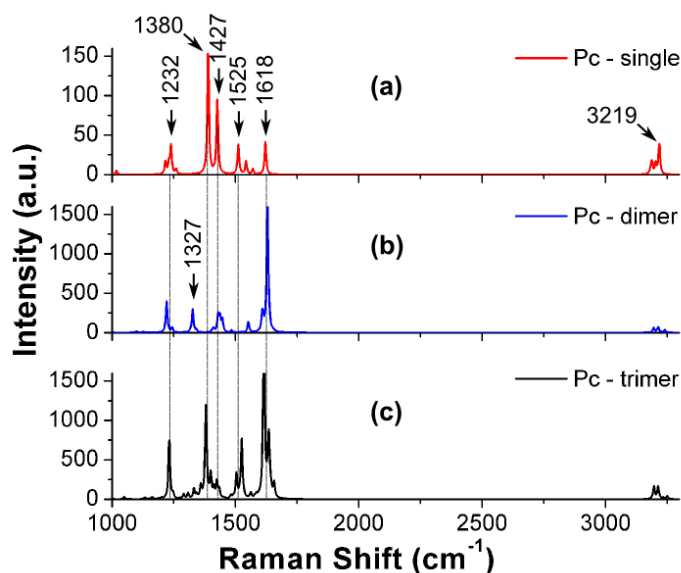


Figure 7.10. Calculated Raman spectra for a single pentacene in (a), dimer in (b) and trimer in (c). In the dimer and trimer configurations, the molecules were arranged parallel, without any off-set. Optimization, and calculation of Raman frequencies done by DFT at the B3LYP/6-31G(d) level.

## 7.2. Conclusions

In conclusion, we investigated the structure and temperature dependence of pentacene monolayers on Ni(111). As-deposited on Ni(111), the pentacene forms a dense monolayer with flat-lying molecules oriented along the  $\langle 1\bar{1}0 \rangle$  directions. Upon annealing above 220 °C, it converts into small domains of graphene, tens of nanometers in size, at temperatures lower than those previously documented (Table 7.1). Improved graphene quality was obtained by annealing at temperatures up to 700 °C. Comparison of molecular adsorption on graphene and adjacent nickel carbide domain demonstrates that at room temperature pentacene preferentially

adsorbs on the nickel carbide. The pentacene to graphene conversion occurs on Cu(111) only at temperatures above 800 °C. We will further investigate the extension of this technique to polycrystalline nickel surfaces, and adapt it to non-UHV conditions as well.

### 7.3. Methods

All experiments were carried out under ultrahigh vacuum (UHV) conditions in a chamber with a base pressure of  $10^{-10}$  mbar. The Ni(111) substrate was cleaned by repeated cycles of sputtering with 1 keV Ar<sup>+</sup> for 15 minutes followed by annealing at 850 °C for 20 minutes.<sup>152</sup>

Epitaxial Cu(111) films of 50-100 nm thickness were grown on Al<sub>2</sub>O<sub>3</sub> (0001) crystals using a method similar to the one described by Katz.<sup>274</sup> To achieve good quality Cu films the substrate was held at 250-300 °C,<sup>275</sup> while the Cu deposition rate was maintained at 0.01 nm/s.

Pentacene (98% purity, ACROS Organics) was sublimated from a Knudsen-type effusion cell with a pyrolytic boron nitride or Al<sub>2</sub>O<sub>3</sub> crucibles, held at approximately 190 °C. During deposition, the substrates were held at room temperature (RT). After deposition and characterization of the room temperature pentacene layer, the samples were annealed at specific temperatures for times varying from 15 minutes to 3 hours. The temperatures are estimated to be accurate to within  $\pm 25$  °C.

STM characterization was performed at RT using a commercial variable-temperature instrument (Aarhus 150, SPECS GmbH) equipped with cut Pt/Ir tips. Bias voltages are reported with respect to the STM tip. To compensate for instrumental drift and creep, the STM images were corrected to reflect known dimensions of experimental features wherever possible, and flattened, smoothed or Fourier filtered to enhance salient details by using the WSxM software.<sup>151</sup> The STM images in this work contain results representative of much larger data sets.

Computational studies were performed within the DFT formalism, based on the local density approximation (LDA). Pseudopotentials constructed with modified Troullier-Martins (TM) scheme,<sup>276</sup> and the Perdew-Zunger (PZ) exchange-correlation energy functional (successfully used for aromatics as coronene)<sup>277</sup> implemented in the SIESTA software package, were employed.<sup>167-169</sup> To model the adsorption of pentacene on Ni(111), a single pentacene molecule was considered on the Ni surface. The minimum-energy of the

pentacene/Ni(111) was determined by investigating different possible adsorption sites with various pentacene-substrate orientations. In all the calculations, an optimum kinetic energy cutoff (from single point calculations) of 240 Ry was used for the plane wave expansion. The Ni(111) surface was modelled with a 2D slab in a periodic 6×8 cell with the inclusion of a vacuum (~1.5 nm) layer to avoid interaction between the slabs. For this metallic system, a three layer slab was found to be sufficiently large to represent (and converge) the Ni(111) surface structure. All the geometry optimizations took the nickel magnetization into account by considering the spin polarization, and employing an algorithm based on the conjugate gradient method.<sup>278</sup> During simulations, the top layer of the nickel surface was allowed to relax, whereas the atoms in all remaining layers were kept fixed in their bulk-like positions.

The optimized shapes of precursor molecular structures result from gas phase DFT calculations by using Gaussian 09 at the B3LYP/6-31G(d) level.<sup>158</sup> Avogadro,<sup>164</sup> and free Discovery Studio Visualization,<sup>165</sup> open-source molecular builders and visualization tools were used for producing basic molecular models.

# Chapter 8

## Summary and Perspectives

The objective of this thesis was to investigate different aspects of the chemistry occurring in surface-bound systems of single molecules or molecular assemblies. Using UHV-STM, the interactions between custom made molecules and transition metal surfaces were addressed through various examples. The need to understand key steps of the reactions mandated the use of systematic studies which could provide insights into the processes.

As described in Chapter 4 and Chapter 6, a new on-surface chemical reaction involving the abstraction of sulfur from thiophene (as part of a large molecule) and subsequent intramolecular cyclization to produce a well-defined polycyclic aromatic product was identified through the use of STM. Although thiophene degradation is a known phenomenon,<sup>279</sup> its use in organic synthesis has been limited to hydrodesulfurization. In the case of the reaction observed in this work, the adsorption of the molecule on the (111) surface of Cu, Pd or Ni not only cleaves the C–S bonds, at specific temperatures, but also stabilizes the reactive products by allowing for inter- or intra-molecular rebonding. Considering the versatile chemistry of thiophene, this reaction could be a useful pathway for the synthesis of new polyaromatic molecules.

The reaction products are markedly affected not only by the type of the surface, but also by the by-products produced in the reaction. For example, hydrogen produced as a by-product is readily desorbed from the surface at temperatures similar to the temperature required for molecular activation (Chapter 5 to Chapter 7), whereas sulfur continues to diffuse and reconstructs in epitaxial domains, residing on most of the studied surfaces and inhibiting molecular diffusion.

Even if the STM, complemented with TOF-SIMS, gave enough evidence to support the cyclization of 2TTA to pentacene, it still failed to clarify two aspects of this mechanism. One is whether any dehydrogenation occurs prior to desulfurization or the cleavage of the thiophene ring, at the position of alpha carbon which suffers an electrophilic attack from the surface. This may be clarified by new experiments in UHV, involving deuteration of the unsaturated pentacene radical, and its subsequent examination by TOF-SIMS. The second

unsolved aspect of the reaction is how the two uncoordinated carbons obtained after desulfurization, at each head of the anthracene core assume a new geometry to bind one another and form a new aromatic ring. DFT studies, calculating the transition states of this process, may provide some elucidation of this process.

Chapter 5 deals with a controlled process for 2D patterning of atomically thick oligomer layers, with nanoscale resolution. By using the same precursor (2TTA) as in the first part of this work, and continuously scanning a surface that contains a confined gas of diffusing molecules at a bias voltage much larger than that used for regular imaging, the STM tip can be used to ‘write’ patterns of oligomers. The organometallics are formed at RT following the tip-induced dehydrogenation of 2TTA on Cu(111). They are qualitatively identical to structures resulting from the Ullmann reaction of a halogenated analogue (TB2TTA). Experiments performed in an identical manner on HOPG or Ag(111) failed to produce any polymers, suggesting that the surface plays an important role in the overall process. This may therefore be a promising approach for creating materials for molecular nanoelectronics, with highly tunable spatial and electronic properties. However, detailed theoretical studies and experimental investigations of whether the reaction could be initiated by other electron sources could further elucidate the mechanism for dehydrogenation in this large molecular system. The process could also be optimized in regards to the yield and density of the oligomer.

Chapter 7 examined the adsorption of pentacene on Ni(111), and shows that it can be efficiently converted into graphene at a temperature lower than previously reported for other precursors. At room temperature, the pentacene assembles in a dense layer comprising molecules lying flat on the surface, without diffusive motion within the layer, and randomly oriented along the  $\langle 1\bar{1}0 \rangle$  directions of the surface. DFT calculations suggest that the structure probably involves adsorption at the “*hollow-fcc*” or “*bridge-top*” positions. Upon annealing above 220 °C (<350 °C),<sup>236</sup> individual pentacene molecules are replaced by domains of graphene. A direct comparison of the adsorption of pentacene on graphene and nickel carbide revealed that the pentacene molecules preferentially adsorb on the nickel carbide, suggesting that the graphene is less reactive. This new mode of obtaining graphene could receive an attractive consideration relevant to directed chemical doping. Nitrogen could be an excellent choice, since its atomic size is comparable with that of carbon. Moreover, this technique could be extended to polycrystalline nickel surface, and adapted to non-UHV conditions.

# Appendix A.

## List of acronyms and common symbols

STM	scanning tunneling microscopy
UHV	ultra high vacuum
RT	room temperature
2D	two dimensional
CVD	chemical vapor deposition
DFT	density functional theory
HOPG	highly ordered pyrolytic graphite
TB2TTA	tetrabromo-trithieno[2',3':5,6:3',2':3,4:3',2':7,8]anthra[1,2- <i>b</i> ]thiophene
TB3TTA	tetrabromo-trithieno[2',3':3,4:2',3':7,8:3',2':5,6]anthra[2,1- <i>b</i> ]thiophene
2TTA	trithieno[2',3':5,6:3',2':3,4:3',2':7,8]anthra[1,2- <i>b</i> ]thiophene
3TTA	trithieno[2',3':3,4:2',3':7,8:3',2':5,6]anthra[2,1- <i>b</i> ]thiophene
Pc	pentacene
ML	monolayer
TOF-SIMS	time-of-flight secondary ion mass spectrometry
HOMO	highest occupied molecular orbital
LUMO	lowest unoccupied molecular orbital
$E_F$	Fermi energy
w.f.	work function
nm	nanometer ( $10^{-9}$ m)
Å	Angstrom ( $10^{-10}$ m)

# Appendix B.

## Résumé

L'imagerie et la caractérisation des événements de la réaction d'une seule molécule sont essentielles à la fois pour élargir notre compréhension de base sur la chimie et pour appliquer cette compréhension aux domaines aux frontières de la technologie, par exemple, dans la nanoélectronique. Poussé par cette demande, le but de ce travail est d'étudier le comportement de quelques molécules aromatiques étroitement liées, en portant une attention particulière à leurs transformations à l'échelle nanométrique spécifique induite par les surfaces supportantes résidentes. Bien que conceptuellement unifié, ce travail a impliqué plusieurs projets nécessitant des approches spécifiques. En général, ce travail se concentre sur les procédés de catalyse à l'échelle nanométrique de avec confinement de surface. A cette échelle, entre autres techniques, la microscopie à effet tunnel (STM) a été un outil important pour révéler des phénomènes catalytiques par l'imagerie d'adsorption dissociative, et l'éventuelle recombinaison des molécules dans diverses assemblées. Basé sur les mécanismes de réaction simples de la création de liaisons libres j'ai ciblé l'observation des comportements différents et représentatifs de molécules aromatiques complexes dans des conditions d'UHV, et j'ai tenté d'imager leur configuration d'équilibre atteinte après l'interaction avec les surfaces.

J'ai commencé par des études du tétrabromo-tetrathieno-anthracène de taille moyenne (TBTTA) sur une surface de Ni(111). Ceux-ci ont par la suite induit la synthèse d'une importante molécule organique semi-conductrice par une réaction sans précédent d'abstraction du soufre à partir d'un dérivé de thiophène. Cette réaction a créé les conditions préalables aux nouvelles liaisons et aux cyclisations C—C intramoléculaires dont le résultat a été un produit imprévu, bien définie, polycyclique à cinq anneaux linéaires, qui a été plus tard identifié comme étant le pentacène. Le processus a été observé avec une résolution moléculaire par STM sous ultravide. Cette réaction n'avait pas de précédent dans la littérature et son observation a mise en évidence la puissance des techniques à sonde locale pour explorer de nouvelles voies chimiques. Cependant, comme la technique STM donne des informations structurales et du contraste chimique limités, elle a été complétée par une technique d'analyse

supplémentaire pour l'identification sans équivoque des produits de réaction, dans notre cas la spectrométrie de masse d'ions secondaires à temps de vol (TOF-SIMS).

Cette réaction a démontré la possibilité de la formation contrôlée et bien définie des produits polycycliques utiles, connus ou potentiellement nouveaux, suite à l'abstraction du soufre. Comme le montre cette étude, les molécules polycycliques planes sont d'excellents candidats pour la découverte des nouvelles réactions par STM. Cette étude met aussi en évidence la capacité des techniques de sonde locale pour révéler des mécanismes chimiques.

Dans des études similaires, j'ai continué avec des explorations systématiques des dérivés non bromée (2TTA et 3TTA) sur la facette (111) de Ni, Cu et Pd. A partir de la réaction de cyclisation, précédemment observé sur la surface de nickel, la planification était d'aller plus loin que la réaction classique d'Ullmann qui est fréquemment utilisée. Par conséquent, ces molécules contenant du soufre ont été utilisés comme précurseurs pour la construction des ensembles polymériques (par désulfuration complète du 3TTA sur Ni(111)), ou des structures proto- polymère médiées par un adatome qui se trouve sur la surface (par déshydrogénation de 2TTA sur Cu(111)). Ce travail démontre également que les architectures moléculaires comprenant des polymères 2D peuvent être modelées sur Cu(111) avec une précision nanométrique en utilisant une pointe STM. Malheureusement, par l'ouverture du cycle, des propriétés utiles du thiophène par rapport à la modification «HOMO-LUMO» sont perdus. Comme le pentacène était le produit de la réaction de la plupart des surfaces, j'ai poursuivi avec l'étude du comportement de pentacène, comme un système indépendant ou comme bloc de construction dans un système conjugué plus complexe et plus vaste - le graphène. Sur la surface (111) de Ni les films de pentacène ont été considérés comme une nouvelle voie de synthèse de graphène, à partir de précurseurs aromatiques de petite dimension, et au température basse.

L'utilité du STM pour ces types d'expériences est claire: STM dispose d'atouts spécialisés, il s'agit d'une méthode de sonde locale de très haute résolution avec une sensibilité aux produits minoritaires.

Mots-clés: le thiophène, le pentacène, STM, la désulfuration, la déshydrogénation, cyclisation, organométallique, structuration, le polymère, le graphène.

# Chapitre 1.

## Introduction

La capacité de diriger l'ensemble des molécules individuelles sur des surfaces est une nécessité de base pour la construction «bottom-up» de dispositifs électroniques moléculaires. Le contrôle complet de ces processus doit tenir compte non seulement de la mise en place et de la disposition de la conformation,<sup>3</sup> mais aussi des questions fondamentales de la composition moléculaire et de la structure au niveau sous-moléculaire.

Une stratégie prometteuse pour relever ce défi est d'étudier et d'exploiter des réactions spécifiques de molécules confinées sur des surfaces réactives dans un environnement ultravide (UHV),<sup>4</sup> en décomposant le système dans des systèmes modèles simples.<sup>2, 6</sup> Une des motivations pour cette tendance vers la chimie de surface est la possibilité déjà prouvée pour la synthèse des matériaux électroniques conjugués, avec contraintes dans une ou deux dimensions.<sup>4, 7</sup> Les chances d'obtenir un film 2D avec des caractéristiques attendues dépendent de facteurs multiples.<sup>8-11</sup> Le choix inspiré d'un précurseur, placé sur la surface appropriée et à la bonne température d'activation, pourrait offrir un rendement satisfaisant de la longueur de conjugaison, et donc une bonne performance du transport, avec la fonctionnalité déterminée par l'interconnexion moléculaire et l'arrangement spatiale.<sup>12, 13</sup> Pourtant, au début de ce processus, à moins dans les situations où les molécules sont délibérément arrangées ou réactionnées sur la surface (par exemple, avec une technique de manipulation),<sup>14</sup> les molécules précurseurs interagissent faiblement et s'associent spontanément en agrégats d'équilibre stable (auto-assemblage), reliées par des liaisons non covalentes (réversibles, et avec une faible stabilité mécanique et une faible interaction électronique).<sup>15</sup>

Pour parvenir à une interaction électronique appropriée pour une application dans l'organoélectronique, le couplage électronique et la robustesse doivent être renforcées, tout en maintenant l'état structurel. Un réseau organique ordonné à longue distance qui répond à ces nécessités, peut être obtenu de manière adéquate et identifié par microscopie à effet tunnel

(STM) comme base de métal-coordination,<sup>16-20</sup> ou liaison covalente conjugué.<sup>7, 19, 21, 22</sup> La liaison forte (covalente) est associée à une forte densité de défauts dans la structure.

La STM a été une des diverses techniques assez sensibles non seulement pour avoir un précieux aperçu dans ces processus fondamentaux se déroulant sur la surface à l'échelle nanométrique, mais aussi pour leur manipulation. Les tendances récentes dans les processus 2D complexes, largement étudiés par la STM, comprennent:

(i) L'utilisation d'une réaction en étapes multiples:<sup>25</sup> dans un premier temps, à température inférieure, une réaction stabilise la forme du précurseur sur la surface (déshalogénéation ou la déshalogénéation d'un type particulier d'atome d'halogène),<sup>24</sup> suivie d'une seconde étape de la réaction, à température plus haute, pour parfaire la forme ou la stabilité chimique du produit final (déshydrogénation,<sup>25</sup> ou déshalogénéation d'un autre type d'atome d'halogène). La réaction Ullmann est bien connue et utilisée pour certaines molécules qui se terminent en halogène, en conjonction avec les surfaces métalliques en tant que plateforme pour la formation 2D de la structure conjuguée,<sup>23</sup> en raison de la facilité (proche de la température ambiante) dans l'activation des liaisons C–X (X = halogène).<sup>19, 24, 26-32</sup> Sur la plupart des surfaces métalliques étudiés, la réaction Ullmann donné également des produits indésirables qui bloquent des sites réactifs sur ces surfaces.

(ii) La déshydrogénation de liaison désignées, prise comme une seule réaction, avant un éventuel recollage C–C qui stabilisent le système nouvellement formée sur la surface.<sup>22, 25, 33-35</sup>

Les systèmes de molécules conjuguées ont attiré beaucoup d'attention au cours des dernières années en raison des propriétés de transport favorables de leurs films deux dimensionnelles.<sup>4, 36-39</sup> Toutefois, de légers changements dans la morphologie du précurseur peuvent induire un changement considérable, non seulement dans les propriétés électroniques des produits,<sup>40</sup> mais surtout, comment nous allons le voir dans le Chapitre 6, même dans les chances d'obtenir des produits de réaction ou des structures similaires.

L'exemple le plus fondamental d'un système  $\pi$  délocalisé 2D est le graphène. Le contrôle de la structure, de la composition et des propriétés électroniques du graphène, et l'extension de sa synthèse en deux dimensions, nécessitent des techniques pour tailler le précurseur à base de carbone (généralement à haute température), ou des précurseurs avec une

densité de carbone similaire à celle du graphène et avec des sites réactifs multiples (qui peuvent être activés à une température inférieure).

Les divers procédés pour la synthèse de graphène ou «nano rubans de graphène» impliquent la croissance épitaxiale sur les surfaces métalliques à des températures allant de 300 à 1000 °C, et le dépôt chimique en phase vapeur (CVD) (ce qui exige habituellement une température excessivement élevée), qui est probablement l'un des plus utilisés.<sup>41, 42</sup> Étant donné que la majorité des précurseurs organiques sont à base d'hydrogène,<sup>43-56 57-64</sup> et que la stabilité de la liaison C—H (438 kJ/mol, dans H—CH<sub>3</sub>; 472 kJ/mol à H—C<sub>6</sub>H<sub>5</sub>) est plus élevée que C—C (377 kJ/mole dans CH<sub>3</sub>—CH<sub>3</sub>),<sup>65</sup> la réaction de déshydrogénation est très défavorable par rapport au craquage de l'hydrocarbure (mais presque deux fois plus favorable que la rupture C=C). Pour contrer cet inconvénient, le couplage Ullmann mentionné ci-dessus est utilisé comme une alternative à la CVD, tout seul,<sup>23, 66-69</sup> ou précédant la déshydrogénation. Sur la surface activée thermiquement,<sup>23, 70</sup> le lien fort C—H est comme une coquille fermée (orbitale  $\sigma$ ) qui peut être activée par des oxydes (formant des liaisons O—H, avec des forces comparables à celle de la liaison C—H), ou par des catalyseurs métalliques. Un atome de métal seul ne peut pas faire abstraction d'un atome d'hydrogène parce que la liaison M—H est plus faible que la liaison C—H. Sur une surface métallique, cependant, à la fois C et H sont coordonnés avec le métal de la surface (réaction considérée comme l'insertion d'un atome de métal dans la liaison C—H), et la somme des énergies de coordination dépasse la résistance de la liaison C—H et rend le processus thermodynamique possible.<sup>71</sup> Les interactions van der Waals entre les molécules et la surface augmentent également le potentiel intramoléculaire, affaiblissant ainsi les liaisons C—H.

Ainsi, dans des conditions physiques suffisantes,<sup>72</sup> ou en présence d'un catalyseur approprié, où l'hydrogène est catalytiquement solvate,<sup>33, 73</sup> la déshydrogénation peut être effectuée à une température raisonnable et avec un minimum de rupture de la liaison C—C. Cette voie de réaction devient plus avantageuse que la cyclo-déshydrogénation thermique où la stabilité et la compatibilité des précurseurs avec les conditions de réaction est cruciale;<sup>74</sup> ou même que la phase de solution où les molécules de graphène/nano-rubans formées, avec une mauvaise solubilité dans les solvants organiques classiques, ont tendance à interagir fortement par « $\pi$ - $\pi$  empiler».<sup>75</sup>

En général, le remplacement des surfaces métalliques comme support pour la croissance de graphène reste un grand défi.<sup>75</sup> Cependant, parmi les catalyseurs métalliques qui conviennent pour les réactions ci-dessus, en plus de Cu(111), Ni(111) a été probablement l'une des surfaces la plus largement étudiée, en raison de la très proche correspondance de sa matrice avec le réseau de graphène,<sup>46, 76</sup> ainsi que de la forte hybridation entre les états  $\pi$  de graphène et les états  $d$  de nickel,<sup>77, 78</sup> qui peuvent conduire à des effets électroniques et magnétiques intéressants.<sup>43, 79, 80</sup>

Contrairement aux graphènes préparés à partir des stratégies «top-down» (l'exfoliation du graphite), l'approche chimique, à base des molécules aromatiques polycycliques («bottom-up»), offre une grande possibilité d'adapter la taille moléculaire, la forme, et la composition des graphènes. Ainsi, une simple comparaison entre tétracène et triphénylène prouve que ces caractéristiques peuvent considérablement modifier les propriétés telles que le potentiel d'ionisation, l'écart HOMO-LUMO, la stabilité thermique, etc., dans les molécules polycycliques isomères ou composées.<sup>81, 82</sup> La synthèse d'un grand système conjugué comme le graphène, à partir de petits systèmes conjugués tels que le semi-conducteur moléculaire pentacène est logique puisque celui-ci a une périodicité interne et la densité d'atomes de carbone identiques. Compte tenu de ces facteurs, l'activation du pentacène au graphène a été rapporté sur Cu(111) à  $\sim 800$  °C.<sup>83</sup> Largement étudié dans cette thèse sur Ni(111), la périodicité des anneaux conjugués de pentacène correspond à celle des atomes de nickel sur la facette (111), au long des directions  $\langle 1\bar{1}0 \rangle$ . En utilisant la réaction de déshydrogénation en une seule étape, les domaines de graphène ont été obtenus à partir du pentacène à une température d'activation beaucoup plus faible que celles précédemment rapporté par d'autres techniques.<sup>84</sup>

Du point de vue électronique, le caractère de graphène n'est ni semi-conducteur (la bande interdite disparaît au niveau des points de Dirac), ni purement métallique (la densité d'états du graphène pur, finit au niveau de Fermi et disparaît dans les points de Dirac).<sup>68, 85</sup> Toutefois, par le dopage, l'énergie de Fermi est éloigné du point de Dirac, et le graphène devient métallique. Cette particularité donne l'occasion à des approches viables (au moins théoriquement), pour régler les propriétés optoélectroniques du graphène sans modifier le squelette conjugué;<sup>22, 86, 87</sup> en incorporant des hétéroatomes dans le précurseur, tels que le soufre dans les tetrathieno-anthracènes (TTA présenté dans cette thèse). Comme l'atome d'azote riche en électrons est périodiquement incorporé dans des molécules aromatiques

polycycliques, et donc dans le graphène obtenu, cet hétéroatome d'azote influe sur la nature électronique, sans modifier la structure.<sup>86</sup> En plus, une combinaison convenable de donneurs d'électrons et d'atomes accepteurs d'électrons peut conduire à un polymère conjugué semi-conducteur, avec bande interdite.<sup>88</sup> En fonction de la conception du précurseur, le remplacement du carbone à des positions spécifiques dans le précurseur (par exemple 1,3,5-tris (4-bromophényl)-benzène (TBB)),<sup>30, 89</sup> par de l'azote, améliore la planéité des pores, dues à l'évitement de la répulsion de l'hydrogène.

Comme indiqué dans ce qui précède, la STM a démontré ses capacités d'imagerie, mais ce qui fait que la STM soit si spécial, c'est la possibilité d'étendre son utilisation au-delà de l'acquisition de l'image (l'espace réel), et d'induire des réactions chimiques avec l'échelle de résolution spatiale nanométrique.<sup>90-96</sup> Son caractère unique, de générer une haute densité de courant, ne peut pas être obtenu si localement avec des sources d'électrons classiques. L'application d'une densité de courant élevée sur une petite zone d'injection ( $\sim 100 \text{ A/cm}^2$ , au courants de tunnel  $\sim 1 \text{ nA}$ ), réduit au minimum le problème de chauffage en raison d'une dissipation thermique rapide des électrons (autrement, l'échantillon pourrait être probablement brûlé). Ce courant d'effet tunnel peut induire:

(i) l'excitation électronique (l'injection d'électrons se produit au niveau du LUMO,<sup>97</sup> et peut impliquer un changement de configuration de liaison),<sup>94, 95</sup> ou,

(ii) le chauffage de vibration, qui se produit par un processus multi-électrons et est généralement initiée à des tensions de tunnel relativement faibles, de l'ordre de centaines de mV.<sup>98-100</sup>

Ainsi, après l'irradiation avec des électrons, l'existence des charges externes en résonance moléculaire peut provoquer un réarrangement géométrique des constituants moléculaires par des allongements/contractions et la distorsion des orbitales moléculaires. Un cas particulier, étudié dans la thèse, est la liaison de la C—H induite par la pointe STM où, de la manière décrite ci-dessus, la liaison C—H est étendue sur la surface dans une position coordonnée favorable pour le clivage induit.

## Énoncé de la thèse et de la structure

Le travail présenté dans cette thèse est divisé en trois parties qui, bien que conceptuellement unifiées sous le même domaine de science de surface, couvrent différentes approches en quatre chapitres originaux.

Chapitre 4, 5, et 6 traitent des «événements de molécule seule» d'iso-molécules comprenant des groupes thiophéniques fusionnés à un noyau anthracène. Les propriétés intéressantes sont associées avec les deux parties thiophéniques (planéité, conjugaison, réduction de la bande interdite) ainsi que avec le noyau anthracène (conjugaison, grande mobilité de porteur).

Le Chapitre 7 traite des grandes assemblages des molécules. Il est en relation avec le Chapitre 4 par le type de la molécule, mais aussi avec le Chapitre 5 par la fonctionnalisation.

### **Chapitre 1**

- Présentation du groupe NFL, motivation du travail, l'histoire des processus les plus pertinents liés à l'obtention des ensembles moléculaires sur des surfaces, et à l'échelle nanométrique. Une liste des acronymes et des symboles communs est présentée à l'Annexe A.

### **Chapitre 2**

- Fournit au lecteur des informations générales sur la terminologie et les processus se produisant à l'échelle nanométrique, sur des surfaces métalliques et dans des conditions ultravide. Ici est aussi présente une longue liste d'exemples résumant diverses réactions, précurseurs et surfaces étudiées au fil des années.

### **Chapitre 3**

- Dédié à la technique expérimentale la plus couramment utilisée pour accomplir le travail exposé ici. Il présente la théorie de base de la STM, ainsi que la description de l'instrument lui-même. De l'espace est accordée aux différentes procédures pour le nettoyage des surfaces ou pour la sublimation de la matière organique.

### **Chapitre 4**

- Il s'agit du premier des quatre chapitres dans lesquels je présente les résultats originaux de mon travail. Il est consacré à l'étude et la description d'un nouveau mécanisme de

réaction (ouverture du cycle thiophénique, la désulfuration et la formation de nouvelles liaisons) qui se produit sur une surface réactive, lors de la transformation des précurseurs de tetrathieno-anthracène (TTA) en un nouveau produit — le pentacène, sur Ni(111).

### **Chapitre 5**

- Décrit le processus de structuration d'oligomères sur les surfaces, avec une résolution nanométrique: à partir d'un gaz de diffusion de monomères moléculaires confinées sur la surface, la pointe du STM peut être utilisée pour la déshydrogénation du précurseur et «écrire» des agrégats moléculaires 2D, définissant une zone bien-délimitée, sur une surface de cuivre.

### **Chapitre 6**

- Dans une étude comparative de la STM, les versions non bromée de TTA, dont les structures ont été décrites ailleurs,<sup>107</sup> ont été étudiés sur la surface monocristallin (111) de Ni, Pd, ou Cu. A titre de comparaison, une feuille de nickel poly cristallin a été ajoutée dans les études. Ces études complètent les observations précédentes (voir Chapitre 4),<sup>19, 20, 108</sup> et fournissent une distinction claire entre les deux phénomènes observées à l'échelle nanométrique - désulfuration et de déshydrogénation, qui sont des sources de création des liaisons libres.

### **Chapitre 7**

- Décrit l'auto-assemblage de molécules individuelles de pentacène sur la surface Ni(111) et les procédés qui suivent le recuit de la surface. Au-dessus de 220 °C, les pentacènes commencent à se déshydrogéner et s'unissent en formant de petits domaines de graphène.

### **Chapitre 8**

- Les conclusions générales.

## Chapitre 4.

### Transformation sans précédent de Tetrathienoanthracene en pentacène sur Ni(111), la STM comme un instrument pour la découverte de nouvelles réactions

La microscopie à effet tunnel (STM) a eu un impact révolutionnaire dans la chimie de surface, par exemple pour permettre l'observation,<sup>177, 178</sup> et l'induction,<sup>91</sup> de réactions chimiques en surface sur les molécules individuelles.<sup>14, 180, 291</sup> Plus précisément, la compréhension du comportement des molécules individuelles peut élucider les procédés essentielles à la synthèse contrôlée de matériaux, avec des applications dans les technologies nanométriques multiples.

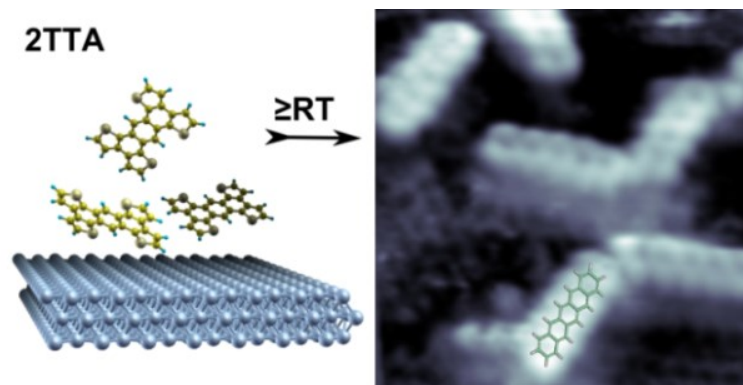


Figure 4.1. La représentation visuelle des processus de transformation de 2TTA en pentacène, sur Ni(111). (Figure reproduite à partir de Laurentiu E. Dinca *et al.*, avec la permission de l'American Chemical Society)

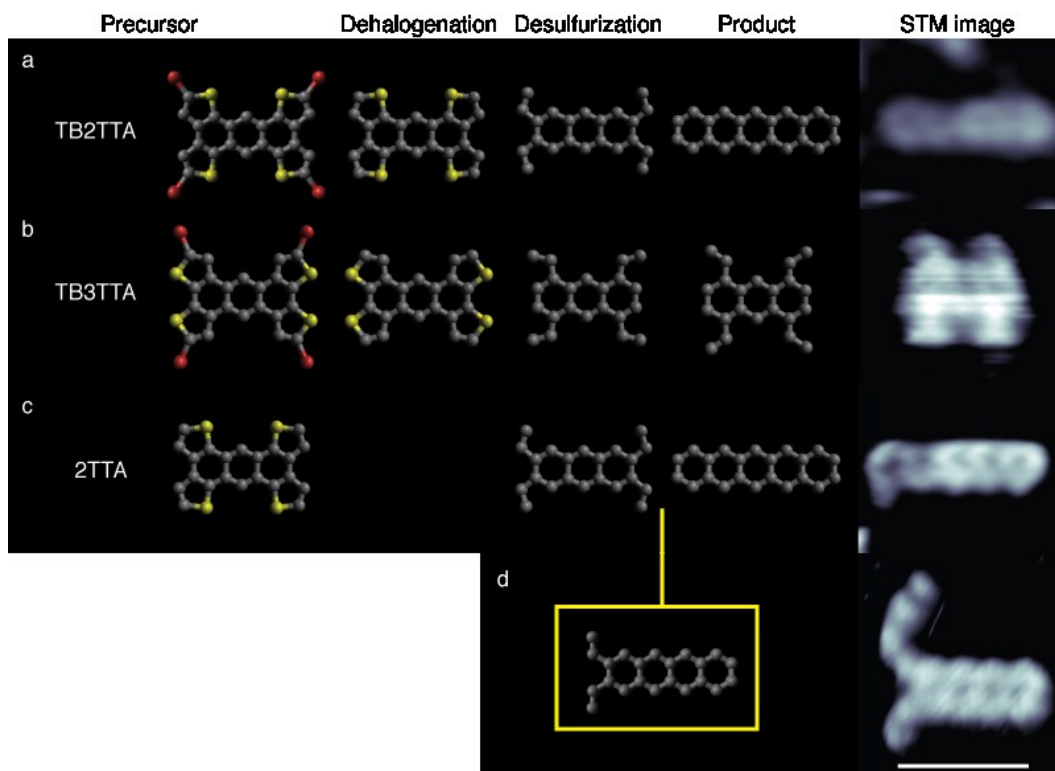


Figure 4.2. Modelés de réaction et images STM représentatifs, obtenues à partir de TTA: (a). schéma de réaction proposé pour la conversion de TB2TTA en Pc; (b) TB3TTA et (c) 2TTA sur Ni(111), (d) un produit partiel de 2TTA qui a été fréquemment observé. La barre d'échelle en bas à droite, d'1 nm, s'applique à toutes les images et les modèles. (Figure et légende reproduits à partir de Laurentiu E. Dinca *et al.*, avec la permission de l'American Chemical Society)<sup>108</sup>

On décrit ici, à l'aide de la STM, l'application d'abstraction de soufre d'un dérivé de thiophène, pour créer les conditions préalables à la création de nouvelles liaisons C—C intramoléculeaires, après le dépôt de 2,5,9,12-tetrabromoanthra[1,2-b:4,3-b':5,6-b":8,7-b''']-tetrathiophene (TB2TTA) sur la surface (111) de nickel, avec la formation de pentacène - le plus populaire des semi-conducteurs organiques (Figure 4.1).<sup>197</sup> Donc, par imagerie avec la STM, une nouvelle réaction impliquant l'abstraction du soufre des thiophènes a été identifiée, avec une cyclisation intramoléculeaire ultérieure, pour produire un produit aromatique polycyclique bien défini. Le produit a été vérifié de façon indépendante à l'aide du TOF-SIMS.

Ces résultats suggèrent les réactions suivantes entre TB2TTA et Ni(111) après dépôt sur la surface du Ni: la molécule subit la déhalogénéation, l'ouverture de cycle, la désulfuration, et l'extraction de deux hétéroatomes de Br et de S (qui forment par la suite des domaines reconstitués sur la surface). Les atomes de carbone sous-coordinnée, à chaque extrémité de la molécule, ont tendance à se lier l'un à l'autre et à terminer chaque extrémité du noyau de l'anthracène dans TB2TTA avec un nouvel anneau benzénique. Accompagnant ce processus, la molécule peut souffrir une déhydrogénation partielle.<sup>86, 87</sup> Ce régime de recollage, illustré à la Figure 4.2(a), décrit la formation du squelette de carbon d'une molécule de pentacène, qui se repose à plat ou presque à plat sur la surface de Ni(111).

Ces résultats illustrent la capacité de la STM pour révéler les détails de réactions moléculaires. La résolution spatiale très élevée de cette méthode de sonde locale offre des possibilités d'étudier les réactions chimiques au niveau d'une seule molécule, permettant l'identification non ambiguë des produits et des intermédiaires minoritaires. Cependant, parce que la STM donne des informations structurelles et du contraste chimique limités, elle doit être complétée par une technique d'analyse supplémentaire pour l'identification sans équivoque des produits, comme TOF-SIMS. Comme cette étude démontre, les molécules planaires polycycliques sont d'excellents candidats pour la découverte de nouvelles réactions par la STM.

## Chapitre 5.

# Impression moléculaire induite par la pointe avec une résolution nanométrique

La demande pour des appareils électroniques plus petits et plus rapides a alimenté la poursuite des méthodes de fabrication de matériel électronique à l'échelle et avec précision nanométrique.<sup>292</sup> Dans ce contexte, les dispositifs à base de matériaux organiques sont une alternative intéressante aux dispositifs semi-conducteurs traditionnels, car ils peuvent être construits à partir des blocs de construction large de seulement quelques atomes.<sup>7, 207, 293-295</sup> Il y a maintenant de nombreuses approches pour créer des structures moléculaires spatialement définies sur des surfaces, comme le «dip-pen» nano lithographié, qui offre une résolution submicronique,<sup>296-299</sup> sur la lithographie «hard-tip soft-spring», qui peut atteindre une résolution en dessous à 50 nm.<sup>216</sup>

Le microscopie à effet tunnel offre la possibilité d'imager, de manipuler,<sup>14</sup> et d'induire des réactions chimiques à l'échelle et résolution spatiale nanométrique.<sup>90-92, 94-96, 222</sup> Dans cette thèse, j'ai créé un nouveau concept pour la polymérisation avec le STM: à partir d'un gaz de monomères moléculaires confiné et diffusé sur une surface, je démontre que la pointe du STM peut être utilisé pour «écrire» des agrégats moléculaires et polymères vitreux définies 2D spatialement, sur une surface de cuivre. Contrairement aux réactions de polymérisation surfacique rapportée précédemment, les réactions de polymérisation induites par la pointe et rapportées ici, ne sont pas auto-propageants, et la zone imprimée avec des molécules peut être définie par la région balayée, permettant un contrôle spatial précis de la région polymérisée.

Le monomère que j'ai utilisé est le tetrathieno[2',3':5,6:3',2':3,4:3',2':7,8]anthra[1,2-b]thiophène (2TTA - illustré à la Figure 5.1(a)).<sup>107</sup> Les polythiophènes sont largement utilisés comme semi-conducteurs organiques grâce à leurs propriétés électro-optiques et magnétiques, comme électrodes de condensateur, matériaux antistatiques, systèmes de communication photo à grande vitesse, capteurs de champ magnétique dans les systèmes de mémoire opto-magnétique ainsi que des transistors organiques et des cellules solaires.<sup>191, 212</sup>

Grace à sa grande mobilité sur Cu(111) à température ambiante, il n'est pas possible d'imager la 2TTA à une couverture sous-monocouche. Cependant, après le balayage de la surface à une tension élevée (3-5 V), l'imagerie de la surface révèle une région «imprimé» avec molécules (polymères) (Figure 5.1(b)). La géométrie des polymères obtenues indique que la polymérisation suit la déshydrogénation, aux mêmes positions où les atomes d'halogène se trouvaient dans les expériences antérieures qui impliquaient TB2TTA (désigné par "H" sur le précurseur de la Figure 5.1(a)).

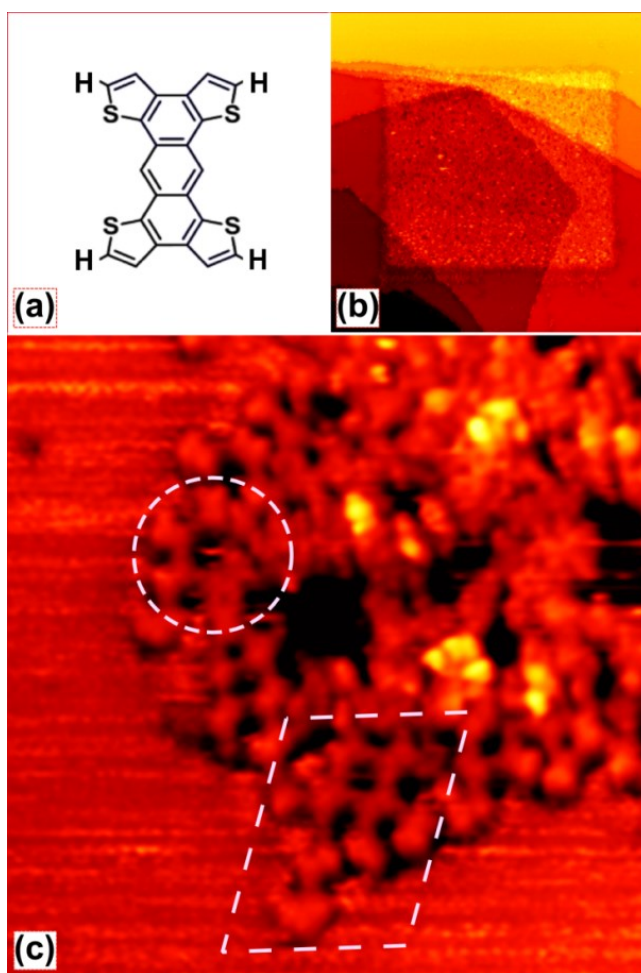


Figure 5.1. Représentation schématique de la molécule tetrathieno [2',3':5,6:3',2':3,4:3',2':7,8]anthra[1,2-b]thiophène (2TTA). (a) Image STM d'une zone rectangulaire de 2TTA "imprimé" sur la surface Cu (111), (b) Paramètres de l'image: 150×150

nm<sup>2</sup> avec une région imprimée de 100×90 nm<sup>2</sup>. (L. E. Dinca *et al.*, résultats reproduits avec la permission de la The Royal Society of Chemistry).<sup>213</sup>

Dans la déshydrogénation et l'oligomérisation induite par la pointe STM, on observe deux facteurs clés qui peuvent travailler ensemble pour favoriser les liaisons intermoléculaires au lieu des liaisons coordonnées sur la surface du Cu: (1) la molécule TTA est grande et donc fortement adsorbée parallèlement à la surface, et (2) à la température ambiante, on peut supposer la présence d'adatoms de Cu qui diffusent librement sur la surface,<sup>218</sup> ce qui facilite la coordination des liaisons libres avec les adatoms du Cu plutôt qu'avec les atomes du substrat. A la température ambiante l'hydrogène libéré n'est pas retenu sur Cu(111),<sup>220</sup> évitant ainsi l'un des problèmes rencontrés dans le couplage d'Ullmann de monomères halogénés en surface, où une accumulation des sous-produits de réaction occupe des sites actifs sur le substrat.<sup>221</sup>

Un nombre limité de processus électroniques, à haute densité de courant, peut induire la rupture des liaisons. Les principaux mécanismes sont le chauffage de vibration et l'excitation électronique.<sup>99</sup> Le chauffage de vibration se fait par un processus multi-électrons et débute généralement à des tensions de tunnel relativement faibles (de l'ordre de centaines de mV).<sup>98, 99</sup> Dans le cas d'excitation électronique, l'injection d'électrons se fait par le biais de l'orbitale moléculaire basse vacante (LUMO).<sup>95, 97</sup> Par la suite, on peut interpréter la déshydrogénation observée comme étant due à l'excitation électronique après l'injection d'électrons dans la LUMO de 2TTA.

Ce travail démontre que les modèles moléculaires comprenant des polymères 2D peuvent être «dessinés» sur Cu (111) avec une précision nanométrique en utilisant une pointe de STM. La réaction induite par la pointe se manifeste par la formation de polymères vitreux et agrégats moléculaires dans les régions balayées à 3-5 V.

Des considérations géométriques montrent que la formation de liaisons libres s'est produite après la déshydrogénation induite de la pointe. Des expériences réalisées d'une manière identique sur HOPG ou Ag(111) n'ont pas produit de polymère, ce qui suggère que la surface joue un rôle important dans la réaction, comme c'est bien connu dans d'autres processus.<sup>179</sup>

## Chapitre 6.

### Réactions de tetrathienoanthracenes catalysées sur des surfaces des métaux de transition, avec ouverture des anneaux thiophénique

La manipulation des réactions chimiques à l'échelle nanométrique, dans un environnement confiné sur des surfaces, nécessite une compréhension extensive des processus chimiques au niveau sous moléculaire.<sup>4</sup> Toutefois, également importantes sont la conception du précurseur organique, ainsi que la surface, pour assurer une réponse chimique appropriée de la surface d'appui en direction du précurseur.

Dans ce cadre-ci, j'ai étudié quelques aspects caractéristiques de l'interaction de deux molécules particulières à base de thiophène, le anthra[1,2-b:4,3-b':5,6-b":8,7-b''']-tetrathiophene (2TTA et 3TTA), avec des métaux de transition.<sup>107, 108</sup> La présentation d'oligomères ou polymères à base de thiophène, et leurs capacités à former des réseaux avec une morphologie de liaison spécifique bénéficient d'une attention considérable, grâce à la possibilité de créer ou de régler la bande interdite dans le graphène comme une système conjugué.<sup>40</sup> Utilisant des iso molécules, de légers changements dans la morphologie des précurseurs peuvent induire un changement important de comportement sur la surface. Contrairement à 2TTA, où l'ouverture du cycle thiophénique et la désulfuration permettent un recollage intra- moléculaire pour former le pentacène,<sup>108</sup> dans 3TTA, due aux considérations stériques, les produits de la même réaction sont laissés dans un état très réactif, avec quatre branches disposées symétriquement, chacune terminée par une liaison non satisfaite. La symétrie «two-fold» de chaque bloc de construction, et la périodicité de cœur proportionnelle avec la surface (111) de nickel, assurent la formation d'une structure rectangulaire.

Pour la molécule 2TTA, les réactions discutées dans cette thèse, et dans une publication,<sup>108</sup> donnent des produits similaires sur des surfaces différentes. La désulfuration du thiophène est la première étape clé dans le processus qui se termine avec la formation d'un

pentacène partiellement saturé avec hydrogènes. Le degré à lequel la réaction se produit est corrélé directement avec la réactivité de la surface de nickel, de palladium et de cuivre, et avec l'énergie nécessaire à fournir au système de l'extérieur. Tandis que sur la surface (111) de nickel et poly-cristalline, la réaction se déroule à proximité de la température ambiante, les surfaces (111) de palladium et de cuivre nécessitent une température de 150 °C (Figure 6.1(c)), et respectivement 250 °C pour une transformation complète du 2TTA à pentacène.

En parallèle avec la désulfuration, si la température de réaction s'élève au-dessus d'une valeur critique, la déshydrogénation se produit à des positions spécifiques dans le précurseur ou dans les produits. Habituellement, la déshydrogénation a lieu après de désulfuration, et on a observé qu'elle se produit seulement pour la pentacène, produit de la surface de nickel et de palladium. Pour le cuivre seulement, la température supérieure du début de la désulfuration renverse cet ordre et montre la sélectivité pour la déshydrogénation, donnant libre cours à la déshydrogénation pour se produire concomitant avec le clivage et la désulfuration des anneaux thiophéniques dans le précurseur, mis en évidence par la phase organique à base de métal, se produisant à 150 °C (Figure 6.2).

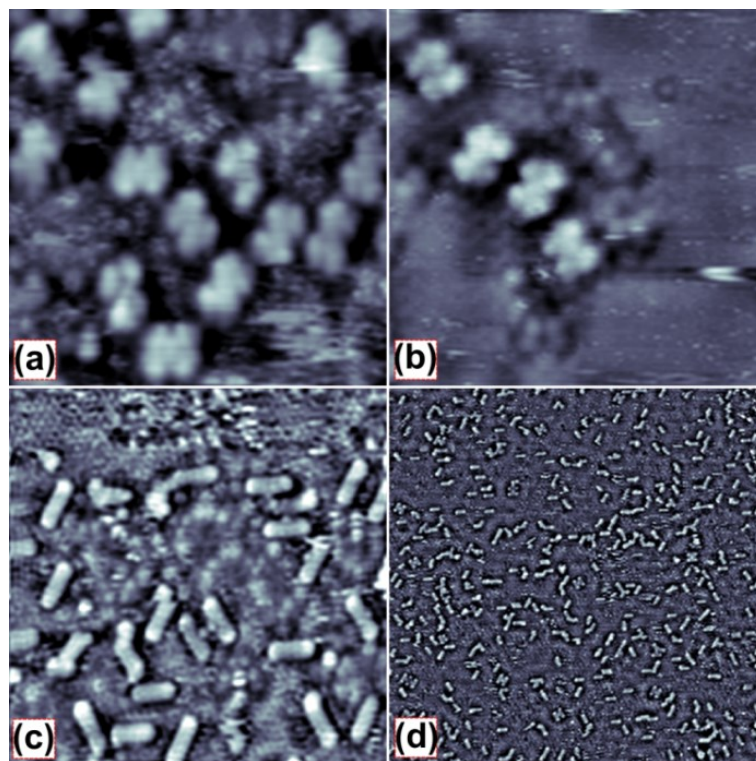


Figure 6.1. Images STM, a la température ambiante, de 2TTA sur Pd(111). (a)  $7 \times 7 \text{ nm}^2$ , telle que déposé, (b)  $7 \times 7 \text{ nm}^2$  après un recuit à  $100 \text{ }^\circ\text{C}$ , (c)  $10 \times 10 \text{ nm}^2$ , recuit à  $150 \text{ }^\circ\text{C}$ , (d)  $50 \times 50 \text{ nm}^2$ , recuit à  $200 \text{ }^\circ\text{C}$ .

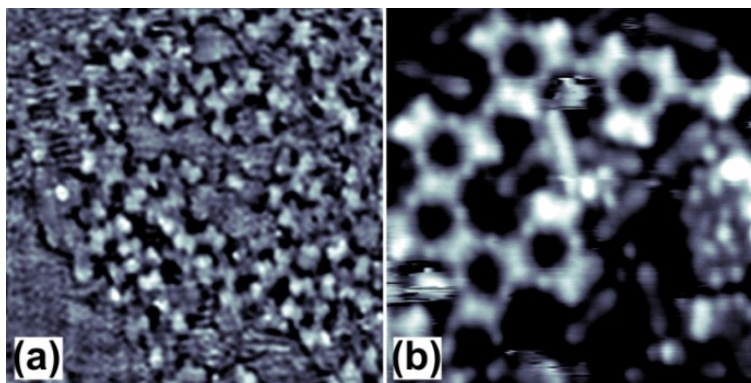


Figure 6.2. Images STM de 2TTA sur Cu(111), après un recuit à  $150 \text{ }^\circ\text{C}$  en: (a)  $7 \times 7 \text{ nm}^2$ , (b)  $8 \times 8 \text{ nm}^2$ ; à température ambiante (a), et à  $-160 \text{ }^\circ\text{C}$  (b).

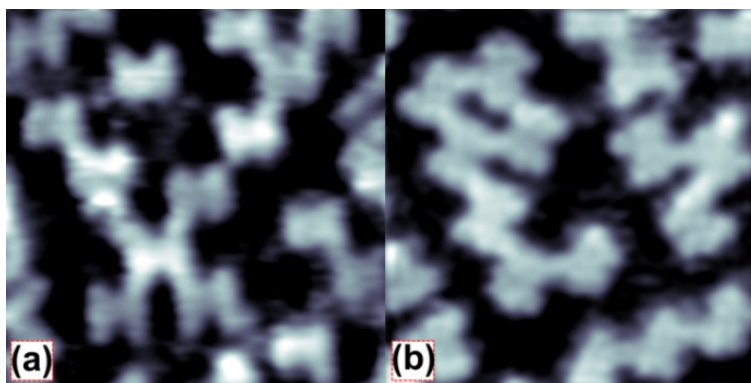


Figure 6.3.  $5 \times 5 \text{ nm}^2$  images STM à température ambiante de 3TTA sur Ni(111).

Au contraire, avec un temps de "passivation" plus long, dû à des considérations géométriques internes, les produits du 3TTA ont une évolution plus complexe avant d'atteindre l'équilibre de charge à la surface (Figure 6.3). Comparant l'évolution des radicaux organiques sur des surfaces de nickel et de palladium, des différences considérables dans la cinétique du même type de sous-produit ont été constatées. La caractéristique commune pour les deux surfaces est que le soufre est un inhibiteur de diffusion pour ces radicaux. Sur le

Ni(111) le soufre a subi la migration, mais la faible mobilité de la matière organique se comporte comme un obstacle, et ces deux processus s'inhibent réciproquement. Au contraire, sur Pd(111) le soufre préfère commencer la reconstruction directement à la position de clivage, sur la surface.

On peut conclure que les deux réactions sur la surface, au niveau intramoléculaire, ont été étudiées ici de façon systématique, comme possibilité de concevoir des architectures polymériques. Avec une bonne conception du précurseur organique, la chimie ancienne – l'ouverture de cycle thiophénique et la désulfuration sur Ni(111), et la déshydrogénation sur les surfaces Cu(111) - pourrait être utilisée comme nouvelle passerelle pour concevoir de nombreux et complexes types de structures macromoléculaires. Selon le contexte utilisé, les deux réactions peuvent assurer quelques avantages clé inhérents. La réaction de désulfuration, sur la surface de Ni délivre facilement des radicaux organiques et des liaisons libres, tandis que la déshydrogénation sur le cuivre, qui se produit à une température supérieure à celle pour la désulfuration, désorbe facilement des sous-produits du surface. Dans le premier cas, cependant, les propriétés utiles du thiophène sont perdues (par rapport à la modification HOMO - LUMO) et le catalyseur est empoisonné.

## Chapitre 7.

### Pentacène sur Ni(111): assemblage moléculaire à température ambiante et conversion en graphène activé par la température

Les molécules aromatiques polycycliques, comme le pentacène, sont largement étudiés pour des applications industrielles dans l'électronique organique grâce à leur possibilité d'être produites dans des cristaux 3-dimensionnelles,<sup>300</sup> et à leur haute mobilité de porteurs de charge.<sup>12, 37, 301, 302</sup> La conversion de molécules aromatiques polycycliques en graphène a attiré beaucoup d'attention récemment,<sup>25, 83</sup> parce qu'elle peut fournir une voie facile pour la synthèse de l'un des matériaux les plus remarquables de ces dernières années.<sup>99</sup> Pour obtenir des couplages C—C covalentes entre les molécules de pentacène, il est nécessaire de produire d'abord la rupture de la liaison C—H avec recollage subséquent des atomes de carbone sous-coordinnés.<sup>83</sup> Sur la surface (111) du Ni en particulier, la croissance du graphène est d'un grand intérêt, due à la très proche correspondance de maille entre les deux matériaux, ainsi qu'à la très forte hybridation entre les états  $\pi$  du graphène et états  $d$  du nickel.<sup>77, 78</sup> Cela conduit à des effets électroniques et magnétiques intéressantes.<sup>46, 103-105</sup>

Poussé par des considérations similaires, j'ai étudié l'absorption du pentacène sur Ni(111) en utilisant la STM et les calculs DFT. L'adsorption du pentacène sur une couche de graphène par rapport à des domaines de Ni-carbure, a été aussi bien explorée ainsi que la conversion thermoactive du pentacène en graphène. Après le dépôt sur Ni(111) à température ambiante, comme le montre la Figure 7.1, le pentacène s'organise dans une structure similaire à la phase de «carrelage aléatoire» rapporté pour Cu(111).<sup>237</sup>

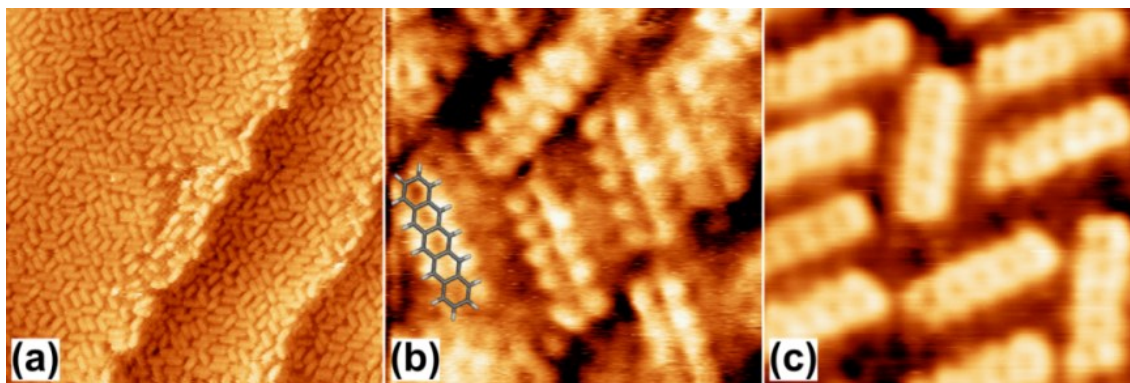


Figure 7.1. Image STM de molécules de pentacène adsorbées sur Ni(111), à la température ambiante. (a)  $30 \times 30 \text{ nm}^2$ , 1,36 nA, 1,83 mV; (b)  $3 \times 3 \text{ nm}^2$ , 1,49 nA, 1,83 mV, et  $3 \times 3 \text{ nm}^2$ , 0,53 nA, 31.13 mV dans (c).

Pour assigner un modèle de la «phase de carrelage aléatoire», nous avons étudié six sites d'adsorption, pour le pentacène, en utilisant la DFT. J'ai considéré une gamme de géométries avec la pentacène alignés au long des directions de symétrie du substrat. Un seul pentacène isolée trouve son minimum d'énergie dans une position “*hollow-fcc*” or “*bridge-top*” (variation de l'énergie plus petite que 0,06 eV), avec ses grands axes alignés le long du  $\langle 1\bar{1}0 \rangle$ .

Le chauffage convertit la monocouche uniforme de molécules individuelles dans des domaines ordonnés avec une périodicité interne compatible avec le graphène. Le processus débute à 220 °C,<sup>236</sup> et la dimension et la qualité de domaines s'améliorent par le chauffage à 250 et 350 °C, comme le montre la Figure 7.2(a) et (c). J'attribue la formation de graphène à la déshydrogénation du précurseur de pentacène, à la diffusion des molécules dans leur forme native et/ou activés, et à l'ultérieur recollage intermoléculaire.

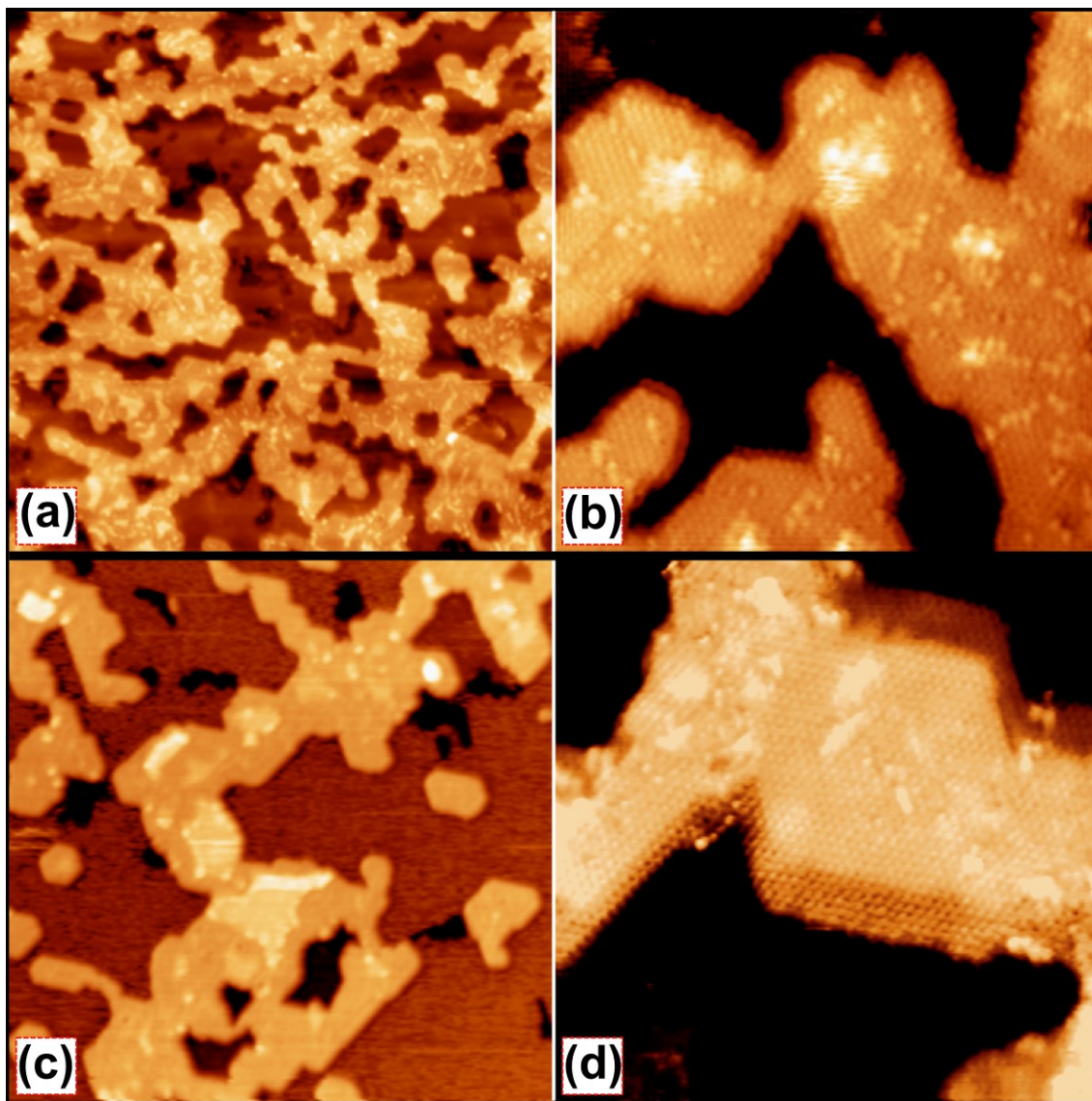


Figure 7.2. Images STM de domaines graphitiques sur Ni(111); chauffé pour 30 min. à 250 °C dans (a) et (b), et pendant 20 min. à 350 °C dans (c) et (d). Paramètres de l'image: 50×50 nm<sup>2</sup>, en (a) et (c); 10×10 nm<sup>2</sup>, en (b) et (d).

La spectroscopie Raman est une technique largement applicable, bien que non universelle,<sup>253</sup> pour obtenir des informations sur le nombre, et la déformation des défauts dans des couches de graphène. Pour le cas particulier du monocouche de graphène sur Ni(111), Dahal et Batzill ont démontré que le signal Raman est supprimé en raison d'une interaction graphène-nickel presque chimique. L'hybridation des électrons *d* de nickel avec des électrons

$\pi$  de graphène induit un décalage vers le bas dans les bandes  $\pi$  et ouvre une bande interdite dans la structure électronique du graphène, annihilant ainsi le couplage électron-phonon essentiel pour obtenir un effet de vibration détectable par la spectroscopie Raman.<sup>253</sup> Conformément à cela, dans notre graphène/Ni(111) on a pas observé de réponse Raman.<sup>272</sup>

Basé uniquement sur les produits finaux, il est difficile de déterminer les régions les plus réactifs sur la surface de Ni(111) pour la déshydrogénation ou la scission du C—C. Des calculs DFT et des rapports expérimentaux suggèrent que les bords des marches sont plus réactifs à dissocier les petites molécules diatomiques telles que le CO, NO, O<sub>2</sub> et N<sub>2</sub>.<sup>269</sup> Les expériences à température ambiante, qui impliquent l'éthylène sur le Ni(111), montrent une réactivité plus élevée pour le bris de la liaison carbone-carbone sur les marches, comparativement au carbone-hydrogène,<sup>154</sup> avec les facettes plats (111) jouant un rôle important dans la déshydrogénation.

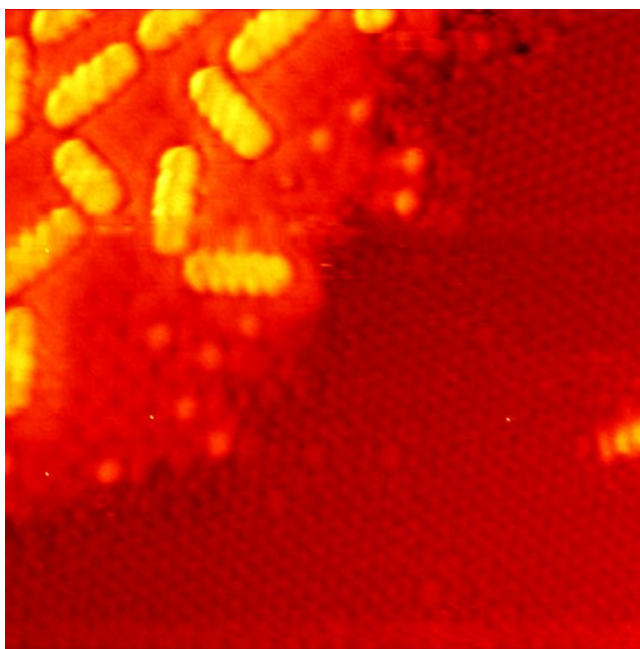


Figure 7.3.  $8 \times 8 \text{ nm}^2$  image STM de pentacène sur une surface (111) du Ni avec des domaines de coexistence de Ni<sub>2</sub>C (supérieur gauche) et graphène (en bas à droite).

J'ai pu titrer la pentacène, en comparant ses propriétés d'adsorption sur le graphène (préparé à 700 °C) et le carbure de nickel (Ni<sub>2</sub>C) (Figure 7.3) en déposant une petite quantité

de pentacène sur des surfaces, où les terrasses de graphène coexistent avec de petits domaines de carbure de nickel à la bordure des marches.<sup>55</sup>

Les molécules ont été imagées préférentiellement sur les domaines de carbure de nickel, ce qui implique à la température ambiante une adsorption beaucoup plus forte sur le carbure de nickel que sur le graphène. Cela est raisonnable si l'on considère que sur le graphène le paysage d'adsorption est essentiellement uniforme, et offre des enthalpies d'adsorption inférieures à ceux des domaines du carbure de nickel.

# Chapitre 8.

## Résumé

L'objectif de cette thèse est d'aborder et de comprendre, au niveau atomistique, les différentes étapes et aspects de la chimie de surface, qui arrivent dans des molécules isolées ou dans des ensembles des molécules liées à la surface. Plus généralement, l'impact de quelques surfaces métalliques sur les molécules aromatiques, produites dans des laboratoires ou industriellement, a été étudié par la STM en UHV; différents exemples sont ensuite présentés et expliqués.

Comme traitée dans le Chapitre 4 et Chapitre 6, une nouvelle réaction chimique en-surface impliquant l'abstraction de soufre de thiophène (dans une autre grande molécule) a été identifiée par la STM, après une cyclisation intramoléculaire et la production d'un produit aromatique polycyclique bien défini. Malgré que la dégradation du thiophène soit un phénomène connu,<sup>279</sup> son utilisation dans la synthèse organique a été limitée à l'hydrodésulfuration ( $C-S \rightarrow C-H$ ). Dans le cas de la réaction observée dans ce travail, l'adsorption de la molécule sur la surface (111) de Ni, Cu et Pd, ne coupe pas seulement les liaisons C-S (à des températures spécifiques), mais aussi stabilise les réactifs intermédiaires, permettant la recombinaison intramoléculaire pour former un nouveau noyau benzénique. Compte tenu la versatilité de la chimie du thiophène, cette réaction pourrait être utile pour la synthèse de nouvelles molécules poly-aromatiques. Il y a cependant un inconvénient, puisque les propriétés utiles du thiophène sont perdues (par rapport à la distance d'HOMO-LUMO). En plus, les produits de réaction sont fortement affectés par la réactivité de la surface, et par conséquent, la dynamique des sous-produits a été considérée. Comme l'hydrogène se désorbe facilement à des températures à laquelle la réaction de déshydrogénation se produit (décrites dans les Chapitre 6), le soufre continue à diffuser et à reconstruire, en résidant sur la plupart des surfaces étudiées.

Le Chapitre 5 traite une nouvelle façon de produire des modèles 2D (motifs organiques) d'une manière contrôlée, liées de façon covalente, avec une résolution à l'échelle nanométrique. J'ai démontré que la pointe du STM peut être utilisé pour «écrire», par

balayage en continu, à une tension de polarisation beaucoup plus grande que celle utilisée dans l'imagerie régulière, et des motifs moléculaires précisément définis ont été obtenus sur Cu(111). Ces motifs moléculaires ont été établis à partir d'un gaz de tetrathieno-anthracène (TTA) des molécules avec une diffusivité limitée sur la surface. Des régions contenant des motifs polymériques vitreux ont été formées par déshydrogénation des molécules TTA, induite par la pointe, qualitativement identiques à des structures résultant de la déshalogénéation d'Ullmann d'une molécule analogue halogénée (présentée au Chapitre 6). Des expériences réalisées d'une manière identique sur HOPG ou Ag(111) n'ont pas réussi à produire des polymères, ce qui suggère que la surface joue un rôle important dans le processus global.

Le Chapitre 7 examine l'adsorption du pentacène sur la surface Ni(111), et sa conversion thermiquement induite en graphène. À température ambiante, il se rassemble seulement une couche dense comprenant des molécules qui se trouvent à plat sur la surface, sans mouvement de diffusion dans la couche, et orientées de façon aléatoire le long des trois directions de la surface. Même si une légère polarisation est remarquée dans l'alignement parallèle aux marches, cet ensemble est similaire à la phase de carrelage-aléatoire imagé à couverture monocouche complète sur la surface (111) de Cu. À partir des calculs DFT, il a été déduit que la structure implique probablement une adsorption à une position "hollow-fcc" ou "bridge-top". Après un chauffage au-dessus de 220 °C (<350 °C), les molécules individuelles de pentacène sont remplacées par des domaines poreux de graphène, larges de plusieurs dizaines de nanomètres, dont la nature a été vérifiée par STM. En comparant avec le carbure de nickel, comme surface de support, la réactivité du graphène montre un caractère passif, similaire à HOPG.

# Bibliography

- (1) Ertl, G. Primary Steps in Catalytic Synthesis of Ammonia. *J. Vac. Sci. Technol. A* **1983**, *1*, 1247-1253.
- (2) Ertl, G.; Freund, H. J. Catalysis and Surface Science. *Phys. Today* **1999**, *52*, 32-38.
- (3) Lin, N.; Stepanow, S.; Ruben, M.; Barth, J. V., Surface-Confined Supramolecular Coordination Chemistry. In *Templates in Chemistry Iii*, Broekmann, P.; Dotz, K. H.; Schalley, C. A., Eds. Springer-Verlag Berlin: Berlin, 2009; Vol. 287, pp 1-44.
- (4) Palma, C.-A.; Samori, P. Blueprinting Macromolecular Electronics. *Nat. Chem.* **2011**, *3*, 431-436.
- (5) Ertl, G. Elementary Steps in Heterogeneous Catalysis. *Angew. Chem., Int. Ed. Engl.* **1990**, *29*, 1219-1227.
- (6) Besenbacher, F.; Lauritsen, J. V.; Linderoth, T. R.; Laegsgaard, E.; Vang, R. T.; Wendt, S. Atomic-Scale Surface Science Phenomena Studied by Scanning Tunneling Microscopy. *Surf. Sci.* **2009**, *603*, 1315-1327.
- (7) Perepichka, D. F.; Rosei, F. Extending Polymer Conjugation into the Second Dimension. *Science* **2009**, *323*, 216-217.
- (8) Lackinger, M.; Heckl, W. M. A STM Perspective on Covalent Intermolecular Coupling Reactions on Surfaces. *J. Phys. D: Appl. Phys.* **2011**, *44*.
- (9) Bartels, L. Tailoring Molecular Layers at Metal Surfaces. *Nat. Chem.* **2010**, *2*, 87-95.
- (10) Yamamoto, T. Cross-Coupling Reactions for Preparation of  $\Pi$ -Conjugated Polymers. *J. Organomet. Chem.* **2002**, *653*, 195-199.
- (11) Xu, L. R.; Yang, L.; Lei, S. B. Self-Assembly of Conjugated Oligomers and Polymers at the Interface: Structure and Properties. *Nanoscale* **2012**, *4*, 4399-4415.
- (12) Coropceanu, V.; Cornil, J.; da Silva, D. A.; Olivier, Y.; Silbey, R.; Bredas, J. L. Charge Transport in Organic Semiconductors. *Chem. Rev.* **2007**, *107*, 926-952.
- (13) Curtis, M. D.; Cao, J.; Kampf, J. W. Solid-State Packing of Conjugated Oligomers: From  $\Pi$ -Stacks to the Herringbone Structure. *J. Am. Chem. Soc.* **2004**, *126*, 4318-4328.

- (14) Otero, R.; Rosei, F.; Besenbacher, F. Scanning Tunneling Microscopy Manipulation of Complex Organic Molecules on Solid Surfaces. *Annu. Rev. Phys. Chem.* **2006**, *57*, 497-525.
- (15) Whitesides, G. M.; Mathias, J. P.; Seto, C. T. Molecular Self-Assembly and Nanochemistry: A Chemical Strategy for the Synthesis of Nanostructures. *Science* **1991**, *254*, 1312-1319.
- (16) Walch, H.; Dienstmaier, J.; Eder, G.; Gutzler, R.; Schloegl, S.; Sirtl, T.; Das, K.; Schmittel, M.; Lackinger, M. Extended Two-Dimensional Metal-Organic Frameworks Based on Thiolate-Copper Coordination Bonds. *J. Am. Chem. Soc.* **2011**, *133*, 7909-7915.
- (17) Stepanow, S.; Lin, N.; Barth, J. V. Modular Assembly of Low-Dimensional Coordination Architectures on Metal Surfaces. *J. Phys.-Condes. Matter* **2008**, *20*, 184002-184016.
- (18) Barth, J. V., Molecular Architectonic on Metal Surfaces. In *Annu. Rev. Phys. Chem.*, Annual Reviews: Palo Alto, 2007; Vol. 58, pp 375-407.
- (19) Cardenas, L.; Gutzler, R.; Lipton-Duffin, J.; Fu, C.; Brusso, J. L.; Dinca, L. E.; Vondracek, M.; Fagot-Revurat, Y.; Malterre, D.; Rosei, F., *et al.* Synthesis and Electronic Structure of a Two Dimensional  $\pi$ -Conjugated Polythiophene. *Chem. Sci.* **2013**, *4*, 3263-3268.
- (20) Gutzler, R.; Cardenas, L.; Lipton-Duffin, J.; El Garah, M.; Dinca, L. E.; Szakacs, C. E.; Fu, C.; Gallagher, M.; Vondracek, M.; Rybachuk, M., *et al.* Ullmann-Type Coupling of Brominated Tetrathienoanthracene on Copper and Silver. *Nanoscale* **2014**, *6*, 2660-2668.
- (21) Gourdon, A. On-Surface Covalent Coupling in Ultrahigh Vacuum. *Angew. Chem., Int. Ed.* **2008**, *47*, 6950-6953.
- (22) In't Veld, M.; Iavicoli, P.; Haq, S.; Amabilino, D. B.; Raval, R. Unique Intermolecular Reaction of Simple Porphyrins at a Metal Surface Gives Covalent Nanostructures. *Chem. Commun.* **2008**, 1536-1538.
- (23) Ullmann, F.; Bielecki, J. Synthesis in the Biphenyl Series. (I. Announcement). *Berichte Der Deutschen Chemischen Gesellschaft* **1901**, *34*, 2174-2185.
- (24) Lafferentz, L.; Eberhardt, V.; Dri, C.; Africh, C.; Comelli, G.; Esch, F.; Hecht, S.; Grill, L. Controlling on-Surface Polymerization by Hierarchical and Substrate-Directed Growth. *Nat. Chem.* **2012**, *4*, 215-220.

- (25) Cai, J.; Ruffieux, P.; Jaafar, R.; Bieri, M.; Braun, T.; Blankenburg, S.; Muoth, M.; Seitsonen, A. P.; Saleh, M.; Feng, X., *et al.* Atomically Precise Bottom-up Fabrication of Graphene Nanoribbons. *Nature* **2010**, *466*, 470-473.
- (26) Blake, M. M.; Nanayakkara, S. U.; Claridge, S. A.; Fernandez-Torres, L. C.; Sykes, E. C. H.; Weiss, P. S. Identifying Reactive Intermediates in the Ullmann Coupling Reaction by Scanning Tunneling Microscopy and Spectroscopy. *J. Phys. Chem. A* **2009**, *113*, 13167-13172.
- (27) Xi, M.; Bent, B. E. Mechanisms of the Ullmann Coupling Reaction in Adsorbed Monolayers. *J. Am. Chem. Soc.* **1993**, *115*, 7426-7433.
- (28) Hassan, J.; Sevignon, M.; Gozzi, C.; Schulz, E.; Lemaire, M. Aryl-Aryl Bond Formation One Century after the Discovery of the Ullmann Reaction. *Chem. Rev.* **2002**, *102*, 1359-1469.
- (29) Gutzler, R.; Walch, H.; Eder, G.; Kloft, S.; Heckl, W. M.; Lackinger, M. Surface Mediated Synthesis of 2d Covalent Organic Frameworks: 1,3,5-Tris(4-Bromophenyl)Benzene on Graphite(001), Cu(111), and Ag(110). *Chem. Commun.* **2009**, 4456-4458.
- (30) Walch, H.; Gutzler, R.; Sirtl, T.; Eder, G.; Lackinger, M. Material- and Orientation-Dependent Reactivity for Heterogeneously Catalyzed Carbon-Bromine Bond Homolysis. *J. Phys. Chem. C* **2010**, *114*, 12604-12609.
- (31) Lipton-Duffin, J. A.; Ivasenko, O.; Perepichka, D. F.; Rosei, F. Synthesis of Polyphenylene Molecular Wires by Surface-Confined Polymerization. *Small* **2009**, *5*, 592-597.
- (32) Bieri, M.; Nguyen, M.-T.; Groening, O.; Cai, J.; Treier, M.; Ait-Mansour, K.; Ruffieux, P.; Pignedoli, C. A.; Passerone, D.; Kastler, M., *et al.* Two-Dimensional Polymer Formation on Surfaces: Insight into the Roles of Precursor Mobility and Reactivity. *J. Am. Chem. Soc.* **2010**, *132*, 16669-16676.
- (33) Treier, M.; Pignedoli, C. A.; Laino, T.; Rieger, R.; Müllen, K.; Passerone, D.; Fasel, R. Surface-Assisted Cyclodehydrogenation Provides a Synthetic Route Towards Easily Processable and Chemically Tailored Nanographenes. *Nat. Chem.* **2011**, *3*, 61-67.
- (34) Zhong, D. Y.; Franke, J. H.; Podiyanchari, S. K.; Blomker, T.; Zhang, H. M.; Kehr, G.; Erker, G.; Fuchs, H.; Chi, L. F. Linear Alkane Polymerization on a Gold Surface. *Science* **2011**, *334*, 213-216.
- (35) Wiengarten, A.; Seufert, K.; Auwärter, W.; Eciya, D.; Diller, K.; Allegretti, F.; Bischoff, F.; Fischer, S.; Duncan, D. A.; Papageorgiou, A. C., *et al.* Surface-Assisted Dehydrogenative Homocoupling of Porphine Molecules. *J. Am. Chem. Soc.* **2014**, *136*, 9346-9354.

- (36) Song, B. J.; Hong, K.; Kim, W.-K.; Kim, K.; Kim, S.; Lee, J.-L. Effect of Oxygen Plasma Treatment on Crystal Growth Mode at Pentacene/Ni Interface in Organic Thin-Film Transistors. *J. Phys. Chem. B* **2010**, *114*, 14854-14859.
- (37) Yun, D.-J.; Rhee, S.-W. Pentacene Thin-Film Transistor with NiO<sub>(x)</sub> as a Source/Drain Electrode Deposited with Sputtering. *J. Electrochem. Soc.* **2008**, *155*, H899-H902.
- (38) Woll, C., *Organic Electronics: Structural and Electronic Properties of Ofets*. Wiley-VCH Verlag GmbH & Co. KGaA: 2009; p 634.
- (39) Nickel, B., Pentacene Devices: Molecular Structure, Charge Transport and Photo Response. In *Org. Electron.*, Wiley-VCH Verlag GmbH & Co. KGaA: 2009; pp 299-315.
- (40) Gutzler, R.; Perepichka, D. F.  $\pi$ -Electron Conjugation in Two Dimensions. *J. Am. Chem. Soc.* **2013**, *135*, 16585-16594.
- (41) Munoz, R.; Gomez-Aleixandre, C. Review of CVD Synthesis of Graphene. *Chem. Vap. Deposition* **2013**, *19*, 297-322.
- (42) Zhang, Y.; Zhang, L.; Zhou, C. Review of Chemical Vapor Deposition of Graphene and Related Applications. *Acc. Chem. Res.* **2013**, *46*, 2329-2339.
- (43) Dzemiantsova, L. V.; Karolak, M.; Lofink, F.; Kubetzka, A.; Sachs, B.; von Bergmann, K.; Hankemeier, S.; Wehling, T. O.; Fromter, R.; Oepen, H. P., *et al.* Multiscale Magnetic Study of Ni(111) and Graphene on Ni(111). *Phys. Rev. B* **2011**, *84*, 205431-205440.
- (44) Rosei, R.; Modesti, S.; Sette, F.; Quaresima, C.; Savoia, A.; Perfetti, P. Electronic Structure of Carbide and Graphitic Carbon on Ni(111). *Phys. Rev. B* **1984**, *29*, 3417-3422.
- (45) Sanchez-Barriga, J.; Varykhalov, A.; Scholz, M. R.; Rader, O.; Marchenko, D.; Rybkin, A.; Shikin, A. M.; Vescovo, E. Chemical Vapour Deposition of Graphene on Ni(111) and Co(0001) and Intercalation with Au to Study Dirac-Cone Formation and Rashba Splitting. *Diam. Relat. Mat.* **2010**, *19*, 734-741.
- (46) Cupolillo, A.; Ligato, N.; Caputi, L. S. Two-Dimensional Character of the Interface- $\pi$  Plasmon in Epitaxial Graphene on Ni(111). *Carbon* **2012**, *50*, 2588-2591.
- (47) Dou, W. D.; Huang, S. P.; Zhang, R. Q.; Lee, C. S. Molecule-Substrate Interaction Channels of Metal-Phthalocyanines on Graphene on Ni(111) Surface. *J. Chem. Phys.* **2011**, *134*, 094705-094711.

- (48) Shikin, A. M.; Prudnikova, G. V.; Adamchuk, V. K.; Moresco, F.; Rieder, K. H. Surface Intercalation of Gold Underneath a Graphite Monolayer on Ni(111) Studied by Angle-Resolved Photoemission and High-Resolution Electron-Energy-Loss Spectroscopy. *Phys. Rev. B* **2000**, *62*, 13202-13208.
- (49) Marchenko, D.; Varykhalov, A.; Rybkin, A.; Shikin, A. M.; Rader, O. Atmospheric Stability and Doping Protection of Noble-Metal Intercalated Graphene on Ni(111). *Appl. Phys. Lett.* **2011**, *98*, 122111-122113.
- (50) Shikin, A. M.; Adamchuk, V. K.; Rieder, K. H. Formation of Quasi-Free Graphene on the Ni(111) Surface with Intercalated Cu, Ag, and Au Layers. *Phys. Solid State* **2009**, *51*, 2390-2400.
- (51) Dedkov, Y. S.; Shikin, A. M.; Adamchuk, V. K.; Molodtsov, S. L.; Laubschat, C.; Bauer, A.; Kaindl, G. Intercalation of Copper Underneath a Monolayer of Graphite on Ni(111). *Phys. Rev. B* **2001**, *64*, 035405-035410.
- (52) Weser, M.; Rehder, Y.; Horn, K.; Sicot, M.; Fonin, M.; Preobrajenski, A. B.; Voloshina, E. N.; Goering, E.; Dedkov, Y. S. Induced Magnetism of Carbon Atoms at the Graphene/Ni(111) Interface. *Appl. Phys. Lett.* **2010**, *96*, 012504-012506.
- (53) Klink, C.; Stensgaard, I.; Besenbacher, F.; Laegsgaard, E. An STM Study of Carbon-Induced Structures on Ni(111) - Evidence for a Carbide-Phase Clock Reconstruction. *Surf. Sci.* **1995**, *342*, 250-260.
- (54) Jacobson, P.; Stoeger, B.; Garhofer, A.; Parkinson, G. S.; Schmid, M.; Caudillo, R.; Mittendorfer, F.; Redinger, J.; Diebold, U. Disorder and Defect Healing in Graphene on Ni(111). *J. Phys. Chem. Lett.* **2012**, *3*, 136-139.
- (55) Jacobson, P.; Stoger, B.; Garhofer, A.; Parkinson, G. S.; Schmid, M.; Caudillo, R.; Mittendorfer, F.; Redinger, J.; Diebold, U. Nickel Carbide as a Source of Grain Rotation in Epitaxial Graphene. *ACS Nano* **2012**, *6*, 3564-3572.
- (56) Peng, Z.; Yan, Z.; Sun, Z.; Tour, J. M. Direct Growth of Bilayer Graphene on SiO<sub>2</sub> Substrates by Carbon Diffusion through Nickel. *ACS Nano* **2011**, *5*, 8241-8247.
- (57) Odahara, G.; Otani, S.; Oshima, C.; Suzuki, M.; Yasue, T.; Koshikawa, T. Macroscopic Single-Domain Graphene Sheet on Ni(111). *Surf. Interface Anal.* **2011**, *43*, 1491-1493.
- (58) Odahara, G.; Otani, S.; Oshima, C.; Suzuki, M.; Yasue, T.; Koshikawa, T. In-Situ Observation of Graphene Growth on Ni(111). *Surf. Sci.* **2011**, *605*, 1095-1098.
- (59) Eizenberg, M.; Blakely, J. M. Carbon Interaction with Nickel Surfaces - Monolayer Formation and Structural Stability. *J. Chem. Phys.* **1979**, *71*, 3467-3477.

- (60) Fujita, D. Nanoscale Synthesis and Characterization of Graphene-Based Objects. *Sci. Technol. Adv. Mater.* **2011**, *12*, 044611-044620.
- (61) Perdigao, L. M. A.; Sabki, S. N.; Garfitt, J. M.; Capiod, P.; Beton, P. H. Graphene Formation by Decomposition of C-60. *J. Phys. Chem. C* **2011**, *115*, 7472-7476.
- (62) Lahiri, J.; Miller, T.; Adamska, L.; Oleynik, II; Batzill, M. Graphene Growth on Ni(111) by Transformation of a Surface Carbide. *Nano Lett.* **2011**, *11*, 518-522.
- (63) Lahiri, J.; Miller, T. S.; Ross, A. J.; Adamska, L.; Oleynik, II; Batzill, M. Graphene Growth and Stability at Nickel Surfaces. *New J. Phys.* **2011**, *13*, 025001-025019.
- (64) Nagashima, A.; Tejima, N.; Oshima, C. Electronic States of the Pristine and Alkali-Metal-Intercalated Monolayer Graphite/Ni(111) Systems. *Phys. Rev. B* **1994**, *50*, 17487-17495.
- (65) Blanksby, S. J.; Ellison, G. B. Bond Dissociation Energies of Organic Molecules. *Acc. Chem. Res.* **2003**, *36*, 255-263.
- (66) Bieri, M.; Blankenburg, S.; Kivala, M.; Pignedoli, C. A.; Ruffieux, P.; Muellen, K.; Fasel, R. Surface-Supported 2d Heterotriangulene Polymers. *Chem. Commun.* **2011**, *47*, 10239-10241.
- (67) Bieri, M.; Treier, M.; Cai, J.; Ait-Mansour, K.; Ruffieux, P.; Groening, O.; Groening, P.; Kastler, M.; Rieger, R.; Feng, X., *et al.* Porous Graphenes: Two-Dimensional Polymer Synthesis with Atomic Precision. *Chem. Commun.* **2009**, 6919-6921.
- (68) Fuhrer, M. S. Graphene Ribbons Piece-by-Piece. *Nat. Mater.* **2010**, *9*, 611-612.
- (69) Bjork, J.; Stafstrom, S.; Hanke, F. Zipping Up: Cooperativity Drives the Synthesis of Graphene Nanoribbons. *J. Am. Chem. Soc.* **2011**, *133*, 14884-14887.
- (70) Martin-Gago, J. A. Polycyclic Aromatics on-Surface Molecular Engineering. *Nat. Chem.* **2011**, *3*, 11-12.
- (71) Kang, D. B.; Anderson, A. B. Theoretical Interpretation of the Cyclohexane → Benzene Reaction on the Pt(111) Surface. *J. Am. Chem. Soc.* **1985**, *107*, 7858-7861.
- (72) Fogel, Y.; Zhi, L.; Rouhanipour, A.; Andrienko, D.; Räder, H. J.; Müllen, K. Graphitic Nanoribbons with Dibenzo[E,L]Pyrene Repeat Units: Synthesis and Self-Assembly. *Macromol.* **2009**, *42*, 6878-6884.
- (73) Resasco, D. E., Dehydrogenation – Heterogeneous. In *Encyclopedia of Catalysis*, John Wiley & Sons, Inc.: 2002.

- (74) Xue, X.; Scott, L. T. Thermal Cyclodehydrogenations to Form 6-Membered Rings: Cyclizations of [5]Helicenes. *Org. Lett.* **2007**, *9*, 3937-3940.
- (75) Chen, L.; Hernandez, Y.; Feng, X.; Müllen, K. From Nanographene and Graphene Nanoribbons to Graphene Sheets: Chemical Synthesis. *Angew. Chem., Int. Ed.* **2012**, *51*, 7640-7654.
- (76) Wintterlin, J.; Bocquet, M. L. Graphene on Metal Surfaces. *Surf. Sci.* **2009**, *603*, 1841-1852.
- (77) Gruneis, A.; Vyalikh, D. V. Tunable Hybridization between Electronic States of Graphene and a Metal Surface. *Phys. Rev. B* **2008**, *77*, 193401-193404.
- (78) Mittendorfer, F.; Garhofer, A.; Redinger, J.; Klimes, J.; Harl, J.; Kresse, G. Graphene on Ni(111): Strong Interaction and Weak Adsorption. *Phys. Rev. B* **2011**, *84*, 201401-201404.
- (79) Adamska, L.; Lin, Y.; Ross, A. J.; Batzill, M.; Oleynik, I. I. Atomic and Electronic Structure of Simple Metal/Graphene and Complex Metal/Graphene/Metal Interfaces. *Phys. Rev. B* **2012**, *85*, 195443.
- (80) Kozlov, S. M.; Viñes, F.; Görling, A. Bonding Mechanisms of Graphene on Metal Surfaces. *J. Phys. Chem. C* **2012**, *116*, 7360-7366.
- (81) Kastler, M.; Schmidt, J.; Pisula, W.; Sebastiani, D.; Müllen, K. From Armchair to Zigzag Peripheries in Nanographenes. *J. Am. Chem. Soc.* **2006**, *128*, 9526-9534.
- (82) Dias, J. R. Phenyl Substituted Benzenoid Hydrocarbons-Relationships of the Leapfrog Algorithm in Regard to Clar's Sextet Rule, Strain-Free, and Perimeter Topology Concepts. *Polycyclic Aromat. Compd.* **2005**, *25*, 113-127.
- (83) Wan, X.; Chen, K.; Liu, D.; Chen, J.; Miao, Q.; Xu, J. High-Quality Large-Area Graphene from Dehydrogenated Polycyclic Aromatic Hydrocarbons. *Chem. Mater.* **2012**, *24*, 3906-3915.
- (84) Roberson, L. B.; Kowalik, J.; Tolbert, L. M.; Kloc, C.; Zeis, R.; Chi, X. L.; Fleming, R.; Wilkins, C. Pentacene Disproportionation During Sublimation for Field-Effect Transistors. *J. Am. Chem. Soc.* **2005**, *127*, 3069-3075.
- (85) Adam, S.; Hwang, E. H.; Galitski, V. M.; Das Sarma, S. A Self-Consistent Theory for Graphene Transport. *Proc. Natl. Acad. Sci. U. S. A.* **2007**, *104*, 18392-18397.
- (86) Takase, M.; Enkelmann, V.; Sebastiani, D.; Baumgarten, M.; Müllen, K. Annularly Fused Hexapyrrolohexaazacoronenes: An Extended  $\Pi$  System with Multiple Interior Nitrogen Atoms Displays Stable Oxidation States. *Angew. Chem., Int. Ed.* **2007**, *46*, 5524-5527.

- (87) Draper, S. M.; Gregg, D. J.; Madathil, R. Heterosuperbenzenes: A New Family of Nitrogen-Functionalized, Graphitic Molecules. *J. Am. Chem. Soc.* **2002**, *124*, 3486-3487.
- (88) Pron, A.; Rannou, P. Processible Conjugated Polymers: From Organic Semiconductors to Organic Metals and Superconductors. *Prog. Polym. Sci.* **2002**, *27*, 135-190.
- (89) Gutzler, R.; Lappe, S.; Mahata, K.; Schmittel, M.; Heckl, W. M.; Lackinger, M. Aromatic Interaction Vs. Hydrogen Bonding in Self-Assembly at the Liquid-Solid Interface. *Chem. Commun.* **2009**, 680-682.
- (90) Ho, W. Single-Molecule Chemistry. *J. Chem. Phys.* **2002**, *117*, 11033-11061.
- (91) Hla, S. W.; Bartels, L.; Meyer, G.; Rieder, K. H. Inducing All Steps of a Chemical Reaction with the Scanning Tunneling Microscope Tip: Towards Single Molecule Engineering. *Phys. Rev. Lett.* **2000**, *85*, 2777-2780.
- (92) Hla, S. W.; Rieder, K. H. STM Control of Chemical Reactions: Single-Molecule Synthesis. *Annu. Rev. Phys. Chem.* **2003**, *54*, 307-330.
- (93) Hla, S. W. Scanning Tunneling Microscopy Single Atom/Molecule Manipulation and Its Application to Nanoscience and Technology. *J. Vac. Sci. Technol., B* **2005**, *23*, 1351-1360.
- (94) Lauhon, L. J.; Ho, W. Single-Molecule Chemistry and Vibrational Spectroscopy: Pyridine and Benzene on Cu(001). *J. Phys. Chem. A* **2000**, *104*, 2463-2467.
- (95) Komeda, T.; Kim, Y.; Fujita, Y.; Sainoo, Y.; Kawai, M. Local Chemical Reaction of Benzene on Cu(110) via STM-Induced Excitation. *J. Chem. Phys.* **2004**, *120*, 5347-5352.
- (96) Okawa, Y.; Aono, M. Materials Science - Nanoscale Control of Chain Polymerization. *Nature* **2001**, *409*, 683-684.
- (97) Katano, S.; Kim, Y.; Hori, M.; Trenary, M.; Kawai, M. Reversible Control of Hydrogenation of a Single Molecule. *Science* **2007**, *316*, 1883-1886.
- (98) Parschau, M.; Rieder, K.-H.; Hug, H. J.; Ernst, K.-H. Single-Molecule Chemistry and Analysis: Mode-Specific Dehydrogenation of Adsorbed Propene by Inelastic Electron Tunneling. *J. Am. Chem. Soc.* **2011**, *133*, 5689-5691.
- (99) Komeda, T. Chemical Identification and Manipulation of Molecules by Vibrational Excitation via Inelastic Tunneling Process with Scanning Tunneling Microscopy. *Prog. Surf. Sci.* **2005**, *78*, 41-85.

- (100) Binnig, G.; Garcia, N.; Rohrer, H. Conductivity Sensitivity of Inelastic Scanning Tunneling Microscopy. *Phys. Rev. B* **1985**, *32*, 1336-1338.
- (101) Clair, S.; Ourdjini, O.; Abel, M.; Porte, L. Tip- or Electron Beam-Induced Surface Polymerization. *Chem. Commun.* **2011**, *47*, 8028-8030.
- (102) Miura, A.; De Feyter, S.; Abdel-Mottaleb, M. M. S.; Gesquiere, A.; Grim, P. C. M.; Moessner, G.; Sieffert, M.; Klapper, M.; Mullen, K.; De Schryver, F. C. Light- and STM-Tip-Induced Formation of One-Dimensional and Two-Dimensional Organic Nanostructures. *Langmuir* **2003**, *19*, 6474-6482.
- (103) Maksymovych, P.; Sorescu, D. C.; Jordan, K. D.; Yates, J. T. Collective Reactivity of Molecular Chains Self-Assembled on a Surface. *Science* **2008**, *322*, 1664-1667.
- (104) Zhou, L.; Ho, P. K. H.; Zhang, P. C.; Li, S. F. Y.; Xu, G. Q. In Situ STM Tip-Induced Electropolymerization of Poly(3-Octylthiophene). *Appl. Phys. A: Mater. Sci. Process.* **1998**, *66*, S643-S647.
- (105) Sullivan, S. P.; Schmeders, A.; Mbugua, S. K.; Beebe, T. P. Controlled Polymerization of Substituted Diacetylene Self-Organized Monolayers Confined in Molecule Corrals. *Langmuir* **2005**, *21*, 1322-1327.
- (106) Okawa, Y.; Aono, M. Linear Chain Polymerization Initiated by a Scanning Tunneling Microscope Tip at Designated Positions. *J. Chem. Phys.* **2001**, *115*, 2317-2322.
- (107) Brusso, J. L.; Hirst, O. D.; Dadvand, A.; Ganesan, S.; Cicoira, F.; Robertson, C. M.; Oakley, R. T.; Rosei, F.; Perepichka, D. F. Two-Dimensional Structural Motif in Thienoacene Semiconductors: Synthesis, Structure, and Properties of Tetrathienoanthracene Isomers. *Chem. Mater.* **2008**, *20*, 2484-2494.
- (108) Dinca, L. E.; Fu, C. Y.; MacLeod, J. M.; Lipton-Duffin, J.; Brusso, J. L.; Szakacs, C. E.; Ma, D. L.; Perepichka, D. F.; Rosei, F. Unprecedented Transformation of Tetrathienoanthracene into Pentacene on Ni(111). *ACS Nano* **2013**, *7*, 1652-1657.
- (109) Oura, K.; Lifshits, V. G.; Saranin, A. A.; Zotov, A. V.; Katayama, M., *Surface Science: An Introduction*. Springer-Verlag: Berlin, 2003; p 440.
- (110) Chadi, D. J. Atomic and Electronic Structures of Reconstructed Si(100) Surfaces. *Phys. Rev. Lett.* **1979**, *43*, 43-47.
- (111) Haiss, W. Surface Stress of Clean and Adsorbate-Covered Solids. *Rep. Prog. Phys.* **2001**, *64*, 591-648.
- (112) Needs, R. J. Calculations of the Surface Stress Tensor at Aluminum (111) and (110) Surfaces. *Phys. Rev. Lett.* **1987**, *58*, 53-56.

- (113) Wan, J.; Fan, Y. L.; Gong, D. W.; Shen, S. G.; Fan, X. Q. Surface Relaxation and Stress of Fcc Metals: Cu, Ag, Au, Ni, Pd, Pt, Al and Pb. *Modell. Simul. Mater. Sci. Eng.* **1999**, *7*, 189-206.
- (114) Bell, A. T. The Impact of Nanoscience on Heterogeneous Catalysis. *Science* **2003**, *299*, 1688-1691.
- (115) Richter, B.; Kuhlenbeck, H.; Freund, H. J.; Bagus, P. S. Cluster Core-Level Binding-Energy Shifts: The Role of Lattice Strain. *Phys. Rev. Lett.* **2004**, *93*, 026805-026808.
- (116) Falicov, L. M.; Somorjai, G. A. Correlation between Catalytic Activity and Bonding and Coordination Number of Atoms and Molecules on Transition Metal Surfaces: Theory and Experimental Evidence. *Proc. Natl. Acad. Sci. U. S. A.* **1985**, *82*, 2207-2211.
- (117) Bahn, S. R.; Jacobsen, K. W. An Object-Oriented Scripting Interface to a Legacy Electronic Structure Code. *Comput. Sci. Eng.* **2002**, *4*, 56-66.
- (118) Barlow, S. M.; Raval, R. Complex Organic Molecules at Metal Surfaces: Bonding, Organisation and Chirality. *Surf. Sci. Rep.* **2003**, *50*, 201-341.
- (119) Wood, E. A. Vocabulary of Surface Crystallography. *J. Appl. Phys.* **1964**, *35*, 1306-1312.
- (120) Masel, R. I., *Principles of Adsorption and Reaction on Solid Surfaces*. 1996; p 818.
- (121) Busseron, E.; Ruff, Y.; Moulin, E.; Giuseppone, N. Supramolecular Self-Assemblies as Functional Nanomaterials. *Nanoscale* **2013**, *5*, 7098-7140.
- (122) Brinck, T.; Murray, J. S.; Politzer, P. Surface Electrostatic Potentials of Halogenated Methanes as Indicators of Directional Intermolecular Interactions. *Int. J. Quantum Chem.* **1992**, *44*, 57-64.
- (123) Clark, T.; Hennemann, M.; Murray, J. S.; Politzer, P. Halogen Bonding: The  $\Sigma$ -Hole. *J. Mol. Model.* **2007**, *13*, 291-296.
- (124) Murray, J. S.; Lane, P.; Politzer, P. Expansion of the Sigma-Hole Concept. *J. Mol. Model.* **2009**, *15*, 723-729.
- (125) Murray, J. S.; Lane, P.; Politzer, P. A Predicted New Type of Directional Noncovalent Interaction. *Int. J. Quantum Chem.* **2007**, *107*, 2286-2292.
- (126) Murray, J. S.; Lane, P.; Clark, T.; Politzer, P.  $\Sigma$ -Hole Bonding: Molecules Containing Group Vi Atoms. *J. Mol. Model.* **2007**, *13*, 1033-1038.

- (127) Arnett, E. M.; Mitchell, E. J.; Murty, T. S. S. R. Basicity. Comparison of Hydrogen Bonding and Proton Transfer to Some Lewis Bases. *J. Am. Chem. Soc.* **1974**, *96*, 3875-3891.
- (128) Nyburg, S. Steric Hindrance in the Dibiphenylene-Ethylene Molecule. *Acta Crystallogr.* **1954**, *7*, 779-780.
- (129) Uwabe, A.; Ueno, M.; Ibuki, K. Molecular Dynamics Simulation of Partially Diffusion-Controlled Reaction between Mono- and Diatomic Molecules. *J. Mol. Liq.* **2009**, *147*, 30-36.
- (130) Everaers, R.; Rosa, A. Multi-Scale Modeling of Diffusion-Controlled Reactions in Polymers: Renormalisation of Reactivity Parameters. *J. Chem. Phys.* **2012**, *136*.
- (131) Dacey, J. R. Surface Diffusion of Adsorbed Molecules. *Ind. Eng. Chem. Res.* **1965**, *57*, 26-33.
- (132) Heeger, A. J. Semiconducting and Metallic Polymers: The Fourth Generation of Polymeric Materials. *J. Phys. Chem. B* **2001**, *105*, 8475-8491.
- (133) Roncali, J. Molecular Engineering of the Band Gap of  $\Pi$ -Conjugated Systems: Facing Technological Applications. *Macromol. Rapid Commun.* **2007**, *28*, 1761-1775.
- (134) Hou, J.; Park, M.-H.; Zhang, S.; Yao, Y.; Chen, L.-M.; Li, J.-H.; Yang, Y. Bandgap and Molecular Energy Level Control of Conjugated Polymer Photovoltaic Materials Based on Benzo[1,2-B:4,5-B']Dithiophene. *Macromol.* **2008**, *41*, 6012-6018.
- (135) Jariwala, D.; Srivastava, A.; Ajayan, P. M. Graphene Synthesis and Band Gap Opening. *J. Nanosci. Nanotechnol.* **2011**, *11*, 6621-6641.
- (136) Reiss, P.; Couderc, E.; De Girolamo, J.; Pron, A. Conjugated Polymers/Semiconductor Nanocrystals Hybrid Materials-Preparation, Electrical Transport Properties and Applications. *Nanoscale* **2011**, *3*, 446-489.
- (137) Cheng, Y. J.; Yang, S. H.; Hsu, C. S. Synthesis of Conjugated Polymers for Organic Solar Cell Applications. *Chem. Rev.* **2009**, *109*, 5868-5923.
- (138) Weder, C. Synthesis, Processing and Properties of Conjugated Polymer Networks. *Chem. Commun.* **2005**, 5378-5389.
- (139) Kline, R. J.; McGehee, M. D. Morphology and Charge Transport in Conjugated Polymer. *Polym. Rev.* **2006**, *46*, 27-45.
- (140) Frederick, B. G.; Leibsle, F. M.; Haq, S.; Richardson, N. V. Evolution of Lateral Order and Molecular Reorientation in the Benzoate/Cu(110) System. *Surf. Rev. Lett.* **1996**, *3*, 1523-1546.

- (141) Kettle, S. F. A., *Physical Inorganic Chemistry: A Coordination Chemistry Approach*. Oxford University Press, Incorporated: 1998.
- (142) Binnig, G.; Rohrer, H.; Gerber, C.; Weibel, E. 7x7 Reconstruction on Si(111) Resolved in Real Space. *Phys. Rev. Lett.* **1983**, *50*, 120-123.
- (143) Binnig, G.; Rohrer, H. Scanning Tunneling Microscopy - from Birth to Adolescence. *Rev. Mod. Phys.* **1987**, *59*, 615-625.
- (144) Chen, C. J., *Introduction to Scanning Tunneling Microscopy*. Oxford University Press: 1993; p 472.
- (145) Sergei N. Magonov; Myung-Hwan Whangbo, *Surface Analysis with STM and AFM: Experimental and Theoretical Aspects of Image Analysis*. Wiley: September 2008; p 335.
- (146) Gadzuk, J. W. Resonance-Assisted, Hot-Electron-Induced Desorption. *Surf. Sci.* **1995**, *342*, 345-358.
- (147) Hla, S. W.; Rieder, K. H. Engineering of Single Molecules with a Scanning Tunneling Microscope Tip. *Superlattices Microstruct.* **2002**, *31*, 63-72.
- (148) Hla, S. W.; Braun, K. F.; Rieder, K. H. Single-Atom Manipulation Mechanisms During a Quantum Corral Construction. *Phys. Rev. B* **2003**, *67*, 201402.
- (149) Bartels, L.; Meyer, G.; Rieder, K. H. Basic Steps of Lateral Manipulation of Single Atoms and Diatomic Clusters with a Scanning Tunneling Microscope Tip. *Phys. Rev. Lett.* **1997**, *79*, 697-700.
- (150) Laegsgaard, E.; Osterlund, L.; Thostrup, P.; Rasmussen, P. B.; Stensgaard, I.; Besenbacher, F. A High-Pressure Scanning Tunneling Microscope. *Rev. Sci. Instrum.* **2001**, *72*, 3537-3542.
- (151) Horcas, I.; Fernandez, R.; Gomez-Rodriguez, J. M.; Colchero, J.; Gomez-Herrero, J.; Baro, A. M. Wsxn: A Software for Scanning Probe Microscopy and a Tool for Nanotechnology. *Rev. Sc. Instrum.* **2007**, *78*, 013705-013712.
- (152) Musket, R. G.; McLean, W.; Colmenares, C. A.; Makowiecki, D. M.; Siekhaus, W. J. Preparation of Atomically Clean Surfaces of Selected Elements: A Review. *Appl. Surf. Sci. (1977-1985)* **1982**, *10*, 143-207.
- (153) Klink, C.; Stensgaard, I.; Besenbacher, F.; Lægsgaard, E. Carbide Carbon on Ni(110): An STM Study. *Surf. Sci.* **1996**, *360*, 171-179.

- (154) Vang, R. T.; Honkala, K.; Dahl, S.; Vestergaard, E. K.; Schnadt, J.; Laegsgaard, E.; Clausen, B. S.; Norskov, J. K.; Besenbacher, F. Ethylene Dissociation on Flat and Stepped Ni(111): A Combined STM and Dft Study. *Surf. Sci.* **2006**, *600*, 66-77.
- (155) Mccarroll, J. J.; Edmonds, T.; Pitkethly, R. C. Interpretation of a Complex Low Energy Electron Diffraction Pattern: Carbonaceous and Sulphur-Containing Structures on Ni(111). *Nature* **1969**, *223*, 1260-1262.
- (156) Gutzler, R.; Fu, C.; Dadvand, A.; Hua, Y.; MacLeod, J. M.; Rosei, F.; Perepichka, D. F. Halogen Bonds in 2d Supramolecular Self-Assembly of Organic Semiconductors. *Nanoscale* **2012**, *4*, 5965-5971.
- (157) Jones, R. O.; Gunnarsson, O. The Density Functional Formalism, Its Applications and Prospects. *Rev. Mod. Phys.* **1989**, *61*, 689-746.
- (158) Frisch, M. J.; Trucks, G. W.; Schlegel, H. B.; Scuseria, G. E.; Robb, M. A.; Cheeseman, J. R.; Scalmani, G.; Barone, V.; Mennucci, B.; Petersson, G. A., *et al.* *Gaussian 09, Revision B.01*, Wallingford CT, 2009.
- (159) Perdew, J. P.; Burke, K.; Ernzerhof, M. Generalized Gradient Approximation Made Simple. *Phys. Rev. Lett.* **1996**, *77*, 3865-3868.
- (160) Stephens, P. J.; Devlin, F. J.; Chabalowski, C. F.; Frisch, M. J. Ab Initio Calculation of Vibrational Absorption and Circular Dichroism Spectra Using Density Functional Force Fields. *J. Phys. Chem.* **1994**, *98*, 11623-11627.
- (161) Yang, Y.; Weaver, M. N.; Merz, K. M. Assessment of the “6-31+G\*\* + Lanl2dz” Mixed Basis Set Coupled with Density Functional Theory Methods and the Effective Core Potential: Prediction of Heats of Formation and Ionization Potentials for First-Row-Transition-Metal Complexes. *J. Phys. Chem. A* **2009**, *113*, 9843-9851.
- (162) Lingwood, M.; Hammond, J. R.; Hrovat, D. A.; Mayer, J. M.; Borden, W. T. Mpw1k Performs Much Better Than B3lyp in Dft Calculations on Reactions That Proceed by Proton-Coupled Electron Transfer (Pcet). *J. Chem. Theory Comput.* **2006**, *2*, 740-745.
- (163) Becke, A. D. Density-Functional Thermochemistry. Iii. The Role of Exact Exchange. *J. Chem. Phys.* **1993**, *98*, 5648-5652.
- (164) Hanwell, M. D.; Curtis, D. E.; Loni, D. C.; Vandermeersch, T.; Zurek, E.; Hutchison, G. R. Avogadro: An Advanced Semantic Chemical Editor, Visualization, and Analysis Platform. *J. Cheminf.* **2012**, *4*, 17.
- (165) Accelrys Software Inc. *Discovery Studio Modeling Environment, Release 4.0*, San Diego: Accelrys Software Inc. **2013**.

- (166) Perdew, J. P.; Wang, Y. Accurate and Simple Analytic Representation of the Electron-Gas Correlation Energy. *Phys. Rev. B* **1992**, *45*, 13244-13249.
- (167) Ordejon, P.; Artacho, E.; Soler, J. M. Self-Consistent Order-N Density-Functional Calculations for Very Large Systems. *Phys. Rev. B* **1996**, *53*, 10441-10444.
- (168) Soler, J. M.; Artacho, E.; Gale, J. D.; Garcia, A.; Junquera, J.; Ordejon, P.; Sanchez-Portal, D. The Siesta Method for Ab Initio Order-N Materials Simulation. *J. Phys.:Condens. Matter* **2002**, *14*, 2745-2779.
- (169) Perdew, J. P.; Zunger, A. Self-Interaction Correction to Density-Functional Approximations for Many-Electron Systems. *Phys. Rev. B* **1981**, *23*, 5048-5079.
- (170) Ritort, F. Single-Molecule Experiments in Biological Physics: Methods and Applications. *J. Phys.:Condens. Matter* **2006**, *18*, R531-R583.
- (171) Moerner, W. E.; Orrit, M. Illuminating Single Molecules in Condensed Matter. *Science* **1999**, *283*, 1670-1676.
- (172) Mehta, A. D.; Rief, M.; Spudich, J. A.; Smith, D. A.; Simmons, R. M. Single-Molecule Biomechanics with Optical Methods. *Science* **1999**, *283*, 1689-1695.
- (173) Kneipp, K.; Wang, Y.; Kneipp, H.; Perelman, L. T.; Itzkan, I.; Dasari, R. R.; Feld, M. S. Single Molecule Detection Using Surface-Enhanced Raman Scattering (Sers). *Phys. Rev. Lett.* **1997**, *78*, 1667-1670.
- (174) Weiss, S. Fluorescence Spectroscopy of Single Biomolecules. *Science* **1999**, *283*, 1676-1683.
- (175) Gross, L.; Mohn, F.; Moll, N.; Liljeroth, P.; Meyer, G. The Chemical Structure of a Molecule Resolved by Atomic Force Microscopy. *Science* **2009**, *325*, 1110-1114.
- (176) Gross, L.; Mohn, F.; Moll, N.; Schuler, B.; Criado, A.; Guitián, E.; Peña, D.; Gourdon, A.; Meyer, G. Bond-Order Discrimination by Atomic Force Microscopy. *Science* **2012**, *337*, 1326-1329.
- (177) Wintterlin, J.; Völkening, S.; Janssens, T. V. W.; Zambelli, T.; Ertl, G. Atomic and Macroscopic Reaction Rates of a Surface-Catalyzed Reaction. *Science* **1997**, *278*, 1931-1934.
- (178) Hamers, R. J.; Avouris, P.; Bozso, F. Imaging Chemical-Bond Formation with the Scanning Tunneling Microscope:  $\text{NH}_3$  Dissociation on Si(001). *Phys. Rev. Lett.* **1987**, *59*, 2071-2074.

- (179) Rosei, F.; Schunack, M.; Naitoh, Y.; Jiang, P.; Gourdon, A.; Laegsgaard, E.; Stensgaard, I.; Joachim, C.; Besenbacher, F. Properties of Large Organic Molecules on Metal Surfaces. *Prog. Surf. Sci.* **2003**, *71*, 95-146.
- (180) Cicoira, F.; Santato, C.; Rosei, F. Two-Dimensional Nanotemplates as Surface Cues for the Controlled Assembly of Organic Molecules. *Top. Curr. Chem.* **2008**, *285*, 203-267.
- (181) Grim, P. C. M.; De Feyter, S.; Gesquiere, A.; Vanoppen, P.; Rucker, M.; Valiyaveetil, S.; Moessner, G.; Mullen, K.; De Schryver, F. C. Submolecularly Resolved Polymerization of Diacetylene Molecules on the Graphite Surface Observed with Scanning Tunneling Microscopy. *Angew. Chem., Int. Ed.* **1997**, *36*, 2601-2603.
- (182) Sakaguchi, H.; Matsumura, H.; Gong, H. Electrochemical Epitaxial Polymerization of Single-Molecular Wires. *Nat. Mater.* **2004**, *3*, 551-557.
- (183) Sakaguchi, H.; Matsumura, H.; Gong, H.; Abouelwafa, A. M. Direct Visualization of the Formation of Single-Molecule Conjugated Copolymers. *Science* **2005**, *310*, 1002-1006.
- (184) Lipton-Duffin, J. A.; Miwa, J. A.; Kondratenko, M.; Cicoira, F.; Sumpter, B. G.; Meunier, V.; Perepichka, D. F.; Rosei, F. Step-by-Step Growth of Epitaxially Aligned Polythiophene by Surface-Confined Reaction. *Proc. Natl. Acad. Sci. U. S. A.* **2010**, *107*, 11200-11204.
- (185) Grill, L.; Dyer, M.; Lafferentz, L.; Persson, M.; Peters, M. V.; Hecht, S. Nano-Architectures by Covalent Assembly of Molecular Building Blocks. *Nat. Nanotechnol.* **2007**, *2*, 687-691.
- (186) Tanoue, R.; Higuchi, R.; Enoki, N.; Miyasato, Y.; Uemura, S.; Kimizuka, N.; Stieg, A. Z.; Gimzewski, J. K.; Kunitake, M. Thermodynamically Controlled Self-Assembly of Covalent Nanoarchitectures in Aqueous Solution. *ACS Nano* **2011**, *5*, 3923-3929.
- (187) Faury, T.; Clair, S.; Abel, M.; Dumur, F.; Gigmes, D.; Porte, L. Sequential Linking to Control Growth of a Surface Covalent Organic Framework. *J. Phys. Chem. C* **2012**, *116*, 4819-4823.
- (188) Zwaneveld, N. A. A.; Pawlak, R.; Abel, M.; Catalin, D.; Gigmes, D.; Bertin, D.; Porte, L. Organized Formation of 2d Extended Covalent Organic Frameworks at Surfaces. *J. Am. Chem. Soc.* **2008**, *130*, 6678-6679.
- (189) Dienstmaier, J. F.; Medina, D. D.; Dogru, M.; Knochel, P.; Bein, T.; Heckl, W. M.; Lackinger, M. Isorecticular Two-Dimensional Covalent Organic Frameworks Synthesized by on-Surface Condensation of Diboronic Acids. *ACS Nano* **2012**, *6*, 7234-7242.

- (190) Matena, M.; Riehm, T.; Stohr, M.; Jung, T. A.; Gade, L. H. Transforming Surface Coordination Polymers into Covalent Surface Polymers: Linked Polycondensed Aromatics through Oligomerization of N-Heterocyclic Carbene Intermediates. *Angew. Chem., Int. Ed.* **2008**, *47*, 2414-2417.
- (191) McCullough, R. D. The Chemistry of Conducting Polythiophenes. *Adv. Mater.* **1998**, *10*, 93-116.
- (192) Huntley, D. R.; Mullins, D. R.; Wingeier, M. P. Desulfurization of Thiophenic Compounds by Ni(111): Adsorption and Reactions of Thiophene, 3-Methylthiophene, and 2,5-Dimethylthiophene. *J. Phys. Chem.* **1996**, *100*, 19620-19627.
- (193) Ma, Z.; Zaera, F. Organic Chemistry on Solid Surfaces. *Surf. Sci. Rep.* **2006**, *61*, 229-281.
- (194) Varnam, A.; Sutherland, J. M., *Beverages: Technology, Chemistry and Microbiology*. Springer: 1994; Vol. 2, p 464.
- (195) Collins, M. A.; Jones, D. N. A Total Synthesis of Estradiol and Its 6,6-Dimethyl Analogue. *Tetrahedron Lett.* **1995**, *36*, 4467-4470.
- (196) Marchalín, Š.; Žúžiová, J.; Kadlečiková, K.; Šafář, P.; Baran, P.; Dalla, V.; Dařch, A. An Expedient Synthesis of 7(S)-Ethyl-8(R or S)-Indolizidinols Based on a Thiophene Reductive Desulfurization. *Tetrahedron Lett.* **2007**, *48*, 697-702.
- (197) Anthony, J. E. Functionalized Acenes and Heteroacenes for Organic Electronics. *Chem. Rev.* **2006**, *106*, 5028-5048.
- (198) Gutzler, R.; Ivasenko, O.; Fu, C.; Brusso, J. L.; Rosei, F.; Perepichka, D. F. Halogen Bonds as Stabilizing Interactions in a Chiral Self-Assembled Molecular Monolayer. *Chem. Commun.* **2011**, *47*, 9453-9455.
- (199) Maurice, V.; Kitakatsu, N.; Siegers, M.; Marcus, P. Low-Coverage Sulfur Induced Reconstruction of Ni(111). *Surf. Sci.* **1997**, *373*, 307-317.
- (200) While Sulfur Is Also Known to Form a  $(\sqrt{3}\times\sqrt{3})R30^\circ$  Phase on Ni(111) (*e.g.*, Perdrea, M. And Oudar, J. Structure, Surf. Sci. 20, 80 (1970)), a Bromine-Based Structure Is More Likely since the Sulfur  $(\sqrt{3}\times\sqrt{3})R30^\circ$  Phase Is Less Stable Than the Observed Rectangular Reconstruction. Furthermore, We Do Not Observe the  $(\sqrt{3}\times\sqrt{3})R30^\circ$  Phase on Surfaces Exposed to the Non-Brominated 2tta Molecule.
- (201) Foresti, M. L.; Aloisi, G.; Innocenti, M.; Kobayashi, H.; Guidelli, R. Crystal Face Effects on Adsorption of Ionic and Non-Ionic Species on Ag Electrodes: An Electrochemical and STM Study. *Surf. Sci.* **1995**, *335*, 241-251.

- (202) Jones, R. G.; Kadodwala, M. Bromine Adsorption on Cu(111). *Surf. Sci.* **1997**, *370*, L219-L225.
- (203) Xu, H.; Yuro, R.; Harrison, I. The Structure and Corrosion Chemistry of Bromine on Pt(111). *Surf. Sci.* **1998**, *411*, 303-315.
- (204) Kane, S. M.; Gland, J. L. Cyclohexanethiol Adsorption and Reaction on the Ni(111) Surface. *J. Phys. Chem. B* **1998**, *102*, 5322-5328.
- (205) Kane, S. M.; Rufael, T. S.; Gland, J. L.; Huntley, D. R.; Fischer, D. A. Role of Hydrogen in Benzene Formation from Benzenethiol on the Ni(111) Surface. *J. Phys. Chem. B* **1997**, *101*, 8486-8491.
- (206) The Presence of the Fully Hydrogenated Pentacene Molecule Can Be Explained by the Fact That in Order to Do Sims, the Sample Was Removed from UHV and Exposed to Atmosphere, a Process That Hydrogenates the Unsaturated Pentacene with Ambient Water Vapour.
- (207) Song, H.; Kim, Y.; Jang, Y. H.; Jeong, H.; Reed, M. A.; Lee, T. Observation of Molecular Orbital Gating. *Nature* **2009**, *462*, 1039-1043.
- (208) Harikumar, K. R.; McNab, I. R.; Polanyi, J. C.; Zabet-Khosousi, A.; Hofer, W. A. Imprinting Self-Assembled Patterns of Lines at a Semiconductor Surface, Using Heat, Light, or Electrons. *Proc. Natl. Acad. Sci. U. S. A.* **2011**, *108*, 950-955.
- (209) Lim, T. B.; Polanyi, J. C.; Guo, H.; Ji, W. Surface-Mediated Chain Reaction through Dissociative Attachment. *Nat. Chem.* **2011**, *3*, 85-89.
- (210) Girard, S. A.; Knauber, T.; Li, C.-J. The Cross-Dehydrogenative Coupling of C<sub>sp</sub><sup>3</sup>-H Bonds: A Versatile Strategy for C-C Bond Formations. *Angew. Chem., Int. Ed.* **2014**, *53*, 74-100.
- (211) Perepichka, I. F.; Perepichka, D. F., *Handbook of Thiophene-Based Materials: Applications in Organic Electronics and Photonics*. Wiley: August 2009; p 910.
- (212) Yamamoto, T. Molecular Assembly and Properties of Polythiophenes. *NPG Asia Mater.* **2010**, *2*, 54-60.
- (213) Dinca, L. E.; MacLeod, J. M.; Lipton-Duffin, J.; Fu, C.; Ma, D.; Perepichka, D. F.; Rosei, F. Tip-Induced C-H Activation and Oligomerization of Thienoanthracenes. *Chem. Commun.* **2014**, *50*, 8791-8793.
- (214) Berner, S.; Brunner, M.; Ramoino, L.; Suzuki, H.; Güntherodt, H. J.; Jung, T. A. Time Evolution Analysis of a 2d Solid-Gas Equilibrium: A Model System for Molecular Adsorption and Diffusion. *Chem. Phys. Lett.* **2001**, *348*, 175-181.

- (215) The Lithography Experiments Can Reach Resolution Close to 50 Nm While Here in the STM the Resolution Is Given by the Scanning Size, Which Could Go Down to Few Nanometers in Size.
- (216) Shim, W.; Braunschweig, A. B.; Liao, X.; Chai, J. N.; Lim, J. K.; Zheng, G. F.; Mirkin, C. A. Hard-Tip, Soft-Spring Lithography. *Nature* **2011**, *469*, 516-521.
- (217) In These Low-Temperature Experiments (at 4.7 and 8 K Respectively), Individual Benzene Molecules Were Dehydrogenated by Tunneling at Much Higher Bias Voltages Than Were Typically Used for Imaging:  $>2.4$  V on Cu(110), and  $2.9 \pm 0.1$  V on Cu(001).
- (218) Stoltze, P. Simulation of Surface Defects. *J. Phys.-Condes. Matter* **1994**, *6*, 9495-9517.
- (219) Giesen, M. Step and Island Dynamics at Solid/Vacuum and Solid/Liquid Interfaces. *Prog. Surf. Sci.* **2001**, *68*, 1-153.
- (220) Greuter, F.; Plummer, E. W. Chemisorption of Atomic Hydrogen on Cu(111). *Solid State Commun.* **1983**, *48*, 37-41.
- (221) El Garah, M.; MacLeod, J. M.; Rosei, F. Covalently Bonded Networks through Surface-Confined Polymerization. *Surf. Sci.* **2013**, *613*, 6-14.
- (222) Stock, T.; Nogami, J. Tunneling Electron Induced Chemisorption of Copper Phthalocyanine Molecules on the Cu(111) Surface. *Appl. Phys. Lett.* **2014**, *104*, 071601-071604.
- (223) Gartland, P. O.; Berge, S.; Slagsvold, B. J. Photoelectric Work Function of a Copper Single Crystal for the (100), (110), (111), and (112) Faces. *Phys. Rev. Lett.* **1972**, *28*, 738-739.
- (224) Skriver, H. L.; Rosengaard, N. M. Surface Energy and Work Function of Elemental Metals. *Phys. Rev. B* **1992**, *46*, 7157-7168.
- (225) Chavy, C.; Joachim, C.; Altibelli, A. Interpretation of STM Images: C60 on the Gold (110) Surface. *Chem. Phys. Lett.* **1993**, *214*, 569-575.
- (226) Lagoute, J.; Kanisawa, K.; Folsch, S. Manipulation and Adsorption-Site Mapping of Single Pentacene Molecules on Cu(111). *Phys. Rev. B* **2004**, *70*, 245415-245420.
- (227) Lesnard, H.; Lorente, N.; Bocquet, M. L. Theoretical Study of Benzene and Pyridine STM-Induced Reactions on Copper Surfaces. *J. Phys.-Condes. Matter* **2008**, *20*, 224012-224019.
- (228) Champness, N. R. Surface Chemistry Making the Right Connections. *Nat. Chem.* **2012**, *4*, 149-150.

- (229) Kittelmann, M.; Rahe, P.; Nimmrich, M.; Hauke, C. M.; Gourdon, A.; Kuehnle, A. On-Surface Covalent Linking of Organic Building Blocks on a Bulk Insulator. *ACS Nano* **2011**, *5*, 8420-8425.
- (230) Ramanathan, M.; Kilbey, I. I. S. M.; Ji, Q.; Hill, J. P.; Ariga, K. Materials Self-Assembly and Fabrication in Confined Spaces. *J. Mater. Chem.* **2012**, *22*, 10389-10405.
- (231) Shi, A.-C.; Li, B. Self-Assembly of Diblock Copolymers under Confinement. *Soft Matter* **2013**, *9*, 1398-1413.
- (232) Geoghegan, M.; Krausch, G. Wetting at Polymer Surfaces and Interfaces. *Prog. Polym. Sci.* **2003**, *28*, 261-302.
- (233) Wintjes, N., *Tailoring Supramolecular Assemblies on a Metal Surface by Specifically Functionalized Porphyrins*. Cuvillier Verlag: 2007; p 84.
- (234) Wang, Y.; Lingenfelder, M.; Fabris, S.; Fratesi, G.; Ferrando, R.; Classen, T.; Kern, K.; Costantini, G. Programming Hierarchical Supramolecular Nanostructures by Molecular Design. *J. Phys. Chem. C* **2013**, *117*, 3440-3445.
- (235) Toyoshima, I.; Somorjai, G. A. Heats of Chemisorption of O<sub>2</sub>, H<sub>2</sub>, CO, CO<sub>2</sub>, and N<sub>2</sub> on Polycrystalline and Single Crystal Transition Metal Surfaces. *Catal. Rev.: Sci. Eng.* **1979**, *19*, 105-159.
- (236) The Accuracy of the Reported Temperature Is within  $\pm 25$  °C.
- (237) Smerdon, J. A.; Bode, M.; Guisinger, N. P.; Guest, J. R. Monolayer and Bilayer Pentacene on Cu(111). *Phys. Rev. B* **2011**, *84*, 165436-165442.
- (238) Rousseau, G. B. D.; Mulligan, A.; Bovet, N.; Adams, M.; Dhanak, V.; Kadodwala, M. A Structural Study of Disordered Sulfur Overlayers on Cu(111). *Surf. Sci.* **2006**, *600*, 897-903.
- (239) Smerdon, J. A.; Rankin, R. B.; Greeley, J. P.; Guisinger, N. P.; Guest, J. R. Chiral "Pinwheel" Heterojunctions Self-Assembled from C<sub>60</sub> and Pentacene. *ACS Nano* **2013**, *7*, 3086-3094.
- (240) Wahlström, E.; Ekvall, I.; Kihlgren, T.; Olin, H.; Lindgren, S.-Å.; Walldén, L. Low-Temperature Structure of S/Cu(111). *Phys. Rev. B* **2001**, *64*, 155406-155412.
- (241) Speller, S.; Rauch, T.; Bomermann, J.; Borrmann, P.; Heiland, W. Surface Structures of S on Pd(111). *Surf. Sci.* **1999**, *441*, 107-116.

- (242) Schoofs, G. R.; Preston, R. E.; Benziger, J. B. Adsorption and Desulfurization of Thiophene on Ni(111). *Langmuir* **1985**, *1*, 313-320.
- (243) Weigelt, S.; Busse, C.; Bombis, C.; Knudsen, M. M.; Gothelf, K. V.; Strunskus, T.; Woll, C.; Dahlbom, M.; Hammer, B.; Laegsgaard, E., *et al.* Covalent Interlinking of an Aldehyde and an Amine on a Au(111) Surface in Ultrahigh Vacuum. *Angew. Chem., Int. Ed.* **2007**, *46*, 9227-9230.
- (244) Dienstmaier, J. F.; Gigler, A. M.; Goetz, A. J.; Knochel, P.; Bein, T.; Lyapin, A.; Reichlmaier, S.; Heckl, W. M.; Lackinger, M. Synthesis of Well-Ordered Cof Monolayers: Surface Growth of Nanocrystalline Precursors Versus Direct on-Surface Polycondensation. *ACS Nano* **2011**, *5*, 9737-9745.
- (245) Ourdjini, O.; Pawlak, R.; Abel, M.; Clair, S.; Chen, L.; Bergeon, N.; Sassi, M.; Oison, V.; Debierre, J. M.; Coratger, R., *et al.* Substrate-Mediated Ordering and Defect Analysis of a Surface Covalent Organic Framework. *Phys. Rev. B* **2011**, *84*, 125421-125429.
- (246) Wang, W. H.; Shi, X. Q.; Wang, S. Y.; Van Hove, M. A.; Lin, N. Single-Molecule Resolution of an Organometallic Intermediate in a Surface-Supported Ullmann Coupling Reaction. *J. Am. Chem. Soc.* **2011**, *133*, 13264-13267.
- (247) Tran-Van, A.-F.; Wegner, H., *Strategies in Organic Synthesis for Condensed Arenes, Coronene, and Graphene*. Springer Berlin Heidelberg: 2013; p 37.
- (248) Ishii, Y.; Song, H. Y.; Kato, H.; Takatori, M.; Kawasaki, S. Facile Bottom-up Synthesis of Graphene Nanofragments and Nanoribbons by Thermal Polymerization of Pentacenes. *Nanoscale* **2012**, *4*, 6553-6561.
- (249) Geim, A. K.; Novoselov, K. S. The Rise of Graphene. *Nat. Mater.* **2007**, *6*, 183-191.
- (250) Batzill, M. The Surface Science of Graphene: Metal Interfaces, CVD Synthesis, Nanoribbons, Chemical Modifications, and Defects. *Surf. Sci. Rep.* **2012**, *67*, 83-115.
- (251) Kwak, J.; Chu, J. H.; Choi, J.-K.; Park, S.-D.; Go, H.; Kim, S. Y.; Park, K.; Kim, S.-D.; Kim, Y.-W.; Yoon, E., *et al.* Near Room-Temperature Synthesis of Transfer-Free Graphene Films. *Nat. Commun.* **2012**, *3*, 645-652.
- (252) Lobo-Checa, J.; Okuda, T.; Hengsberger, M.; Patthey, L.; Greber, T.; Blaha, P.; Osterwalder, J. Hidden Surface States on Pristine and H-Passivated Ni(111): Angle-Resolved Photoemission and Density-Functional Calculations. *Phys. Rev. B* **2008**, *77*, 075415-075422.
- (253) Dahal, A.; Batzill, M. Graphene-Nickel Interfaces: A Review. *Nanoscale* **2014**, *6*, 2548-2562.

- (254) Gamo, Y.; Nagashima, A.; Wakabayashi, M.; Terai, M.; Oshima, C. Atomic Structure of Monolayer Graphite Formed on Ni(111). *Surf. Sci.* **1997**, *374*, 61-64.
- (255) Giovannetti, G.; Khomyakov, P. A.; Brocks, G.; Karpan, V. M.; van den Brink, J.; Kelly, P. J. Doping Graphene with Metal Contacts. *Phys. Rev. Lett.* **2008**, *101*, 026803-026806.
- (256) Massimi, L.; Lisi, S.; Pacile, D.; Mariani, C.; Betti, M. G. Interaction of Iron Phthalocyanine with the Graphene/Ni(111) System. *Beilstein J. Nanotechnol.* **2014**, *5*, 308-312.
- (257) MacLeod, J. M.; Rosei, F. Molecular Self-Assembly on Graphene. *Small* **2014**, *10*, 1038–1049.
- (258) Martínez-Galera, A. J.; Nicoara, N.; Martínez, J. I.; Dappe, Y. J.; Ortega, J.; Gómez-Rodríguez, J. M. Imaging Molecular Orbitals of Ptcd<sub>a</sub> on Graphene on Pt(111): Electronic Structure by STM and First-Principles Calculations. *J. Phys. Chem. C* **2014**, *118*, 12782-12788.
- (259) Bianchini, F.; Patera, L. L.; Peressi, M.; Africh, C.; Comelli, G. Atomic Scale Identification of Coexisting Graphene Structures on Ni(111). *J. Phys. Chem. Lett.* **2014**, *5*, 467-473.
- (260) Addou, R.; Dahal, A.; Sutter, P.; Batzill, M. Monolayer Graphene Growth on Ni(111) by Low Temperature Chemical Vapor Deposition. *Appl. Phys. Lett.* **2012**, *100*, 021601-021603.
- (261) Iwasaki, T.; Zakharov, A. A.; Eelbo, T.; Waśniowska, M.; Wiesendanger, R.; Smet, J. H.; Starke, U. Formation and Structural Analysis of Twisted Bilayer Graphene on Ni(111) Thin Films. *Surf. Sci.* **2014**, *625*, 44-49.
- (262) Usachov, D.; Brzhezinskaya, M.; Shikin, A. M.; Adamchuk, V. K. Electronic Structure of Pentacene on Ni(110): Comparison with Graphene. *Fullerenes, Nanotubes and Carbon Nanostruct.* **2010**, *18*, 487-492.
- (263) Talyzin, A. V.; Luzan, S. M.; Leifer, K.; Akhtar, S.; Fetzer, J.; Cataldo, F.; Tsybin, Y. O.; Tai, C. W.; Dzwilewski, A.; Moons, E. Coronene Fusion by Heat Treatment: Road to Nanographenes. *J. Phys. Chem. C* **2011**, *115*, 13207-13214.
- (264) Baker, B. G.; Johnson, B. B.; Maire, G. L. C. Photoelectric Work Function Measurements on Nickel Crystals and Films. *Surf. Sci.* **1971**, *24*, 572-586.
- (265) Voloshina, E.; Dedkov, Y. Graphene on Metallic Surfaces: Problems and Perspectives. *Phys. Chem. Chem. Phys.* **2012**, *14*, 13502-13514.

- (266) Zhao, W.; Kozlov, S. M.; Hofert, O.; Gotterbarm, K.; Lorenz, M. P. A.; Vines, F.; Papp, C.; Gorling, A.; Steinruck, H. P. Graphene on Ni(111): Coexistence of Different Surface Structures. *J. Phys. Chem. Lett.* **2011**, *2*, 759-764.
- (267) Gao, H.-Y.; Held, P. A.; Knor, M.; Mück-Lichtenfeld, C.; Neugebauer, J.; Studer, A.; Fuchs, H. Decarboxylative Polymerization of 2,6-Naphthalenedicarboxylic Acid at Surfaces. *J. Am. Chem. Soc.* **2014**, *136*, 9658-9663.
- (268) Liu, Z. P.; Hu, P. General Rules for Predicting Where a Catalytic Reaction Should Occur on Metal Surfaces: A Density Functional Theory Study of C-H and C-O Bond Breaking/Making on Flat, Stepped, and Kinked Metal Surfaces. *J. Am. Chem. Soc.* **2003**, *125*, 1958-1967.
- (269) Norskov, J. K.; Bligaard, T.; Logadottir, A.; Bahn, S.; Hansen, L. B.; Bollinger, M.; Benggaard, H.; Hammer, B.; Sljivancanin, Z.; Mavrikakis, M., *et al.* Universality in Heterogeneous Catalysis. *J. Catal.* **2002**, *209*, 275-278.
- (270) Patera, L. L.; Africh, C.; Weatherup, R. S.; Blume, R.; Bhardwaj, S.; Castellarin-Cudia, C.; Knop-Gericke, A.; Schloegl, R.; Comelli, G.; Hofmann, S., *et al.* In Situ Observations of the Atomistic Mechanisms of Ni Catalyzed Low Temperature Graphene Growth. *ACS Nano* **2013**, *7*, 7901-7912.
- (271) Allard, A.; Wirtz, L. Graphene on Metallic Substrates: Suppression of the Kohn Anomalies in the Phonon Dispersion. *Nano Lett.* **2010**, *10*, 4335-4340.
- (272) Busse, C.; Lazic, P.; Djemour, R.; Coraux, J.; Gerber, T.; Atodiresei, N.; Caciuc, V.; Brako, R.; N'Diaye, A. T.; Blugel, S., *et al.* Graphene on Ir(111): Physisorption with Chemical Modulation. *Phys. Rev. Lett.* **2011**, *107*, 036101-036104.
- (273) De Arco, L. G.; Zhang, Y.; Kumar, A.; Zhou, C. W. Synthesis, Transfer, and Devices of Single- and Few-Layer Graphene by Chemical Vapor Deposition. *IEEE Trans. Nanotechnology* **2009**, *8*, 135-138.
- (274) Katz, G. The Epitaxy of Copper on Sapphire. *Appl. Phys. Lett.* **1968**, *12*, 161-163.
- (275) Reddy, K. M.; Gledhill, A. D.; Chen, C.-H.; Drexler, J. M.; Padture, N. P. High Quality, Transferrable Graphene Grown on Single Crystal Cu(111) Thin Films on Basal-Plane Sapphire. *Appl. Phys. Lett.* **2011**, *98*, 113117-113119.
- (276) Troullier, N.; Martins, J. L. Efficient Pseudopotentials for Plane-Wave Calculations. *Phys. Rev. B* **1991**, *43*, 1993-2006.
- (277) Kosugi, T.; Miyake, T.; Ishibashi, S.; Arita, R.; Aoki, H. Ab Initio Electronic Structure of Solid Coronene: Differences from and Commonalities to Picene. *Phys. Rev. B* **2011**, *84*, 020507- 020511.

- (278) Shewchuk, J. R., *An Introduction to the Conjugate Gradient Method without the Agonizing Pain*. Carnegie Mellon University: 1994; p 56.
- (279) Duben, A. J. Huckel Theory Examination of Hydrodesulfurization of Thiophene and Monomethylthiophenes. *J. Phys. Chem.* **1978**, *82*, 348-354.
- (280) Tourillon, G.; Garnier, F. New Electrochemically Generated Organic Conducting Polymers. *J. Electroanal. Chem.* **1982**, *135*, 173-178.
- (281) Maksymovych, P.; Yates, J. T. Propagation of Conformation in the Surface-Aligned Dissociation of Single  $\text{CH}_3\text{SSCH}_3$  Molecules on Au(111). *J. Am. Chem. Soc.* **2006**, *128*, 10642-10643.
- (282) Weigelt, S.; Busse, C.; Bombis, C.; Knudsen, M. M.; Gothelf, K. V.; Laegsgaard, E.; Besenbacher, F.; Linderoth, T. R. Surface Synthesis of 2d Branched Polymer Nanostructures. *Angew. Chem., Int. Ed.* **2008**, *47*, 4406-4410.
- (283) Okawa, Y.; Aono, M. Nanoscale Control of Chain Polymerization. *Nature* **2001**, *409*, 683-684.
- (284) Richardson, N. V.; Campuzano, J. C. The Adsorption of Thiophene on a Cu(111) Surface. *Vacuum* **1981**, *31*, 449-451.
- (285) Di Giovannantonio, M.; El Garah, M.; Lipton-Duffin, J.; Meunier, V.; Cardenas, L.; Fagot Revurat, Y.; Cossaro, A.; Verdini, A.; Perepichka, D. F.; Rosei, F., *et al.* Insight into Organometallic Intermediate and Its Evolution to Covalent Bonding in Surface-Confined Ullmann Polymerization. *ACS Nano* **2013**, *7*, 8190-8198.
- (286) Krasnikov, S. A.; Doyle, C. M.; Sergeeva, N. N.; Preobrajenski, A. B.; Vinogradov, N. A.; Sergeeva, Y. N.; Zakharov, A. A.; Senge, M. O.; Cafolla, A. A. Formation of Extended Covalently Bonded Ni Porphyrin Networks on the Au(111) Surface. *Nano Res.* **2011**, *4*, 376-384.
- (287) Blunt, M. O.; Russell, J. C.; Champness, N. R.; Beton, P. H. Templating Molecular Adsorption Using a Covalent Organic Framework. *Chem. Commun.* **2010**, *46*, 7157-7159.
- (288) McCarty, G. S.; Weiss, P. S. Formation and Manipulation of Protopolymer Chains. *J. Am. Chem. Soc.* **2004**, *126*, 16772-16776.
- (289) Saywell, A.; Schwarz, J.; Hecht, S.; Grill, L. Polymerization on Stepped Surfaces: Alignment of Polymers and Identification of Catalytic Sites. *Angew. Chem., Int. Ed.* **2012**, *51*, 5096-5100.

- (290) Schlogl, S.; Heckl, W. M.; Lackinger, M. On-Surface Radical Addition of Triply Iodinated Monomers on Au(111)-the Influence of Monomer Size and Thermal Post-Processing. *Surf. Sci.* **2012**, *606*, 999-1004.
- (291) Rosei, F.; Schunack, M.; Naitoh, Y.; Jiang, P.; Gourdon, A.; Laegsgaard, E.; Stensgaard, I.; Joachim, C.; Besenbacher, F. Properties of Large Organic Molecules on Metal Surfaces. *Prog. Surf. Sci.* **2003**, *71*, 95-146.
- (292) Rogers, J. A.; Huang, Y. G. A Curvy, Stretchy Future for Electronics. *Proc. Natl. Acad. Sci. U. S. A* **2009**, *106*, 10875-10876.
- (293) De Feyter, S. Surface Patterning from 2d to 3d. *Nat. Chem.* **2011**, *3*, 14-15.
- (294) Kushmerick, J. Nanotechnology Molecular Transistors Scrutinized. *Nature* **2009**, *462*, 994-995.
- (295) Dadvand, A.; Moiseev, A. G.; Sawabe, K.; Sun, W. H.; Djukic, B.; Chung, I.; Takenobu, T.; Rosei, F.; Perepichka, D. F. Maximizing Field-Effect Mobility and Solid-State Luminescence in Organic Semiconductors. *Angew. Chem., Int. Ed.* **2012**, *51*, 3837-3841.
- (296) Braunschweig, A. B.; Huo, F. W.; Mirkin, C. A. Molecular Printing. *Nat. Chem.* **2009**, *1*, 353-358.
- (297) Zhong, X.; Bailey, N. A.; Schesing, K. B.; Bian, S. D.; Campos, L. M.; Braunschweig, A. B. Materials for the Preparation of Polymer Pen Lithography Tip Arrays and a Comparison of Their Printing Properties. *J. Polym. Sci. Pol. Chem.* **2013**, *51*, 1533-1539.
- (298) Bellido, E.; de Miguel, R.; Ruiz-Molina, D.; Lostao, A.; Maspoch, D. Controlling the Number of Proteins with Dip-Pen Nanolithography. *Adv. Mater.* **2010**, *22*, 352-355.
- (299) Chai, J. A.; Wong, L. S.; Giam, L.; Mirkin, C. A. Single-Molecule Protein Arrays Enabled by Scanning Probe Block Copolymer Lithography. *Proc. Natl. Acad. Sci. U. S. A.* **2011**, *108*, 19521-19525.
- (300) Campbell, R. B.; Robertson, J. M.; Trotter, J. The Crystal and Molecular Structure of Pentacene. *Acta Cryst.* **1961**, *14*, 705-711.
- (301) Sheraw, C. D.; Jackson, T. N.; Eaton, D. L.; Anthony, J. E. Functionalized Pentacene Active Layer Organic Thin-Film Transistors. *Adv. Mater.* **2003**, *15*, 2009-2011.
- (302) Kim, S. C.; Lee, S.; Gomez, E. D.; Anthony, J. E.; Loo, Y. L. Solvent-Dependent Electrical Characteristics and Stability of Organic Thin-Film Transistors with Drop Cast Bis(Triisopropylsilylethynyl) Pentacene. *Appl. Phys. Lett.* **2008**, *93*, 103302-103304.

